Estimation of phase error limits for PSK-modulated sweep-spread carrier signal

K.G. Kebkal *, R. Bannasch **, A.G. Kebkal **

* State oceanarium of Ukraine, 7, Epronovskaya, 99024 Sevastopol, Ukraine, *kebkal@ua.fm*

** Evologics GmbH, Ackerstrasse 71-76 (ACK1), Berlin, 13355 Germany, *info@evologics.de*

Abstract - Sweep-Spread Carrier (S2C) communication method that has been recently developed especially for application in shallow water channels realizes frequency spread of a transmitted signal via its multiplication with a sequence of linear sweeps. This provides significant processing improvement on receiving side enabling clear separation of multipath arrivals by converting their time delays into their frequency reallocations. To provide a most effective and inexpensive filtering, a matched filter is considered to be a core part of the S2C demodulator, which uses a synchronous replica of the sweep-spread carrier signal as the reference signal for the matched filtering. However, if a frequency modulated carrier is applied for data transmission, the mechanism of evaluation of the information parameter (phase) have no strict mathematical justification. By use of frequency modulated carrier the output of matched filter contains the desired phase value, however, the methodical error of evaluation of filter output (its real and imaginary part) is unknown value, which cannot be found via estimation of define integral of correspondent oscillation function. The paper derives expression, which allows to evaluate the methodical error in analytical way in form of integrals of elementary oscillation functions.

I Introduction

During acoustic communication over underwater channels of practical interest incoherent or half-coherent modulation schemes are mostly used [2]. While incoherent receivers are characterized with a small frequency efficiency and correspondingly small datarate, and coherent detectors do not provide stable communication (owing to unstable properties of equalizers), half-coherent demodulation schemes represent a compromise solution for acoustic telemetry systems especially designed for practical applications in dynamic multipath acoustic channels. Generation of a transmitting symbol and evaluation of a digital estimate in receiver side is usually realized via differential phase shift keying (DPSK). Digital estimate of DPSK symbol is defined not via its own value (zero or one), but via comparison of current estimate with previous one.

Symbol estimate is usually computed by means of matched filtering. If the traditional (frequency constant) carrier is used, the mechanism of estimation of information parameter is mathematically justified: output of the matched filter consist of cosine and sine function of evaluated phase angle, as well as components, which determine methodical errors of estimation of real and imaginary part of matched filter output. In conventional case (use of frequency constant carrier) these errors do not extend certain permissible value [3]. It is well-known that they can be found in result of integration of following functions on the interval of the transmitting symbol:

$$e_{xc}(i) = \frac{\sqrt{E}}{T}\int_0^T \cos(2\omega_0 t + \theta_i + \theta_r)dt = \\ = \sqrt{E}\frac{\sin(\omega_0 T)}{\omega_0 T}\cos(\omega_0 T + \theta_i + \theta_r) \quad (1)$$

$$e_{xs}(i) = \frac{\sqrt{E}}{T}\int_0^T \sin(2\omega_0 t + \theta_i + \theta_r)dt = \\ = \sqrt{E}\frac{\sin(\omega_0 T)}{\omega_0 T}\sin(\omega_0 T + \theta_i + \theta_r) \quad (2)$$

where E - is energy-flux density of acoustic wave, T - symbol duration, ω_0 - (angular) carrier frequency, θ_i - discrete phase value (transmitting information), θ_r - arbitrary phase, usually random value uniformly distributed between 0 and 2π. Maxima of these errors take on following values:

$$\max(|e_{xc}(i)|) = \max(|e_{xs}(i)|) = \sqrt{E}\frac{\sin(\omega_0 T)}{\omega_0 T} \quad (3)$$

In practical underwater applications (for telemetry frequencies and datarates used) the ratio $\frac{\sin(\omega_0 T)}{\omega_0 T}$ takes on minor values. Giving a correspondent symbol duration and carrier frequency, maximum values of (1) and (2) become negligible and the errors do not have a serious effect on result of phase estimation.

If non-conventional (frequency modulated) sweep-spread carrier [1] is applied for data transmission, the mechanism of evaluation of the information parameter (phase) have no strict mathematical justification. By use of frequency modulated carrier the output of matched filter also contains the desired phase value, however, the methodical error of evaluation of filter output (its real and imaginary part) cannot be found via estimation of define integral of correspondent oscillation function.

This can be explained in the following way. Let the carrier signal is a linearly increasing frequency modulated

0-7803-8669-8/04/$20.00

(LIFM) oscillation. Thus, a transmitting PSK symbol can be represented in form:

$$s_y(i,t) = \exp\left\{\sqrt{\frac{2E}{T}}\exp[j(\omega_b t + mt^2 + \theta_i)]\right\} \quad (4)$$

where E, T, θ_i defined above, $m = \frac{\omega_e - \omega_b}{2T}$ - the gradient of frequency modulation of the carrier signal [1], ω_b and ω_e - beginning and final angular frequency values of the LIFM carrier signal.

In absence of interference and attetuation the received signal can be written as:

$$r_y(i,t) = \sqrt{\frac{2E}{T}}\cos(\omega_0 t + mt^2 + \theta_i + \theta_r) + n(t) \quad (5)$$

Let a matched filter or its analog is used for demodulation of the signal. And let us find a scalar product of the received signal and heterodyne signal (its in-phase as well as quadrature components). If the signal is powerful enough, the output of the matched filter is equal to $y(i) = y_c(i) + jy_s(i)$, where

$$\begin{aligned} y_c(i) &= \sqrt{\frac{2}{T}}\int_0^T r_y(t)\cos(\omega_b t + mt^2)dt = \\ &= \sqrt{E}\cos(\theta_i + \theta_r) + \\ &+ \frac{\sqrt{E}}{T}\int_0^T \cos(2\omega_b t + 2mt^2 + \theta_i + \theta_r)dt \quad (6) \end{aligned}$$

$$\begin{aligned} y_s(i) &= \sqrt{\frac{2}{T}}\int_0^T r_y(t)\sin(\omega_b t + mt^2)dt = \\ &= \sqrt{E}\sin(\theta_i + \theta_r) + \\ &+ \frac{\sqrt{E}}{T}\int_0^T \sin(2\omega_b t + 2mt^2 + \theta_i + \theta_r)dt \quad (7) \end{aligned}$$

The right side of each equation ($y_c(i)$ or $y_s(i)$) is also represented by two items. Analogously to the conventional case the first item is a variable containing desired phase value. The second one is a variable that modifies the desired phase value and represents a methodical error, which is connected to the method of matched filtering. The error is referred later as $e_{yc}(i)$ in the equation for $y_c(i)$ and correspondingly as $e_{ys}(i)$ for $y_s(i)$. Further, evaluation of $e_{yc}(i)$ and $e_{ys}(i)$ is carried out.

The second item of the right side in (6) and (7) is rewritten in form:

$$e_{yc}(i) = \frac{\sqrt{E}}{T}\int_0^T \cos(2\omega_b t + 2mt^2 + \theta_i + \theta_r)dt \quad (8)$$

$$e_{ys}(i) = \frac{\sqrt{E}}{T}\int_0^T \sin(2\omega_b t + 2mt^2 + \theta_i + \theta_r)dt \quad (9)$$

It is obvious that functions, whose integrals must be evaluated, are not harmonic signals. They represent linearly rising frequency modulated signals with doubled frequency gradients. It is evident that an antiderivative of function like $sin(x^2)$ or $cos(x^2)$ is not an elementary function and its integration cannot be carried out in analytical way. The special case of such integral computation (on the interval of $\pm\infty$) [4] does not satisfy practical applications, because in practical case the filter have to deal with short symbol durations and correspondingly narrow integration intervals. Thus, magnitude of phase error is unknown if the sweep spread carrier is used.

In order to justify the principal possibility of application of matched filters in receivers working with symbols transmitted by means of LIFM carrier, an evaluation of (maximum) error in process of phase estimation is desired.

Evaluation of maximum error on the output of the matched filter cannot be carried out by means of simple geometrical constructions. In contrast to a harmonic oscillation, the square of each halfwave of LIFM oscillation has its own (different from others) value. At that, for example, subtraction of the square of each negative halfwave from the square of positive halfwave never gives a zero result. Therefore, conclusion about maximum possible error cannot be provided by geometrical analysis or logical argumentation.

II Evaluation of phase error limits for PSK-symbols with a sweep spread carrier

To find solution, some known data are initially used. It is obvious that in equation (4) for LIFM carrier with $m = 0$ a conventional harmonical signal is to deals with. In this case the maximum phase error is defined in (3). If possible to prove that maximum error on output of the matched filter, which processes symbols with LIFM carrier ($m > 0$), has a value less than (3), then the application of matched filters for LIFM symbols is justified satisfying requirements on accuracy of phase estimation in received PSK symbol.

Thus, it is necessary to prove that the following expression

$$\max_t \left| \int_0^T cos(\omega t + mt^2 + \theta)dt \right| < \max_t \left| \int_0^T cos(\omega t + \theta)dt \right| \quad (10)$$

is valid for all ω, t, θ and positive m earlier used in [1].

To prove validity of (10), some statements must be formulated and proved, at first.

Statement 1. *Define integral of function of linearly increasing frequency-modulated sine oscillation with zero beginning phase and beginning frequency ω on the interval of its first positive halfwave has a value, which is less than a value of define integral of function of harmonic sine oscillation, evaluated on the interval its first positive halfwave, with the same amplitude, frequency ω and zero beginning phase.*

To prove the statement, two squares will be compared. The first one is the square that is circumscribed with the curve of LIFM sine oscillation $\cos(\omega t + mt^2 - \pi/2)$ on the interval of its first positive halfwave. The second one is the

square that is circumscribed with the curve of a harmonic sine oscillation $\cos(\omega t - \pi/2)$ on the interval of its first positive halfwave, as well. These functions are represented in fig. 1 with solid line and dotted line correspondingly.

Initially, special points, arguments and interested time intervals are defined. The first point is the extremum of function. For the functions in fig. 1 the first extremum is achieved at time point, where the function argument is equal to zero. Then, for the LIFM signal this time point is given by $\tau_{xfm} = \dfrac{\sqrt{\omega^2 + 2\pi m} - \omega}{2m}$, and for the harmonic signal of frequency ω this time point is $\tau_{xm} = \pi/2\omega$. The second value of interest is the instant frequency of the LIFM oscillation at the time point τ_{xfm}. It can be obtained from the equation

$$\begin{aligned} &f(t + \tau_{xfm}) = \\ &= cos(\omega(t + \tau_{xfm}) + m(t + \tau_{xfm})^2 - \pi/2) = \\ &= cos((\omega + 2m\tau_{xfm})t + mt^2 + (\omega\tau_{xfm} + m\tau_{xfm}^2 - \pi/2)). \end{aligned} \tag{11}$$

Following from (11), at time point τ_{xfm} the instant frequency of the signal (first item of the argument) is equal to

$$\omega_{xfm} = (\omega + 2m\tau_{xfm}). \tag{12}$$

The third value of interest is the time interval between zero crossing points (duration of the first halfwave), that is the time interval between time points, where the function is equal to $-\pi/2$ and $\pi/2$. Then, for the LIFM signal this time is given by $\tau_{zfm} = \dfrac{\sqrt{\omega^2 + 4\pi m} - \omega}{2m}$, and for the harmonic oscillation by $\tau_{zm} = \pi/\omega$.

Proof.

While the compared squares do not depend on the fact, how the correspondent functions are allocated in time, the first positive halfwaves are superposed so that their extremuma are situated opposite to a certain zero time point like in fig. 2. It means, the ordinate axis with reference point that is equal to zero is positioned in τ_{xfm} after beginning of the LIFM oscillation or in τ_{xm} after beginning of the harmonic oscillation.

Further the functions represented in fig. 2 are compared on two separate intervals $[-\tau_{xfm}, 0]$ and $[0, \tau_{zfm} - \tau_{xfm}]$.

On the interval $[0, \tau_{zfm} - \tau_{xfm}]$ the compared functions can be written as $\cos(\omega t)$ and $\cos(\omega_{xfm}t + mt^2)$, and if

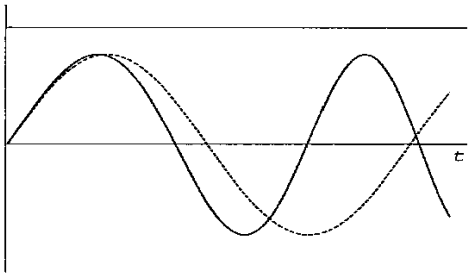

Fig. 1. Compared functions: LIFM oscillation (solid line) and harmonic oscillation (dotted line)

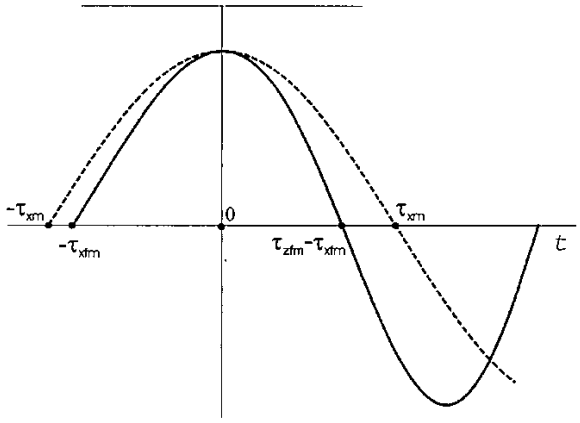

Fig. 2. Compared functions after superposition of their first extremuma

the following expression

$$\cos(\omega_{xfm}t + mt^2) < cos(\omega t) \tag{13}$$

is true, then, while both functions descend on this interval, the inequation $\omega_{xfm}t + mt^2 > \omega t$ must be valid. To verify that, the inequation (keeping in mind (12)) is rewritten in form

$$\omega t + (2m\tau_{xfm} + mt)t > \omega t \tag{14}$$

While inside the interval time t is positive and the item in parenthesis is positive, as well, then the inequation (14) and correspondingly (13) are valid.

In the line of negative time values the compared functions (inside of $[-\tau_{xfm}, 0]$) can be written as $\cos(\omega\hat{t})$ and $\cos(\omega_{xfm}\hat{t} - m\hat{t}^2)$, where $\hat{t} = -t$. It is necessary to notice that the frequency gradient m is negative here, because instant frequencies of the LIFM oscillation decrease in the line of decreasing time. Similarly, if the following expression

$$\cos(\omega_{xfm}\hat{t} - m\hat{t}^2) = \cos((\omega + 2m\tau_{xfm})\hat{t} - m\hat{t}^2) < \cos(\omega\hat{t}) \tag{15}$$

is valid, then, while both functions (inside the interval) descend in the direction of decreasing time, the inequation $\omega\hat{t} + (2m\tau_{xfm} - m\hat{t})\hat{t} > \omega\hat{t}$ must be also valid. It is obvious that the inequation is valid inside the interval $0 < \hat{t} < 2\tau_{xfm}$, or turning back to current time (ascending values) the inequation is valid inside the interval $-2\tau_{xfm} < t < 0$. Since the interval of interest $[-\tau_{xfm}, 0]$ is situated inside the obtained $[-2\tau_{xfm}, 0]$, one can conclude that the inequation (15) is also valid.

Thus, in entire interval $[-\tau_{xfm}, \tau_{zfm} - \tau_{xfm}]$ the function $\cos(\omega_{xfm}t + mt^2)$ takes on values that are less than those of the function $\cos(\omega t)$. Correspondingly, in the same interval, the square, which is circumscribed with the curve $\cos(\omega_{xfm}t + mt^2)$, is less than the square, which is circumscribed with the curve $\cos(\omega t)$.

Moreover, since the duration of the first positive halfwave of the harmonic oscillation exceeds the duration

of the first positive halfwave of the LIFM oscillation, the following expression is also valid:

$$\int_{-\tau_{zfm}}^{\tau_{zfm}-\tau_{xfm}} cos(\omega_{xfm}t + mt^2)dt \; < \; \int_{-\tau_{zfm}}^{\tau_{zfm}-\tau_{xfm}} cos(\omega t)dt \; < \; \int_{-\tau_{zm}}^{\tau_{zm}} cos(\omega t)dt.$$

Turning back to original allocation of the oscillations in time, in which the beginning points of the compared halfwaves coincide, and bringing the ordinate axis back to original point like in fig. 1, one can conclude that

$$\int_0^{\tau_{zfm}} cos(\omega t + mt^2 - \pi/2)dt < \int_0^{\tau_{zm}} cos(\omega t - \pi/2)dt. \quad (16)$$

This validity of this expression proves the validity of Statement 1.

It is necessary also to notice that changing the beginning phase to the opposite value, one can analogously justify the validity of the following inequation:

$$\left| \int_0^{\tau_{zfm}} cos(\omega t + mt^2 + \pi/2)dt \right| < \left| \int_0^{\tau_{zm}} cos(\omega t + \pi/2)dt \right|. \quad (17)$$

In order to formulate the next statement, the oscillation to be compared are represented in fig. 3 (the positive halfwave interval is considered here).

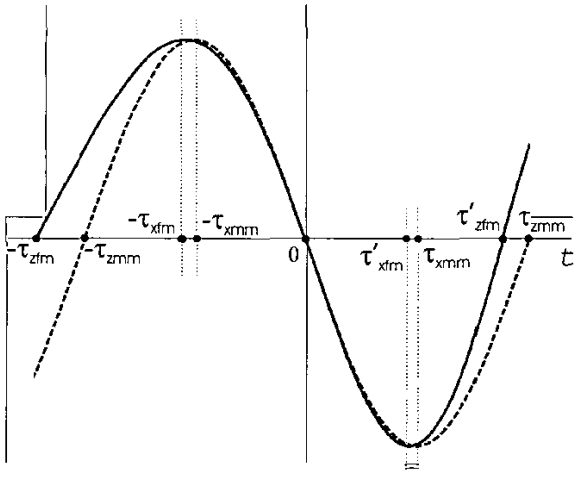

Fig. 3. Compared functions after frequency modification of the harmonic signal

As follows from fig. 3 the oscillations are allocated in time so that the last points of their positive halfwaves coincide. Let the completion of the first positive halfwave occurs in τ_{zfm} after beginning of the LIFM oscillation or in τ_{zmm} after beginning of the harmonic oscillation. We shell compare the function of LIFM oscillation, the same as above, with harmonic oscillation with the frequency, which achieves the LIFM oscillation at the moment of completion of its first positive halfwave.

Statement 2. *Define integral of function of linearly increasing frequency-modulated sine oscillation with zero beginning phase on the interval of its first positive halfwave has a value, which exceeds a value of define integral of function of harmonic sine oscillation, evaluated on the interval of its first positive halfwave, with the same amplitude, zero beginning phase, but with a frequency that achieves the LIFM oscillation at the moment of completion of its first positive halfwave.*

To prove the statement, we shell compare the square, which is circumscribed with the curve of function $cos(\omega t + mt^2 - \pi/2)$ on the interval of its first positive halfwave, with the square, which is circumscribed with the curve of function $cos(\omega_{zfm}t - \pi/2)$ on the interval of its first positive halfwave, as well.

Similarly, special points, arguments and interested time intervals are defined. Duration of first halfwave τ_{zfm} for the LIFM oscillation has the same value as above: $\tau_{zfm} = \dfrac{\sqrt{\omega^2 + 4\pi m} - \omega}{2m}$. Duration of the first halfwave of the harmonic oscillation τ_{zmm} is specified via $\tau_{zmm} = \pi/\omega_{zfm}$, where ω_{zfm} is equal to the instant frequency that achieves the LIFM oscillation at the moment of completion of its positive halfwave and is obtained analogously to (11) from the formula:

$$\begin{aligned} &f(t + \tau_{zfm}) = \\ &= cos(\omega(t + \tau_{zfm}) + m(t + \tau_{zfm})^2 - \pi/2) = \\ &= cos((\omega + 2m\tau_{zfm})t + mt^2 + (\omega\tau_{zfm} + m\tau_{zfm}^2 - \pi/2)). \end{aligned} \quad (18)$$

As follows from (18), at the moment τ_{zfm} the instant frequency (first item in the argument) achieves the value

$$\omega_{zfm} = (\omega + 2m\tau_{zfm}). \quad (19)$$

The extremum of the LIFM oscillation on the interval of its first halfwave is equal to $\tau_{xfm} = \dfrac{\sqrt{\omega^2 + 2\pi m} - \omega}{2m}$ as before, and the extremum of the harmonic oscillation with the frequency ω_{zfm} on the interval of its first halfwave is achieved in $\tau_{zmm} = \pi/2\omega_{zfm}$.

Proof.

As well as during the proof of the first statement, the first positive halfwaves of compared functions are superposed so that their extremuma are situated opposite to a certain zero time point like in fig. 3. Similarly, the functions that are represented in the figure are compared separately on the intervals $[-\tau_{zmm}, 0]$ and $[0, \tau_{zmm}]$.

On the interval of $[0, \tau_{xfm}]$ the compared functions can be written as $\cos(\omega_{zfm}t)$ and $\cos(\omega_{xfm}t + mt^2)$, and if the following expression

$$\cos(\omega_{xfm}t + mt^2) > \cos(\omega_{zfm}t) \quad (20)$$

is true, then, since the compared functions descend, the inequation $\omega_{xfm}t + mt^2 < \omega_{zfm}t$ must be valid. After substitution ω_{xfm} and ω_{zfm}, it becomes obvious that the time interval $[0, 2(\tau_{zfm} - \tau_{xfm})]$ is that one, on which the

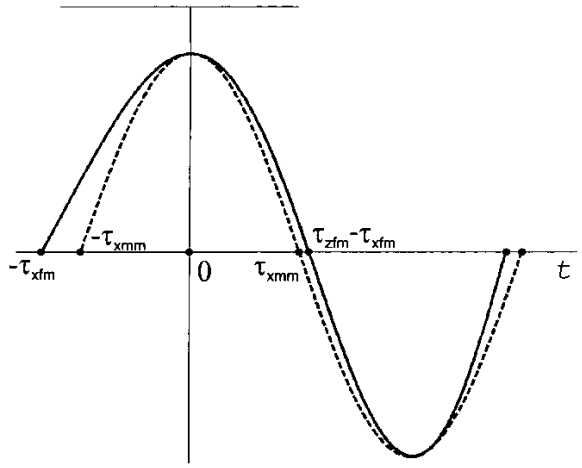

Fig. 4. Comparison of the LIFM oscillation function with the harmonic function, modified in frequency, on the interval of the first positive halfwave

inequation is valid. The interval of interest $[0, \tau_{xmm}]$ is situated inside of the last one, therefore the expression (20) is valid, as well.

In the line of decreasing time (inside of $[-\tau_{xmm}, 0]$) the compared functions can be written correspondingly as $\cos(\omega_{zfm}\hat{t})$ and $\cos(\omega_{xfm}\hat{t} - m\hat{t}^2)$, where $\hat{t} = -t$. Just as above, it ought to be noticed that the frequency gradient m is negative here as well, because instant frequencies of the LIFM oscillation decrease in the line of decreasing time.

If the following inequation

$$\cos(\omega_{xfm}\hat{t} - m\hat{t}^2) > \cos(\omega_{zfm}\hat{t}) \tag{21}$$

is valid, then, since both functions descend in the direction of negative time values, the following inequation

$$\omega_{xfm}\hat{t} - m\hat{t}^2 < \omega_{zfm}\hat{t} \tag{22}$$

must be true.

Just as above, after substitution of ω_{xfm} and ω_{zfm}, it becomes obvious that the time interval, on which inequation (22) is valid, is equal to $[-2(\tau_{zfm} - \tau_{xfm}), 0]$. The interval of interest $[-\tau_{xmm}, 0]$ is situated inside of the last one, therefore one can conclude that expression (21) is valid, as well.

Thus, on entire interval $[-\tau_{xmm}, \tau_{xmm}]$ the function $\cos(\omega_{xfm}t + mt^2)$ takes on values less than those of the function $\cos(\omega_{zfm}t)$. Correspondingly, in the same interval the square, which is circumscribed with the curve $\cos(\omega_{xfm}t + mt^2)$, is less than the square, which is circumscribed with the curve $\cos(\omega_{zfm}t)$. It means that the following expression

$$\int_{-\tau_{xmm}}^{\tau_{xmm}} cos(\omega_{zfm}t)dt < \int_{-\tau_{xmm}}^{\tau_{xmm}} cos(\omega_{xfm}t + mt^2)dt$$

is valid.

Moreover, since duration of the first halfwave of the harmonic oscillation less than duration of the first halfwave of the LIFM oscillation, and since the LIFM function takes on only positive values on the interval of its first positive halfwave, the following inequation

$$\int_{-\tau_{xmm}}^{\tau_{xmm}} cos(\omega_{zfm}t)dt < \int_{-\tau_{xfm}}^{\tau_{zfm}-\tau_{xfm}} cos(\omega_{xfm}t + mt^2)dt$$

is valid, as well.

Turning back to original allocation of the oscillations in time, when beginning points of the compared halfwaves coincide, and bringing the ordinate axis back to original point, one can conclude that

$$\int_{0}^{\tau_{zmm}} cos(\omega_{zfm}t - \pi/2)dt < \int_{0}^{\tau_{zfm}} cos(\omega t + mt^2 - \pi/2)dt. \tag{23}$$

This validity of the expression proves the validity of Statement 2.

In order to formulate the next statement, the oscillations to be compared are represented in fig. 3, but the interval of interest is the negative halfwave here.

As follows from the figure the oscillations are allocated in time so that the initial points of their negative halfwaves coincide. In the same way as above, the beginning of the first negative halfwave occurs in τ_{zfm} after beginning of the LIFM oscillation or in τ_{zmm} after beginning of the harmonic oscillation. We shell compare here the function of LIFM oscillation, the same as above, and harmonic oscillation with a frequency, which achieves the LIFM oscillation at the moment of beginning of its first negative halfwave.

Statement 3. *A module of define integral of function of linearly increasing frequency-modulated sine oscillation with zero beginning phase on the interval of its first negative halfwave has a value, which is less than a value of a module of define integral of function of harmonic sine oscillation, evaluated on the interval of its first negative halfwave, with the same amplitude, zero beginning phase, but with a frequency that achieves the LIFM oscillation at the moment of beginning of its first negative halfwave.*

Thus, we compare the square, which is circumscribed with the curve of function $cos(\omega t + mt^2 - \pi/2)$ on the interval of its first negative halfwave, with the square, which is circumscribed with the curve of function $cos(\omega_{zfm}t - \pi/2)$ on the interval of its first negative halfwave, as well.

After consideration of the interval of the first negative halfwave in fig. 3, one can conclude that apart from the sign the compared halfwaves are similar to those used during the proof of the Statement 1.

Since the module of integral of the LIFM oscillation as well as of the harmonic oscillation takes on positive values on the interval of both negative as well as positive halfwaves, the Statement 3 can be justified in the same

way as Statement 1; hence the following inequation

$$\left|\int_{\tau_{zfm}}^{\tau'_{zfm}} cos(\omega t + mt^2 - \pi/2)dt\right| < \left|\int_{\tau_{zmm}}^{2\tau_{zmm}} cos(\omega t - \pi/2)dt\right| \tag{24}$$

is valid.

Relying on statements 1-3, there is a lemma that is formulated and proved below.

Lemma 1. *A module of integral of function of linearly increasing frequency-modulated sine oscillation with zero beginning phase, evaluated on the interval of its first positive halfwave, has a value, which exceeds a value of a module of integral of the same function and the same beginning phase, evaluated on the interval of its first negative halfwave.*

To prove Lemma 1, the oscillations to be compared are represented in fig. 3.

Proof.

Based on Statement 2, it is true that

$$\int_{-\tau_{zmm}}^{0} cos(\omega t - \pi/2)dt < \int_{-\tau_{zfm}}^{0} cos(\omega t + mt^2 - \pi/2)dt, \tag{25}$$

and following from validity of Statement 3, the next expression is valid as well:

$$\left|\int_{0}^{\tau'_{zfm}} cos(\omega t + mt^2 - \pi/2)dt\right| < \left|\int_{0}^{\tau_{zmm}} cos(\omega t - \pi/2)dt\right| \tag{26}$$

and since

$$\left|\int_{0}^{\tau_{zmm}} cos(\omega t - \pi/2)dt\right| = \left|\int_{\tau_{zmm}}^{0} cos(\omega t - \pi/2)dt\right| \tag{27}$$

then one can conclude that

$$\left|\int_{0}^{\tau'_{zfm}} cos(\omega t + mt^2 - \pi/2)dt\right| < \left|\int_{\tau_{zfm}}^{0} cos(\omega t + mt^2 - \pi/2)dt\right|. \tag{28}$$

The equation (28) proves the validity of Lemma 1.

To justify the validity of (10), it is necessary to prove that for the LIFM oscillation in fig. 5 the following expression is valid for every oscillation duration (every integer or broken number of halfwaves, $(k \geq 0)$), on which the integral of function is evaluated :

$$0 \leq \int_{t_0}^{t_k+\alpha_k} \cos(\omega t + mt^2 - \pi/2)dt \leq \int_{t_0}^{t_1} \cos(\omega t + mt^2 - \pi/2)dt, \tag{29}$$

where $0 \leq \alpha_k \leq t_{k+1} - t_k$.

Lemma 2. *Define integral of function of linearly increasing frequency-modulated sine oscillation with zero beginning phase and beginning frequency ω, evaluated on an arbitrary interval of time, has a value, which is less than a value of define integral, evaluated on the same time interval, of a harmonic function of the same amplitude, beginning phase and frequency ω.*

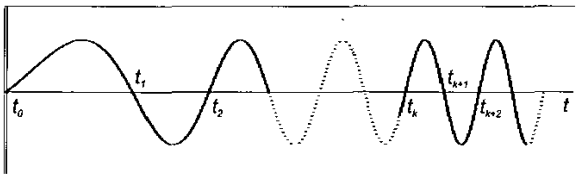

Fig. 5. LIFM carrier oscillation

To simplify expressions, the following notation is introduced:

$$\phi(t) = \omega t + mt^2 - \pi/2.$$

To prove the validity of the Lemma 2, the method of induction is applied.

Basis. Since validity of (29) is obvious for $k = 0$, we choose the value of $k = 1$ as the basis value and consider the following expression:

$$0 < \int_{t_0}^{t_1+\alpha_1} \cos\phi(t)dt < \int_{t_0}^{t_1} \cos\phi(t)dt. \tag{30}$$

This can be rewritten in form:

$$0 < \int_{t_0}^{t_1} \cos\phi(t)dt + \int_{t_1}^{t_1+\alpha_1} \cos\phi(t)dt < \int_{t_0}^{t_1} \cos\phi(t)dt. \tag{31}$$

Since the integral $\int_{t_1}^{t_1+\alpha_1} \cos\phi(t)dt$ (see fig. 6) has a negative value, the right part of the inequation in expression (31) is valid. Moreover, according to Lemma 1 the sum of integrals $\int_{t_0}^{t_1} \cos\phi(t)dt$ and $\int_{t_1}^{t_1+\alpha_1} \cos\phi(t)dt$ is positive and therefore the left inequation in expression (31) is also valid.

Induction. Let the following expression

$$0 < \int_{t_0}^{t_k+\alpha_k} \cos\phi(t)dt < \int_{t_0}^{t_1} \cos\phi(t)dt \tag{32}$$

with $0 \leq \alpha_k \leq t_{k+1} - t_k$ is valid for a k. It is necessary to prove that the following expression with $0 \leq \alpha_{k+1} \leq t_{k+2} - t_{k+1}$

$$0 < \int_{t_0}^{t_{k+1}+\alpha_{k+1}} \cos\phi(t)dt < \int_{t_0}^{t_1} \cos\phi(t)dt \tag{33}$$

is valid also for a $k+1$.

For odd k the integral with limits between 0 and $t_{k+1} + \alpha_{k+1}$ can be rewritten in form:

$$\int_{t_0}^{t_{k+1}+\alpha_{k+1}} \cos\phi(t)dt = \int_{t_0}^{t_k} \cos\phi(t)dt + \int_{t_k}^{t_{k+1}+\alpha_{k+1}} \cos\phi(t)dt \quad (34)$$

Let the second item of the right part is evaluated. Firstly, the instant frequency, which achieves the LIFM oscillation at instant t_k, must be obtained. Similarly to (12) and (19) this frequency is defined as $\omega_{t_k} = \omega + mt_k$. Then, moving the ordinate axis to the instant t_k, such as in fig. 7, the second item in (34) can be represented in form:

$$\int_{t_k}^{t_{k+1}+\alpha_{k+1}} \cos(\omega t + mt^2 - \pi/2)dt = -\int_{t_0'}^{t_1'+\alpha_1'} \cos(\omega_{t_k} t + mt^2 - \pi/2)dt, \quad (35)$$

where t_0' is new beginning point of time axis, t_1' is duration of the first halfwave of the LIFM oscillation with the beginning frequency ω_{t_k}, and α_1' is defined with limits $0 \le \alpha_1' \le t_2' - t_1'$.

While k is odd, the first halfwave, on the interval between t_0' and t_1', is negative, and the second halfwave is positive. Then, for every α_1', which is limited from t_0' to $t_2' - t_1'$, the value of integral is negative due to validity of the Lemma 1. Based on negativity of second item of right side in (34) and on assumption of induction (expression (32)), validity of right side in (33) follows. To prove the validity of left side of equation (33), the expression (34) is rewritten in form:

$$\int_{t_0}^{t_{k+1}+\alpha_{k+1}} \cos\phi(t)dt = \int_{t_0}^{t_{k-1}} \cos\phi(t)dt + \int_{t_{k-1}}^{t_{k+1}} \cos\phi(t)dt + \int_{t_{k+1}}^{t_{k+1}+\alpha_{k+1}} \cos\phi(t)dt \quad (36)$$

The limits of integration are shown in fig. 7 above. For odd k the third item of (36) is positive, because it represents an integral of $\cos\phi(t)$ on the interval of its positive halfwave between t_{k+1} and $t_{k+1}+\alpha_{k+1}$. Based on validity of the second and third items and on assumption of induction for the first item, validity of left part in expression (33) follows.

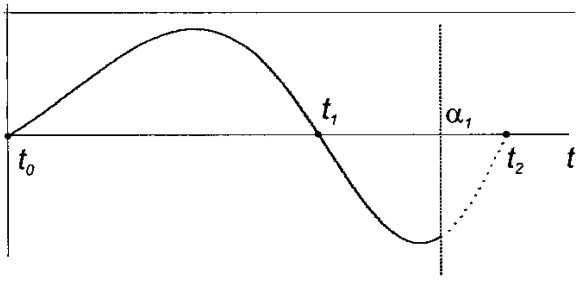

Fig. 6. Interval of the LIFM oscillation for k=0

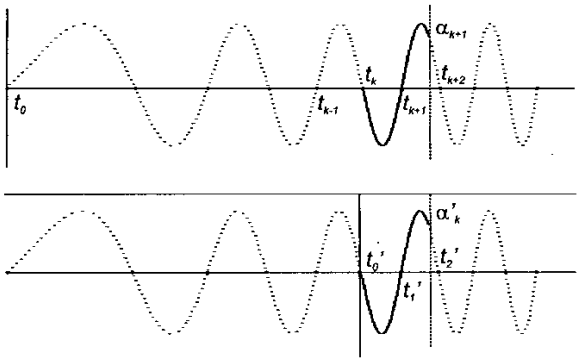

Fig. 7. The interval of the LIFM oscillation for odd k

Thus, for odd k the expression (33) is justified.

For even k (fig. 8) the expression (34) is represented in form:

$$\begin{aligned}
&\int_{t_0}^{t_{k+1}+\alpha_{k+1}} \cos\phi(t)dt = \\
&= \int_{t_0}^{t_k} \cos\phi(t)dt + \int_{t_k}^{t_{k+1}+\alpha_{k+1}} \cos\phi(t)dt < \\
&< \int_{t_0}^{t_k} \cos\phi(t)dt + \int_{t_k}^{t_{k+1}} \cos\phi(t)dt = \\
&= \int_{t_0}^{t_{k+1}} \cos\phi(t)dt = \int_{t_0}^{t_k+\alpha_k} \cos\phi(t)dt \qquad (37)
\end{aligned}$$

where $\alpha_k = t_{k+1} - t_k$ (compare the result with items of (32)). Then, based on assumption of induction for right part of (32, validity of right side in (33) follows for all even k. While on the interval between t_0 and t_k the number of positive halfwaves is equal to number of negative halfwaves for even k (fig. 8), then according to Lemma 1 the sum of integrals, where one is evaluated on the interval of positive halfwave and second one is evaluated on the interval of next negative halfwave, gives a positive value. Furthermore, according to Lemma 1, as well, the sum of integrals, where one is limited between t_k and t_{k+1} and second one is limited between t_{k+1} and $t_{k+1}+\alpha_{k+1}$, gives also a positive value. Based on positivity of the integral on entire interval between t_0 and $t_{k+1}+\alpha_{k+1}$, validity of left side in (33) follows, as well. Thus, the verity of (33) is justified for all k, what allows to assert that the following expression is valid for all α_k and t_k:

$$0 < \int_{t_0}^{t_{k+1}+\alpha_{k+1}} \cos\phi(t)dt < \int_{t_0}^{t_1} \cos\phi(t)dt. \quad (38)$$

To evaluate possible values, which takes on define integral of the LIFM oscillation, Statement 1 can be used.

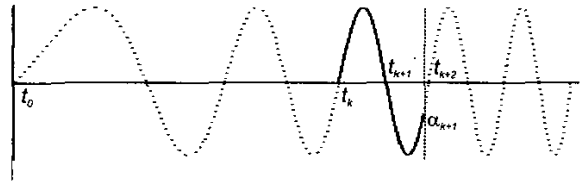

Fig. 8. Interval of the LIFM oscillation for evan k

Then, expression (38) can be rewritten in form:

$$0 < \int_{t_0}^{t_{k+1}+\alpha_{k+1}} \cos(\omega t + mt^2 - \pi/2)dt < \int_{t_0}^{t_1} \cos(\omega t - \pi/2)dt \tag{39}$$

for every α_k and t_k.

This expression defines limits, which ever takes on the integral of the LIFM oscillation, especially the right limit that is evaluated in analytical way in form of integral of an elementary function.

It is necessary to note that shifting the phase on the opposite value, validity of the following expression can be similarly proved for all α_k and t_k:

$$0 < \left| \int_{t_0}^{t_{k+1}+\alpha_{k+1}} \cos(\omega t + mt^2 + \pi/2)dt \right| < \left| \int_{t_0}^{t_1} \cos(\omega t + \pi/2)dt \right|. \tag{40}$$

Proof of validity of expressions (39) and (40) was carried out for a fixed (zero) value of the beginning phase (fig. 5). However, practical usefulness consist in particular in consideration of a general case, when the beginning phase can take on every arbitrary value θ.

Theorem. *A maximum value of define integral of function of linearly increasing frequency-modulated sine oscillation with an arbitrary beginning phase and beginning frequency ω, evaluated on an arbitrary interval of time, has a value, which is less than a maximum value of define integral, evaluated on the same time interval, of a harmonic function with the same amplitude, frequency ω and arbitrary beginning phase.*

Let the argument of cosin function in (29) is represented in form:

$$\varphi(t) = \phi(t) - \theta.$$

The oscillation shown in fig. 9 is considered below. If its beginning phase θ takes on an arbitrary value inside the interval $(0..\pi)$, then the integral of the oscillation can be represented as following sum of items:

$$\int_0^{t_k+\alpha_k} \cos\varphi(t)dt = \int_0^{t_0} \cos\varphi(t)dt + \int_{t_0}^{t_k+\alpha_k} \cos\varphi(t)dt. \tag{41}$$

where $0 \le \alpha_k \le t_{k+1} - t_k$.

It is obvious that according to Lemma 2 the second item is a positive value, which is limited according to in-

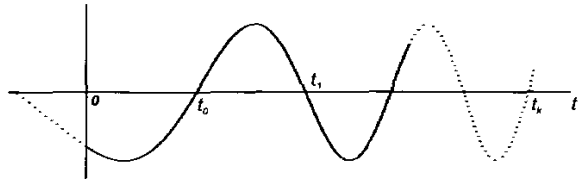

Fig. 9. Interval of the LIFM oscillation with an arbitrary beginning phase θ

equation:

$$0 < \int_{t_0}^{t_k+\alpha_k} \cos\varphi(t)dt < \int_{t_0}^{t_1} \cos\varphi(t)dt, \tag{42}$$

where $0 \le \alpha_k \le t_{k+1} - t_k$.

In the same time, it is obvious that the first item in (41) takes on negative values, if beginning phase is equal to a value between 0 and π (fig. 9). Based on this fact and according to validity of Lemma 1, validity of the next expression follows:

$$\int_0^{t_k+\alpha_k} \cos\varphi(t)dt < \int_{t_0}^{t_1} \cos\varphi(t)dt. \tag{43}$$

To obtain the left limit, it is necessary to evaluate the first item of right side in (41). The value of integral $\int_0^{t_0} \cos\varphi(t)dt$ depends on beginning phase θ and takes on a minimum value with $\theta = \pi$, that is:

$$\int_0^{t_0} \cos(\omega t + mt^2 - \pi/2 - \theta)dt \ge \int_0^{t_0} \cos(\omega t + mt^2 - 3\pi/2)dt. \tag{44}$$

Right side of inequation (44) represents a negative value, therefore according to Lemma 1 and according to validity of (43), validity of the expression below follows:

$$\int_0^{t_0} \cos(\omega t + mt^2 - 3\pi/2)dt + \int_{t_0}^{t_k+\alpha_k} \cos\varphi(t)dt < 0, \tag{45}$$

then, taking into account (44), the left limit can be specified in following form:

$$\int_0^{t_0} \cos(\omega t + mt^2 - 3\pi/2)dt + \int_{t_0}^{t_k+\alpha_k} \cos\varphi(t)dt < \int_0^{t_k+\alpha_k} \cos\varphi(t)dt. \tag{46}$$

Thus, considering (43) and (46), the interval of values, which takes on the integral $\int_0^{t_k+\alpha_k} \cos\varphi(t)dt$, can be defined via expression:

$$-\int_0^{t_0} \cos\phi(t)dt < \int_{t_0}^{t_k+\alpha_k} \cos\varphi(t)dt - \int_0^{t_0} \cos\phi(t)dt < \int_0^{t_k+\alpha_k} \cos\varphi(t)dt < \int_{t_0}^{t_1} \cos\varphi(t)dt. \tag{47}$$

If θ has the opposite sign, the following expression

$$-\int_{t_0}^{t_1}\cos\varphi(t)dt < \int_{0}^{t_k+\alpha_k}\cos\varphi(t)dt < \int_{0}^{t_0}\cos\phi(t)dt. \quad (48)$$

can be in similar way justified.

While according to Lemma 1 it is true that

$$\left|\int_{0}^{t_0}\cos\phi(t)dt\right| > \left|\int_{t_0}^{t_1}\cos\varphi(t)dt\right|, \quad (49)$$

then, for every beginning phase θ, the following expression is valid, as well:

$$-\int_{0}^{t_0}\cos\phi(t)dt < \int_{0}^{t_k+\alpha_k}\cos(\phi(t)-\theta)dt < \int_{0}^{t_0}\cos\phi(t)dt. \quad (50)$$

Thus, module of integral of the LIFM oscillation $\cos(\omega t + mt^2 - \pi/2 - \theta)$, evaluated on its entire duration, has a value, which is less than module of integral of this oscillation, found on the interval of its first halfwave. Hence, by using validity of Statement 1 ((16) and (17)), *the expression (50) can be rewritten in form:*

$$-\int_{0}^{t_0}\cos(\omega t-\pi/2)dt < \int_{0}^{t_k+\alpha_k}\cos(\omega t+mt^2-\pi/2-\theta)dt < \int_{0}^{t_0}\cos(\omega t-\pi/2)dt. \quad (51)$$

III Conclusion

The paper derives that the integral of the LIFM oscillation function $\cos(\omega t + mt^2 - \pi/2 - \theta)$, evaluated on its entire duration, is limited by interval of values, which can be calculated in analytical way in form of integrals of elementary oscillation functions like $\cos(\omega t - \pi/2)$ (see 51).

Validity of expression (51) allows to make conclusion about valid use of linearly increasing frequency-modulated oscillations (as carrier signals) in underwater telemetry systems, which demodulators consist of matched filtering circuits.

References

[1] Kebkal K.G.and Bannasch R. (2002) "Sweep-spread carrier for underwater communication over acoustic channels with strong multipath propagation," *J. Acoust. Soc. Am.*, vol.112, pp. 2043-2052.

[2] Kilfoyle D. B. and Baggeroer A B., "The state of the art in underwater acoustic telemetry," *IEEE Journal of Oceanic Engineering*, vol. 25, No. 1, pp. 4-27, January 2000.

[3] Sklar B., Passband modukation and demodulation. // Digital Communications. Fundumentals and applications. 2d Edt.:Russian Transl. - "Willams" Edition, Moscow, St.-Peterburg, Kiev. 2003, pp. 195-266.

[4] I.N. Bronstein and K.A. Semendjajew. Taschenbuch der Mathematik. Verlag Harri Deutsch, Thun und Frankfurt am Main, 1989.

IEEE Access
Multidisciplinary | Rapid Review | Open Access Journal

Date of publication xxxx 00, 0000, date of current version xxxx 00, 0000.

Digital Object Identifier 10.1109/ACCESS.2023.Doi Number

Robust Underwater Acoustic Communication Using the Overlapped Chirp Spread Carrier Technique in Doubly Spread Environments

CHANG-HYUN YOUN[1], HYOUNG-IN RA[1], KYUNG-WON LEE [1] and KI-MAN KIM [1]

[1]Department of Radio Communication Engineering, Korea Maritime and Ocean University, 727 Taejong-ro, Yeongdo-gu, Busan, South Korea

Corresponding author Ki-Man Kim (e-mail: kimkim@kmou.ac.kr).

ABSTRACT The performance of underwater acoustic communication is significantly affected by multipath propagation and Doppler spread. In this paper, we propose a new communication technique called overlapped chirp spread carrier (OCSC) by modifying the existing sweep spread carrier (SSC) technique, which is robust in a multipath propagation environment. Our proposed OCSC technique uses a repeated carrier wave by combining up-chirp and down-chirp signals and estimates and corrects the Doppler shift frequency of the received signal by utilizing the characteristics of the correlation function of each up-chirp and down-chirp. To demonstrate the performance of the proposed OCSC technique, we provide the results of a simulation using an underwater channel simulator and sea trial conducted in the East Sea. As a result of the sea trial, when demodulating using only the estimated Doppler shift frequency, the uncoded bit error rate reached 0.135. However, when our proposed correction method was applied to the estimated Doppler frequency, the uncoded bit error rate decreased to 0.001.

INDEX TERMS bit error rate, multipath propagation, Doppler spread, overlapped chirp spread carrier, sea trial, underwater acoustic communication

I. INTRODUCTION

Underwater acoustic communication is used in various applications, such as underwater navigation, underwater vehicles, underwater sensor networks, marine environment monitoring, and military purposes [1-7]. However, unlike radio frequency (RF) communication, underwater acoustic communication has many obstacles, such as high propagation loss, frequency selective fading, narrow bandwidth, and fast time variability [8-10]. The speed of the sound wave changes according to the depth, salinity, and temperature of the water, and the movement path of the sound wave changes due to refraction [11]. In addition, as sound waves are transmitted, there are problems; these include multipath propagation by the seafloor or sea level and the Doppler shift effect caused by the movement of wind, ocean currents, and transceivers [12-13]. Especially in shallow water environments where the depth is not deep, multipath propagation is the main problem and degrades the performance because it causes ISI (Inter Symbol Interference) due to its long delay time. Many studies have been conducted on spread spectrum techniques with less affected modulation methods in this type of multipath propagation environment [14-17].

Spread spectrum techniques are methods of spreading and transmitting the bandwidth of the signal widely and include frequency hopping spread spectrum (FHSS), direct sequence spread spectrum (DSSS), and chirp spread spectrum (CSS) [18]. FHSS is a technique that involves dividing the entire bandwidth and transmitting information using a hopping code, whereby the frequency is changed over time. This method is particularly effective in environments where a Doppler frequency is present, but it only uses a partial amount of the energy in the transmitted signal, causing it to be vulnerable in environments with a low signal-to-noise ratio (SNR) [19]. DSSS assigns a pseudo-noise sequence to each symbol to spread the signal across the bandwidth. DSSS is highly resilient in environments with low SNR, with advantages of power and bandwidth efficiency for long-distance communication when compared to FHSS. However, DSSS is highly sensitive to Doppler frequency variability and requires complex synchronization at the receiving end, which can be a significant disadvantage [20]. CSS is a spread spectrum technique that addresses the limitations of SNR and Doppler frequency sensitivity found in the previously mentioned spread spectrum techniques. In this technique, symbols are composed of linear frequency modulation (LFM) signals, where the frequency changes linearly with time. CSS is

designed to overcome the disadvantages of FHSS and DSSS and is a more robust spread spectrum technique [21].

Based on the study of these CSS signals, Lee *et al*. [22] applied a differential coding method; the size of the matched filter was doubled, and the performance was improved by taking advantage of the fact that the time-bandwidth product cost increases. Azim *et al*. [23] proposed dual-mode chirp spread spectrum (DM-CSS) modulation for low-power wide-area networks. DM-CSS achieved higher spectral efficiency than other models, such as long-range modulation. Zhu *et al*. [24] proposed an orthogonal chirp division multiplexing (OCDM) method that used a chirp signal for carrier modulation; under multipath propagation conditions where the delay spread was longer than the guard interval, the conventional orthogonal frequency out-performed the orthogonal frequency division multiplexing (OFDM). Kebkal *et al*. [25] proposed an SSC (sweep spread carrier) technique using a periodically repeated up-chirp signal as a carrier. Unlike the conventional CSS technique, the SSC technique transmitted a chirp signal as a carrier signal rather than information. This technique separated multipath arrival by converting it into frequency at the receiving end according to the absolute value of the time delay according to multipath propagation.

In underwater acoustic communication, due to the environmental characteristics, Doppler shift frequency occurs due to waves, wind, ocean current, and the mobility of the transceiver. This causes the deterioration of communication performance; thus, to improve communication performance, it is essential to compensate for the distortion caused by the Doppler shift effect. Techniques for estimating the Doppler shift frequency of the received signal have been greatly studied [26-27]. In general, a communication packet transmits a preamble signal at the beginning of a data section that transmits information, and the preamble signal indicates the exact starting point of a data frame. In addition to finding the starting point, the approximate Doppler shift frequency of the data frame can be determined using the Doppler bank [28]. However, when the Doppler bank method is applied, the number of matched filters is increased to increase the accuracy of the Doppler shift frequency estimation value; thus, there is a disadvantage in the large amount of calculations needed at the receiving end.

In this paper, we propose an overlapping chirp spread carrier (OCSC) technique that uses a signal in which a periodically repeated up-chirp signal and a down-chirp signal are combined as a carrier frequency by modifying the existing SSC technique. Compared to the existing SSC method, this method increases the transmission rate because it can transmit phase-modulated pulses to each of the up-chirp and down-chirp signals, and it is also robust in a multipath transmission environment. In addition, the Doppler shift frequency can be estimated through the chirp signal and the cross-correlation function. However, errors can be included in the estimated Doppler shift frequencies, and a correction method for these errors is presented. Moreover, the results of simulations and sea trials using the proposed OCSC technique are presented.

The remainder of this paper proceeds as follows: Section 2 explains the existing SSC method; Section 3 elucidates the proposed OCSC method and the concept of Doppler shift frequency estimation and correction; Section 4 describes the simulation results based on the bellhop model using the estimated Doppler shift frequency and presents the results in terms of the bit error rate; Section 5 examines the results from sea experiments; and Section 6 provides the conclusion.

II. Traditional SSC technique

The SSC technique is a communication method that uses only continuous up-chirp signals as carrier waves to transmit phase-modulated pulses. Since this technique has robust characteristics in a multipath propagation environment, it has an advantage of overcoming an ISI that arises in these conditions.

The SSC signal utilizes a periodic up-chirp signal, which sweeps from the minimum frequency f_{min} to the maximum frequency f_{max}, as the carrier during the sweep time of T_s. The SSC signal is described by the following equation:

$$c^{up}(t) = A_c \, exp[j2\pi(f_{min}\tau(t) + k\tau(t)^2)] \tag{1}$$

where A_c is the amplitude of the signal, $k = (f_{max} - f_{min})/2T_S$ and is a coefficient representing the rising frequency variation rate, $\tau(t) = t - T_S \left\lfloor \frac{t}{T_S} \right\rfloor$ and is a continuous chirp-shaped periodic sweep with cycle duration T_S.

The term $\left\lfloor {}^{t}/_{T_S} \right\rfloor$ is defined as the final integer not greater than ${}^{t}/_{T_S}$, where N is the number of chirp pulses that compose the carrier waveform, and $T_C = NT_S$ is the overall carrier time. Fig. 1 shows the concept of the SSC method in the time-frequency domain.

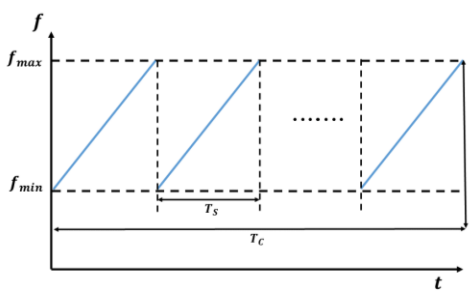

FIGURE 1. Concept of the SSC modulation [25]

A signal encoded by phase shift keying (PSK) is represented as follows:

$$s^{up}(t) = \sum_{n=-\infty}^{\infty} A_s \, exp[jD_n p(t - nT)] \tag{2}$$

where A_s represents the amplitude of the signal, and $p(t)$ is a pulse for phase modulation. D_n is the phase encoded data symbol being communicated, and T is the signal interval. After being modulated onto the carrier, the signal transmitted over the channel is expressed as follows:

$$x(t) = Re[s^{up}(t)c^{up}(t)] \quad (3)$$

III. Proposed OCSC technique

A. OCSC signal

The OCSC technique is an extension of the existing SSC technique. In contrast to the SSC technique, which uses only the up-chirp signal as the carrier, the OCSC technique combines and repeats both the up-chirp and down-chirp signals with a constant symbol period, as shown in Fig. 2. Furthermore, the OCSC technique transmits binary modulated pulses for each up-chirp and down-chirp, leading to a doubled transmission speed compared to the SSC technique. The OCSC technique is described in (4).

$$x(t) = Re[s^{up}(t)c^{up}(t) + s^{down}(t)c^{down}(t)] \quad (4)$$

where $s(t)$ means up-chirp and down-chirp phase-modulated pulses, and $c^{down}(t)$ means down-chirp carrier. The expression describing $c^{down}(t)$ is shown in (5).

$$c^{down}(t) = A_c\, exp[j2\pi(f_{max}\tau(t) + w\tau(t)^2)] \quad (5)$$

where, $w = (f_{min} - f_{max})/2T_S$ and is a coefficient representing the falling frequency variation rate.

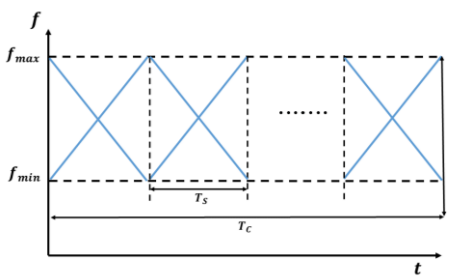

FIGURE 2. Concept of the OCSC modulation

B. Doppler shift frequency estimation in OCSC modulation

To estimate the Doppler frequency, the cross-correlation function is calculated between each symbol, and the peak position is identified. The amount of change in the interval between the identified peaks is then used to estimate the Doppler frequency. The OCSC is a form in which up-chirp and down-chirp signals are combined for each symbol. Therefore, if the up-chirp matched filter and down-chirp matched filter are applied alternately for each symbol, the peak point for the up-chirp and the peak point for the down-chirp appear for each symbol, and the Doppler frequency can then be estimated by measuring the amount of change between the peak points for the up-chirps and down-chirps.

The variables T_{up} and T_{down} represent the times at which the matched filtering maximum appears in the up-chirp and down-chirp, respectively. When the OCSC signal has a Doppler shift frequency of 0 Hz, the time interval T_s can be calculated as follows:

$$T_s = T_{down}(i) - T_{up}(i) \quad (6)$$

where i means the index of the up and down chirp peaks. If there is a Doppler shift, the time interval Ts between T_{up} and T_{down} has a variation of Δ because the signal is compressed or expanded. It is expressed as follows:

$$T_{down}(i) - T_{up}(i) = T_s + \Delta(i) \quad (7)$$

The Doppler shift frequency (f_d) can be estimated by utilizing the variation value Δ. Specifically, when the up and down peaks are paired, the Doppler shift frequency estimation can be expressed as follows:

$$f_d(i) = \frac{(f_{min} - f_{max}) \times \Delta(i)}{2T_s} \quad (8)$$

Since the number of Doppler shift frequencies estimated from the received OCSC signal is N/2, the Doppler shift frequency of the entire OCSC signal can be expressed as follows via rearrangements with (7) and (8):

$$\widehat{f_d} = \frac{1}{N/2}\sum\left[\frac{(f_{min} - f_{max}) \times (T_{down}(i) - T_{up}(i) - T_s)}{2T_s}\right] \quad (9)$$

Finally, to estimate the Doppler shift frequency of the OCSC signal, the estimated Doppler shift frequencies are averaged. Fig. 3 illustrates the process for estimating the Doppler shift frequency of the OCSC signal.

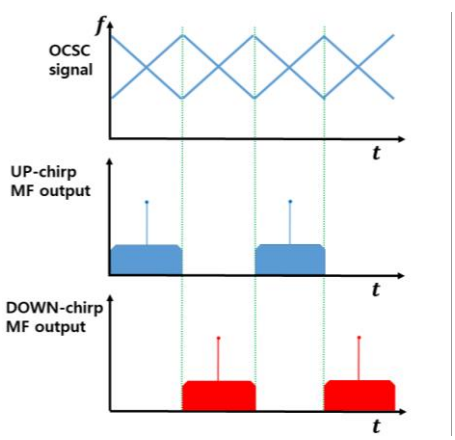

(a)

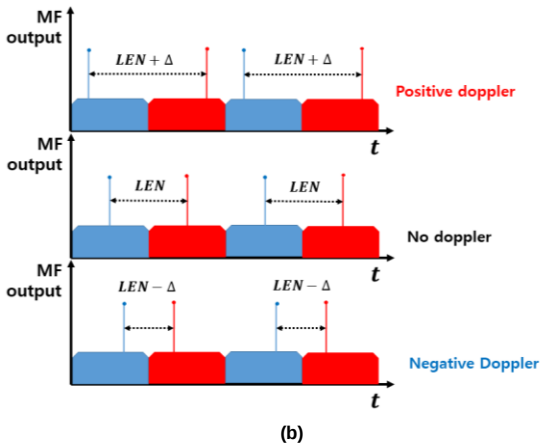

(b)

FIGURE 3. Process of estimating the OCSC signal Doppler shift frequency. (a) Application of matched filtering to the OCSC signal, (b) Doppler shift effect on the positive Doppler and negative Doppler.

C. Doppler shift frequency correction

The estimation of the Doppler shift frequency using the correlation function between the up-chirp and down-chirp is prone to error due to decreased correlation characteristics between the OCSC signal and the chirp signal during pulse synthesis. When the OCSC signal experiences a Doppler shift, the chirp-sweep time of the signal changes, leading to a reduction in the correlation characteristics with the chirp signal. Therefore, in this paper, the effect of the Doppler shift frequency estimated using the OCSC signal and its correction were verified through simulation.

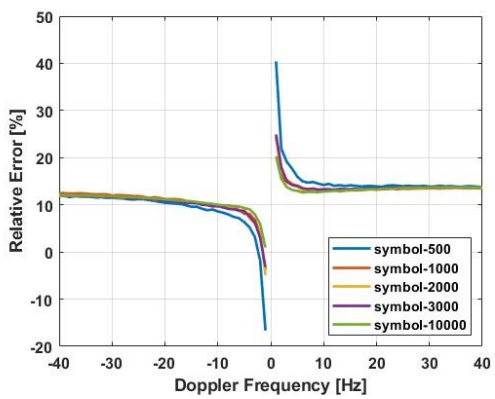

FIGURE 4. Relative error of the Doppler frequency using the OCSC method.

Initially, while changing the amount of data in the OCSC signal, that is, the number of symbols, to 500, 1000, 2000, 3000, 5000, and 10000, the relative error aspect of the Doppler shift frequency estimation value was confirmed through simulation. As shown in Fig. 4, the relative error patterns were similar. Therefore, it was confirmed that our method proposed could be applied regardless of the amount of information. Here, the error increased significantly around the Doppler shift frequency 0 and was determined by calculating the error shown on the axis in the form of [(B-A)/B] × 100, where A is the estimated Doppler shift frequency and B is the actual Doppler shift frequency. Since the error is a number and the denominator is a small value close to 0, the relative error value appeared large, but the difference between the estimated Doppler shift frequency and the actual Doppler shift frequency was a very low value.

Next, to generalize the relative error patterns, each case of positive Doppler and negative Doppler was represented in polynomial form using nonlinear least square curve fitting (Fig. 5). Finally, the estimated Doppler shift frequency is corrected by substituting the estimated Doppler shift frequency into the polynomial derived by fitting the nonlinear least squares (LS) curve to compensate for the errors.

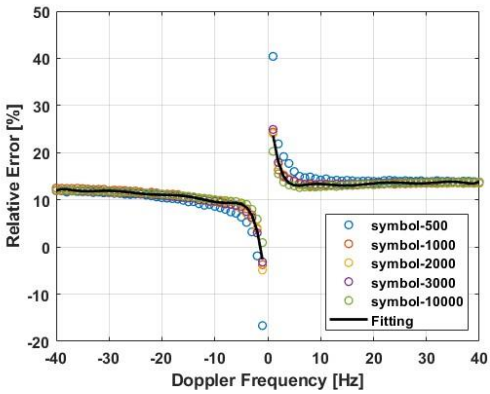

FIGURE 5. Polynomial equation plotting for error appearance using nonlinear LS fitting.

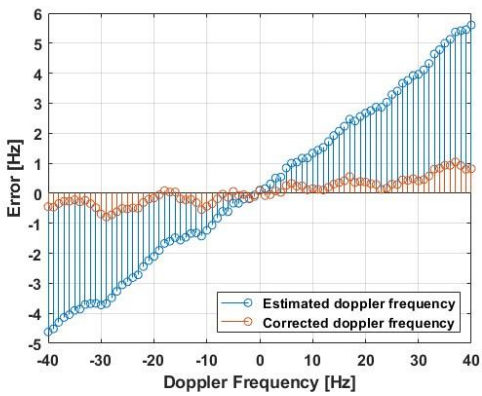

FIGURE 6. Comparison of the error with the estimated and corrected Doppler frequency.

A simulation was conducted to validate the effectiveness of the proposed Doppler shift frequency correction method. The OCSC signal was set to have a data amount of 1,000 bits, T_s was 10 ms, and SNR of -3 dB. Doppler shift frequencies ranging from -40 Hz to +40 Hz were used for the simulation. The simulation results are shown in Fig. 6, where the x-axis represents the virtually generated Doppler shift frequency, and the y-axis represents the error between the virtually generated Doppler shift frequency and the estimated Doppler shift frequency.

The blue value represents the estimated Doppler shift frequency error, while the red value represents the corrected Doppler shift frequency error. From the correction of the Doppler shift frequency using the estimated Doppler shift frequency, an error of less than approximately 1 Hz was obtained

IV. Simulations and Results

The performance of the OCSC method under multipath propagation and Doppler channel conditions was evaluated using the bellhop model-based VirTEX simulator [29]. The simulation was conducted using actual sound speed data from the West Sea of South Korea, representing a shallow sea environment, and from the East Sea of South Korea, representing a deep water environment. No separate error correction technique was applied to the generated communication signal. The parameters applied to the simulation are shown in Table 1.

Table 1. Simulation parameters

PARAMETER	VALUE
Sampling frequency	192 kHz
Carrier frequency	11 kHz
Data rate	100 bps
Bandwidth	2 kHz
Sweep time	10 ms
SNR	-10, -5 , 0 dB
Doppler shift frequency	-40 ~ 40 Hz

A. shallow water channel

Shallow water environments are prone to multipath propagation because the water depth is not deep. Fig. 7(a) shows the sound speed distribution in the West Sea applied to the simulation. In the simulation, it is assumed that the transmission distance between the transmitter and receiver is 100 m, the water depth is 20 m, and the depths of the transmitter and receiver are approximately 5 m and 15 m, respectively. Fig. 7(b) shows the ray tracing, and the channel impulse response is shown in Fig. 7(c).

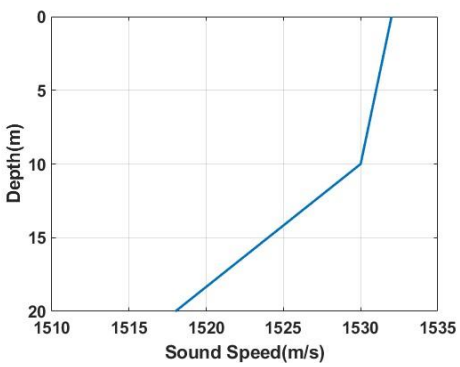

(a)

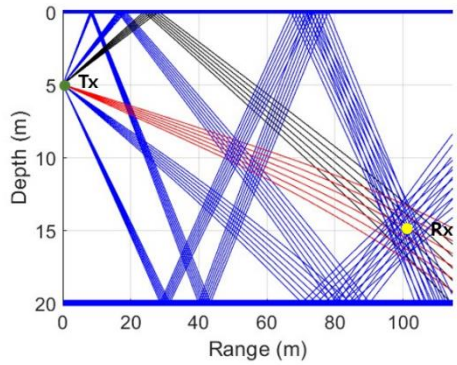

(b)

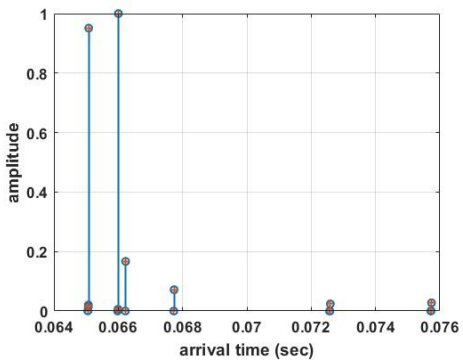

(c)

FIGURE 7. Shallow water channel using the VirTEX simulator. (a) Sound speed profile, (b) Ray tracing, (c) Channel impulse response.

Fig. 8 shows the simulation results according to the SNR. In the figure, red data represents the result at 0 dB, green at -5 dB, and black at -10 dB. Fig. 8(a) shows the respective errors according to the estimated Doppler shift frequency and the corrected Doppler shift frequency. The error of the estimated Doppler shift frequency indicated by ‘X’ increased as the given Doppler shift frequency increased regardless of the value of SNR, but the error of the corrected Doppler shift frequency indicated by ‘◯’ remarkably low.

Fig. 8(b) shows the result from the uncoded bit error rate using the estimated Doppler shift frequency and the corrected Doppler shift frequency at various SNR. In the figure, ‘☐’ represents the bit error rate when the Doppler shift frequency is not compensated

When the Doppler value is small, the data are demodulated, but when the Doppler value changes even slightly, the data are not demodulated. ‘X’ represent the bit error rate when compensated with the estimated Doppler shift frequency.

When the Doppler value is within ± 10 Hz, the data are demodulated, and when it is higher than 10 Hz, the error rate increases. Finally, ‘◯’ represent the bit error rate when compensated with our corrected Doppler shift frequency method. Most of the data demodulation is accurate in all sections. Therefore, the performance is improved by correcting the estimated Doppler shift frequency.

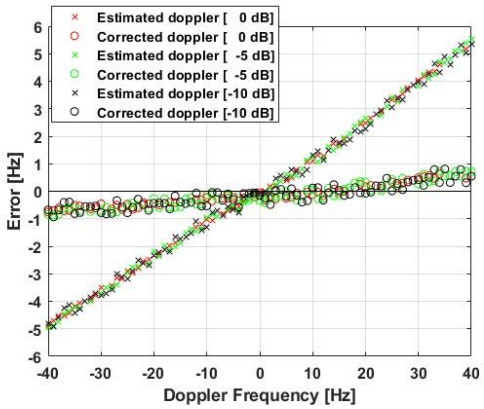

(a)

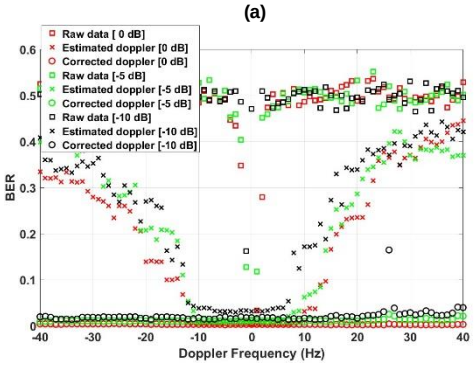

(b)

FIGURE 8. Results from passing through the VirTEX West sea channel. (a) Estimated Doppler frequency error and (b) Uncoded BER.

B. Deep water channel

In the deep water environment, even if multipath exists in the received signal, there is a relatively long delay time due to the deep water depth, unlike the shallow sea environment. Fig. 9(a) shows the sound speed distribution in the East Sea applied to the simulation. In the simulation, it is assumed that the transmission distance between the transmitter and receiver is 5 km, the water depth is 1,000 m, and the depths of the transmitter and receiver are approximately 200 m and 300 m, respectively. In Fig. 9(c), multipath propagation appears after approximately 140 ms.

Fig. 10 represents the result of passing through the deep water channel. Similar to Fig. 8, Fig. 10(a) confirms that the error of the corrected Doppler frequency is significantly lower than that of the estimated Doppler frequency. Fig. 10(b) shows the uncoded bit error rate using the estimated and corrected Doppler frequencies.

When compensated with the estimated Doppler frequency, the data can be demodulated when the Doppler value is within 10 Hz, but the error rate increases when the value is higher than that. However, when the corrected Doppler frequency is compensated, the data can be demodulated in all sections.

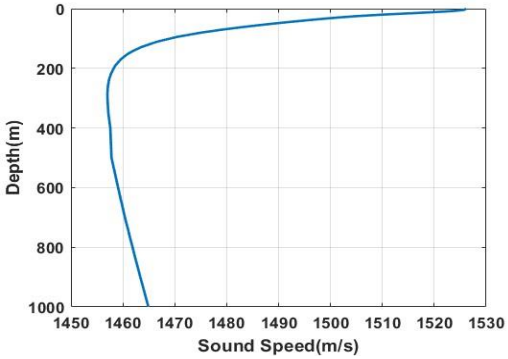

(a)

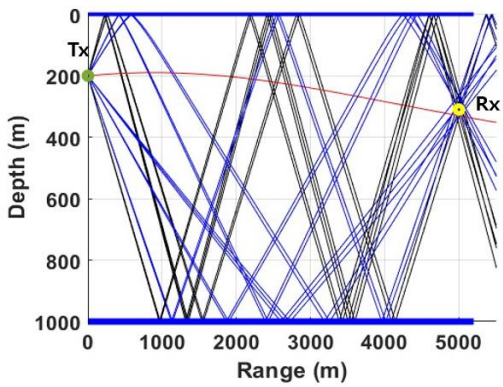

(b)

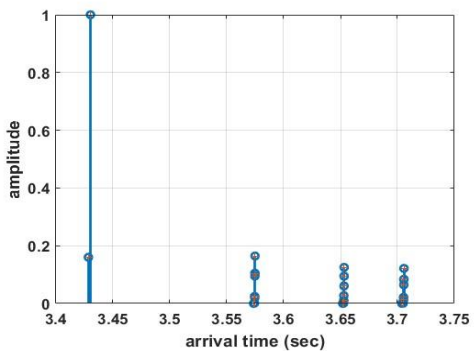

(c)

FIGURE 9. Deep water channel using the VirTEX simulator. (a) Sound speed profile, (b) Ray tracing and (c) Channel impulse response.

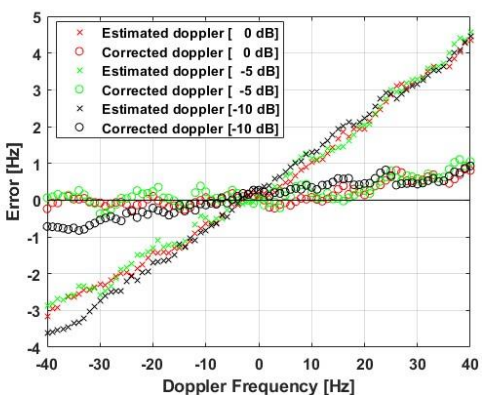

(a)

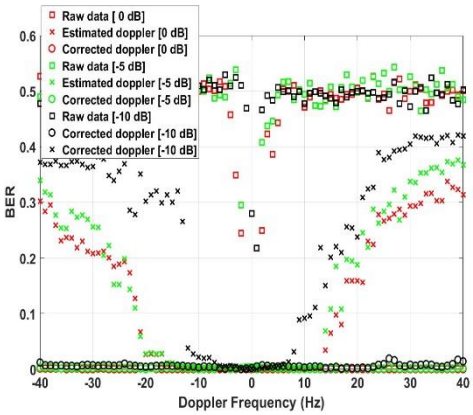

(b)

FIGURE 10. **Result from passing through the VirTEX East sea channel. (a) Estimated Doppler frequency error and (b) uncoded BER.**

Table 2 compares the calculation time and error between the Doppler shift frequency estimation and correction method using the proposed OCSC technique and the Doppler shift frequency estimation method, which is one of the existing Doppler shift frequency estimation methods. Here, the error was obtained as the root mean square (RMS) of the difference between the actual Doppler value and the estimated Doppler value. Although the processing time varies depending on the resolution of the Doppler bank, in this simulation, the resolution of the Doppler bank was set to 0.2 Hz.

Table 2. **Program operation time and performance according to each**

Case	Operation time	RMS error
Doppler bank	5.943 s	0.022
Doppler estimation	3.891 s	1.997
Doppler correction	3.938 s	0.346

When comparing Doppler bank method and the proposed method, there is no difference in the error rate of the compensated data when Doppler frequency correction is performed. However, the Doppler bank method has a disadvantage that the computation time greatly increases according to the resolution, but the proposed method has the advantage of a smaller computation amount than the Doppler bank method. The time calculated in the simulation was measured using Matlab's built-in functions ‘tic’ and ‘toc’, and the specifications of the computer used were Intel Core i7-7700K / 4.20 GHz CPU / RAM: 32 GB.

V. Sea Trial and Results

A. Experimental environment

An offshore sea trial was conducted near Pohang, South Korea, in March 2023, to verify the performance of our proposed method. However, due to poor weather conditions at the time of the trial, a rather high wave height of approximately 3 m was measured. Consequently, the transmission distance was set to 100 m. The water depth at the test point was approximately 20 m, with the transmitter water depth and receiver water depth being 5 m and 15 m, respectively, based on sea level. A schematic diagram of the marine experiment is depicted in Fig. 11.

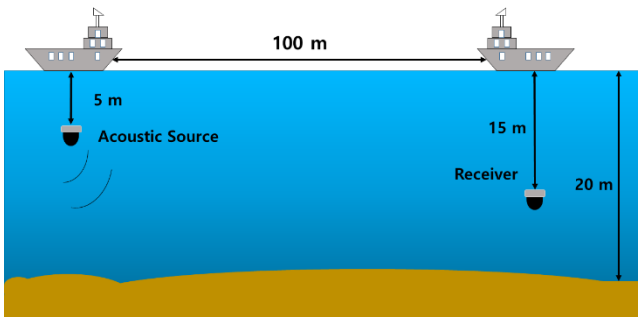

FIGURE 11. **Schematic of the sea trial.**

In the trial, the ITC-1007 model was used as the projector, and the signal was designed to consider the transmission characteristics of this projector. The OCSC signal had a center frequency of 11 kHz, a bandwidth of 2 kHz, a sweep time of 10 ms, and a transmission rate of 200 bps with a total of 1,000 bits transmitted. Virtual Doppler was inserted into the transmission signal due to the inability to configure the actual Doppler channel environment caused by weather conditions. The virtual Doppler was transmitted at 10 Hz intervals ranging from -40 Hz to 40 Hz.

The symbols of the OCSC signal were binary PSK modulated, and pulse shaping was performed using a raised cosine filter with a roll-off coefficient of 0.5. The packet of the transmitted signal is shown in Fig. 12 and was accordingly configured.

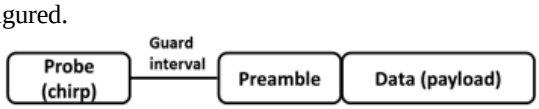

FIGURE 12. **Packet structure.**

To determine the starting point of the received signal, a chirp signal with a duration of 1 second was transmitted, and a guard interval of 0.5 seconds was inserted between the probe signal and the preamble signal. The preamble signal was transmitted before the data period to accurately synchronize the data frame. For the preamble signal, a total of 510 bits were transmitted by repeating an m-sequence of 255 bits twice consecutively using binary PSK modulation. Thus, the length of one packet of the OCSC signal was approximately 7.5 seconds.

B. Channel characteristics

To assess the transmission characteristics of the channel, the LFM signal was repeatedly transmitted. The carrier frequency of the LFM signal was 11 kHz, the bandwidth was 2 kHz, the ping interval was 1 s, and the ping length was 50 ms. The channel characteristics were measured and are shown in Fig.

13. Although the experiment was conducted in a stationary trial, it was estimated that the transceiver terminal's movement due to the influence of the ocean current caused a Doppler frequency shift of approximately -1.2 Hz.

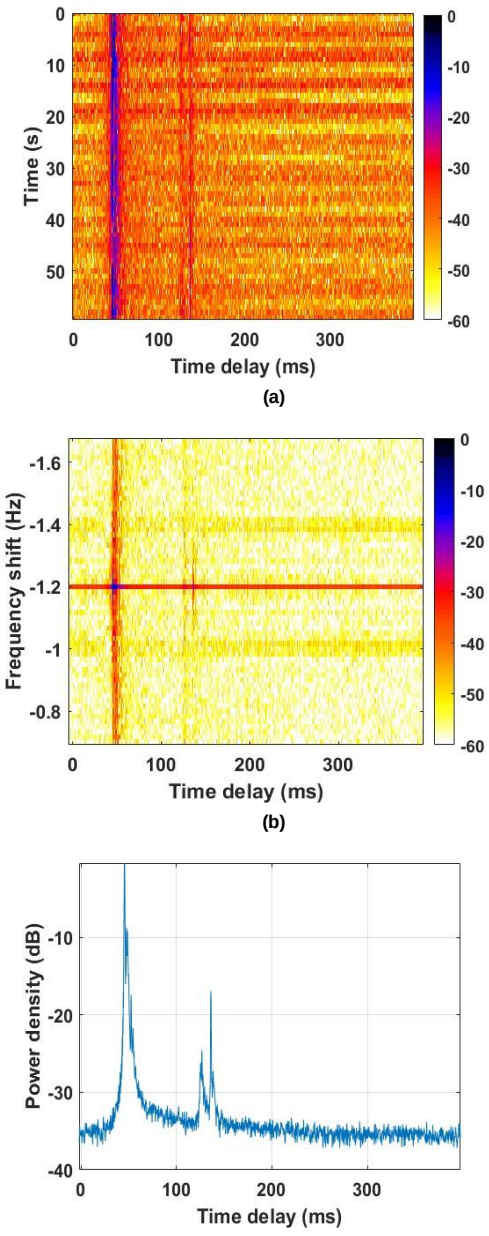

FIGURE 13. Underwater channel characteristics in sea trial. (a) Channel impulse response, (b) Delay-Doppler spread function, and (c) Power delay profile.

The power delay profile of the channel is shown in Fig. 13(c). Multipaths were observed with a time difference of approximately 2 ms based on the direct path, multipaths after approximately 90 ms were observed, and the magnitude difference was more than 17 dB compared to the direct path. The impact was determined to be insignificant.

C. Sea trial results

The OCSC signal was subjected to data modulation and demodulation in the order shown in Figure 14. In the transmitter, odd and even bits were separated from the transmission bit string, and a raised cosine filter was applied to shape the pulse train. The pulse train was then transmitted via OCSC modulation using up-chirp and down-chirp.

The received signal, after passing through the channel, first underwent bandpass filtering to remove unnecessary frequency components, and then frame synchronization was performed. The Doppler shift frequency was estimated using the previously proposed technique, corrected again, and the received signal's Doppler shift frequency was compensated. The OCSC signal was then demodulated, and phase correction was performed using a phase-locked loop (PLL). Finally, the data were demodulated

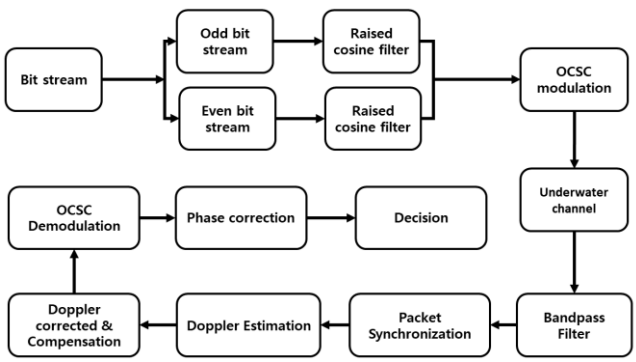

FIGURE 14. Block diagram of OCSC transmission.

The results of the communication test are presented in Fig. 15. Fig. 15(a) shows the errors of virtual Doppler, estimated Doppler, and corrected Doppler. In Fig. 15(b), the red line represents the estimated Doppler shift frequency, while the black line represents the uncoded bit error rate with corrected Doppler shift frequency compensation. Although the virtual Doppler shift frequency used in the trial ranged from -40 Hz to 40 Hz, the actual Doppler shift was affected by ocean currents, resulting in an error between the virtual Doppler shift frequency and the relatively estimated and corrected Doppler shift frequencies.

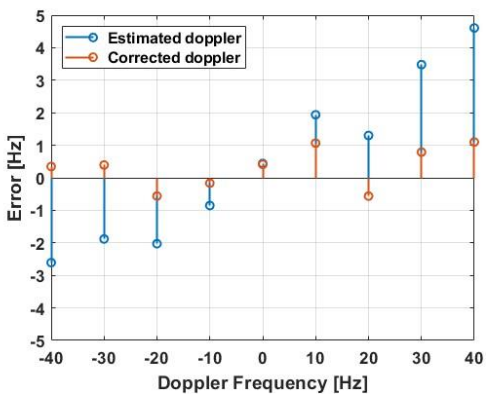

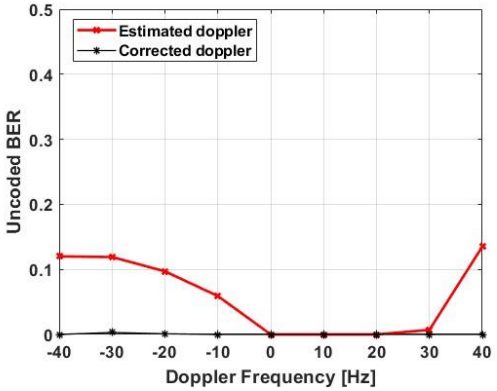

(b)

FIGURE 15. Results of a sea trial. (a) Estimated Doppler frequency error and (b) uncoded BER.

VI. Conclusions

Underwater acoustic communication has the heavy time spread by multipath and Doppler spreads. In this paper, an OCSC method of underwater acoustic communication is proposed to improve the performance of the SSC method using a chirp signal as a carrier. In our proposed method, carriers combined with up-chirp and down-chirp signals are used to double the transmission rate compared to the conventional SSC method. The Doppler shift frequency is estimated through the cross-correlation function of the up-chirps and down-chirps, and then it is corrected. To confirm the performance of our proposed method, simulations and sea trials were performed, and the results were provided. In the simulation, the proposed Doppler transition frequency estimation and correction were compared in terms of performance and calculation time with the existing Doppler transition frequency estimation method, and the proposed OCSC technique performed better in terms of calculation time than the existing Doppler bank method. In the trial, the virtual Doppler shift frequency was included in the transmission signal and transmitted to assess the performance of our Doppler shift frequency estimation and our proposed correction method. As a result of the sea trial, when the estimated Doppler shift frequency was compensated, the uncoded bit error rate ranged from a minimum of 0 to a maximum of 0.135; however, when the estimated Doppler shift frequency was corrected and compensated, the majority of the results were 0. In the future, research on the change in the transmission method according to the change in the channel environment is needed that includes sea trials in the actual Doppler shift environment.

REFERENCES

[1] S. Climent, A. Sanchez, J. V. Capella, N. Meratnia, and J. J. Serrano, ‘‘Underwater acoustic wireless sensor networks: Advances and future trends in physical, MAC and routing layers,’’ *Sensors*, vol. 14, no. 1, pp. 795–833, Jan. 2014.

[2] Y. Yao, Y. Wu, M. Zhu, D. Li, and J. Tao, ‘‘Efficient on-off keying underwater acoustic communication for seafloor observation networks,’’ Appl. Sci., vol. 10, no. 6, p. 1986, Mar. 2020.

[3] E. T. Michailidis, G. Tuna, G. Gezer, S. M. Potirakis, and K. Gulez, “ANN-based control of a multiboat group for the deployment of an underwater sensor network”, *International Jounal of Distributed Sensor Networks*, vol. 2014, Article ID 786154, pp.12 , 2014.

[4] J. Potter, J. Alves, D. Green, G. Zappa, I. Nissen, and K. McCoy, “The JANUS underwater communications standard,” in *Underwater Communications and Networking (UComms)*, 2014. IEEE, 2014, pp. 1–4.

[5] M. Stojanovic, ‘‘Recent advances in high-speed underwater acoustic communications,’’ *IEEE J. Ocean. Eng*., vol. 21, no. 2, pp. 125–136, Apr. 1996.

[6] B. Dushaw, “The acoustic thermometry of ocean climate (atoc) project: Towards depth-averaged temperature maps of the north Pacific ocean,” in *Proc. Int. Symp. Acoust. Tomogr*. Thermometry, 1999, pp. 8–9.

[7] M. Stojanovic, ‘‘Acoustic (underwater) communications,’’ in *Encyclopedia of Telecommunications*, J. G. Proakis, Ed. New York, NY, USA: Wiley, 2003.

[8] M. Stojanovic, ‘‘High-speed underwater acoustic communications,’’ *in Underwater Acoustic Digital Signal Processing and Communication Systems*. New York, NY, USA: Springer, 2002, pp. 1–35.

[9] R. J. Urick, *Principles of underwater sound-2*, New York:Tata McGraw-Hill Education, 1975,pp. 99-197

[10] P. Du, X. Zhu and Y. Li, “Direct Sequence Spread Spectrum Underwater Acoustic Communication Based on Differential Correlation Detector, ” 2018 IEEE International Conference on Signal Processing, Communications and Computing (ICSPCC), Qingdao, 2018, pp. 1-5, doi: 10.1109/ICSPCC.2018.8567803.

[11] G. Han, C. Zhang, L. Shu, N. Sun, and Q. Li, ‘‘A survey on deployment algorithms in underwater acoustic sensor networks,’’ *Int. J. Distrib. Sensor Netw*., vol. 9, no. 12, 2013, Art. no. 314049.

[12] H. S. Paul Van Walree and T. Jenserud, “Characterization of overspread acoustic communication channels,” in *Proc. 10th Eur. Conf. Underwater Acoust*., Jul. 2010, pp. 952–958.

[13] T. C. Yang, ‘‘Measurements of temporal coherence of sound transmissions through shallow water,’’ *J. Acoust. Soc. Amer*., vol. 120, no. 5, pp. 2595–2614, Nov. 2006.

[14] L. Freitag, M. Stojanovic, S. Singh, and M. Johnson, “Analysis of channel effects on direct-sequence and frequency-hopped spreadspectrum acoustic communication,” *IEEE J. Ocean. Eng*., vol. 26, no. 4, pp. 586–593, Oct. 2001.

[15] G. Loubet, V. Capellano, and R. Filipiak, “Underwater spread spectrum communications,” in *Proc. OCEANS Conf*., Halifax, NS, Canada, 1997, pp. 574–579.

[16] F. zhou, B. LlU, D. Nie. G. Yang, W Zhang, and D. Ma, “M-ary Cyclic Shift Keying Spread Spectrum Underwater Acoustic Communications Based on Virtual Time-reversal Mirror," *Sensors*, vol. 19, pp. 3577-3593,2019.

[17] A. W. Lam and S. Tantaratana, “Theory and Applications of SpreadSpectrum Systems: A Self-Study Course”. *IEEE*, 1994.

[18] C. He and J. Huang and Q. Zhang, "M-ary chirp spread spectrum modulation for underwater acoustic communication." Proceedings of the TENCON 2005 IEEE Region 10th Annual Conference, pp.1-4, 2005

[19] W. B. Yang and T. C. Yang, “High-frequency FH-FSK underwater acoustic communications: the environmental effect and signal processing,” *in Proc. High Freq. Ocean Acoust*. Conf. 728, 106-113 (2004).

[20] T. Yang and W. Yang, “Performance analysis of direct-sequence spreadspectrum underwater acoustic communications with low signal-to-noiseratio input signals,” *Journal of Acoustical Society of America*, vol. 123, no. 2, pp. 842–855, (2008).

[21] E. J. Kaminsky, “Chirp slope keying for underwater communication,” *Electrical Engineering Faculty publication*, 5778, 894-905 (2005).

[22] Lee, Joohyoung, et al. "Long-range acoustic communication using differential chirp spread spectrum." *Applied Sciences* 10, 8835 (2020).

[23] Azim, Ali Waqar, et al. "Dual-Mode Chirp Spread Spectrum Modulation." *IEEE Wireless Communications Letters 11.9*,pp.1995-1999, (2022).

[24] P. Zhu, X. Xu, X. Tu, Y. Chen and Y. Tao, "Anti-multipath orthogonal chirp division multiplexing for underwater acoustic communication", *IEEE Access*, vol. 8, pp. 13305-13314, 2020.

[25] K. G. Kebkal and R. Bannasch, ‘‘Sweep-spread carrier for underwater communication over acoustic channels with strong multipath propagation,’’ *J. Acoust. Soc. Amer*., vol. 112, no. 5, pp. 2043–2052, Nov. 2002.
[26] B. S. Sharif, J. Neasham, O. R. Hinton and A. E. Adams, "A computationally efficient Doppler compensation system for underwater acoustic communications", *IEEE J. Ocean. Eng.*, vol. 25, no. 1, pp. 52-61, Jan. 2000.
[27] Doppler shift estimation for underwater acoustic signals", *Proc. ACM Int. Conf. Underwater Netw. Syst.*, pp. 27, 2012.
[28] O. Rabaste and T. Chonavel, ‘‘Estimation of multipath channels with long impulse response at low SNR via an MCMC method,’’ *IEEE Trans. Signal Process*., vol. 55, no. 4, pp. 1312–1325, Apr. 2007.
[29] J. S. Kim, H. C. Song, W. S. Hodgkiss, and M. Siderius, ‘‘Virtual time series experiment (VIRTEX) simulation tool for underwater acoustic communications,’’ *J. Acoust. Soc. Amer*., vol. 126, no. 4, p. 2174, 2009.

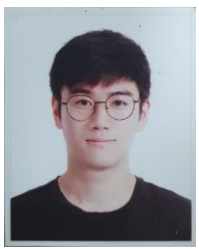

CHANG-HYUN YOUN received the B.S. degree in Department of Radio Communication Engineering from Korea Maritime and Ocean University, South Korea, in 2022. He is currently pursuing a master's degree at Korea Maritime and Ocean University. His research interests include sonar signal processing, underwater acoustic communications, underwater wireless optical communications, and underwater acoustic source localization.

HYOUNG-IN RA received the B.S. and M.S. degrees in Department of Radio Communication Engineering from Korea Maritime and Ocean University, South Korea, in 2019 and 2022, respectively. He is currently pursuing a Ph.D. at Korea Maritime and Ocean University. His research interests include sonar signal processing, underwater acoustic communications, underwater wireless optical communications, and underwater acoustic source localization.

KYUNG-WON LEE received the B.S. degree in Department of Radio Communication Engineering from Korea Maritime and Ocean University, South Korea, in 2023. He is currently pursuing a master's degree at Korea Maritime and Ocean University. His research interests include sonar signal processing, underwater acoustic communications, underwater wireless optical communications, and underwater acoustic source localization.

KI-MAN KIM received the B.S., M.S., and Ph.D degrees in electronic engineering from Yonsei University, Seoul, South Korea, in 1988, 1990, and 1995, respectively. He was a Fellow at Yonsei Medical Center, from 1995 to 1996. In 1996, he joined the faculty of the Department of Radio Communication Engineering, Korea Maritime and Ocean University, where he is currently a professor. His research interests include array signal processing, underwater acoustic communication, and source localization.

Peer-Reviewed Technical Communication

An Efficient Receiver Structure for Sweep-Spread-Carrier Underwater Acoustic Links

Leonardo Marchetti and Ruggero Reggiannini

***Abstract*—In this paper, we present an improved receiver architecture for sweep-spread-carrier modulation, a spread-spectrum technique proposed to effectively contrast the effects of time dispersion over multipath propagation channels in underwater acoustic wireless links. The proposed structure is capable of taking advantage of the energy received from all propagation paths rather than only from the strongest path, as envisaged in the pioneering paper introducing this modulation technique. A hardware version of the modem was implemented in the laboratory and its behavior was assessed and compared, using standard propagation models, to that exhibited by the traditional single-path-based scheme in terms of bit error rate. Results are presented showing that gains of a few decibels can be achieved in signal-to-noise-plus-interference ratio. Issues relevant to carrier/symbol synchronization, channel estimation, and sensitivity to Doppler distortion are also addressed.**

***Index Terms*—Maximal ratio combining, multipath propagation, multiple-branch receiver, rake receiver, spread spectrum, sweep-spread carrier, underwater acoustic communications.**

I. Introduction

UNDERWATER acoustic (UWA) communication systems have attracted considerable attention in recent years due to the growing interest for issues related to exploration, surveillance, and exploitation of the submarine environment (e.g., [1]–[6]). Most of these applications require some form of wireless communication capability between submerged terminals such as autonomous underwater vehicles (AUVs), platform/mother ships, nodes of underwater networks, etc. As is well known, the UWA multipath channel is plagued by several impairments, notably: 1) severe time dispersion due to the low sound propagation speed with consequent possible distortion of the received waveform; 2) for the same reason, amplification of Doppler shifts/rates associated to relative movements of terminals, possibly leading to significant signal distortion for wide signal bandwidths; 3) large propagation delays; and 4) lowpass behavior of the propagation channel caused by sound absorption, leading to strong limitation of bandwidth usage. These factors considerably limit transmission rates and coverage of UWA links in comparison with their electromagnetic radio counterparts and call for the search of more specific and robust signaling schemes. Comprehensive accounts of the above issues along with presentation and discussion of specific transmission schemes can be found in, for example, [3]–[6] and references therein.

A few years ago, an unconventional interesting spread-spectrum transmission technique was proposed in [7] and applied to the UWA channel. The basic idea is to employ a sawtooth-frequency-modulated waveform as signal carrier [termed sweep-spread carrier (S2C)], with linear frequency ramps, such as to facilitate separation at the receiver of the signal replicas collected from the various channel paths. Actually, since these replicas undergo different propagation delays, they are mapped to different positions on the frequency axis when the received signal is downconverted to baseband using a locally generated copy of the S2C synchronized to the strongest path. A proper design of the signal parameters permits to space the spectral replicas associated with the various paths far enough from one another so as to avoid their overlap. It is therefore possible to single out the strongest path with no interference from the others, thus canceling multipath-induced distortion.

From the pioneering paper [7] to date a number of improvements and variants of the initial scheme of the S2C receiver have been proposed and analyzed. In particular, the patent document [8] presents some conceptual receiver architectures making use of the energy received through multiple propagation paths instead of that from the strongest path only. Specifically, in [8, Fig. 19], a receiver block diagram is sketched wherein two signal replicas collected from different paths are processed by parallel receiver branches, and their individual phases and relative delay are corrected before the waveforms are applied to a block identified as "combined demodulator." The document however does not specify how the cited phases and delays are estimated, nor does it provide details about the operation of the demodulator. Furthermore, it was out of the scope of [8] to analyze and compare the performance of the above architectures. Additional related qualitative and quantitative results can be found in [9]–[11] addressing the impact of imperfect separation (and consequent onset of mutual interference) of the signal replicas being processed by the receiver branches on the estimation of their indi-

Manuscript received July 14, 2014; revised October 17, 2014, January 10, 2015, and June 03, 2015; accepted June 09, 2015. This work was supported in part by Tuscany Region, Italy in the framework of the project V-FIDES within the PAR FAS 2007-2013 program.

Associate Editor: S. Zhou.

L. Marchetti was with the Department of Information Engineering, University of Pisa, Pisa 56122, Italy. He is now with Intermarine S.p.A., 19038 Sarzana SP, Italy (e-mail: l.marchetti@intermarine.it).

R. Reggiannini is with the Department of Information Engineering, University of Pisa, Pisa 56122, Italy (e-mail: ruggero.reggiannini@iet.unipi.it).

Digital Object Identifier 10.1109/JOE.2015.2445251

vidual phases and relative delays, needed for combined demodulation.

In this paper, we make some steps ahead, by proposing and discussing a further implementation of the S2C receiver which integrates the schemes presented in the above references. As in [8], we consider an advanced receiver structure capable of enhancing the power efficiency of the scheme in [7] through exploitation of the energy received from multiple nonnegligible acoustic paths rather than only from the strongest path.

This goal can be achieved by first identifying the paths of significant level, then performing extraction and parallel elaboration for each of them, and finally combining the decision metrics from each processing branch. A noteworthy difference with respect to the schemes enumerated in [8] is that here we resort to an optimal approach to combine the branch outputs. The resulting multiple-branch receiver architecture is similar to that used for the reception of direct-sequence spread-spectrum (DS–SS) signals over time-dispersive wireless links, known as "rake receiver" [12, Ch. 13.5], but the context considered here is different as we now have to face the peculiar issues related to the unconventional format of the S2C waveform, involving, for instance, a different mechanism through which the received signal replicas interfere with each other after the despreading/demodulation stage.

A further contribution of this paper is to propose and assess a synchronization technique for the joint recovery of carrier and clock references for each of the signal replicas processed by the receiver. Its accuracy is provided in terms of root-mean-square (RMS) synchronization errors.

A real-time hardware version of the modem, complete with synchronization functions, was implemented in the laboratory and its behavior was assessed over standard UWA channel emulators and compared to that exhibited by the traditional strongest-path-based scheme in terms of bit error rate (BER) versus signal-to-noise ratio (SNR). Moreover, the sensitivity of the multiple-branch receiver to residual Doppler distortion is assessed and compared to that exhibited by the single-branch scheme.

The paper is organized as follows. In Section II, we briefly review signal and channel models, while in Section III, we illustrate the modem architecture with emphasis on the multiple-branch receiver section. Section IV discusses the algorithms for channel estimation and carrier/timing synchronization. Section V defines conditions for path resolvability, provides details on how the received waveform is processed in the multiple-branch structure, and also describes the system hardware implementation. Section VI presents simulation setup and results. Conclusions are finally drawn in Section VII.

II. Signal and Channel Models

Now we briefly review the S2C signal format paralleling the presentation in [7], which the reader is referred to for further details. We assume information is transmitted in the form of data packets, each starting with a preamble of P known pilot symbols, to be employed for carrier and symbol synchronization/tracking, followed by a payload of D symbols. Letting T denote the symbol spacing, the packet length is $T_B = (P + D)T$. The number of packets and the instants for their transmission depend on both the amount of information to be transferred and the specific link protocols, and are not of interest for the paper scope.

Focusing then on a generic packet at the transmitter side, the signal at baseband, before spectral expansion and frequency upconversion, is a conventional linearly modulated waveform

$$s(t) = \sum_{i=0}^{P+D-1} a_i g(t - iT) \tag{1}$$

where

$$\mathbf{a} \triangleq [a_0, \ldots, a_{P+D-1}]^T = [p_0, \ldots, p_{P-1}, d_0, \ldots, d_{D-1}]^T$$

denotes the vector of (differentially encoded) quadrature phase-shift keying (QPSK) symbols in the packet, and $g(t)$ is a root-raised-cosine pulse with rolloff factor α. In particular, the pseudorandom sequence $\mathbf{p} \triangleq [p_0, \ldots, p_{P-1}]^T$ of pilot symbols is common to all packets, while the sequence $\mathbf{d} \triangleq [d_0, \ldots, d_{D-1}]^T$ represents a specific data segment.

After spectral spreading and frequency upconversion, the bandpass signal to be fed to the acoustic projector can be written as

$$x(t) = \Re\{s(t)c(t)\} \tag{2}$$

where $c(t)$ denotes a frequency-modulated carrier achieving both frequency conversion and bandwidth expansion, as follows:

$$c(t) = \exp\left\{j2\pi\left[f_L\tau(t) + m\tau^2(t)\right]\right\} \tag{3}$$

where $\tau(t)$ is a sawtooth-shaped periodic sweep function, with period T_{sw}

$$\tau(t) = t - \left\lfloor \frac{t}{T_{sw}} \right\rfloor T_{sw} \tag{4}$$

$\lfloor z \rfloor$ being the largest integer not exceeding z. In (3), f_L represents the lower limit of the frequency ramps, while $2m$ is the ramp slope. The instantaneous carrier frequency during a ramp is proportional to the derivative of the argument of the exponential in (3)

$$f_i(t) = f_L + 2m\left(t - \left\lfloor \frac{t}{T_{sw}} \right\rfloor T_{sw}\right). \tag{5}$$

It follows that the upper frequency limit is $f_H = f_L + 2mT_{sw}$. The limits f_L and f_H, along with the sweep interval T_{sw}, usually taken as an integer multiple of the symbol spacing, are key design parameters as they define the slope $2m = (f_H - f_L)/T_{sw}$ of the ramps and characterize the ability of the receiver to resolve the multipath channel structure (i.e., to separate the signal replicas arriving from the various paths).

After spreading and frequency upconversion, the signal bandwidth amounts to approximately $B \approx f_H - f_L$, i.e., it is expanded by a factor (spreading factor)

$$\mathcal{M} \triangleq \frac{f_H - f_L}{\frac{1+\alpha}{T}} \tag{6}$$

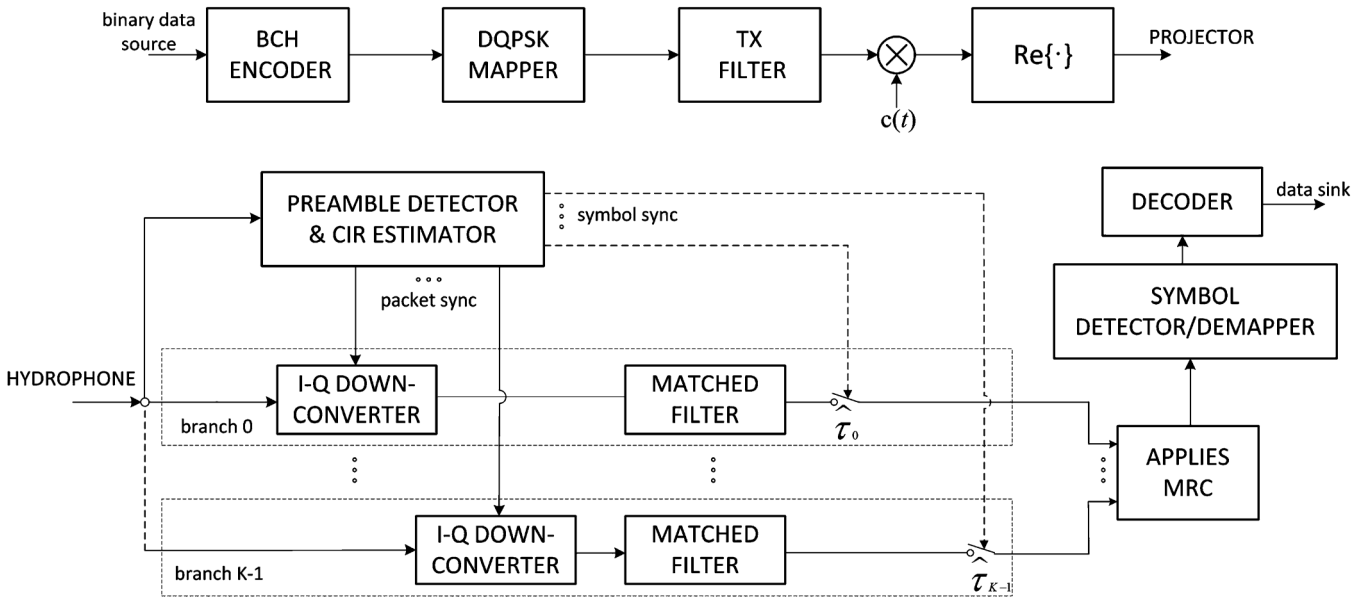

Fig. 1. Modem architecture.

with respect to a conventional narrowband signal, $\mathcal{M}$ usually being much greater than unity.

A general expression of the multipath time-varying UWA channel impulse response is as follows:

$$r_c(t, t_0) = \sum_{k=0}^{N_p(t_0)-1} h_k(t_0)\delta\left[t - t_0 - \tau_k(t_0)\right] \qquad (7)$$

where $N_p(t_0)$ is the number of (nonnegligible-level) paths and $h_k(t_0)$ and $\tau_k(t_0)$ are the (complex-valued) gain and delay of the kth path, respectively, all evaluated at the instant of application of the impulse $t = t_0$. In the following, we assume that the channel variations are negligible in a time span comparable to the packet length, so that the information about the channel parameters in (7), estimated from the packet preamble, can be considered reliable throughout the whole payload segment. This is not a severe constraint since transmission on the UWA link is normally preceded by a procedure of adjustment of the transmission parameters to the channel conditions. Accordingly, the dependence of the model in (7) on t_0 can be dropped and all channel parameters can be regarded as random variables (RVs) instead of random processes. Therefore, the received waveform can be written as

$$y(t) = \sum_{k=0}^{N_p-1} y_k(t) + w(t) \qquad (8)$$

where $w(t)$ is additive white Gaussian noise (AWGN) of double-sided spectral density $N_0/2$, accounting for both external and internal disturbance sources affecting the receiver, and $y_k(t)$ is the waveform received through the kth path, i.e., scaled by the coefficient h_k and delayed by τ_k

$$y_k(t) = \Re\left\{h_k s(t - \tau_k) c(t - \tau_k)\right\}. \qquad (9)$$

We observe that the main purpose of this paper is to propose a multiple-branch receiver architecture alternative to the schemes presented in [8] and to demonstrate that it may lead to a significant gain in power efficiency in comparison with the basic scheme in [7]. In this perspective, we felt it adequate to assume the relatively simple path model (9) and to limit the receiver functions to those strictly required to pursue the above goal. In particular, we decided not to tackle in detail the issues related to time variability and Doppler distortion, that in a practical receiver must be dealt with at an early stage of processing of the incoming packets. This approach is in line with that followed in [7]. However, in Section VI, we provide results about the sensitivity of multiple-branch and single-branch receivers to residual Doppler errors on each receiver branch.

III. Modem Architecture

A functional block diagram of the S2C modem is depicted in Fig. 1. The transmitter section consists of a standard S2C modulator similar to that discussed in [7]. The information bits are fed to a BCH encoder followed by a DQPSK symbol mapper. The resulting symbol sequence is used to build the data packet (function not detailed in the figure) that is passed through the shaping filter and finally applied to the S2C frequency upconverter.

The receiving section includes a block for preamble detection and channel impulse response (CIR) estimation, whose task is to identify, for each packet, the times of arrival of the preamble from the K strongest paths and also to estimate the (complex-valued) gains of these paths. This leads to the receiver architecture indicated in Fig. 1, wherein each of the K parallel branches is used to process the signal received from a single path. Specifically, with regard to the kth branch, the input is applied to an in-phase and quadrature converter which multiplies it by a replica of the S2C waveform synchronized with that received from the kth path. In this way, the signal spectrum relative to that path is despread and exactly converted to baseband, while subsequent matched filtering removes interference from the other paths provided that their spectra do not overlap

the "good" spectrum at baseband, i.e., their differential propagation delays with respect to the kth path are sufficiently large. The design criteria for this condition to hold true are discussed in Section V.

As the next step, the matched filter output is sampled at symbol rate at instants $iT + \hat{\tau}_k$, where $\hat{\tau}_k$ is an estimate of τ_k provided by the CIR estimator. Assuming exact intersymbol interference (ISI) cancellation, from (1), (8), and (9), the generic sample takes on the form

$$v_{k,i} = h_k a_i + w_{k,i}, \qquad i = 0, \ldots, D-1 \tag{10}$$

where the term $w_{k,i}$ denotes the noise sample generated from $w(t)$ in (8) after the above processing steps through the kth branch.

Finally, the K samples relevant to the symbol a_i are combined according to the maximal ratio combining (MRC) criterion [12, Ch. 13.4] before being fed to the symbol detector and the decoder. With regard to the MRC block, we observe that a sufficient condition for the noise terms $\{w_{k,i}\}_{k=0}^{K-1}$ to be mutually uncorrelated is that the differential delays between the various paths obey the same conditions allowing separation of the respective signal replicas, to be established in Section V. Indeed, the spectra of two incoming signal replicas can be separated by the despreader/demodulator on condition that their relative delay and the slope of the frequency ramps are sufficiently large. When this happens, the noise processes at the output of the matched filters on the respective receiver branches occur as well to be generated from the demodulation of frequentially nonoverlapping segments of the broadband input noise, and are therefore uncorrelated, this independently of the wideband noise spectral shape.

Finally, it is noted that when $K = 1$, the receiver structure reduces to that discussed in [7] where only the strongest path is processed.

IV. Timing and Channel Estimation

As mentioned earlier, the first operation to be accomplished at the receiver site is estimation of the timing of arrival of the signal replicas propagating along the channel paths. This permits to synchronize locally generated copies of the S2C waveform with those associated with the K strongest paths and then proceed to separate the signal replicas received from these paths. Another important related task is estimation of the complex-valued channel gains so as to identify the strongest paths and correctly apply the MRC technique.

Both the above operations are carried out by means of a correlator, as is now briefly outlined. Let $s_P(t)$ denote the baseband continuous-time version of the preamble separated from the payload, as follows:

$$s_P(t) = \sum_{i=0}^{P-1} p_i g(t - iT) \tag{11}$$

and also let

$$x_T(t) = s_P(t)c(t) \tag{12}$$

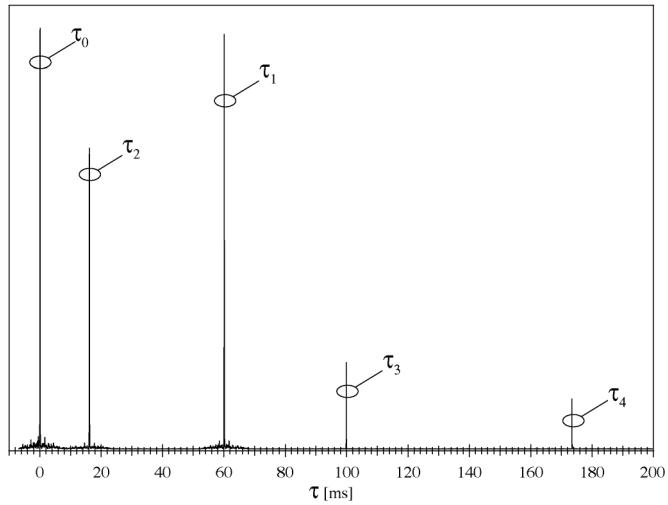

Fig. 2. Sample correlation function (square modulus). The vertical scale is arbitrary. The number of paths is $N_p = 5$, and the other system parameters are specified in Section VI.

denote the complex-valued bandpass version of the preamble incorporating both frequency upconversion and bandwidth expansion. It is noted from (2) that the real part of (12) represents the transmitted preamble.

Using for simplicity continuous-time notation, the task of the correlator is to calculate the inner product between the template function (12) and a newly received segment of the input waveform, and then take its squared modulus, as follows:

$$z(t) = |r(t)|^2, \qquad t \in \mathcal{T} \tag{13}$$

where

$$r(t) = \int_0^{T_P} y(t + \tau - T_P) x_T^*(\tau) d\tau, \tag{14}$$

$\mathcal{T}$ is a time interval in which the preamble is expected to be received and $T_P = PT$ is the preamble length. The receiver stores the functions (13) and (14) in memory along with the raw received waveform $y(t)$ for subsequent processing.

When path delays are sufficiently spaced from one another and the signal-to-noise-plus-interference ratio on the paths is high, the squared correlation $z(t)$ exhibits a definite peak in correspondence with each of the delays $\{\tau_k\}$. This can be verified observing that the width of the correlation peaks is approximately equal to the inverse of the bandwidth of the template waveform to be detected. Fig. 2 shows an example of such a function, obtained from the set of parameters specified in Section VI. Here the symbol spacing is 1.5 ms and the template signal bandwidth is approximately equal to the difference between the upper and lower limits of the frequency ramp, i.e., 16 kHz. Thus, the correlation peaks have a width in the order of 0.1 ms, which represents a measure of the delay resolution capability of the correlator. In the time scale of Fig. 2, covering several tens of symbols, and in comparison with typical values of differential delays (see Table II in Section VI), these peaks are very narrow and easily detectable at the operating SNRs.

More specifically, assuming for a moment that the receiver is driven by a single noiseless signal replica received from the kth

path [see (9)], it is found that (13) peaks at the instant $T_P + \tau_k$, and the corresponding value for the inner product (14) is

$$r(T_P + \tau_k) = \frac{E_{S_P}}{2} h_k \tag{15}$$

where $E_{S_P} = \int_0^{T_P} |s_P(\tau)|^2 d\tau$ is the energy of $s_P(t)$. From (15), it is seen that at the instant where the squared correlation peaks, the inner product yields a value proportional to the path gain h_k, while the squared peak level is proportional to $|h_k|^2$. Therefore, (14) provides all information necessary for path sorting, ramp synchronization, and implementation of the MRC detector.

Collecting the above, once correlation (13) has been calculated, a maximum search procedure must be initiated to obtain an estimate of the delay associated to each preamble replica arriving at the receiver. Of course, the procedure must be capable of detecting "good" correlation peaks against false peaks produced by noise and possibly by sidelobes associated to good peaks. This can be achieved through a simple approach consisting of the following steps. First, the noise level must be estimated by the receiver during the silent periods before transmissions or between the transmission of two consecutive messages. Knowledge of the noise level along with the correlator parameters allows to infer the noise-only statistics of the correlator output, and to fix a threshold λ yielding a desired tradeoff between false and missed detection probabilities, with reference to limit conditions characterized by the least operating SNRs, e.g., when the distance between terminals is at the limit of coverage. As the next step, the search algorithm looks for the peaks exceeding the threshold and tries to classify them according to their strength and differential delays. This operation is aimed at identifying the "best" paths, i.e., those with largest level and with sufficient delay from one another so as to be easily separable by the despreading/demodulation block. The algorithm starts by estimating the delay associated to the strongest replica (assumed relevant to the path of index zero), as follows:

$$\hat{\tau}_0 = \arg \max_{\substack{z(t)>\lambda \\ t\in\mathcal{T}}} z(t). \tag{16}$$

The delays associated to the other $N_p - 1$ paths of significant gain are identified by looking for the other local maxima of $z(t)$, using the following iterative approach:

$$\hat{\tau}_i = \arg \max_{\substack{z(t)>\lambda \\ t\in\mathcal{T} \\ t\notin\mathcal{I}_i}} z(t), \qquad i = 1, 2, \ldots, N_p - 1 \tag{17}$$

where $\mathcal{I}_i$ denotes a set of subintervals of $\mathcal{T}$ centered around the values of delay already identified through step $i-1$, that must be excluded from the search at the current step i, i.e.,

$$\mathcal{I}_i = \{(\hat{\tau}_0 - T_{\rm cor}, \hat{\tau}_0 + T_{\rm cor}) \cup \cdots \cup (\hat{\tau}_{i-1} - T_{\rm cor}, \hat{\tau}_{i-1} + T_{\rm cor})\}. \tag{18}$$

In this way, the N_p strongest paths are orderly identified along with their delays. However, problems may arise at this stage if the peaks are spaced too tightly, i.e., if the corresponding relative path delays are too close to one another. As noted earlier, the width of the correlation peaks is given approximately by the inverse of the template signal bandwidth. This provides a measure of the delay resolution capability of the correlator, inasmuch as peaks that are spaced less than this measure cannot be distinguished. A further aspect to be taken into account is the presence of sidelobes around the correlation peaks in (13), which for very strong signal level could exceed the threshold and be misdetected as additional independent peaks. To avoid the latter type of error, it is convenient that the length $2T_{\rm cor}$ of the windows centered on the correlation peaks be selected large enough to include a few sidelobes as well, at the cost of accepting a further slight degradation in the detector resolution properties. With reference to the set of parameters in the example of Section VI, the parameter $2T_{\rm cor}$ can be fixed at 1 ms (covering the main correlation lobe plus a few sidelobes on each side), which is still far smaller than the channel delay spread in a typical scenario.

When the above procedure of multiple path detection and classification is over, the receiver must select a number $K \leq N_p$ of paths to be processed in its K branches. A reasonable criterion is to select the strongest K paths, but some of these could be discarded at this stage if their differential delay is not sufficient to ensure adequate separation of their spectra after despreading/demodulation.

In addition to estimating the delay of the main usable paths of the UWA channel, the receiver must proceed to evaluate the relevant complex-valued path gains in view of their usage within the MRC block (see Fig. 1). As noted earlier, these gains are provided by (15) as a byproduct of the same correlation algorithm employed for path delay estimation.

V. Design Issues and Hardware Implementation

A. Conditions for Path Resolvability

Recalling the discussions in Sections II and III, for the K-branch receiver of Fig. 1 to work properly it is required that, for each branch, the signal spectrum converted to baseband does not collide with the spectra of the signal replicas being processed by the other branches. This allows the signal at baseband to be extracted by means of a simple (lowpass) matched filter. For these conditions to be met, it is necessary that the differential delays between all pairs of paths do not drop below a certain threshold. A further constraint is that the maximum differential delay must not exceed T_{sw} to avoid ambiguities in delay estimation.

More specifically, with no loss of generality, we can treat $\{\tau_k\}_{k=0}^{K-1}$ as differential delays with respect to τ_0, arranged in nondecreasing order, i.e., we set $\tau_0 = 0 \leq \tau_1 \leq \cdots \leq \tau_{K-1}$. Then, the constraints to be put on these differential delays are as follows (see also [7]):

$$\begin{cases} 2m\delta\tau_{\min} \geq \dfrac{1+\alpha}{T} \\ -2m\delta\tau_{\max} + f_H - f_L \geq \dfrac{1+\alpha}{T} \end{cases} \tag{19}$$

where

$$\delta\tau_{\min} = \min_{0\leq i,j\leq K-1} |\tau_i - \tau_j|, \qquad i \neq j$$

is the minimum (absolute) differential path delay and

$$\delta\tau_{\max} = \max_{0\leq i,j\leq K-1} |\tau_i - \tau_j| = \tau_{K-1}, \qquad i \neq j$$

is the maximum differential path delay, or channel time dispersion. Using (6) in (19) yields

$$\begin{cases} T_{sw} \leq \mathcal{M}\delta\tau_{\min} \\ T_{sw} \geq \dfrac{\mathcal{M}}{\mathcal{M}-1}\delta\tau_{\max}. \end{cases} \tag{20}$$

For the existence of values of T_{sw} satisfying both above conditions it is required that

$$1 \leq \frac{\delta\tau_{\max}}{\delta\tau_{\min}} \leq \mathcal{M} - 1. \tag{21}$$

The first inequality in (20) sets a lower limit to the absolute difference between the arrival times of any two signal replicas. When the difference exceeds this limit, the receiver is able to accurately resolve the channel multipath structure. Otherwise, when two received replicas are spaced too closely, after despreading they will overlap in the frequency domain, thus preventing their exact separation. On the other hand, the second inequality in (20) puts an upper limit to the differential path delays, approximately equal to T_{sw} when $\mathcal{M}$ is large. Actually, a signal replica delayed more than T_{sw} with respect to the one traveling on the shortest path would generate a timing estimate affected by an ambiguity equal to an integer multiple of T_{sw} that could not be detected and recovered, with a negative impact on the MRC algorithm.

Fig. 3 shows a realization of power spectral density of the received signal after downconversion/despreading for a five-ray scenario, assuming that downconversion is carried out for the strongest path. Transmission parameters are the same as in the example of Fig. 2. Inspection of the figure reveals that in this case all paths are resolvable (apart from a marginal overlap of two small spectral replicas located midway on the frequency axis), and in particular the useful signal (whose spectrum lies around the origin) can be recovered by means of a lowpass filter, without (or with negligible) interference from the other replicas. The latter signal components, carrying useful power as well, can in turn be extracted by multiplication of the received waveform by properly delayed replicas of $c(t)$ followed by lowpass filtering, as illustrated in Section III. More specifically, from Fig. 3, it is seen that, in addition to the signal spectrum centered on the origin, there are eight other spectral replicas generated by the paths with delays τ_1, τ_2, τ_3, and τ_4. Indeed, recalling (19) and the ensuing discussion, the kth path gives rise to two spectral components (identified with the indices k_1 and k_2 in Fig. 3), centered around the frequencies $2m\tau_k$ and $f_H - f_L - 2m\tau_k$, $k = 1, 2, 3, 4$, respectively. The actual values of these frequencies are specified in Table II.

B. Merging Branch Outputs

As mentioned earlier, the receiver is made up of K parallel branches, designed to jointly extract and elaborate up to K replicas of the signal received from the multipath UWA channel. The kth branch proceeds to despread/downconvert the received signal through its multiplication by $c(t - \hat{\tau}_k)$, as described in Section IV, where $\hat{\tau}_k$ is an estimate of the propagation delay on the kth path. Assuming error-free delay estimates and exact resolvability of the signal on all branches according to the criteria identified in Section V-A, the sampled

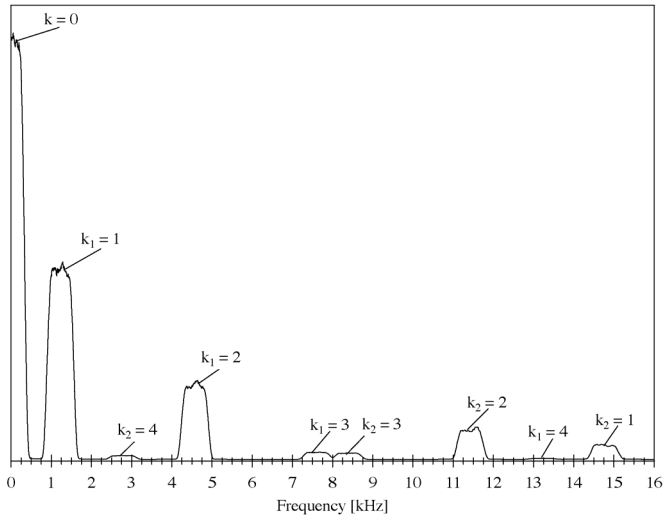

Fig. 3. Power spectral density of the received signal after downconversion/despreading of the strongest path ($k = 0$). The vertical scale is arbitrary. The system parameters are the same as in Fig. 2 and are specified in Section VI.

output of the kth branch takes on the form of (10). All branch outputs are then combined according to the MRC optimality criterion, as follows:

$$q_i = \sum_{k=0}^{K-1} \hat{h}_k^* v_{k,i} \tag{22}$$

where $\hat{h}_k$ is the estimate of the kth path gain. The sequence of samples (22) is then fed to the decoder/data detector for further processing.

As mentioned in the Introduction, the above approach is reminiscent of that employed in the so-called "rake receiver" proposed for conventional DS–SS modulations [12, Ch. 13.5], even though the context here is different from that envisaged in typical electromagnetic wireless links. Actually the mechanism generating mutual interference between two replicas of the signal arriving from different paths is not the same in DS–SS and S2C. In the case of a DS–SS system, the spreading code is normally designed so as to be self-uncorrelated, i.e., it is sufficient to shift two signal replicas by just one code chip, and the mutual interference, after the despreading and matched filtering stages, is reduced by approximately the spreading factor. This interference does not decrease further if the delay between replicas grows. In the frequency domain, the presence of the interfering signal results in a small increase in the (approximately white) spectral level of noise and interference. Conversely, in the case of an S2C system, achievement of orthogonality between the signal replicas relies on the ability of the frequency ramp to separate their spectra, and in turn this depends jointly on the relative time delay between the paths and on the slope of the ramp itself. It follows that, due to the presence of the out-of-band ripple in the baseband signal spectrum and the rolloff region (with sidelobes as well) of the matched filter responses, the amount of mutual interference depends on the frequency-domain distance between the spectra after despreading/demodulation: the larger this distance, i.e., the larger the relative delay between the two replicas and/or the ramp slope, the lower will be the interference, and *vice versa*.

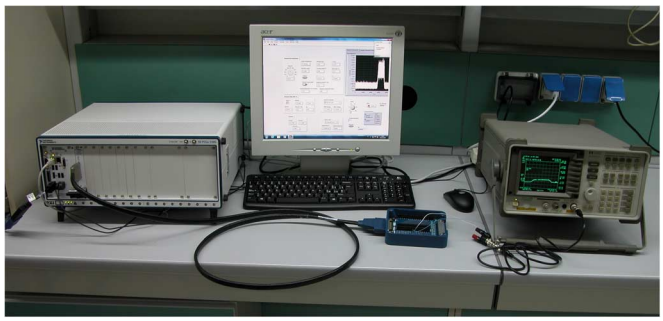

Fig. 4. Test bench: NI chassis hosting controller and data acquisition board, PC with LabView, spectrum analyzer.

Furthermore, the demodulation process in the S2C system is affected by occasional frequency jumps of the interfering replicas (see, e.g., [7, Fig. 4]), representing a specific form of disturbance that is absent in the DS–SS context.

However, assuming the K paths can be resolved, we can borrow from the rake receiver the expression of the asymptotic gain in power efficiency

$$G_R = \frac{\sum_{k=0}^{K-1} E\left\{|h_k|^2\right\}}{E\left\{|h_0|^2\right\}} \tag{23}$$

where $E\{\cdot\}$ denotes statistical expectation that can be achieved with respect to the receiver operating on the single path of gain h_0. This result has been confirmed by simulations (Section VI).

C. Hardware Implementation

Now we briefly present our real-time implementation of the modem architecture discussed in the foregoing sections. The testbed is based on National Instruments (NI) hardware [13], controlled by LabView (LV) applications. Specifically, we used the chassis NI PXIe-1085 equipped with the controller NI PXIe-8135 and the data acquisition board NI PXIe-6361. The entire system is controlled by an LV-based code that exploits the built-in functions provided in the RF Communications toolkit. The transmitter and receiver sections of the modem were both entirely implemented in hardware. Fig. 4 shows the complete test bench used for the modem implementation, composed by the controller board within the chassis, a PC running *ad hoc* LV application software and also a spectrum analyzer.

VI. Simulation Results

The transmission architecture in Fig. 1 was implemented and assessed using the hardware testbed described in Section V-C, in conjunction with the software package Bellhop [14], a popular open-source simulator of the UWA environment. In particular, this simulator permits to identify both the coherent and noncoherent channel profile, i.e., for a fixed number of paths, their complex-valued (modulus and phase) gains, or simply their RMS values, versus propagation delay, to be associated to an arbitrary UWA operating scenario.

For simplicity, in the following, we limit our consideration to a single scenario, characterized by shallow water (130 m) with sound-speed profile versus depth typical of the summer period and plotted in the left section of Fig. 5. The values assumed for the main geometric and acoustic parameters of the UWA scenario are summarized in Table I, while Fig. 6 provides a pictorial

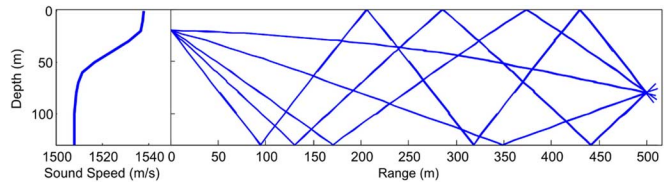

Fig. 5. Ray tracing produced by Bellhop.

TABLE I
Main Acoustic and Geometric Parameters of the UWA Scenario

TX depth	20 m
RX depth	80 m
Horizontal distance	500 m
Bottom type	gravel
Bottom depth	130 m
Surface (for reflection properties only)	sea state 0
Sound-speed profile	see Fig. 5
Center frequency	26 kHz
TX launching angles	0° : +180°

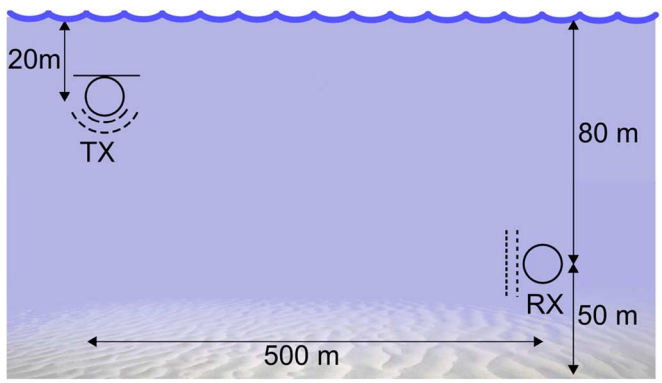

Fig. 6. Geometry of the UWA link.

representation of the link geometry. In the right section of Fig. 5, we also show the curves produced by the Bellhop ray tracing tool that can be used to calculate the channel power-delay profile.

Using the ambient parameters of Table I and the Bellhop tool it is possible to create a multipath propagation model with a fixed number of paths. Here we limit our attention to the first five strongest paths (direct plus four experiencing single or multiple reflections from the surface and/or the bottom). We note that simulations carried out with a larger number of paths (up to 15) showed negligible deviations from the results obtained with five paths.

With reference to the link geometry of Fig. 6, the resulting power-delay profile is visible in Table II. From Bellhop, it can be seen that the power associated to these five paths amounts to more than 96% of the total received power in the above scenario. For simplicity, the powers associated to the paths in Table II are normalized so that they sum up to unity. Moreover, the attenuation over the direct path is assumed deterministic, while the other path coefficients are modeled as independent identically distributed circular Gaussian variables with zero mean and normalized powers given in column 2, rows 1–4 of Table II. As to the spectral shifts specified in the last column of Table II, their meaning is defined at the end of Section V-A.

TABLE II
POWER-DELAY PROFILE FOR THE FIVE-PATH CHANNEL

Path	Normalized power	Relative delay [ms]	Spectral shifts [kHz]
0	0.388	0	0
1	0.380	16.11	1.227, 14.773
2	0.198	60.04	4.575, 11.425
3	0.025	99.84	7.607, 8.393
4	0.009	173.49	13.218, 2.782

TABLE III
PHYSICAL LAYER PARAMETERS

T_{sw}	210 ms
T_P	$2T_{sw}$
$\mathcal{M}$	20
α	0.2
Symbol spacing	1.5 ms
Payload length	1024 symbols
Modulation	DQPSK
Codec	uncoded, BCH (1431, 2047)
Data rate (payload)	1333 bit/s, 931 bit/s
f_L	18 kHz
f_H	34 kHz
T_{cor}	$8/(f_H - f_L)$

Finally, the physical layer communication parameters used throughout the trials are specified in Table III.

The five-path channel defined by Table II was implemented on the NI testbed using the previously described model. In particular, for every channel realization, the receiver input is generated by combining five versions of the transmitted waveform, each with a different delay and attenuation according to the statistics specified in Table II and remarks thereof. The SNR, defined as the ratio between the average energy per symbol received through all considered paths to the noise power spectral density, is varied by injecting AWGN with variable spectral level.

Specifically, our purpose here is to compare the performance of the conventional receiver in [7] with that achievable by the multiple-branch parallel structure in Fig. 1 where we assume $K = 3$. This seems a reasonable choice to achieve a substantial gain without exceeding in receiver complexity. To this aim, we observe that, from (23) and from the values in the first three rows of Table II, corresponding to the three strongest paths, the maximum expected gain of the three-branch receiver is $G_R \approx 3.96$ dB. This margin seems to be actually achievable in view of the fact that the parameters $\delta\tau_{\min}$ and $\delta\tau_{\max}$ do largely satisfy condition (21): $\delta\tau_{\max}/\delta\tau_{\min} \approx 10.77 \ll \mathcal{M} - 1$. Further to be noted, since the three considered signal components can be exactly separated by the receiver, the relative phase rotations associated to the path gains are immaterial, and the receiver performance is only affected by the noncoherent power-delay profile.

Fig. 7 shows plots of the BER versus SNR obtained for uncoded transmission assuming error-free channel estimation and carrier/symbol synchronization in all receiver branches. The plots were obtained from Monte Carlo simulations over a large number of channel and symbol realizations. The two curves of BER are relevant to the conventional single-branch receiver $(K = 1)$ and to the three-branch receiver $(K = 3)$. It is observed that the latter scheme asymptotically outperforms the former by around 3.3 dB, very close to the asymptotic gain G_R.

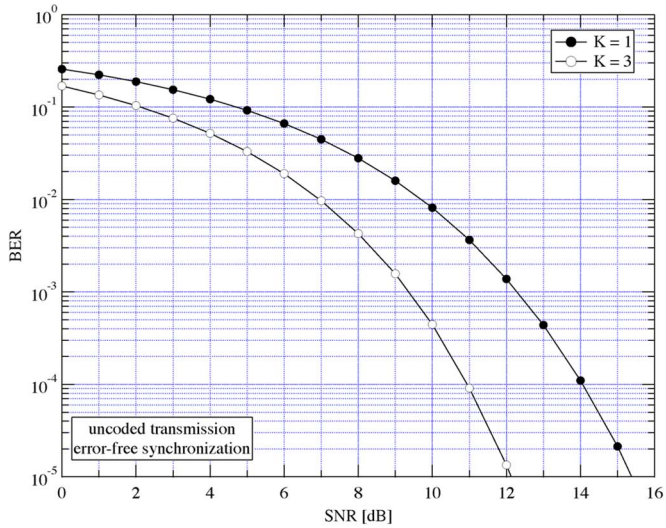

Fig. 7. BER versus SNR, uncoded transmission, five-path channel, single-branch receiver, and three-branch receiver.

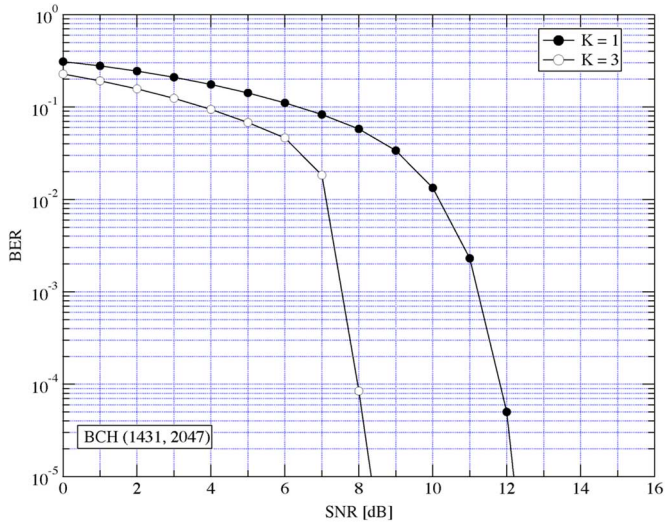

Fig. 8. BER versus SNR, coded transmission, five-path channel, single-branch receiver, and three-branch receiver.

Fig. 8 shows curves of BER versus SNR for the same single-branch and three-branch receivers, obtained in the more realistic situation in which the transmitter employs a BCH encoder, with coding rate $r = 1431/2047 \simeq 0.7$, and the receiver actually incorporates the channel estimator and the carrier/symbol synchronizer discussed in Section IV. The benefit in terms of SNR gain provided by the multiple-branch receiving structure is still apparent. For example, at BER $= 10^{-5}$, this gain is around the asymptotic value of 4 dB, while the advantage provided by the BCH encoder with respect to uncoded transmission (curves in Fig. 7) is more than 3 dB.

In passing, we also assessed the receiver behavior with the MRC replaced by the simpler scheme known as equal gain combiner (EGC) [12, Ch. 13.4] where the combination rule is as in (2) with $\hat{h}_k^*$ replaced by $\hat{h}_k^*/|\hat{h}_k|$. This led to a negligible performance degradation (results not shown) with respect to MRC in the scenario of Table II, as is to be expected when there is no definite predominant path, as in links where the transmit and receive transducers are weakly directive, and thus the strength of the surface-reflected (and possibly bottom-reflected) path is comparable to that of the direct path. Conversely, when the path levels are strongly unbalanced, the MRC approach is likely to exhibit an edge.

It is now appropriate to briefly discuss the performance of the path delay estimator which, as we have seen, plays an important role for synchronization of the despreading waveforms in the multiple-branch receiver, as well as for symbol timing recovery.

As discussed in Section IV, the delay is estimated by determining the instant at which the squared correlation (13) exhibits a peak. Of course, a necessary condition to get an accurate estimate is that the sampling rate at the receiver input be adequately high. The results presented here are obtained using a sampling rate of 100 kHz, a condition which, recalling the data of Table III, corresponds to taking 100 samples per symbol and slightly more than three samples per cycle at the highest instantaneous frequency f_H of the waveform $c(t)$. In addition, to further improve the accuracy of the above estimator, we resorted to a parabolic interpolator operating on the highest sample of the squared correlation and on the adjacent two. This scheme was considered satisfactory insofar as a further increase of the sampling rate was observed not to entail any additional gain in terms of root-mean-square estimation error (RMSEE).

Fig. 9 shows plots of RMSEE affecting the delay estimates for the three strongest paths of the five-path scenario defined by Tables I–III as a function of SNR. As expected, the lowest curve is the one relevant to the strongest (direct) path ($k = 0$) while the other two curves, relative to paths experiencing a single ($k = 1$) or a double ($k = 2$) reflection, are somewhat shifted versions of the former along the SNR axis, where the shifts are to be ascribed to the different (statistically smaller) path gains. Also to be noted, when the SNR grows, all curves do not decrease indefinitely, but rather they tend asymptotically to different constant (floor) values. This behavior can be explained observing that even though the five signal replicas are sufficiently shifted from one another as to be substantially uncorrelated, nevertheless they exert a mutual irreducible disturbance whose impact is felt even when the noise vanishes. Accordingly, the different floor levels are related to the different values of signal-to-mutual-interference ratio existing between the signal replicas.

Furthermore, we found that the delay estimates are substantially unbiased for all paths, and this holds true in general provided that the correlation peaks are well separated from one another, i.e., when conditions (21) are met.

We also assessed the sensitivity of the data detector to residual errors after estimation and compensation of the Doppler-induced distortion on each receiver branch. Indeed, in the presence of relative motion between the transmitter and the receiver, the signal replicas received from the channel paths are compressed or expanded in time by the factors $b_k \triangleq \nu_k/c_s$,

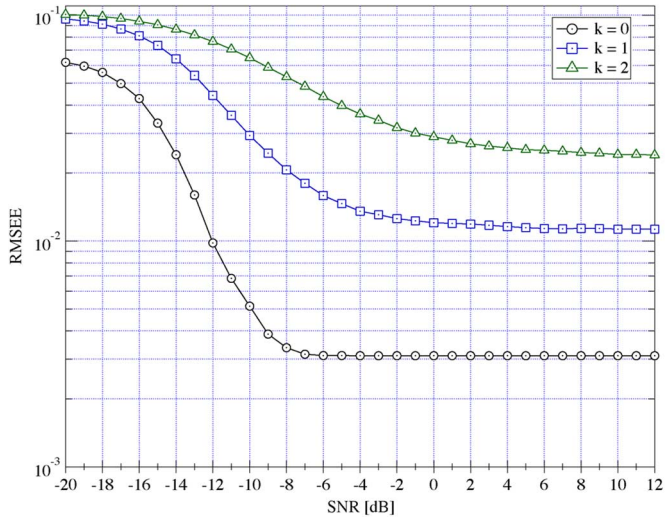

Fig. 9. RMSEE versus SNR, five-path channel, delay estimate for $k = 0, 1, 2$.

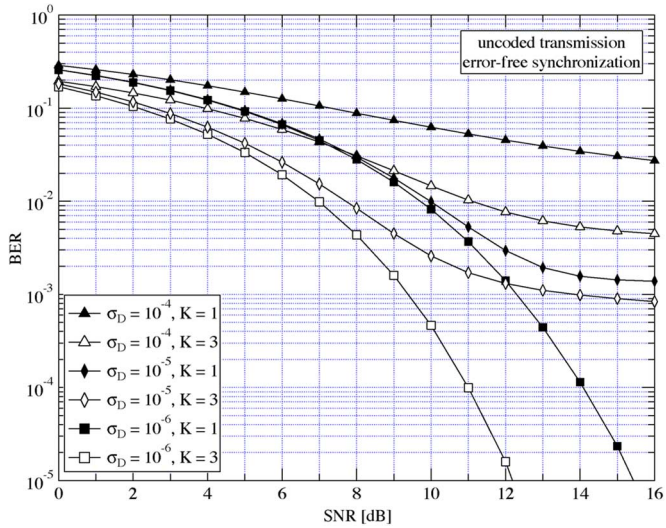

Fig. 10. BER versus SNR with residual Doppler distortion, uncoded transmission, five-path channel, single-branch receiver, and three-branch receiver.

$k = 1, \ldots, K$, where ν_k is the relative speed between the two terminals, and c_s is the sound speed. We note that 1) this distortion cannot be merely regarded as a frequency shift, in view of the large relative bandwidth occupied by the S2C waveform, entailing different Doppler shifts at the band edges; and 2) each path undergoes a specific distortion depending on its angle of arrival at the receiver. As noted at the end of Section II, when the above effects cannot be neglected, the receiver must incorporate a block for estimation of the factors b_k and cancellation of the Doppler distortion from each receiver branch. Here we do not focus on any specific algorithm for estimation/cancellation of the Doppler distortion, and limit ourselves to evaluate the sensitivity of the receiver BER to errors in the estimation of the b_k's. Our aim is to provide a measure of the errors the receiver can tolerate with negligible performance loss and also to compare the behavior of the multiple-branch receiver versus the single-branch receiver to this specific type of channel impairment. To proceed we let ϵ_k denote the error in the estimation (and subsequent compensation) of b_k for the kth receiver branch, and model the quantities ϵ_k, $k = 1, \ldots, K$, as independent zero-mean Gaussian RVs with equal variance σ_D^2.

In Fig. 10, we provide some results for the uncoded case, in the form of BER curves versus SNR obtained in the same conditions as Fig. 7, except for the presence of the residual Doppler errors ϵ_k on the receiver branches. Similar results were observed for coded transmission. Inspection of the figure reveals that these errors affect the multiple-branch and single-branch receivers approximately in the same way. Specifically, we note that: 1) the impact of residual Doppler distortion is negligible provided that σ_D is around 10^{-6} or smaller; 2) larger values of σ_D, say $\sigma_D = 10^{-5}$ or $\sigma_D = 10^{-4}$, progressively degrade the receiver performance and introduce a floor in the BER curves; and 3) in any case, the multiple-branch receiver exhibits a significant edge over the single-branch structure for a given σ_D.

VII. Conclusion

We have proposed and assessed an alternative implementation of a receiver for S2C transmissions over time-dispersive UWA channels, based on a multiple-branch parallel architecture. Each branch has the task to extract and process the signal received from one of the paths, and the outputs of the branches are finally combined together in an optimal way. We have shown that the above structure is capable of significantly improving the system power efficiency with respect to the classical single-path-based S2C receiver. In particular, we have identified conditions allowing the signal replicas from the various paths to be exactly separated. A real-time version of the system has been implemented on a hardware testbed, and its performance has been assessed in the laboratory using typical UWA channel models. For the common situation where in addition to the direct path there are also a few single- or double-bounce reflected paths of nonnegligible level, we have shown that it is possible to achieve power gains of a few decibels in comparison with the single-path receiver. We also discussed an algorithm for synchronization of the despreading signal and for symbol timing recovery, and analyzed its impact on the receiver performance. Finally, we assessed the sensitivity of the multiple-branch receiver to residual Doppler distortion, showing that it still provides a significant margin with respect to the single-branch structure.

References

[1] D. B. Kilfoyle and A. B. Baggeroer, "The state of the art in underwater acoustic telemetry," *IEEE J. Ocean. Eng.*, vol. 25, no. 1, pp. 4–27, Jan. 2000.

[2] E. M. Sozer, M. Stojanovic, and J. G. Proakis, "Underwater acoustic networks," *IEEE J. Ocean. Eng.*, vol. 25, no. 1, pp. 72–83, Jan. 2000.

[3] M. Stojanovic and J. Preisig, "Underwater acoustic communication channels: Propagation models and statistical characterization," *IEEE Commun. Mag.*, vol. 47, no. 1, pp. 84–89, Jan. 2009.

[4] P. A. van Walree, "Propagation and scattering effects in underwater acoustic communication channels," *IEEE J. Ocean. Eng.*, vol. 38, no. 4, pp. 614–631, Oct. 2013.

[5] M. Stojanovic, J. A. Catipovic, and J. G. Proakis, "Phase-coherent digital communications for underwater acoustic channels," *IEEE J. Ocean. Eng.*, vol. 19, no. 1, pp. 100–111, Jan. 1994.

[6] S. Zhou and Z. Wang, *OFDM for Underwater Acoustic Communications*. New York, NY, USA: Wiley, 2014.

[7] K. G. Kebkal and R. Bannasch, "Sweep-spread carrier for underwater communication over acoustic channels with strong multipath propagation," *J. Acoust. Soc. Amer.*, vol. 112, no. 5, pp. 2043–2052, Nov. 2002.

[8] R. Bannasch and K. G. Kebkal, "Method and devices for transmitting and receiving information," U.S. Patent 6,985,749 B2, Jan. 2006.

[9] K. G. Kebkal, A. K. Kebkal, and G. A. Ermolin, "Mathematic and experimental evaluation of phase errors when receiving hydro-acoustic PSK-signals with sweep-spread carrier in reverberant underwater environments," in *Proc. MTS/IEEE OCEANS Conf.*, Bergen, Jun. 10–13, 2013, DOI: 10.1109/OCEANS-Bergen.2013.6608155.

[10] K. G. Kebkal, V. K. Kebkal, O. G. Kebkal, and R. Petroccia, "Clock synchronization in underwater acoustic networks during payload data exchange," in *Proc. 2nd Int. Conf. Exhibit. Underwater Acoust.*, Rhodes, Greece, Jun. 22–27, 2014, pp. 1181–1190.

[11] K. G. Kebkal, A. G. Kebkal, and V. K. Kebkal, "Synchronization tools of acoustic communication devices in control of underwater sensors, distributed antennas, autonomous underwater vehicles," in *Gyroscopy and Navigation*. Austin, TX, USA: Pleiades Publishing, 2014, vol. 5, pp. 222–230.

[12] J. G. Proakis and M. Salehi, *Digital Communications*, 5th ed. New York, NY, USA: McGraw-Hill, 2007.

[13] National Instruments [Online]. Available: http://www.ni.com/

[14] Ocean Acoustics Library [Online]. Available: http://oalib.hlsresearch.com/

Leonardo Marchetti received the M.Sc. degree in telecommunications engineering and the Ph.D. degree in information engineering from the University of Pisa, Pisa, Italy, in 2010 and 2015, respectively.

From 2011 to 2014, he was with the Department of Information Engineering, University of Pisa, first as a CNIT Research Fellow and then as a Ph.D. student. Since 2015, he has been with Intermarine S.p.A., Sarzana SP, Italy, as a Combat System Manager of the Production Department. His research interests focused on the area of multicarrier multiantenna wireless communication systems, and underwater communication systems.

Ruggero Reggiannini received the Dr.Ing. degree in electronics engineering from the University of Pisa, Pisa, Italy, in 1978.

From 1978 to 1983, he was engaged in the design and development of underwater acoustic systems. Since 1984, he has been with the Department of Information Engineering, University of Pisa, where he is currently Full Professor of Radio Communications. He is the author of several scientific papers. He has participated in several projects with private and public organizations.

Dr. Reggiannini has served as editor for the IEEE Transactions on Communications.

Development of upper-layer protocols with S2CR acoustic modems emulator

Conference Paper · September 2012

DOI: 10.13140/RG.2.1.2300.1768

3 authors:

Oleksiy G. Kebkal
EvoLogics GmbH
165 PUBLICATIONS **1,486** CITATIONS
SEE PROFILE

Maksym Komar
Evologics GmbH
14 PUBLICATIONS **202** CITATIONS
SEE PROFILE

Konstantin Georgievich Kebkal
250 PUBLICATIONS **1,908** CITATIONS
SEE PROFILE

Development of upper-layer protocols with S2CR acoustic modems emulator

Oleksiy Kebkal
EvoLogics GmbH
Berlin, Germany
Email: lesha@evologics.de

Konstantin Kebkal
EvoLogics GmbH
Berlin, Germany
Email: kebkal@evologics.de

Maksym Komar
EvoLogics GmbH
Berlin, Germany
Email: komar@evologics.de

***Abstract*—Modern underwater acoustic modems are sophisticated devices, designed to help for solving challenging practical tasks, like monitoring the underwater infrastructure in offshore industry, positioning and data exchange during cooperative missions of underwater vehicles, precise positioning of distributed underwater nodes. Most of these applications are unique, and each requires development of complex software with implemented custom protocols for data exchange between the nodes of underwater acoustic sensor network. The software has to meet strict requirements to its long-term reliability and must undergo extensive testing. As deployment, maintenance and recovery costs of underwater systems are notably high, to keep the development costs within reasonable limits, development and implementation of the software should be preferably done by means of a high-quality emulation/simulation environment.**

The paper describes a real-time emulator of EvoLogics underwater acoustic modems. The emulator provides a fully-featured emulation of the data-link layer and includes a simplified simulator of the physical layer that accounts for signal propagation delays, multipath propagation, data packet collisions, packet synchronization errors and bit errors with a user-defined bit error rate. The emulator substitutes acoustic modem hardware when running testbed scenarios during development and testing of the upper layer protocols and applications. The emulator provides fully featured support of its cross-layer synchronization mechanism, allowing to develop positioning protocols or hybrid protocols combining communication with positioning on the upper layer protocol.

I. Introduction

Modern underwater acoustic modems are sophisticated devices that support not only point-to-point data exchange between two systems, but also enable a complex integration of underwater acoustic sensor networks. These acoustic devices must solve challenging practical tasks, like monitoring underwater infrastructure of offshore industry, positioning and data exchange during cooperative missions of underwater vehicles, precise positioning of the nodes of distributed underwater systems etc.

Most of these applications are unique, and each requires development of complex software implementing custom protocols for data exchange between the nodes of an underwater acoustic sensor network. The software has to meet strict requirements to its long-term reliability and must undergo extensive testing. As deployment, maintenance and recovery costs of underwater systems are notably high, to keep the development costs within reasonable limits, development and implementation of the software must be performed in a high-quality simulation environment.

Existing network simulators, for example, the NS2-Miracle[1], are highly useful tools for research and development, but a network simulator alone is not sufficient for many aspects of software development including algorithm design, simulation, verification and testing of the target system. An essential step forward was made with the recent releases of network simulator extensions, such as the SUNSET[2] and the DESERT[3], which enable interfacing real acoustic modems into the testbed framework, substituting the simulations of the physical and data-link layers.

Nevertheless, this approach has its shortcomings. Using expensive real modem hardware for simulation-related purposes elevates development costs. On the other hand, the NS2-Miracle itself does not implement physical and data-link layer protocols of commercially available modems, Therefore, the difference between the real hardware and its implementation in the simulator, the difference in the interfaces in the simulator and the hardware and other factors, specific for the simulator, cause an essential difference in implementation of the same upper layer protocol for the simulation environment and for the real hardware.

In this paper, we describe a real-time emulator of EvoLogics S2CR series underwater acoustic modems. The emulator provides a fully-featured emulation of the data-link layer and includes a simplified simulator of the physical layer that accounts for signal propagation delays, multipath propagation, data packet collisions, packet synchronization errors and bit errors with a user-defined bit error rate.

This emulator can substitute acoustic modem hardware when running testbed scenarios on a network simulator. In addition, it can serve as a standalone solution for development and verification of custom network protocols.

The emulator fully supports the cross-layer synchronization mechanisms implemented in S2C modems, and thus allows to develop positioning protocols and hybrid protocols that combine communication with positioning on a upper layer protocol.

In the following sections, we will also elaborate on applying the code developed with the emulator to real acoustic modems.

The rest of the paper is organized as follows. Section II describes the S2C protocol stack, implemented in the Evo-

Logics' acoustic modems. Section III presents the concept of the acoustic modems emulator and explains the purposes of its development. Section IV addresses the practical issues of the whole development process, from modeling to sea trials. Section V describes the practical experience of using the emulator. Section VI outlines the plans for the emulator's future development, the final section VII sums up the paper.

II. Introduction to S2C Protocol Stack

The S2CR series underwater acoustic modems, manufactured by EvoLogics GmbH, comprise the following components:

- transducer with the transmit/receive amplifier
- a digital stack
- optional USBL antenna
- optional Wake Up module

The physical properties of the transducer type define the beam pattern of the acoustic modem and the frequency range. Both the properties define the range of the applications, where the particular model of the acoustic modem can be used. The acoustic modems comprise also the matched transmit/receive amplifier, optimized according to the characteristics of the particular transducer type.

The ultra-short baseline antenna (USBL-antenna) is an optional module comprising a grid of 5 receivers integrated together with the transducer into one housing with the receive amplifiers for each channel of the grid.

The Wake Up Module is an optional integrated electronic unit that can turn parts of the device off to save power. The Wake Up Module helps optimizing power consumption for battery-powered deployments by checking for incoming acoustic signals or incoming data on the host interface and turning rest of the device on only when such a signal is detected. Once the device completes receiving or transmitting data, everything but the Wake Up Module is switched off.

The digital stack consists of the ADC, DAC, DSP and FPGA that implement the physical layer protocol, further referred to as S2CPhy, and a host processor, implementing the D-MAC data-link layer protocol. We will describe both protocols in the sections below.

A. S2C physical layer protocol

The physical layer implements the patented S2C (Sweep Spread Carrier) signal modulation technique. S2C is based on the assumptions that, for an underwater acoustic channel, a received acoustic signal is well described by a sum of multipath components with random amplitudes and phases, and that the multipath intensity profile is discrete.

In these conditions, one of the most promising approaches to digital communication is the spread spectrum modulation.

A spread spectrum signal is characterized by a short auto-correlation response. The broader the spectrum spread, the shorter its response. After passing the underwater acoustic channel, the received signal is a sum of multipath components and, after matched filtering, it can be presented as a series of time-shifted correlation responses. For a signal with broad spectrum spread, these responses can be isolated, eliminating the signal distortion associated with multipath propagation. In particular, the phase distortions of an isolated multipath component can be significantly reduced.

S2C method utilizes broad-spectrum signals with continuously varying frequency. These signals are well known in radio location, where they are used for increasing the probability of successful signal detection.

It is known, that if the such a signal has a large base, at least 95 percent of its energy is concentrated in the given frequency band, and its auto-correlation response is short.

S2C technique utilizes the method of continuous carrier frequency variation, where the information is coded by discrete manipulation of one or several carrier parameters. In contrary to other common methods of digital underwater acoustic communication, an S2C signal is characterized by two levels of modulation: first – the internal modulation – for continuous variation of the carrier frequency (analog modulation), second – the external modulation – for coding the information within the signal (discrete manipulation). With the frequency band ranging from one to tens of kHz, the signal can be just hundreds of microseconds long, and the transmission speed can reach tens of kbits per second.

Implementation and application of the S2C method demonstrate one of its key advantages: with continuous carrier modulation instantaneous frequencies of the incoming multipath components are shifted away from the instantaneous frequencies of previously received multipath components. Therefore, the band-selective distortions of the received signal are weakened. This leads to increased bitrate, reliability and efficiency of the data transmission.

The key concepts of the S2C method are implemented on the physical layer of the S2C protocol stack, the S2CPhy. This protocol is implemented in the DSP and the FPGA of the digital stack and performs the following tasks:

1) estimation of the parameters of the underwater acoustic channel:
   - obtaining the multipath intensity profile (evaluating the intensities and the propagation delays of multipath components);
   - selection of the most intensive component for receiver synchronization;
   - determining the propagation delay and the Doppler shift of the most intensive component;
2) packet and symbol synchronization
   - evaluating the beginning and the end of a data packet;
   - evaluating the reception time of every symbol in the series (accounting for the Doppler shift);
3) modulation:
   - transforming the sequence of bytes into a sequence of words according to the manipulation rate, in particular, transforming into a sequence of bit pairs;
   - defining the signal envelope according to the modulation type selected;

- defining the signal envelope according to the carrier sweep;

4) demodulation:
   - synchronized processing of the received signals with the in-phase and squared components of the reference signal;
   - evaluation of the complex envelope of the received signal
   - evaluation of the discrete signal value;
   - determination of the bit pair that corresponds to a discrete phase value of the received signal.
5) positioning:
   - evaluation of the pulse response of the channel to select a multipath component that corresponds to the shortest propagation path;
   - determination of the time difference between the acoustic front incidence on the elements of the USBL grid.

B. D-MAC data-link layer protocol

Design of an improved data-link layer protocol called D-MAC is based on the recently developed data delivery algorithms of acoustic modems that implement the S2C Technology. According to the new data-link layer protocol, two different types of data are supported, namely burst data and instant messages [4].

Burst Data: Establishing a connection for burst data delivery requires an estimation of the channel's parameters. As described in [5], the delivery algorithm optimizes the channel's utilization efficiency and adapts the bitrate to the highest possible value for a particular underwater acoustic channel. All data received from the user is buffered and then dynamically split into smaller packets according to channel parameters. The receiver side assembles the split data together and sends it to the remote user in the original format.

Instant Messages: Establishing a connection is not required for delivering instant messages. A fixed bitrate (relatively low and acceptable for a wide range of acoustic channel parameters [4]) is used for delivering short instant messages, as the algorithm minimizes delivery time of such messages. Delivery of instant messages doesn't interrupt the ongoing burst data transmission, since instant messages are delivered as an extension of service messages. An instant message can be $O(10^2)$ bits long.

On one hand, a low bit error rate implies a low transmission rate so the instant messages tend to be long to transmit. On the other hand, duration of a message must be less than the channel coherence time [6]. Thus, the bitrate must be high enough to make sure that the message duration meets the time constraints, forced by the channel coherence time. A physical layer protocol, based on the S2C technology [7] provides reliable transmission of instant messages with a 1 kbps bitrate. This is valid even for channels with highly dynamical parameters like confined water bodies with moving network nodes.

TABLE I
CLASSIFICATION OF INSTANT MESSAGES

Instant Message					
Asynchronous			Synchronous		
Robust	Unicast	Broadcast	Robust	Unicast	Broadcast

On the data-link layer, message delivery time can be made as short as possible by transmitting the message with a fixed low bitrate without handshaking and adaptation of the communication system to channel parameters.

Instant messages can be classified according to message addressing type, acknowledgment and synchronization requirements. Table I displays a classification of instant messages.

Asynchronous instant messages delivery is based on an ALOHA-like scheme when there is no ongoing burst data exchange between the nodes of an acoustic network. Asynchronous instant messages can also be delivered as parts of service messages of the burst data delivery protocol.

Media access control for synchronous instant messages transmission must be implemented by upper level protocols. To fulfill this task, the D-MAC protocol implements a custom interface for synchronization with the physical layer, allowing the upper level protocols to point out the time for transmission of a synchronous instant message and also obtain the message arrival time. Synchronous instant messages cannot be transmitted during burst data exchange.

III. S2C MODEM EMULATION CONCEPT

The major purpose of the modem emulator is to minimize development costs of upper layer protocols and to simplify the integration of acoustic modems into underwater infrastructure.

The main consideration for modem emulator design was that an application, developed with the emulator, must work with real acoustic modems without any code modifications.

This defines the following requirements the modem emulator must meet:

- real-time emulation of a large number of network nodes;
- same source code for both the emulator and the real modem firmware;
- equal command set for both the emulator and the modem;
- remote emulator access via Internet.

The requirement for real-time emulation directly derives from the main purpose of the emulator. Time diagrams of both the emulator and the modem must match to ensure the protocols and upper layer applications operate identically on the emulator and the modem. One must take into consideration, that upper layer protocols can utilize both the data exchange functionality of the modems and the distance measurement functionality to solve positioning tasks either in parallel with the data exchange or in its absence.

The modem's firmware is constantly evolving, since, as the modems find new applications, they support integration with a growing range of external sensors and other devices. The data-link layer is the one that gets the most changes, and it is the one most "visible" to upper layer protocols. If the emulator source

code significantly differs from the firmware, every firmware update would, first, require a modification of the emulator code and, second, would demand a wide range of tests performed to verify the identity of the emulator and the firmware.

A more effective approach, as it turns out, is to launch the code, developed for the modem firmware, on another platform, namely the x86. The platform-dependent part of the code was contained within a compact driver, implemented in two versions – the one for the modem firmware and the other for the x86 emulation.

Utilizing the same source code for both the firmware and the emulator also guarantees the identity of the command sets that control them, making them indistinguishable for upper layer protocols.

A multitude of instances of acoustic modem emulator comprising an underwater acoustic network can be configured and launched on the manufacturer's server. The user is granted remote access to this acoustic network. Each modem can be accessed via TCP/IP socket.

This approach ensures prompt updates of the code and makes the usage of the emulator platform-independent, as the user does not need additional equipment to install and run the emulator.

According to the design objectives, the components of the modem emulator are the following:

- the data-link layer
- the core module that controls the data exchange between the data-link layer and the physical layer
- the physical layer simulator
- the acoustic channel simulator

As mentioned above, the emulator and the real acoustic modems use the same data-link layer source code, compiled for the target platform. The platforms supported are the ARM, x86, x86_64.

This approach saves time and effort spent on support and development of the emulator, ensures full compatibility of the data-link layer protocols of the emulator and the modems, reducing development time for system integration of the modems or, for R&D purposes, shortens the path from simulations to final trials.

Cross-layer communication between the data-link and the physical layers is provided by a Linux-core driver that implements a platform-dependent code, specific for the acoustic modem hardware. This code provides low-level access to the data exchange interfaces of the data-link and the physical layers. Within the emulator, this driver redirects the data-link layer's requests back to the user-space of the physical layer simulator and back from the simulator to the data-link emulator.

This data-link layer implementation, separated between a platform-dependent core driver and the main POSIX-compliant code, enables using the same code base for the modem emulator and the real modem.

The physical layer simulator imitates it by replying to the data-link layer's requests according to the cross-layer data exchange specification. The simulator's parameters are its three-dimensional coordinates and the acoustic channel's bit error rate.

The simulator transfers the data to be transmitted to the dispatcher that enables the data exchange between modems. The simulator includes the time-stamp of transmission start and its own coordinates within the data. Having received data packets from the dispatcher, the physical layer simulator imitates a propagation delay by holding the packet for a timeout that corresponds to the signal propagation time between the signal source and the receiver, and detects collisions, dropping the collided packets.

To calculate the propagation time, it is possible to introduce a sound speed profile for testing positioning protocols.

The last component, the acoustic channel simulator, is effectively the dispatcher of the data-link layer packets. The main function of the component is to receive the packets from a physical layer simulator and forward them to the other physical layer simulators, connected to the dispatcher.

IV. From emulation to sea trials

In most publications on communication protocols for underwater acoustic sensor networks, known to the authors of the paper, experimental results were obtained by simulations with the NS2 and NS3 – the network simulators, well-known in the academic community. Experimental results from real-world trials, on a lake or at the sea, is rather exceptional.

One of the crucial obstacles for real-world experiments is the high cost of both the underwater equipment and the vessel time at sea. Nevertheless, there is an another equally important factor, namely the essential difference between protocol implementation for simulation and for real-world experiment purposes.

A big step forward from modeling towards experimental studies was made with the recent releases of SUNSET and DESERT frameworks, both based on NS2-Miracle[1], capable of working with real modem hardware in testbed scenarios.

A common source code base can now implement upper layer protocols for simulations and for testbed scenarios with real hardware.

The only link missing was a fully-featured acoustic modem emulator, eliminating the need for real modems during the R&D and testing, as well as extending the number of possible test scenarios, hardly manageable even with real modems at the development stage.

In particular:

- the emulator allows arbitrary propagation delays between network nodes, while deploying real modems on essential distances is too much effort for development purposes;
- the emulator supports real-time testing of multiple underwater acoustic network nodes at once, while several dozens of modems, batteries, buoys, anchor chains and other accessories are an unaffordable luxury for a network protocol developer;
- the emulator fully supports the S2C modems' cross-layer synchronization mechanisms, essential for implementing

positioning protocols that consume too much time, cost and effort for real-life R&D testing;
- the physical layer simulator supports collision detection and user-defined demodulation and synchronization error rates, allowing to test applications and upper layer protocols in different operating conditions and debug the code to improve system stability without involving expensive underwater infrastructure.

The next step paving the way from modeling to open-sea trials was the launch of EvoLogics White Line Science Edition underwater acoustic modems that provide the user with a firmware sandbox for launching custom applications or upper layer protocols. The sandbox allows to run tcl/expect scripts for quick development of test scenarios or applications, as well as to launch C/C++ applications or the SUNSET or DESERT frameworks.

V. Usage experience

The emulator of the S2CR underwater acoustics modems series underwent beta-testing last year. Our academic partners were granted access to the emulator to develop and debug upper layer protocols and get ready for joint trials. Furthermore, commercial customers were granted emulator access to simplify system integration of S2C modems they purchased: the customers were able to use the emulator and get accustomed with the modems before the actual hardware delivery.

This August, the authors of this paper conducted joint trials with the SIGNET group from the University of Padova (Italy). The purpose of the trials was to test the SIGNET group's SUN[8] protocol – a dynamic source routing protocol for underwater acoustic sensor networks. Our colleagues from the University of Padova already had strong experience with the S2C emulator. Via remote access, they had used it to debug and test the SUN protocol within the framework of a research-oriented NS-Miracle network simulator.

Because of that experience, preparing for the field tests, namely the transition from the S2C emulator to real S2C hardware, went easily and took just a few days.

The trials involved the White Line Science Edition modems (the S2CR 18-34 WiSE), and were held at the Werbellinsee lake near Berlin, Germany. The test results were presented in [8].

During their research and development process, our colleagues from the University of Padova found several uses for the emulator and provided the following feedback [9]:

- the emulator is a learning tool, as it allows one to get confident with the AT commands that control S2C modems;
- it is very useful for designing and refining sophisticated interactions with the modem, for example, the emulator can be used to test and improve network protocols and applications that involve several message exchanges with the modem on the basis of, e.g., a suitably designed finite state machine;
- the emulator allows to plan and refine experiments before conducting them on real hardware.

Based on this experience, the following benefits of working with the emulator can be noted:

- the emulator enables the researchers and developers to test their network protocols and/or application solutions without the modem hardware directly connected to their computers, moreover, it allows to use several different (virtual) modems at once and provides the freedom of working over remote access;
- Using the emulator saves time during code debugging and refinement. It is quicker and much easier to use one's own computer to modify the code and test it than to use the actual modem for this purpose;
- Furthermore, solutions that were designed and tested with the emulator are easily exportable to the actual modem hardware.

VI. Future development

The underwater acoustic modem emulator is constantly evolving, since the growing experience of its application inspires new ideas for further developments of the original concept.

Having used the emulator, our partners contributed with some suggestions that helped devise the development plan introducing the following features:

- user-friendly customization of the emulator settings using web-based configuration utilities;
- a user-friendly topology constructor to set up the actual network topology;
- a log visualization tool, allowing to view and analyze the events log (e.g., packet flows, packets disregarded for errors and/or collisions);
- supporting mobile network nodes with custom user-defined mobility models;
- user-defined parametrization of the synchronization and demodulation error as a function of distance between nodes;
- possibility to run the emulator as a virtual machine on the user's computer.

VII. Conclusions

The emulation approach described above was developed to open more opportunities for researchers and developers of upper layer protocols and other applications that use underwater acoustic modems. The ability to test and debug an application with a modem emulator allows to significantly reduce development costs and increase the reliability of the solutions developed, as open-sea trials require too much time, cost and effort.

The emulator usage experience, both during internal testing and within a partner cooperation, proved it a valuable solution. The transition from using the emulator to deploying real acoustic modems took from days to a week, depending on the complexity of the experiment and the need for personnel training.

The emulator can be used either as a standalone solution for research and comparison of different approaches and upper layer protocols, or as an additional tool to speed up the development process.

ACKNOWLEDGMENTS

The authors would like to thank the SIGNET group of the University of Padova (Italy) and Dr. Riccardo Masiero for the interesting discussions and for the feedback about emulator usage. Thanks also go out to Ms. Mariia Pleskach for valuable remarks during preparation of the paper.

REFERENCES

[1] (2012, Aug.) The network simulator - ns-2. [Online]. Available: http://nsnam.isi.edu/nsnam/index.php/ User Information

[2] C. Petrioli, R. Petroccia, J. Shusta, and L. Freitag, "From underwater simulation to at-sea testing using the ns-2 network simulator," in *OCEANS, 2011 IEEE - Spain*, june 2011, pp. 1 –9.

[3] R. Masiero, S. Azad, F. Favaro, M. Petrani, G. Toso, F. Guerra, P. Casari, and M. Zorzi, "Desert underwater: An ns-miracle-based framework to design, simulate, emulate and realize test-beds for underwater network protocols," in *OCEANS, 2012 - Yeosu*, may 2012, pp. 1 –10.

[4] O. Kebkal, M. Komar, K. Kebkal, and R. Bannasch, "D-mac: Media access control architecture for underwater acoustic sensor networks," in *OCEANS, 2011 IEEE - Spain*, june 2011, pp. 1 –8.

[5] O. Kebkal, "On the use of interwoven order of oncoming packets for reliable underwater acoustic data transfer," in *OCEANS 2009 - EUROPE*, may 2009, pp. 1 –7.

[6] B. Sklar, *Digital communications: fundamentals and applications*, ser. Prentice Hall Communications Engineering and Emerging Technologies Series. Prentice-Hall PTR, 2001.

[7] K. G. Kebkal and R. Bannasch, "Sweep-spread carrier for underwater communication over acoustic channels with strong multipath propagation," *The Journal of the Acoustical Society of America*, vol. 112, no. 5, pp. 2043–2052, 2002.

[8] G. Toso, R. Masiero, P. Casari, O. Kebkal, M. Komar, and M. Zorzi, "Field experiments for dynamic source routing: S2c evologics modems run the sun protocol using the desert underwater libraries," in *OCEANS, 2012 - Hampton Roads*, in press.

[9] R. Masiero, personal communication, 2012.

Mathematic and Experimental Evaluation of Phase Errors when Receiving Hydro-Acoustic PSK-Signals with Sweep-Spread Carrier in Reverberant Underwater Environments

Konstantin G. Kebkal,
Evologics GmbH,
Ackerstrasse 76, 13355 Berlin,
Germany
kebkal@evologics.de

Angelika K. Kebkal
Evologics GmbH,
Ackerstrasse 76, 13355 Berlin,
Germany
angelina.kebkal@evologics.de

Gleb A. Ermolin
State Oceanarium of Ukraine,
Epronovskaja 7, 99024 Sevastopol
Ukraine
g-ermolin@mail.ru

***Abstract*—When propagating in water, acoustic signals experience distortions and thus received signals can essentially distinct from those which were transmitted. Basic distortions originate from interference of multipath arrivals comprising random energies, phases and Doppler shifts. Assuming an underwater acoustic environment for middle and high telemetry frequencies as a channel with (in wide sense) stationary uncorrelated scattering, each multipath arrival of a received signal is characterized with a random propagation delay, random energy and (equally distributed) phase, as well as random Doppler shift. Based on such assumption, a receive signal with sweep-spread carrier was represented with a mathematical model, which was used for derivation of a analytical expression for estimation of maximum phase errors expected to be registered in underwater acoustic channels with given multipath. The use of the mathematical expressions allowed to quantify the upper limit of phase errors in different conditions of the multipath channel (different excess propagation delays and relative attenuations of delayed multipath arrivals). Expected phase errors obtained by means of this expression and values measured during physical experiments demonstrated a good agreement.**

Keywords— underwater communication; underwater telemetry; underwater modem; sweep-spread carrier; S2C technology

I. INTRODUCTION

Because of the layered inhomogeneity of ocean waters, reception of a hydro-acoustic signal from horizontal directions is accompanied by a strong and long reverberation usually consisting of distinct multipath arrivals with random energies and random excess propagation delays.

Utilization of signals built upon sweep-spread carrier (S2C) technology (phase-manipulated signals with frequency swept carrier) enables the receiver to resolve multiple arrivals in time-frequency domain and thus to separate one of the arrivals and suppress the others [1]. However, even if multipath arrivals are well resolved, one of them can still contribute some "noise" into estimation of the parameters (phase and amplitude) of the another one. This noise depends on time delays between the arrivals, as well as on the ratios between their amplitudes.

One of the purposes of this paper was to analytically estimate the phase error of a phase-manipulated signal with linearly swept carrier (S2C-signal); particularly the error that can be expected in the receiver due to effect of multipath propagation. Another purpose was to experimentally validate the analytical results.

The next section presents the derivation of an analytical expression for estimation of maximum phase errors expected to be registered when using phase-manipulated S2C signals in underwater acoustic channels with given (measured) multipath. This section describes the methodology of preparation and conduction of physical experiments. The third section contains detailed analysis of communication channel conditions, analysis of received signals, as well as comparison of experimental and analytical results.

II. THEORY

When propagating in water, acoustic signals experience distortions and thus received signals can essentially distinct from those which were transmitted. Basic distortions originate from interference of multipath arrivals having random energies, phases and Doppler shifts. Assuming underwater acoustic environment for middle and high telemetry frequencies as a channel with (in wide sense) stationary uncorrelated scattering, each multipath arrival of a received signal has a random propagation delay, random energy and (equally distributed) phase, as well as random Doppler shift. Therefore the receive signal with sweep-spread carrier can be mathematically modelled as the sum of N multipath arrivals:

$$r_i(t) = \sum_{k=0}^{N} \left\{ v\left(K_k\left(t-\tau_k\right)\right) * s_{i,k}'\left(K_k\left(t-\tau_k\right), \psi_k\right) \right\} + n(t),$$

where

$$s_{i,k}'\left(K_k\left(t-\tau_k\right), \psi_k\right) = \sqrt{\frac{2E}{T}} \cos\left(2\pi f_L K_k\left(t-\tau_k\right) + \int_{o}^{K_k(t-\tau_k)} \upsilon(\tau) d\tau + \theta_i + \psi_k \right),$$

T – signal length, E – energy, τ_k – random propagation delay of k-th multipath, θ_i – discrete phase (encoded information), ψ_k – random phase shift of the k-th multipath, $K_k = 1 - \frac{v_k}{c}$ –

978-1-4799-0002-2/13/$31.00 ©2013 IEEE

Doppler coefficient for the k-th multipath, $\upsilon(\tau)$ - function of frequency spread (sweeping), $v(K_k(t-\tau_k))$ – amplitude envelope of the k-th multipath, $*$ – convolution, $n(t)$ – ambient noise (for middle and high telemetry frequencies – usually Gaussian noise).

In this paper the effect of multipath propagation is considered without accounting for Doppler effects.

In simple case, when frequency spread is given as a linear sweep, and so the phase-manipulated signal with the frequency spread carrier is representable as $s_i(t)=\sqrt{\frac{2E}{T}}\cos\left(2\pi f_L t+Gt^2+\theta_i\right)$, the received signal can be written as:

$$r_i(t)=\sqrt{\frac{2E}{T}}\sum_n \alpha_n \cos\left(2\pi\left(f_L-\Delta f_n\right)t+Gt^2+\theta_i+\theta_n\right)+n(t)$$

where α_n and τ_n – attenuation coefficient and excess propagation delay of the arrival with index n correspondingly (multipath with index 0 is referenced as synchronous with the reference signal, whereas other arrivals as asynchronous), $\Delta f_n=G\tau_n/\pi$ – instantaneous frequency shift of the n-th multipath relatively to the instantaneous frequency of the synchronous multipath, $G=2\pi f_d/T$ – frequency gradient, f_d – deviation of the instant frequency from the centre of the frequency range occupied with transmitted (frequency spread) signal, $\theta_n=G\tau_n^2-2\pi f_L\tau_n$ – shift of the beginning phase of the n-th multipath arrival relatively to the beginning phase of the synchronous arrival. (Electroacoustic conversion is assumed to be ideal: rectangular voltage response and liner phase response of the transmitter).

In result of processing of the receive signal that is synchronized in time t_0 with the reference signal $s(t)=\sqrt{\frac{2}{T}}\cos\left(2\pi f_L t+Gt^2\right)$, the output of the quadrature demodulator can be written as

$$R_i(t_0)=\int_{-\infty}^{\infty} r_i(t)\left(s\left(t+t_0\right)+jH\left(s\left(t+t_0\right)\right)\right)dt,$$

where $H(\cdot)$ – Hilbert transform.

In a result of multipath propagation the signal at the output of the optimal quadrature demodulator can be written as $R_i(t_0)=Q_c(i)+jQ_s(i)$, where $Q_c(i)$ and $Q_s(i)$ – in-phase and quadrature components which in presence of negligibly weak ambient noise can be represented as $Q_c(i)\approx I_c(i)+O_{m,c}(i)$ and $Q_s(i)\approx I_s(i)+O_{m,s}(i)$, where $I_c(i)=\alpha_0\sqrt{E}\cos(\theta_i)$ and $I_s(i)=\alpha_0\sqrt{E}\sin(\theta_i)$ – real and imaginary parts of the synchronous multipath arrival, $O_{m,c}(i)$ and $O_{m,s}(i)$ – residuals causing a phase error due to multipath. The residuals can be expressed as

$$\begin{aligned}O_{m,c}(i) &= \sum_n \alpha_n \frac{\sqrt{E}}{T}\int_0^T \cos(-\Delta\omega_n t+\theta_i+\theta_n)dt= \\ &= \sqrt{E}\sum_n \alpha_n \frac{\sin\left(\Delta\omega_n T/2\right)}{\Delta\omega_n T/2}\cos\left(\Delta\omega_n T/2-\theta_i-\theta_n\right)\end{aligned}$$

$$\begin{aligned}O_{m,s}(i) &= \sum_n \alpha_n \frac{\sqrt{E}}{T}\int_0^T \sin(-\Delta\omega_n t+\theta_i+\theta_n)dt= \\ &= -\sqrt{E}\sum_n \alpha_n \frac{\sin\left(\Delta\omega_n T/2\right)}{\Delta\omega_n T/2}\sin\left(\Delta\omega_n T/2-\theta_i-\theta_n\right)\end{aligned}$$

where $\Delta\omega_n=2\pi\Delta f_n$, $n=1,..,M-1$, M - number of multipath components.

In line with this, the deviations of in-phase and quadrature outputs of the demodulator, caused with n-th multipath arrival, remain in the range given as $\left|O_{m,s}\right|<\sqrt{E}\sum_n \alpha_n\left|\frac{\sin(2\pi f_d\tau_n)}{2\pi f_d\tau_n}\right|$ and $\left|O_{m,c}\right|<\sqrt{E}\sum_n \alpha_n\left|\frac{\sin(2\pi f_d\tau_n)}{2\pi f_d\tau_n}\right|$. Since the phase estimate of the synchronous multipath arrival of the received signal is determined as $\hat{\Theta}_i=arctg\left(\frac{Q_s(i)}{Q_c(i)}\right)\approx arctg\left(\frac{I_s(i)-O_{m,s}(i)}{I_c(i)-O_{m,c}(i)}\right)$, the error of the phase estimation can be written as:

$$\Delta\hat{\Theta}_{i,n}\approx\Theta_i-arctg\left(\frac{\begin{array}{l}\alpha_0\sqrt{E}\sin(\theta_i)+\\ \alpha_n\sqrt{E}\,\frac{\sin(\omega_d\tau_n)}{\omega_d\tau_n}\sin(\omega_d\tau_n+\psi)\end{array}}{\begin{array}{l}\alpha_0\sqrt{E}\cos(\theta_i)+\\ \alpha_n\sqrt{E}\,\frac{\sin(\omega_d\tau_n)}{\omega_d\tau_n}\cos(\omega_d\tau_n+\psi)\end{array}}\right),\quad (1)$$

where Θ_i - phase of the transmitted signal, which is here equal to the phase of the synchronous multipath arrival, $\omega_d=2\pi f_d$, and ψ - random phase shift.

As the greatest interest is the analysis of the largest phase error for each excess propagation delay τ_n, there was found such ψ, by which the phase error estimation $\Delta\hat{\Theta}_i$ for each given τ_n is maximum. After finding the derivation of the expression (1) with respect to ψ and equating it to zero, the expression for ψ, maximizing $\Delta\hat{\Theta}_{i,n}$ is obtained as

$$\psi=-\arccos\left(-\frac{\alpha_n}{\alpha_0}\frac{\sin(\omega_d\tau_n)}{\omega_d\tau_n}\right)+\theta_i+\omega_d\tau_n \qquad (2)$$

After substituting (2) into (1), modelling the worst case (when the asynchronous multipath arrivals have always phases which are conditioning maximum phase errors of the synchronous arrival) the maximum phase error can be given as the following expression:

$$\Delta\hat{\Theta}_{i,n}^{\max} = \theta_i - arctg\left(\frac{\sin\left(\theta_i - \arcsin\left(-\frac{\alpha_n}{\alpha_0}\frac{\sin(\omega_d\tau_n)}{\omega_d\tau_n}\right)\right)}{\sin\left(\theta_i + \arccos\left(-\frac{\alpha_n}{\alpha_0}\frac{\sin(\omega_d\tau_n)}{\omega_d\tau_n}\right)\right)}\right) \quad (3)$$

For preliminary validation of expression (3), there was conducted following analysis. In the most adverse conditions, a delayed arrival with index n has the same energy as the synchronous one, i.e. $\alpha_n=\alpha_0$, and the excess propagation delay is negligibly small, i.e. $\tau_n = 0$. Then expression (3) can be written as $\Delta\hat{\Theta}_{i,n}^{\max} = \theta_i - arctg\left(ctg\left(\theta_i\right)\right)$, which is equal to $\pi/2$ for each θ_i. That is, in most adverse conditions instead of true phase of the synchronous arrival there will be registered a value biased on $\pi/2$.

With increasing excess propagation delay τ_n, the maximum phase error changes. With increasing $\omega_d\tau_n$ the function type $\sin x/x$ represents a monotonically decreasing oscillation. Particularly the arcsine function in the nominator monotonously decreases, whereas the arccosine function monotonously increases. In the limit, with infinite τ_n : $\Delta\hat{\Theta}_{i,n}^{\max} = \theta_i - arctg\left(\frac{\sin\left(\theta_i\right)}{\sin\left(\theta_i + \pi/2\right)}\right) = 0$. That is, when excess propagation delay increases, the influence of the delayed arrival onto the phase estimation of the synchronous arrival, and correspondingly on the maximum phase error decreases, and in the limit vanishes.

According to (3), in propagation conditions given via delays τ_n and relative attenuations of the asynchronous multipath α_n/α_0, the maximum phase error also depends on the sweep-spreading bandwidth of the transmitted signal (ω_d).

The relation to frequency spread is important for practical use. Several examples are illustrated in Fig. 1 and Fig. 2 for different conditions: solid line for sweep-spreading bandwidth given with ω_d = 5 kHz, dashed line with ω_d = 10 kHz, and dotted line with ω_d = 20 kHz. With increasing frequency spread (frequency band occupied with transmitted signal), the maximum phase error estimated for synchronous multipath becomes less. This circumstance points out to appropriateness of possibly large frequency spreads of transmitted signals used during communication in underwater acoustic channels with intensive multipaths. (Expressions (1)-(3) can be also applied for the evaluation of the frequency spread necessary for sufficient decrease of the maximum phase error in underwater acoustic channels with given or measured multipath characteristics.)

Expression (3) can be extended for estimation of maximum phase errors in underwater acoustic channels with intensive multipath. Combined influence of several multipath components can be obtained straightforwardly by simply adding distortions which contribute each of the asynchronous arrivals, i.e. maximum phase error can be estimated as:

$$\Delta\hat{\Theta}_i^{\max} = \sum_n \Delta\hat{\Theta}_{i,n}^{\max} . \quad (4)$$

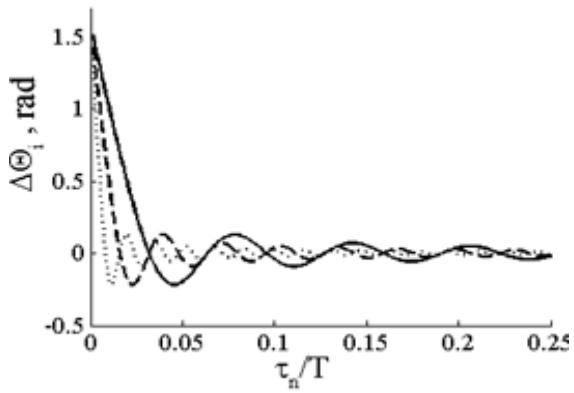

Fig. 1. Relationship between maximum phase error and the relative delay of asynchronous multipath component, with ω_d =5; 10; 20 kHz

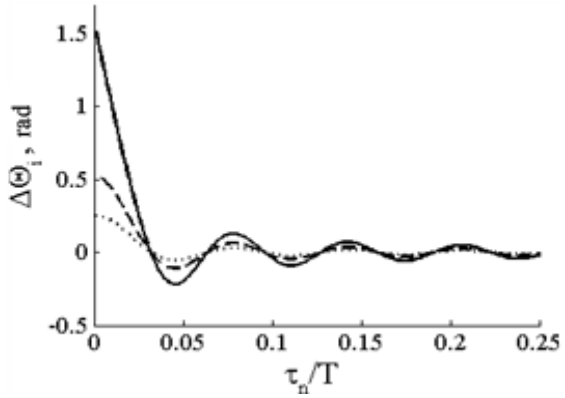

Fig. 2. Relationship between maximum phase error and the relative delay of asynchronous multipath component, with α_n/α_0 = 1.0, 0.5, 0.25

The analytical expressions can also be used for estimation of not only maximum errors, but also expected errors: with known distribution of phases and amplitudes of the multipaths, expression (1) can be used for estimation of expected errors as

$$\Delta\hat{\Theta}_i = \sum_n \Delta\hat{\Theta}_{i,n} . \quad (5)$$

In the following sections an experimental verification is presented. As later demonstrated, the maximum phase errors obtained in experiments (conducted in shallow water channels) and the analytical estimations made by means of expression (3), demonstrated a good agreement.

III. EXPERIMENT

A. Experimental setup

The experiments were conducted on 13.07.2012 in shallow waters of the Cossachija bay, Sevastopol, Ukraine. One of the modems was placed under anchored pontoon, the other one – under an anchored boat. The depth of the modem under the pontoon was 5 m (water depth – 6 m). The depth of the modem under the boat was 14 m (the water depth – 16 m). The transmission distance was 328 m. The noise level was 35-37 dB (one-Hertz-band near the transducer resonance). The weather was calm: wind 2-4 m/s, sea state 1-2. Due to moderate pitching and drift of the surface platforms during the experiments, the depth of the modem varied within a range of ± 0.5 m, and the horizontal movements of the receiver in relation to the anchorage was up to 10 m. The relative transmitter-receiver velocities stayed under 0.3 m/s.

In the experiments the underwater acoustic modems S2CR18/34WiSE were used (suffix WiSE stays for White Line Science Edition). Modem transducer had a smooth transmit voltage response in the operation frequency range between 18 and 34 kHz with variations up to 6 dB at the frequency band edges. The transducer had a weakly pronounced resonance by 26 kHz and was characterized with omnidirectional transmit diagram in horizontal plane and weakly expressed directivity in vertical plane (about 120 °). The transmit level of the signals was 169 dB re 1 uPa/m.

When using the modems of White Line Science Edition, the user has access to so-called "sandbox", what offers an open environment for development of user-defined TCL/Expect scripts and C/C++ software applications (particularly for flexible testing of newly developed protocols directly onboard of modem's hardware platform, e.g. the protocols implemented in NS2/Miracle framework [2]-[4]).

For execution of the experiments a TCL script has been designed enabling the execution of particular scenario for data exchange between the modems, logging both the results of data exchange and the service information (containing estimated channel characteristics) directly onboard of the modem's hardware platform.

The data exchange scenario contained several steps:

- data source transmitted so-called instant message [5] to the recipient – a special type of data package designed for delivery of short messages (up to 64 bytes) with the fixed bit rate 1 kbps; the instant messages contained the settings for the next coming transmission session, in particular the bit rate, packet length, package length, and others;
- after receiving the instant message the recipient returned an acknowledgement;
- upon receive of the acknowledgement the source sent data sequence, so called burst data (with the agreed setting such as bit rate, packet length, package length, etc.) to the recipient;
- after receiving the burst data the recipient returned an instant message acknowledging received data;
- source of the burst data transmitted an instant message to the recipient containing the settings for the following session.

Upon receipt of each of the message types (instant message or burst data), the receiver estimated the channel characteristics, in particular, the impulse response, propagation delays and intensities of all multipath arrivals, received waveforms for sync-impulses and data symbols, input and output signal-to-noise ratio, the time of each data block reception, as well as the result of data transfer, particularly the phase and the amplitude of each data symbol, the locations of bit errors in bit sequences received. Estimation of the channel characteristics and the results of data transfer were logged into internal data-logger of the modem (32 GB storage).

B. Structure and parameters of transmit signals

The transmit data were M-sequences, 2048 bits in length. Before transmitting, each sequence was split into packets and transmitted in packages (the structure of the data package is in Fig. 3).

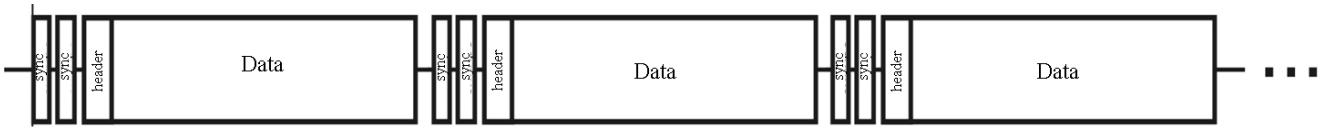

Fig. 3. Structure of the data package (train of packets)

As in Fig. 3 each packet included a pair of sync pulses, the header, and payload data. After each of the packets a pause followed. The duration of the payload data in each of the packets was 1 s. The number of packets per package depended on the bitrate. The range of bitrates used in the experiments was between 1 and 14 kbps. Data symbols were generated as differential QPSK pulses.

The sequence of symbols – sweep-spread pulses – represented a series of linear sweeps followed with no pauses between them. The length of every sweep was equal to the length of the data symbol. Symbol durations (sweep lengths) stayed in the range between 0.14 and 2 ms.

C. Characteristics of the communication channel

For evaluation of the channel characteristics, there were used synchronisation pulses (broadband linear sweeps, bandwidth 16 kHz, duration 2.048 ms), transmitted directly before each of the instant messages and each of the burst data packets. After processing the pulses in the receiver, there were estimated the multipath intensity profile, and based on that the number of multipath arrivals, the excess propagation delays of the arrivals, and the normalized values of their energies (the normalization was done by dividing the energy of each of the arrivals by the energy of the synchronous arrival).At that there were taken into account only so-called "significant" arrivals, which energies were not less than 10 dB smaller relatively to the energy of the dominant arrival.

The overview of the channel characteristics is represented with Fig. 4a,b,c. The number of multipath arrivals varied from 1-4 at the beginning to 2-6 at the end of the tests (Fig. 4a). The excess propagation delays demonstrated increasing trend: at the beginning of the test they remained within 100-600 ms, but at the end of the test they were spread larger, achieving 1400 ms (Fig. 4b). The channel was characterized with rapid variations of excess propagation delays and levels of multipath arrivals. The sum of energies of non-synchronous multipath arrivals varied from smaller values being well below the energy of the synchronous arrival to much larger values significantly exceeding the energy of the synchronous arrival (Fig. 4c).

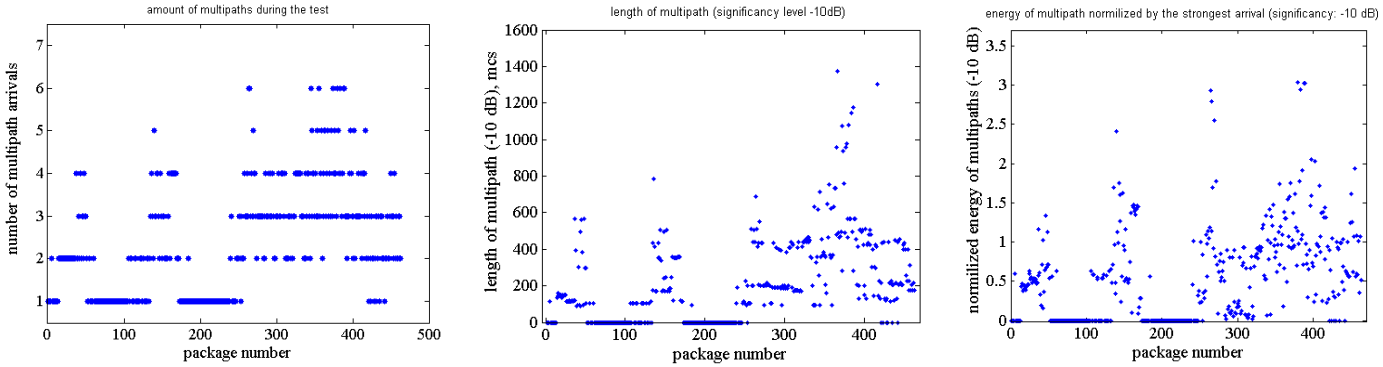

a) b) c)

Fig. 4. Characteristics of the communication channel: a) number of multipath arrivals, b) length of multipath intensity profile, c) ratio between the energy of non-synchronous multipath arrivals to the energy of the synchronous arrival

These conditions represented a large variety of channel characteristics enabling extended verification of the analytical expression (3).

D. Characteristics of receive signals

To analyse the influence of each of the factors, the energy of received signal was split into following components: energy of ambient noise E_n, energy of synchronous arrival E_s, as well as energy of each of the asynchronous multipath arrivals E_{mn}.

The algorithm of estimation of each of the energy components contained following steps. Initially assuming that the input signal consists of two components: a deterministic signal (synchronous arrival) and the random process (ambient noise and asynchronous arrivals), the powers of these two components were estimated. Given the operation frequencies, the random process should be close to Gaussian noise and thus its power should be numerically equal to the variance of receive signal dispersion. Then, estimating the variance of the dispersion and subtracting it from the input signal power, the difference should be numerically equal to the power of the deterministic signal (E_s/T – power of the synchronous arrival).

Assuming the ambient noise power is unchangeable over a short time (at least a second), the ambient noise power and the power of the random process caused by interaction of the asynchronous multipath arrivals may be also split into two components. Particularly, by measuring the ambient noise power E_n/T immediately before the signal reception and subsequent subtracting the E_n/T from the variance of the signal dispersion, the difference should be numerically equal to the power of the random process.

Obviously the credibility of such estimations has to be validated, what was done during the analysis. Most appropriate channel for validation of the noise power estimation is the channel with no multipaths (or when receive signals do not contain significant multipath arrivals). In such a channel the signal dispersion is induced with ambient noise only. Respectively, the variance of the signal dispersion measured on the receiver input must be numerically equal to the ambient noise power E_n/T directly measured shortly before each of the signal packets was received. Accounting for the ambient noise power, expected maximum phase error (i.e. three standard deviations) is represented in Fig.5a with the solid blue line). This figure demonstrates also the directly measured maximum of the phase error (brawn dotted line) during the reception of the signal packets. As demonstrated, the expected maximum error for each of the packets and the measured maximum error in corresponding packets stay in good agreement. Some differences may be due to some influence of negligible, "weak" multipath arrivals (below the significance level of –10 dB), as well as due to some variation of the ambient noise power on the time interval equal to the duration of the signal packet

(about a second). Anyway, in general, the estimation of the noise power shortly before signal reception remains trustworthy for entire time interval of the signal reception.

Noteworthy to say that the propagation conditions were in general more complicated in the second half of the experiment: the number of multipath arrivals and excess propagation delays increased. Apart of that in background of the increasing trend there were observed several intervals with sudden leaps in channel complexity, especially during transmission of the packet numbers: 31-49, 131-162, 260-270, and 300-420.

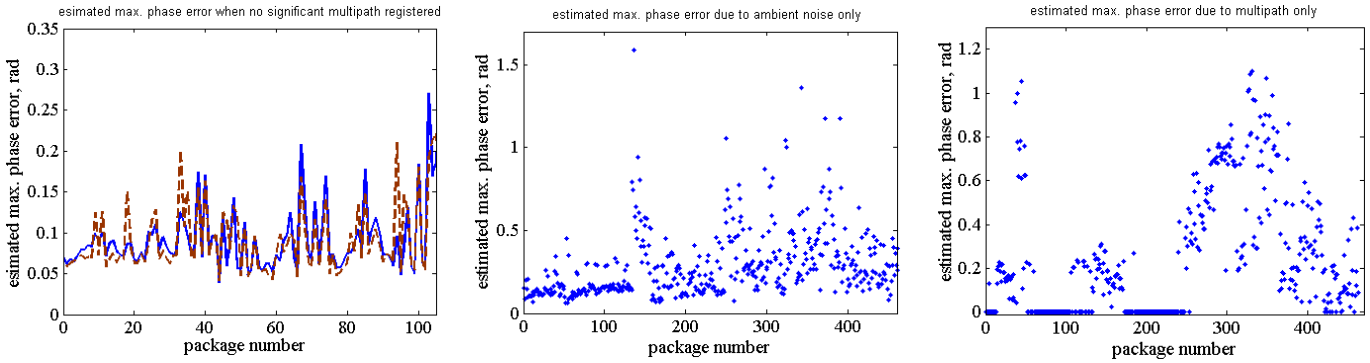

a) b) c)

Fig. 5. Characteristics of receive signals: a) comparison of maximum phase error estimations based on ambient noise measurements and its indirect evaluations, b) estimated maximum phase errors due to ambient noise only, c) estimated maximum phase errors due to multipath only

Fig.5b shows the estimate of maximum phase error caused only by influence of ambient noise (based on the estimation of E_n) for all packets received during the test.

Fig.5c demonstrates the estimate of maximum phase error caused by influence of the effect of multipath propagation only (based on the estimation of E_{mi}), i.e. due to interactions of asynchronous multipath arrivals. For calculation of the estimate of maximum phase error, the analytical expression (3) was used. Since each of the received data packets contains synchronization pulses, the estimation of the channel impulse response and correspondingly the estimation of the multipath intensity profile were facilitated, and thus the receiver possessed all necessary parameters (i.e. levels of multipath arrivals and their excess propagation delays) for estimation of maximum phase errors expected in each of varying channel conditions. (Since data sequences transmitted in the test were deterministic, correct phase values of all received data symbols were known.)

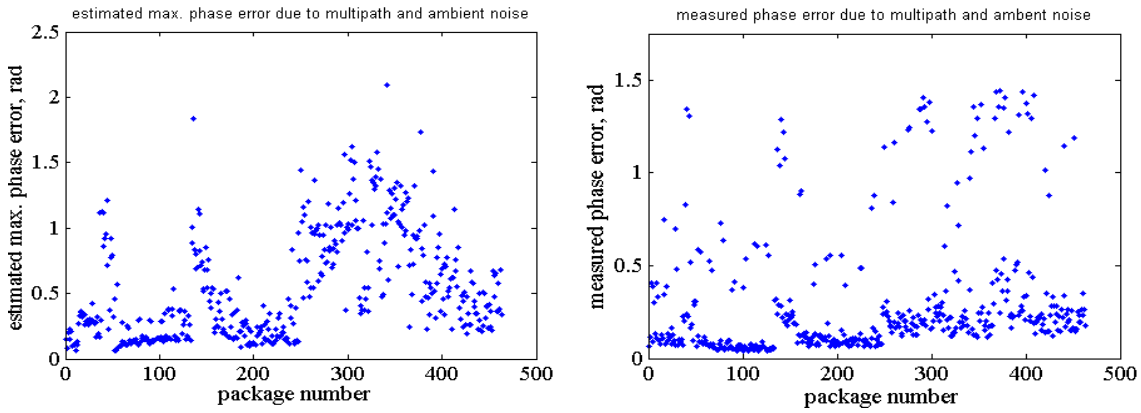

a) b)

Fig. 6. Characteristics of receive signals: a) estimated maximum phase errors due to both multipath and ambient noise, b) measured maximum phase errors due to both multipath and ambient noise

Fig. 6a shows expected estimates of maximum phase error, which could be observed due to the influence of both factors: multipath propagation (measured intensity of multipath propagation was used in expression (3)), as well as ambient noise (measured shortly before each packet received). Analysis of Fig. 6a says that in the first half of the experiment the estimate of maximum phase error should be smaller than in the second half. This observation is consistent with Fig. 4a,b,c, and

confirm that the propagation conditions were indeed more complicated in the second half of the experiment; particularly when the total energy of the asynchronous multipath arrivals significantly increased (Fig. 4c).

Fig. 6b demonstrates the actual (measured) values of phase errors, i.e. the result of phase dispersion due to the effects of the multipath propagation and the ambient noise. Analysis of Fig.6b indicated that measured values of the phase errors are larger during the second half of the experiment, what is also consistent with the increasing complexity observed in the channel. In addition, with the overall trend of increasing phase dispersion, there were observed abrupt bursts of measured phase errors, especially during receive of packet numbers 31-49, 131-162, 260-270, 300-420. There occurrence also stays in good agreement with the conditions of the channel conditions observed at these intervals (Fig.4a,b,c).

This is important to notice that direct quantitative comparison of the results in Fig.6a and Fig.6b does not make sense. The results shown in these figures are suitable for a qualitative comparison only. This circumstance is due to the fact that Fig.6a provides analytical estimates of maximum phase errors, which may be registered in the receiver in conditions of given multipath intensity profile and ambient noise, whereas Fig.6b demonstrates the real measurements of phase errors registered in the receiver in these conditions. In fact, during estimation of maximum phase errors there was assumed always the worst case, when all multipath arrivals have such parameters, which together cause the largest dispersion of the phase from the expected value (since each symbol of transmitted data sequence is known on the receiver side, the calculation of the dispersion is well facilitated). However, in practice worst cases are rather rare. Phases of all multipath arrivals are randomly distributed in the interval between 0 and 2π. Therefore the overall influence of all asynchronous multipaths on the phase error of the synchronous arrival should be usually much smaller than the maximum one. Correspondingly, expected phase errors should be also much less than the maximum error estimated by means of (3).

True value of the phase error depends on the phase distribution of each of asynchronous multipath arrivals. For example, assuming the uniform phase distribution in the range between 0 and 2π and the uniform distribution of asynchronous arrivals amplitudes in the interval between 0 and 1 (normalized values), expected phase error should be about nine times smaller than the maximum one obtained by means of expression (3). As follows from comparison of Fig. 6a and Fig. 6b, indeed, while having similar trend, the measured phase errors are usually much smaller, particularly about six times less in comparison with the maximum estimates obtained by means of expression (3). Phase errors equal or close to analytical maxima were in fact recorded fairly seldom (less than 10% of all estimates): in cases, when the analytical estimates of maximum phase errors have large values, about 0.5-2 radians, there were observed (measured) phase errors in the range 0.3-1.5 radians.

Fig. 7a demonstrates the output signal-to-interference-and-noise ratios (SINR), obtained as the ratios between the standard deviations of the phase error at the decoder input to the width of the phase sector specific for the phase manipulation method used ($\pi/2$ for QPSK). As can be seen in the figure, in the first half of the experiment, the output SINR varied in the range between 4 and 18 dB (in average about 12.5 dB). In the second half of the experiment, the output SINR varied in the range between –5 and +15 dB (in average about 8.5 dB). Essential difference between output SINRs in first and second half of the experiment can be explained by a significant increase in the number of multipath arrivals and their excess propagation delays. Partly, the decrease of the output SINR can also be attributed to some increase in the ambient noise level.

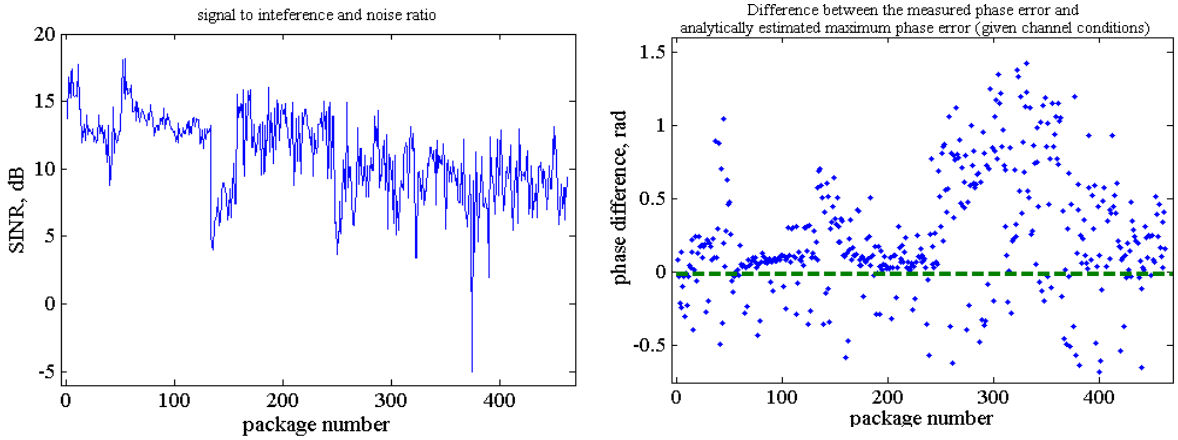

a) b)

Fig. 7. Characteristics of receive signals: a) output SINR evaluated at decoder input, b) comparison of maximum phase errors obtained by means of analytical expression (3) and experimental phase errors measured in underwater channel

As noted above, when ambient noise can neglected and phase error of the received signal is caused with multipath only, the analytical expression (3) should give only phase error estimates being larger than or equal to phase errors measured

in the physical channel. However, when phase errors of the received signal can be caused not only with multipaths (i.e. ambient noise cannot be neglected), the measured phase errors may exceed expected value obtained by means of expression (3). Fig.7b demonstrates the comparison of maximum phase errors obtained by means of expression (3) and experimental phase errors measured in the shallow water channel with ambient noise levels sometimes close to levels of the received signals (sometimes only a few dB difference). This comparison is represented as the difference between estimated and experimental phase error maxima (calculated once per received data packet). As follows from the figure, the vast majority (80%) of these differences are positive. The explanation of the fact that almost 20% of the differences were negative (i.e. experimental error is higher than the estimated maximum) can consist in the influence of the relatively strong ambient noise onto the phase error. With this in mind, the comparison confirms that theoretical and experimental results stay in good consistency, an correspondingly the expression (3) yields an adequate estimation of the maximum phase error which can be caused by the effect of multipath propagation. The use of expression (3) for estimation of the maximum error (based on measured impulse responses, or multipath intensity profiles) is justification for practical applications.

As noted above, in case of a known statistical distribution of all multipaths' phases and amplitudes the maximum phase error estimate obtained by means of expression (3) can also be used for estimation of the standard deviation of the received phase. In turn, the standard deviation gives an opportunity to evaluate the SINR at the detector input, what allows to appropriately select error correction method and sufficient data redundancy corresponding to given channel complexity. However, issues related to investigation of statistical distributions of multipaths' phases and amplitudes in various underwater acoustic channels are beyond the scope of the current work are the subjects of detailed considerations in future papers.

IV. Conclusion

The use of the mathematical model of S2C signal (phase-manipulated signal with sweep-spread carrier) allowed to quantify the upper limit of phase errors which can occur in given conditions of multipath channel (given via excess propagation delays and strengths of multipath arrivals). Analytical expression providing maximum phase error estimate for phase manipulated sweep-spread carrier signals is derived. Comparison of analytical estimates and experimental values of maximum phase errors demonstrated good consistency of theory and experiment: maximum phase errors obtained in experiments conducted in shallow water channels and analytical estimates made by means of expression (3) demonstrated good agreement.

Demonstrated results justify the use of the analytical expression (3) for estimations of maximum phase errors in practical applications; measured impulse responses (or multipath intensity profiles) facilitate the estimations.

On the assumption of further improvements, there was demonstrated the possibility of the use of expression (3) as a basis for estimations of SINRs (being based on measurements of actual channel impulse responses), and consequently the possibility to make reasonable selection of error correction algorithms and sufficient code redundancies corresponding to the given complexities of underwater acoustic channels.

Acknowledgment

This work has been supported by BMWi – the German Federal Ministry of Economics and Technology, project number 03SX265C.

References

[1] Kebkal K. and Bannasch. R. (2002) "Sweep-Spread Carrier for Underwater Communication over Acoustic Channels with Strong Multipath Propagation. Journal of Acoustic Society of America," vol.112, issue 5, pp. 2043-2052.

[2] C. Petrioli and R. Petroccia, "SUNSET: Simulation, emulation and reallife testing of underwater wireless sensor networks," in Proceedings of IEEE UComms 2012, Sestri Levante, Italy, September, 12–14 2012.

[3] C. Petrioli, R. Petroccia, J. Shusta, and L. Freitag, "From underwater simulation to at-sea testing using the ns-2 network simulator," in OCEANS, 2011 IEEE - Spain, june 2011, pp. 1 –9.

[4] R. Masiero, S. Azad, F. Favaro, M. Petrani, G. Toso, F. Guerra, P. Casari, and M. Zorzi, "Desert underwater: An ns-miracle-based framework to design, simulate, emulate and realize test-beds for underwater network protocols," in OCEANS, 2012 - Yeosu, may 2012, pp. 1 –10.

[5] Kebkal O.G. Instant Messaging for Underwater Acoustic Communication. Proccedings of the 4th International Conference on Underwater Acoustic Measurements: Technologies and Results, Kos, Greece, 20– 24 June, 2011. – ISBN: 978-960-98883-5-6.

Statistical Characteristics of Digital Hydroacoustic Signal with Sweep-Spread Carrier in the Receiver Predetection Point

K. G. Kebkal
EvoLogics GmbH
Ackeststrasse 76,
13355 Berlin Germany

R. Bannasch
EvoLogics GmbH
Ackeststrasse 76,
13355 Berlin Germany

O. G. Kebkal
EvoLogics GmbH
Ackeststrasse 76,
13355 Berlin Germany

***Abstract*- After matched filtering of receive signal with continuously spread carrier (sweep-spread carrier, S2C), the ratio between the signal and environmental noise increases. With increase of the ratio the influence of environmental noise on the probability of error in determining the discrete values of the signal rapidly decreases. However, the ratio of other kind – between the signal energy and the energy of delayed multipath components with random parameters – remains unchanged, since the amount of energy reflected by boundaries of underwater acoustic channels, layers and different objects is proportional to energy of transmitted signal. Thus it is more important to investigate the influence of random multipaths on the characteristics of the received signal, rather than the influence of Gaussian noise. There was determined that the interference of random multipath components of the sweep-spread signal causes a normal distribution of its quadrature components. There was made the quantitative assessment of the probability distribution of these components, in particular, the analytical expressions for variances of the distributions as functions of amplitude, base of the signal, Rice coefficient and the amount of multipaths. These expressions show that with increase of the signal base *B* the variance of the distribution at the output of the optimal demodulator decreases inversely proportional to *B*. In Rayleigh channels the most probable value of the signal with sweep-spread carrier is square root *B* times smaller than the most probable value of the signal with a frequency-constant carrier. In Rician channels the most probable value of the demodulator output signal is equal to the amplitude of the dominant multipath component. Taking into account *B* times smaller distribution variance of the signal with sweep-spread carried the amplitude of such signal was more often situated in close vicinity of the most probable value than the amplitude of the signal with frequency-constant carrier. To verify the analytical expressions, there were carried out numerical experiments. The results of verification demonstrated good agreement between analytical model and numerical experiment.**

I. INTRODUCTION

Because of layered inhomogeneity of ocean waters the transmission of hydro-acoustic signal in the horizontal direction is accompanied with a large number of reflections – the multipath components. Excess propagation delay of these components can be distributed over a long interval of time. Thus to model the received signal, it is important to take into account basic characteristics of multipath propagation.

For frequencies that are typical in digital hydro-acoustic communication every single path of signal propagation in a multipath medium usually does not experience any frequency-selective fading, is quasi-stationary and contains only Gaussian noise. In practice, the absence of frequency selective fading means that the coherency bandwidth of the channel is much larger than the frequency bandwidth of a transmitted signal. Quasi-stationarity means that the characteristics of the propagation medium (along each path) change relatively slow, i.e. transmission characteristics of the medium remain unchanged during the transmission time of a single digital signal.

Fig. 1 illustrates an optimal quadrature demodulator which is typically used in receivers of spread spectrum signals. It consists of multipliers of received signal $r(t)$ with a reference signal $s_s(t) = s(t)$ and its Hilbert transform $s_c(t) = H\{s(t)\}$, as well as two integrators.

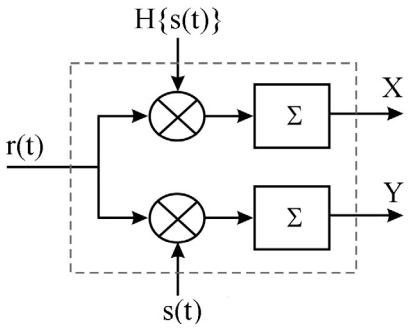

Figure 1. Optimal quadrature demodulator

When using signals with sweep-spread carrier there is usually no need for equalization of the received signal, because in result of matched filtering of a synchronous multipath component, all other (asynchronous) components can be suppressed. Accordingly, the detector of the digital value of the received signals can follow directly after the optimal quadrature demodulator. This fact determines the location of the receiver pre-detection point as the point at the output of the demodulator.

Let the input of the demodulator receives samples of the received signal with a sampling rate not less than the Nyquist frequency, and the output of the demodulator outputs the quadrature components with a rate corresponding to a repetition rate of digital signals (symbols or bits). Concerning the random values of the quadrature components, as well as a random envelope of the output signal, below a derivation of mathematical expressions is represented which allow for estimation of statistical distributions parameters of the quadrature components and the envelope of the output signal.

978-1-61284-4577-0088-0/11/$26.00 ©2011 IEEE

II. Statistical characteristics of S2C signals in Rayleigh channels

One of the most important channel type is the Rayleigh channel. On the output of the channel a receive signal consists of multiplicity of random multipath components. The channel of this type takes place for example during a long range data transmission in the horizontal direction.

In case of linearly swept carrier, i.e. $s_{fm}(t) = A\exp(j\omega_L t + Gt^2)$, where A – amplitude, $G = (\omega_H - \omega_L)/2T$, – frequency gradient, ω_L and ω_H - initial and final carrier frequencies, the multipath signal at the input of a quadrature demodulator can be written as [1]:

$$r_{fm}(t) = \mathrm{Re}\left\{\begin{array}{l} A\exp\left(j\left(\omega_L t + Gt^2\right)\right)\times \\ \times\left(\sum_{n=1}^{N}\left(\alpha_n\cos\left(-2G\tau_n t + \phi_n\right) + j\alpha_n\sin\left(-2G\tau_n t + \phi_n\right)\right)\right) \end{array}\right\},$$

where α_n –attenuation coefficient along the path with index *n*, ϕ_n – phase of the signal along the path with index *n* , *N* - number of multipath components comprising the received signal, and τ_n - excess propagation delay (relatively to synchronization time) of the *n*-th multipath component. After demodulation of the signal and corresponding transformation of its arguments, the quadrature components can be written as follows:

$$\begin{aligned} X_{fm}(t) &= \frac{2}{T}\int_0^T r_{fm}(t)\,\mathrm{Re}\left\{s_{fm}(t)\right\}dt = \\ &= \sum_{n=1}^{N} A\frac{\sin(\pi\Delta f\tau_n)}{\pi\Delta f\tau_n}\alpha_n\cos(\pi\Delta f\tau_n - \phi_n) \end{aligned}, \quad (1)$$

$$\begin{aligned} Y_{fm}(t) &= \frac{2}{T}\int_0^T r_{fm}(t)\,\mathrm{Im}\left\{s_{fm}(t)\right\}dt = \\ &= \sum_{n=1}^{N} A\frac{\sin(\pi\Delta f\tau_n)}{\pi\Delta f\tau_n}\alpha_n\sin(\pi\Delta f\tau_n - \phi_n) \end{aligned}, \quad (2)$$

where Δf - difference between initial f_L and final f_H frequencies of the carrier.

Perform the assessment of envelope distribution of the received signal in the form $R_{fm} = \sqrt{X_{fm}{}^2 + Y_{fm}{}^2}$. For each of the excess propagation delays τ_n the values of attenuation α_n and phase ϕ_n are random variables, uniformly distributed on the interval [0,1] and]-π, + π[, respectively. Random amplitude of the *n*-th (asynchronous) multipath component at the output of the demodulator depends on the excess propagation delay and is defined as $A_n = A\frac{sin(\pi\Delta f\tau_n)}{\pi\Delta f\tau_n}\alpha_n$.

Accordingly, X_{fm} represents a weighted sum of a large number of products of random variables, in particular, the amplitudes of *n*-th multipath $A_n = A\alpha_n$ which is uniformly distributed within the interval $\left[0, A\frac{sin(\pi\Delta f\tau_n)}{\pi\Delta f\tau_n}\right]$, and the cosine of the phase ϕ_n uniformly distributed within the interval $[-1,1]$. Using the method of functional transformation of random values [2], which experience algebraic transformations, the distribution of the product of uniformly distributed A_n and $\cos\phi_n$ can be obtained as

$$U(\beta_n) = \frac{1}{2A\frac{sin(\pi\Delta f\tau_n)}{\pi\Delta f\tau_n}}\left(\ln\left|A\frac{sin(\pi\Delta f\tau_n)}{\pi\Delta f\tau_n}\right| - \ln|\beta_n|\right),$$

where $|\beta_n| \le A\frac{sin(\pi\Delta f\tau_n)}{\pi\Delta f\tau_n}$. Thus X_{fm} represents the sum of random values, distributed according to the law $U(\beta_n)$, and if N is large then (according to the central limit theorem) the distribution is normal.

It can be shown that the mean value is zero ($m_{fm,x} = 0$), what also follows from the obvious assumption of equal probabilities of the phases ϕ_n of multipath components in a channel with diffuse scattering of transmitted power.

Dispersion of a random value having the distribution $U(\beta_n)$ can be found in the following form:

$$D_n = \frac{1}{2A\frac{sin(\pi\Delta f\tau_n)}{\pi\Delta f\tau_n}}\int_{-A\frac{sin(\pi\Delta f\tau_n)}{\pi\Delta f\tau_n}}^{A\frac{sin(\pi\Delta f\tau_n)}{\pi\Delta f\tau_n}}\beta_n^2\left(\ln\left|A\frac{sin(\pi\Delta f\tau_n)}{\pi\Delta f\tau_n}\right| - \ln|\beta_n|\right)d\beta_n = \frac{A^2}{9}\left(\frac{sin(\pi\Delta f\tau_n)}{\pi\Delta f\tau_n}\right)^2.$$

Given the fact that the excess propagation delays τ_n take values from - ∞ to + ∞, with sufficiently large N the variance of the distribution of the multipath signal can be written as:

$$D_{fm,x} = \sum_1^N D_n \approx \frac{A^2N}{9}\frac{1}{T}\frac{1}{\pi\Delta f}\int_{-\infty}^{+\infty}\left(\frac{sin(\pi\Delta f\tau_n)}{\pi\Delta f\tau_n}\right)^2 d(\pi\Delta f\tau_n) = \frac{NA^2}{9\Delta fT} .$$

Finally, the variance of the random variable X_{fm} is given by: $D_{fm,x} = \frac{NA^2}{9B}$, where - $B = \Delta fT$ signal base.

At the output of the demodulator the random variable Y_{fm} also represents the sum of a large number of random values, each of which is the product of the amplitude of *n*-th multipath component $A_n = A\frac{sin(\pi\Delta f\tau_n)}{\pi\Delta f\tau_n}\alpha_n$ (uniformly distributed in the interval $\left[0, A\frac{sin(\pi\Delta f\tau_n)}{\pi\Delta f\tau_n}\right]$) and the cosine of the phase ϕ_n uniformly distributed in the interval $[-1,1]$.

Accordingly, the random value Y_{fm} is distributed similar to X_{fm}, i.e. normally with the mean value $m_{fm,y} = 0$ and variance $D_{fm,y} = \frac{NA^2}{9B}$.

In the channel with diffuse power scattering the random variables X_{fm} and Y_{fm} are statistically independent and have equal variances. Thus the distribution of the module of the received signal R_{fm} is known [3] and can be described by the Rayleigh distribution [4]: $p(R_{fm}) = \frac{R_{fm}}{\sigma_{fm}^2}\exp\left(-\frac{R_{fm}^2}{2\sigma_{fm}^2}\right)$, where the variance of the distribution $\sigma_{fm}^2 = D_{fm,x} = D_{fm,y} = \frac{NA^2}{9B}$.

Similarly a variance derivation of a signal having frequency-constant carrier can be carried out. The variance of such a signal with frequency-constant carrier can be written as $\sigma_{cw}^2 = D_{cw,x} = D_{cw,y} = \frac{NA^2}{9}$.

The comparison of σ_{fm}^2 and σ_{cw}^2 demonstrates that with increase of the signal base B the variance of receive signal (at the output of the demodulator) decreases inversely proportional to B.

Accordingly, the most probable value of the signal with a sweep-spread carrier is $\sqrt{B}$ times smaller than the most probable value of the signal with a frequency-constant carrier. Fig. 2 shows the receive signal distribution (solid line is related to the sweep spread carrier, dashed line – to frequency-constant carrier). The distributions r_{cw} and r_{fm} correspond to the normalized (by means of σ_{fm}) distributions R_{cw} and R_{fm}, respectively.

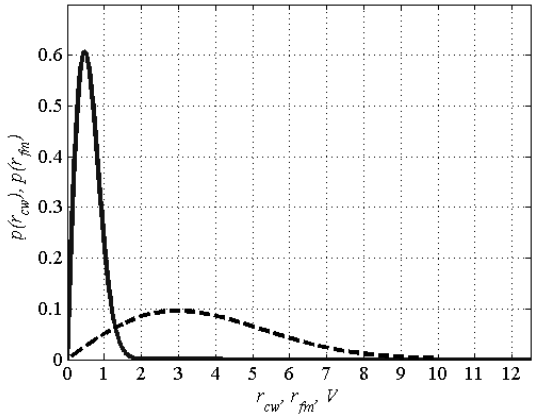

Figure 2. Theoretical distribution of the signal amplitude at the output of the demodulator for A = 1 and N = 100 (Rayleigh channel)

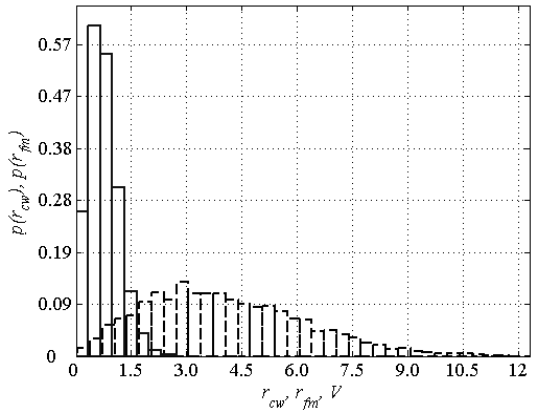

Figure. 3. Numerical simulation of the signal amplitude at the output of the demodulator for A = 1 and N = 100 (Rayleigh channel)

To verify the distribution curves obtained analytically, Fig. 3 contains the results of numerical simulations carried out for the propagation conditions used above (channel with diffuse power scattering, the signal amplitude $A = 1$, the number of multipath components $N = 100$, the signal base $B = 35$). As can be seen from the graphs in Fig. 2 and Fig. 3, at the output of the demodulator the most probable value of the signal with the frequency-constant carrier (dashed line) is in both cases about 3 V. In turn, the most probable value of the signal with the sweep spread carrier (solid line) is in both cases about 0.5 V. The results show a good consistency; analytical model can be used for estimation of variances of random values of the received signals.

III. Statistical characteristics of S2C signal in Rician channels

Another important type of hydro-acoustic channels is described by the model of Rice. At the output of the channel the signal consists of a set of multipath components, one of which is deterministic and has dominating power over the others. Channels of this type take place for example during a medium of short range data transmission in the horizontal direction (several hundred meters to several kilometers).

If the receiver of hydro-acoustic communication signals is synchronized on the receive time of the dominating multipath component, the values of quadrature components of the demodulator can be written as:

$$X_{fm}(t) = A\alpha_0\cos(\phi_0) + \sum_{n=1}^{N}\frac{1}{K_r}A\frac{\sin(\pi\Delta f\tau_n)}{\pi\Delta f\tau_n}\alpha_n\cos(\pi\Delta f\tau_n - \phi_n), \quad (3)$$

$$Y_{fm}(t) = A\alpha_0\sin(\phi_0) + \sum_{n=1}^{N}\frac{1}{K_r}A\frac{\sin(\pi\Delta f\tau_n)}{\pi\Delta f\tau_n}\alpha_n\sin(\pi\Delta f\tau_n - \phi_n), \quad (4)$$

where α_0 – coefficient of attenuation along the dominant path, ϕ_0 – phase of the dominating multipath component, and K_r – a positive number indicating the excess of the energy of the dominant/synchronous multipath component above the energy of all other/asynchronous multipaths.

It is known [4] that the signal, represented by a mixture of dominant multipath component and a set of delayed and attenuated multipaths, has mean values of its quadrature components which do not equal to zero. The random values of the quadrature components are normally distributed around nonzero mean which depends on the amplitude of the dominant multipath. Similarly to findings of the previous

section, it can be shown that the second component of the right-hand side of expressions (3) and (4) is characterized by a normal distribution, and the expression (3) and (4) represent the sum of one deterministic and many normally distributed values. Thus for a signal with a sweep-spread carrier the probabilities distribution of its quadrature components are qualitatively similar to the probability distributions of quadrature components of signals with frequency-constant carrier, but due to differences in the variances they differ quantitatively:

$$p(X^{fm}) = \frac{1}{\sigma_{fm}\sqrt{2\pi}} \exp\left(-\frac{(X^{fm} - X_0^{fm})^2}{2\sigma_{fm}^2} \right), \quad \ldots \quad (5)$$

$$p(Y^{fm}) = \frac{1}{\sigma_{fm}\sqrt{2\pi}} \exp\left(-\frac{(Y^{fm} - Y_0^{fm})^2}{2\sigma_{fm}^2} \right), \quad \ldots \quad (6)$$

where X_0^{fm} , Y_0^{fm} – the mean values of quadrature components, σ_{fm}^2 - variance of every of the quadrature components of the signal with the sweep spread carrier. While the quadrature components of the receive signal are with offset normally distributed values, the signal envelope has a Rician distribution [4]:

$$p(R_{fm}) = \frac{R_{fm}}{\sigma_{fm}^2} \exp\left(-\frac{R_{fm}^2 + \left(Z_0^{fm}\right)^2}{2\sigma_{fm}^2} \right) I_0\left(\frac{R_{fm} Z_0^{fm}}{\sigma_{fm}^2} \right).$$

where $Z_0^{fm} = \sqrt{(X_0^{fm})^2 + (Y_0^{fm})^2}$ – module of the dominant multipath component of the signal with the sweep-spread carrier, and I_0 – modified Bessel function of first type and zero order.

For a normalized signals, that is, with $\alpha_0 = 1$ and $0 \le \alpha_n \le 1$ the mean values of the quadrature components of signals with frequency-constant carrier and sweep spread carrier are equivalent and equal to A, but their variances are different. Since the excess propagation delay of the dominant (synchronous) multipath component is equal to zero, the function $\frac{\sin(\pi\Delta f \tau_0)}{\pi\Delta f \tau_0} = 1$ and value of the first term of expressions (3) and (4) is maximum (the first terms of expressions 3 and 4 are equal). However, the delayed multipath components are characterized by a nonzero τ_n , respectively, $\left| \frac{\sin(\pi\Delta f \tau_n)}{\pi\Delta f \tau_n} \right| < 1$ and the values which construct the second term of expressions (3) and (4) can be very small.

Similarly to the derivation of dispersions made above, it can be shown that for a signal with the sweep-spread carrier the variances of its quadrature components are equal to $\sigma_{fm}^2 = \frac{NA^2}{9K_r^2 B}$. At the same time for a signal with a frequency-constant carrier, these dispersions can be written as $\sigma_{cw}^2 = \frac{NA^2}{9K_r^2}$. Similarly to previous case, the comparison of variances σ_{fm}^2 and σ_{cw}^2 demonstrate that with increase of the signal base B the variance of receive signal distribution (at the output of the demodulator) decreases inversely proportional to B.

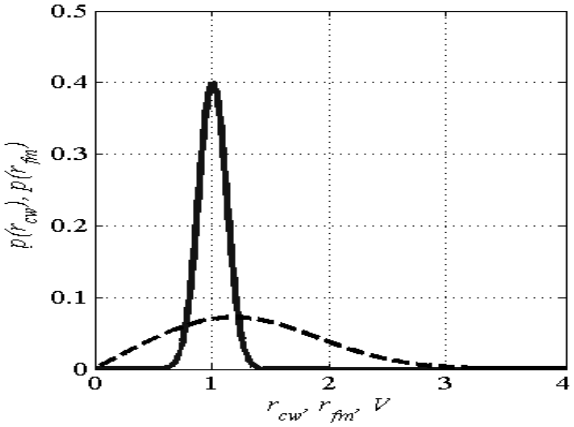

Figure 4. Theoretical distribution of the signal amplitude at the output of the demodulator for A = 1, N = 100, K_r = 10 (Rician channel)

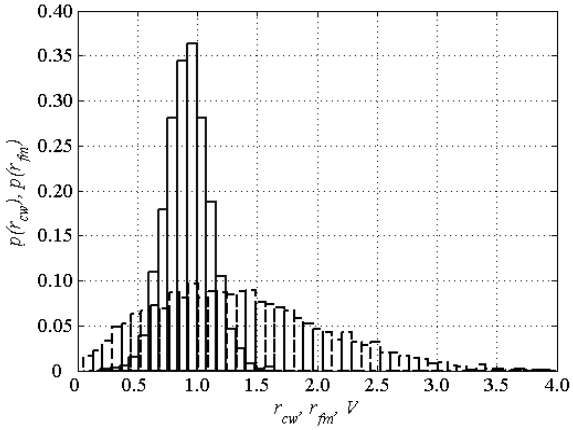

Figure 5. Numerical simulation of the signal amplitude at the output of the demodulator for A = 1, N = 100, K_r = 10 (Rician channel)

Fig. 4 shows an example of the probability distribution of the receive signal at the output of the demodulator for two cases: transmission of frequency-constant carrier (dashed line) and sweep spread carrier (solid line). Conditions for obtaining the distribution curves were: the signal amplitude $A = 1$, the number of multipaths $N = 100$, the signal base $B = 35$ and the ratio between the energy of the dominant multipath component and the energy of all other multipaths K_r =10. (The distributions r_{cw} , r_{fm} are also normalized by means of σ_{fm} values of distributions R_{cw} , R_{fm} , respectively). As follows from the form of the distribution (Rician distribution), the most probable value of the amplitude of the receive signal at the output of the demodulator is equal to the amplitude of the dominant multipath component. Taking into account B times smaller variance of the quadrature components, the amplitude of the signal with the sweep spread carrier (at the output of the

demodulator) is more often situated in the close vicinity of the most probable value, than the amplitude of the signal with the frequency-constant carrier.

To verify the theoretical curves, Fig. 5 demonstrates the results of numerical experiment carried out under conditions of signal propagation described above. Results that obtained analytically (Fig. 4) and by means of numerical simulations (Fig. 5) demonstrate that the most probable value of the signal with the frequency-constant carrier (dashed line) at the output of the demodulator is in both cases equal to approximately 1 V. In turn, the most likely values of the signal with the sweep-spread carrier (solid line) at the output of the demodulator in both cases are also equal and have approximately 1 V.

Good agreement of analytical and numerical models is obvious.

IV. Conclusions

The interaction of independent random multipath components at the output of the optimal quadrature demodulator determines a Gaussian process. The variance of this process is numerically equal to its average power, and since the variance is obtained analytically, in future it becomes possible to construct and to analytically investigate two-dimensional probability distributions of receive signals with sweep-spread carriers in the pre-detection point, as well as the envelope and phase distributions of the signal at this point. These tasks, as well as an estimation of the probability of erroneous determination of discrete signal values (envelope and phase), namely the probability as a function of the ratio between the energy of synchronous multipath component and the energy of the random process conditioned with random multipath components, are planned to be discussed in subsequent articles.

References

[1] K.G. Kebkal and R. Bannasch, "Sweep-Spread Carrier for Underwater Communication over Acoustic Channels with Strong Multipath Propagation," *J. Acoust. Soc. Am.*, 2002, vol. 112(5), pp. 2043 – 2052.

[2] B.R. Levin, *Theoretical Principles of Statistical Radio Engineering*. Moscow: Sovetskoye Radio, 1969, vol. 1. (rus)

[3] A.S. Sadomovskij. *Radio Systems of Data Transmissions*. Ulianovsk, Russia: UlGTU, 2001, – 104 p. (rus)

[4] J.G. Proakis. *Digital Communications*, 4th ed., 2000, McGraw Hill.

Evaluation of underwater acoustic channel capacity in conjunction with application of sweep-spread carrier signals

Konstantin Kebkal, Alexey Kebkal and Rudolf Bannasch

***Abstract*—Since the sweep-spread carrier (S2C) technology uses broadband frequency swept carrier signals with high frequency-sweep rates, the instant frequencies of multipath components have different values, what create sufficient background for their separation in frequency domain. The paper shows that after filtering the receiving signal with a filter, matched to the S2C reference signal, the strength and number of the multipath components significantly decreases. This provides considerable increase of coherence bandwidth of the communication channel and, in consequence, significant increase of achievable data rates. In this way the channel capacity can be substantially enhanced. The paper represents experimental data on evaluation of the underwater acoustic channel capacity during data transmission by use of a) S2C carrier signal and b) traditional constant-frequency carrier signal.**

***Index Terms*—underwater telemetry, underwater acoustic communication, sweep-spread carrier, spread spectrum, S2C technology.**

I. Introduction

TIME spread of a receive signal is caused with multipath propagation in transmitting signal. Due to multipath propagation the intersymbol interference can often achieve tens or even hundreds of symbol lengths. Moreover, due to wave and transmitter/receiver movements the transmitting channel represents nonstasionary behavior: impulse response of such a channel represents a complicated function of time and frequency [1]. The influence of such channel is represented particularly in small-scale fading of the receive signal inducing its significant amplitude and phase fluctuations. In shallow water telemetry the small-scale fading has usually Rayleigh nature: receive signals consists of many multiple reflections and do not have a dominant (direct) arrival. In these conditions the coherence bandwidth can vary in a wide range of values. Time spread in shallow water channels usually remains in the range between some milliseconds and some tens of milliseconds providing coherence bandwidth values between several tens of hertz and several kilohertz. Coherence bandwidth of deep water channels usually achieve bigger values, i.e. ranges from several hertz to several tens of kilohertz.

It is well known, that extended time spreads cause accordingly small coherence bandwidths and correspondingly low data rates. Coherence bandwidth corresponds to reciprocal of time spread within an accuracy of a constant factor. Therefore, if the impulse response of the channel can be somehow processed on the receiver side, the coherence bandwidth would accordingly change. For example, if the length of time-spread multipath signal would be reduced by means of special processing procedure, the coherence bandwidth would grow. In the following section a theoretical substantiation of the technique is represented, in which sweep-spread carrier signal [3] is used and which allows to passively suppress multipath components and, thus, to improve characteristics of the receive signal, especially the coherence bandwidth of the transmitting channel, and accordingly, achievable data rate. Below the comparison of properties of two different types of carrier signals is represented, both during propagation in multipath channels. One of the carriers is traditional one comprising constant frequency, and another one comprising the S2C signal.

K.Kebkal is with the Technical University Berlin, Berlin, Germany e-mail: kebkal@bionik.tu-berlin.de

R. Bannasch and A. Kebkal are with EvoLogics GmbH, spin off in Technical University Berlin, Germany

Manuscript received April 19, 2007; revised January 19, 2007.

II. Influence of multipath channel onto frequency-constant carrier and sweep-spread carrier signals

A. Frequency-Constant Carrier Signal

Let the sequence of digital data symbols is encoded by means of phase manipulations. Thus every symbol, generated on the interval $iT <= t < (i+1)T$, can be represented in the form:

$$s_x(i,t) = Re\left\{\sqrt{\frac{2E}{T}} exp[j(\omega_0 t + \theta_i)]\right\} \qquad (1)$$

where E - is energy-flux density of acoustic wave, T - symbol duration, ω_0 - (angular) carrier frequency, θ_i - discrete phase value (information to transmit).

If the signal is transmitted via multipath channel with M paths of different length and comes to receiver significantly exceeding the noise level, then the output of a quadrature matched filter on the interval of i-th symbol can be written as $x(i) = x_c(i) + jx_s(i)$ [4], where

$$x_c(i) \approx \alpha_0\sqrt{E}\cos(\theta_i + \theta_0) + \sum_l \alpha_l\sqrt{E}\cos(\theta_i + \theta_l) \qquad (2)$$

$$l = 1, ..., M-1$$

$$x_s(i) \approx \alpha_0\sqrt{E}\sin(\theta_i + \theta_0) + \sum_l \alpha_l\sqrt{E}\sin(\theta_i + \theta_l) \qquad (3)$$

$$l = 1, ..., M-1$$

The right side of every expression for $x_c(i)$ and $x_s(i)$ can be represented with two items. The first one is a variable containing desired value of the phase angle. The second one is a variable inducing the error in evaluation of the phase angle caused by multipath interference. This item is referred later as the residual $O_x(i)$.

Analysis of $x_c(i)$ and $x_s(i)$ shows that, while using conventional PSK scheme (phase encoding of a frequency-constant carrier signal), the error of phase estimation will strongly depend on the energy of multipath interferers. Thus, for accurate evaluation of the phase angle it is desirable that second item in the right side of (2) and (3) were suppressed.

Usually the output of the matched filter is processed with an additional tricky unit (equalizing filter), working in time domain and actively suppressing the multipath. However, as indicated later, the use of alternative type of carrier signals - sweep-spread carrier signals - allows to successfully combat against multipath by means of just match filtering (without active suppressing of multipath arrivals and correspondingly without further complicated processing).

B. Sweep-Spread Carrier Signal

Now let data is transmitted using the sweep-spread carrier signal. Thus, a phase-manipulated sweep-spread carrier signal can be represented on the interval $iT <= t < (i+1)T$ as:

$$s_y(i,t) = Re\left\{\sqrt{\frac{2E}{T}}\exp[j(\omega_b t + mt^2 + \theta_i)]\right\} \quad (4)$$

where E, T, θ_i defined above and have the same meaning also here, $m = \dfrac{\omega_b - \omega_e}{2T}$ is a frequency gradient of every section of the S2C carrier [3], ω_b and ω_e are beginning and final values of the angular frequency of the S2C signal.

And let the signal propagates in the same multipath channel as in the previous case, where multipath arrivals have various delays $\tau_0 \neq \tau_k$ and τ_0 and τ_k are correspondingly excess propagation delays of the "useful" arrival and unwanted k-th multipath arrivals creating reverberation. After propagation the received signal can written as

$$r_y(i,t) = \sqrt{\frac{2E}{T}}\sum_k \alpha_k \cos[(\omega_b - \Delta\omega_k)t + mt^2 + \theta_i + \theta_k] + n(t) \quad (5)$$

$$k = 0, ..., M-1$$

where $\Delta\omega_k$ is frequency resolution of the multipath component coming to receiver with excess propagation delays τ_k. The resolution can be defined via expression: $\Delta\omega_k = 2m\tau_k$ [3].

To demodulate the signal, a quadrature matched filter is used. If the signal-to-noise ratio is big enough, than the output of the filter will be equal to $y(i) = y_c(i) + jy_s(i)$ [4], with

$$\begin{aligned} y_c(i) &= \sqrt{\frac{2}{T}}\int_0^T r_y(t)\cos(\omega_b t + mt^2)dt \approx \\ &\approx \alpha_0\sqrt{E}\cos(\theta_0 + \theta_i) + \\ &+\sqrt{E}\sum_l \alpha_l \frac{\sin\left(\dfrac{-\Delta\omega_l T}{2}\right)}{\left(\dfrac{-\Delta\omega_l T}{2}\right)}\cos\left(\frac{-\Delta\omega_l T}{2} + \theta_i + \theta_l\right) \end{aligned} \quad (6)$$

$$l = 1, ..., M-1$$

$$\begin{aligned} y_s(i) &= \sqrt{\frac{2}{T}}\int_0^T r_y(t)\sin(\omega_b t + mt^2)dt \approx \\ &\approx \alpha_0\sqrt{E}\sin(\theta_0 + \theta_i) + \\ &+\sqrt{E}\sum_l \alpha_l \frac{\sin\left(\dfrac{-\Delta\omega_l T}{2}\right)}{\left(\dfrac{-\Delta\omega_l T}{2}\right)}\sin\left(\frac{-\Delta\omega_l T}{2} + \theta_i + \theta_l\right) \end{aligned} \quad (7)$$

$$l = 1, ..., M-1$$

where $\Delta\omega_l$ is a frequency deviation of the l-th multipath component, which is kept synchronous with the reference, and θ_l is a phase offset of the l-th multipath component relatively to the phase of the synchronous component [3].

The right side of $y_c(i)$ and $y_s(i)$ is represented with two items. Similar to the previous case, the first one is a variable containing desired value of the phase angle. The second one is a variable contributing to the error in evaluation of the phase angle induced with multipath interference. This item is referred later as residual $O_y(i)$.

Comparison of expressions (2), (3), (6), (7) shows that residuals $O_x(i)$ and $O_y(i)$ are significantly different and the main difference consists in the fact that the energy content of multipaths in (6) and (7) is reduced with multiplier $\dfrac{\sin(\Delta\omega_l T/2)}{\Delta\omega_l T/2}$ and thus $\max(|O_y(i)|) < \max(|O_x(i)|)$. It means that residual component of matched filtering will depend mach less on the energy of multipath interferers while using the sweep-spread carrier.

This effect is equivalent to filtering or truncation of multipaths and the more the delay of the multipath component, the better suppression of the component that can be achieved.

It must be noted here the fundamental difference between such filtering and equalizing filtering: while equalizing filters represent complicated units used for lacalization of multipath arrivals in time domain and their active suppression, matched filters represent simple units used for passive suppression of all multipath (asynchronous arrivals) spread in time-frequency around synchronous arrival. At that, the suppression rate depends on time-frequency distance between synchronous and asynchronous arrivals, an well as on frequency bandwidth occupied with the sweep-spread carrier signal.

III. Comparison of coherence bandwidth for frequency-constant and swept carrier signals

Let us define a complicated time spreading channel with large amouts of multipath, in which the main portion of multipaths comes to receiver within the time interval $[0, T_{spd}]$, and let us the amplitudes of these arrivals are random within this time and comprise the uniform distribution around unity. In this case the function of excessive propagation delay $S_o(\tau)$ can be represented in rectangular form

$$S_o(\tau) = \begin{cases} 1, & \tau \le T_{spd} \\ 0, & \tau > T_{spd}, \end{cases} \tag{8}$$

and in expressions for residual items in (2) and (3)

$$\max(|O_x(i)|) = \sum_l \alpha_l \sqrt{E}, \tag{9}$$

and, in turn, in (6) and (7)

$$\max(|O_y(i)|) = \sqrt{E} \sum_l \alpha_l \frac{\sin\left(\frac{-\Delta\omega_l \tau}{2}\right)}{\left(\frac{-\Delta\omega_l \tau}{2}\right)}. \tag{10}$$

the amplitudes of multipath arrivals α_l are all equal to unity. However, due to the multiplier $\frac{\sin(\Delta\omega_l \tau/2)}{\Delta\omega_l \tau/2}$ the strength of

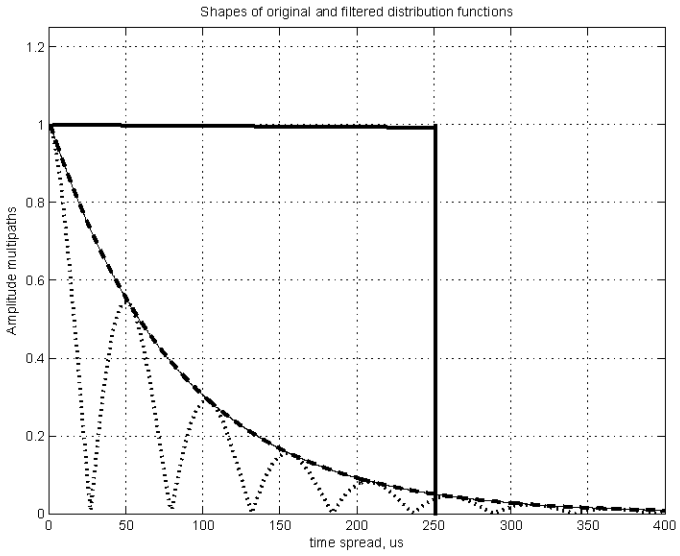

Fig. 1. Original (solid line) and filtered distribution function (dotted line)

multipath in (10) is much lower then in (9). Fig. 1 represents the comparison of original distribution function $S_o(\tau)$ (solid line) and filtered distribution function $S_f(\tau)$ (dashed line). To simplify the comparison, the $S_f(\tau)$ can be also represented as exponentially damped cosin, which is always equal to or less than correspondent exponent $S_e(\tau)$ (dotted line)

$$S_e(\tau) = \exp(-a\tau)$$

In order to compare the coherence bandwidths of the channel during transmission of data with different carrier signals, let us give a realistic relation of $S_o(\tau)$ and $S_e(\tau)$, for example, when the exponent suppresses the asynchronous multipath to such extent that at time T_{spd} all delayed multipaths are attenuated to practically achievable ratio $1/20$ from their original values [6].

Now, coherence bandwidths, corresponding to multipath spread function $S_o(\tau)$ and $S_e(\tau)$, can be found by means of Fourier transform:

$$F_o(\omega) = FT\{S_o(\tau)\} = \frac{\sin(\omega T_{spd})}{\omega T_{spd}}. \tag{11}$$

$$F_e(\omega) = FT\{S_e(\tau)\} = \frac{a^2}{a^2 + \omega^2 T_{spd}^2}. \tag{12}$$

As expected, Fourier transform of given $S_o(\tau)$ is $sinc$ function, and Fourier transform of given $S_e(\tau)$ is Lorenzian. In

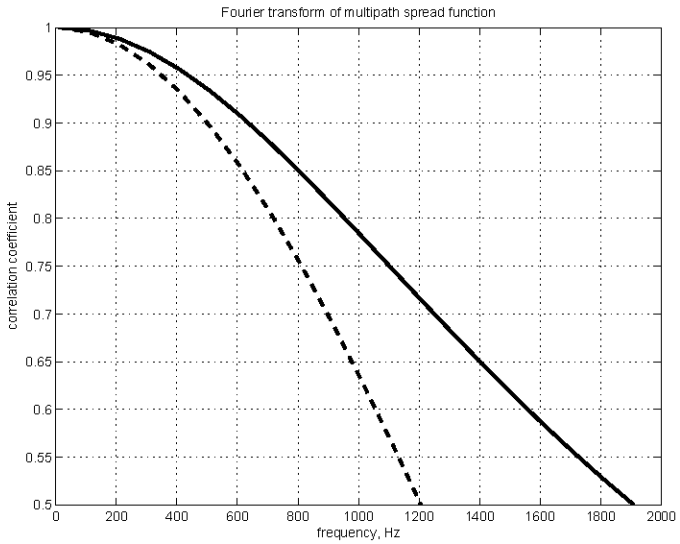

Fig. 2. Fourier transform of original (dashed line) and filtered distribution functions (solid line)

general, in mobile communication the frequency components of receive signal experience nearly equal impairments if they correlate with each other with a coefficient exceeding 0.5. Thus, putting a realistic time spread value and this coefficient, the coherence bandwidth can be found from (11) and (12). Fig. 2 represents the comparison of coherence bandwidth estimations for these expressions. The dashed line corresponds to frequency-constant carrier used for data transmission in given multipath channel. The solid line corresponds to sweep-spread carrier used for data transmission in the same multipath channel. It is obvious, that matched filtering of data symbols transmitted with sweep-spread carrier allows to "influence" the function of multipath time spread on the receiver side and, thus, to significantly increase coherence bandwidth of the transmitting channel.

In general, the coherence bandwidth is connected to data throughput over given channel: the wider the coherence bandwidth, the more data rate that can be achieved.

Next section represents experimental material, which confirms the ability of the S2C receiver to successfully work with datarates significantly exceeding standard estimates of coherence bandwidth in given transmitting channel.

IV. EXPERIMENT

A. Mathematical simulation

To estimate the coherence bandwidth of different transmitting channels various functions of excess propagation delay (impulse response) $S(\tau)$ were simulated. As in the previous section the duration of a multipath spread was set to 250 mcs. The quantity of multipath components was set equal to 8. The values of excess propagation delay for every multipath component were generated randomly in the range between 0 and 250 mcs. To achieve a representative sampling, 500 random impulse responses $S(\tau)$ have been generated. Each of the multipath structures was exposed to processing similar to that is carried out in S2C the receiver.

The structure $S(\tau)$ was multiplied on the autocorrelation function of the S2C carrier. Multiplication was carried out after synchronization of this structure with maximum value of the autocorrelation function (the mostly strong multipath component was always used for the synchronization). The

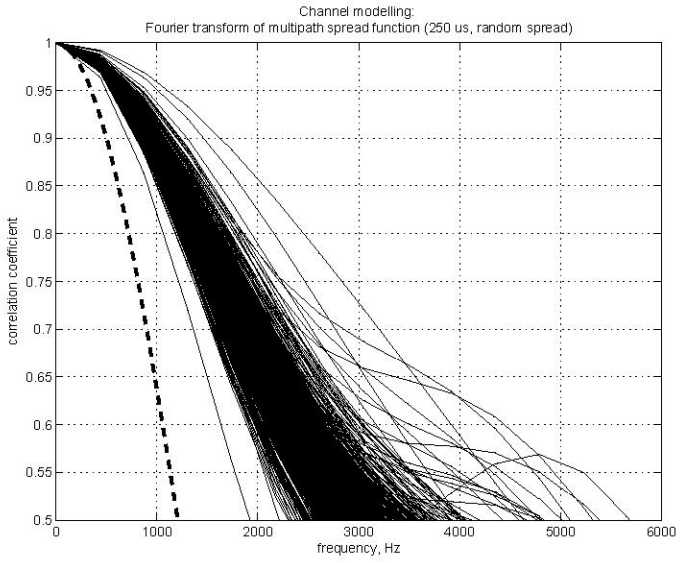

Fig. 3. Mathematic simulation: estimation of coherence bandwidth

result was exposed to Fourier transform and resulting curves were imposed against each other and represented in the figure (Fig. 3). As follows from Fig. 3 the estimation of coherence bandwidth lays in range from 1950 up to 4500 Hz, and as follows from comparison with Fig. 2 this result is well coordinated with the theoretical estimation (the estimation of the minimum value of the coherence bandwidth was 1950 Hz). Also, the values of coherence bandwidth, achieved as a result of numerical simulation, were better in tests, where sweep-spread carrier was used (numerous thin solid lines). The dotted line depicts the coherence bandwidth for tests, where frequency-constant carrier was used: significant difference is obvious.

B. Physical experiment

Estimation of coherence bandwidth in channels of practical interest and its comparison with achieved data rate was carried out on July, 13, 2006 during sea trials in shallow water channels in La Ciotat (in cooperation with iXSea and iXSurvey).

The sweep-spread carrier was used. The carrier occupied the frequency band between 55-70 kHz (by -3 dB). QPSK was used for data encoding.

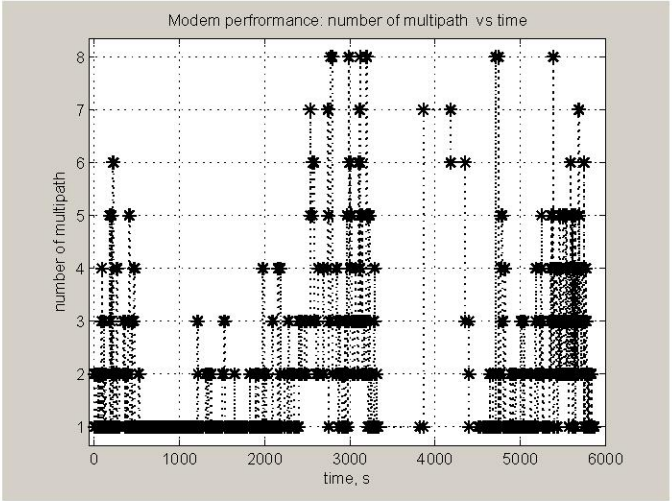

Fig. 4. Number of multipath vs time

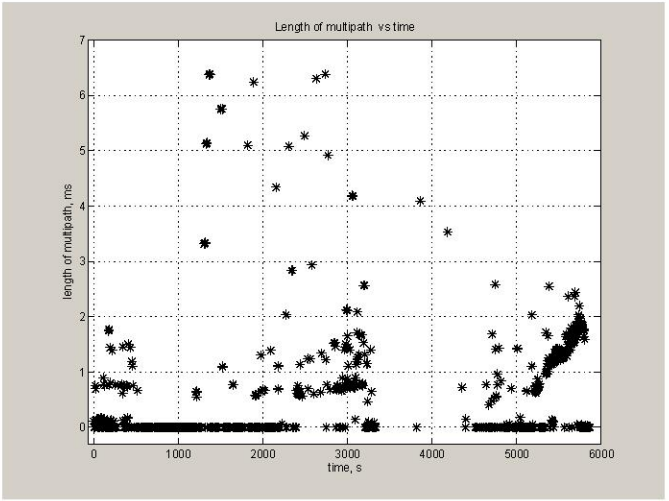

Fig. 5. Length of multipath vs time

The surface modem was put on a frame under the bottom of a catamaran on depth of 3 meters. The remote modem was put on towed object, which always changed its depth between 10 and 170 meters. Bottom depth was 150-200 m. Data transmission was carried out in a direction from surface modem to remote modem, then the data received by the remote modem were immediately transmitted back. During transmission the distance between surface and remote modems varied from 240 up to 750 m (Fig. 6). During the test the distance between modems continuously changed by etching or stretching of the towing cable. Velocity of relative movements between surface and remote modems reached 1.4 nm. Speed of vessel movements was 2-7 nm. By speed manipulation during

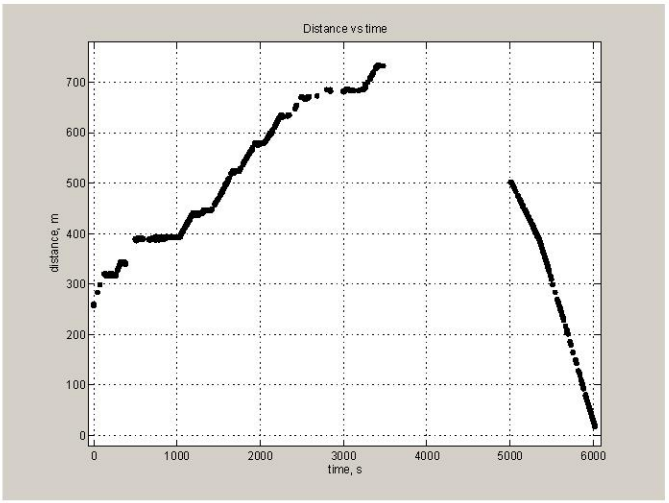

Fig. 6. Length of multipath vs time

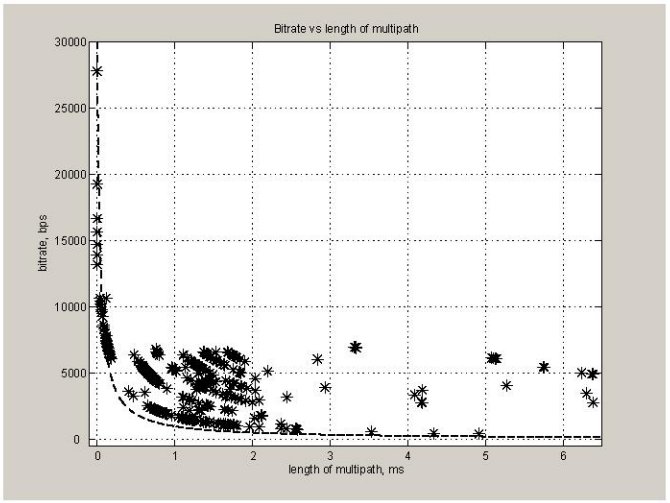

Fig. 8. Bitrate vs length of multipath

the towage and data transmission the depth of the remote modem continuously changed. Part of the test time the channel had rater slant geometry: during vessel movement with 2-3 nm the (inclination) angle of direct line, connecting surface and towed modems, was approximately 20-30 degrees relative to sea surface. At increase of speed of towage up to 5 units the channel became practically horizontal: the inclination angle decreased downto 10-15 degrees.

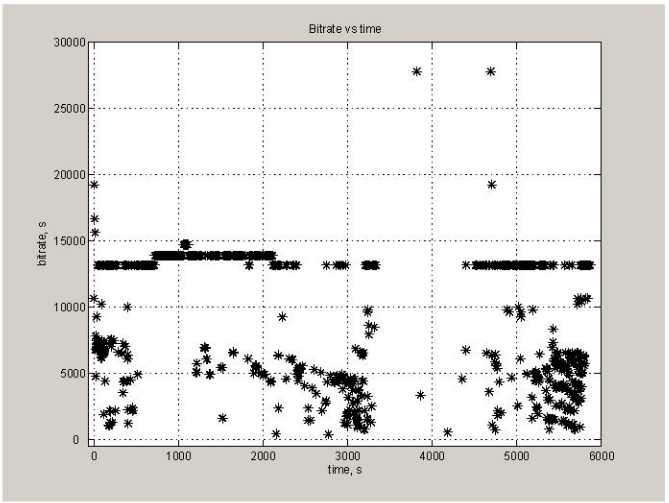

Fig. 7. Bitrate vs time

Properties of the transmitting channel are represented in Fig. 4 and Fig. 5. As follows from Fig. 4, the channel had high complexity: the amount of multipath components was between 2 and 5, sometimes increasing up to 6-8. The maximum value of the excess propagation delay of receive signal was within the range between 0.2-2 ms, sometimes increasing up to 6.5 ms (Fig. 5). Quick changes of the amount of multipath components, as well as quick changes of excess propagation delays, were frequently registered.

In Fig. 7 the change of datarate in time is represented. As follows from the figure, in most cases the datarate was equal to 13-14 kbit/s. From time to time datarate went down to 2-12 kbit/s. The average value of the data rate comprised 11 kbit/s. Comparing Fig. 6 and Fig. 7 the increase of communication distance does not essentially influence the data rate.

In Fig. 8 the dependency of datarate on excess propagation delay of the signal in multipath channel is shown. As follows from the figure, the transmitting channel was characterized by rather long values of excess propagation delays, usually between 0.5-3.0 ms, sometimes this value grew up to 6.5 ms. Asterisks depict practically achieved values of datarate for given multipath spreads. The dotted curve depicts expected value of the coherence bandwidth, calculated in standard way [5]. Practically achieved datarates essentially exceed expected value of coherence bandwidth in entire interval of propagation delays. As follows from the figure, the practically achieved values well coincide with results of simulation given in previous section. For example, theoretically estimated value of datarate for conditions mentioned in previous section (equal amplitudes and multipath spread equal to 250 mcs), corresponds to 7.8 kbit/s (provided that each symbol contains 2 bits). At that, the practically achieved values are situated within the range of 7-8 kbit/s.

With increase of datarate the error probability naturally grows. For datarates of up to 15 kbit/s the probability of bit error had the order 10^{-3}. For higher datarates the probability of bit error increases to the order of 10^{-2}.

For estimation of influence of the channel on the transmitted signal a special estimation was carried out: a ratio of excess propagation delay to symbol length, as well as a difference between practical frequency bandwidth and expected coherence bandwidth were calculated. Fig. 9 represents the difference between transmitted signals bandwidth and estimated coherence bandwidth of the channel. As follows from the figure, in grate majority of cases, this difference had positive value. The bandwidth of successfully transmitted signals exceeded the coherence bandwidth up to 4 kHz, what was equivalent to improvement of data throughput up to 4 kbit/s in comparison with the communication techniques working with frequency-

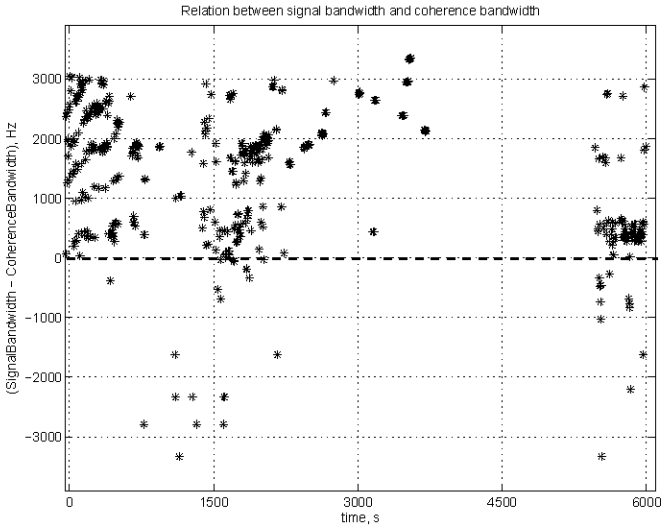

Fig. 9. Difference between transmitted signals bandwidth and estimated coherence bandwidth of the channel

constant carrier. In Fig. 10 the ratio of maximum value of excess propagation delay to data symbol length is shown. As follows from the figure, in most cases the data symbol length was much less (2 to 17 times) than the excess propagation delay of the signal in transmitting channel (about 17 data symbols were placed on the interval between first and last multipath components), The data represented in Fig. 9 and Fig. 10 testify to high complexity of data transmission conditions.

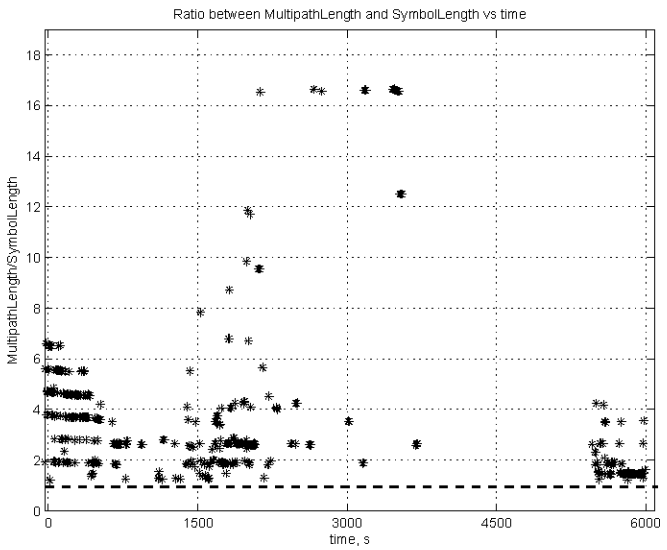

Fig. 10. Ratio of maximum value of excess propagation delay to data symbol length

V. Conclusion

Comparison of residuals (9) and (10) indicates that demodulation of S2C signals by means of matched filters can decrease the influence of multipath interference on the receive signal. When the residual (9) directly depends on the energy and the number of multipath arrivals and does not depend on the time profile of the multipaths, the residual (10) rapidly decreases with increasing excess propagation delays of multipath arrivals in relation to synchronous arrival according to pattern $\frac{sin\ x}{x}$. Hence, by means of proper adjustment of S2C parameters, the dependency of demodulation success on properties of the complicated transmitting multipath channel can dramatically decrease.

Use of sweep-spread carrier technology [3] allows to passively suppress multipath components on receiver side and, thus, to improve characteristics of receive signal. Experimental data confirmed the theoretical expectation and demonstrated significant improvement of such important feature of the S2C technique as the ability to enhance the coherence bandwidth and data throughput in complicated communication channels.

Acknowledgment

The authors would like to thank iXSea and iXSurvey for the opportunity to test the S2C acoustic telemetry in many different condition in channels of practical interest.

References

[1] Catipovic A.J. Performance Limitations in Underwater Acoustic Telemetry. *IEEE Journal of Oceanic Engineering*, vol. 15, No. 3, pp. 205-216. (July 1990)

[2] Kilfoyle D. B. and Baggeroer A B., "The state of the art in underwater acoustic telemetry," *IEEE Journal of Oceanic Engineering*, vol. 25, No. 1, pp. 4-27, January 2000.

[3] Kebkal K.G. and Bannasch R., "Sweep-spread carrier for underwater communication over acoustic channels with strong multipath propagation," *J. Acoust. Soc. Am.*, vol.112, pp. 2043-2052.

[4] K. Kebkal, A. Kebkal, R. Bannasch. Matched Filtering for Demodulation of Phase Encoded Sweep-Spread Carrier Symbols Propagating via Reverberant Underwater Environments. Proceedings of the 8th European Conference on Underwater Acoustics ECUA 2006. Carvoeiro, Portugal 2006, pp. 869-877.

[5] Bernard Sklar, Digital communications. Fundamentals and applications. Prentice Hall PRT, New Jersey, 2001. 11.

[6] K. Kebkal, R. Bannasch, A. Kebkal. Theory and experiment for evaluation of the methodical error for a matched filtered phase-encoded sweep-spread carrier signal. Proceedings of the 1st International Conference on Underwater Acoustic Measurements: Technologies and Results, Heraklion, Greece, July 2005.

[7] Vakman D.E. Complex signals and uncertainty principle in radiolocation. / Edition "Sovetskoe Radio", Moscow, 1965. 304 p. (rus)

Underwater Acoustic Communication Based on Virtual Time Reversal and Sweep-Spread Carrier

LI Wen-cong YUAN Fei* CHEN Ke-yu ZHU Yi
Key Laboratory Underwater Acoustic Communication and Marine Information Technology of the Ministry of Education
Xiamen University, Xiamen, China
*Corresponding Author: yuanfei@xmu.edu.cn

***Abstract*—Underwater acoustic (UWA) channel was one of the most complex wireless communication channel because of extensive multipath problem. Multipath problem will lead to severe inter-symbol interference (ISI) and frequency selective fading. To build a reliable high rate UWA communication system in multipath environment, Sweep-Spread Carrier (SSC) system based on Virtual Time Reversal Mirror (VTRM) was introduced. The system requires phase modulation for more than once in every period, so the communication rate could be enhanced. To ensure the reliability of the high rate system, Virtual Time Reversal Mirror combining with Orthogonal Matching Pursuit Channel Estimation was introduced to solve the multipath problem. The ISI in the underwater channel is suppressed because of the temporal compression and spatial focusing, resulting in the channel power focusing. The simulation experiment adopted Bellhop simulation model to verify algorithm performance, then conducting a poor experiment as a further verification. The performance of the system introduced was proved to be significantly enhanced.**

Keywords—underwater; multipath; Sweep-Spread Carrier; Virtual Time Reversal Mirror

I. INTRODUCTION

Underwater acoustic (UWA) channel was one of the most complex wireless communication channel because of the narrow bandwidth, high ambient noise, extensive multipath, large transmission delay, random fluctuation and Doppler frequency shift and so on[1].

Designed for high data rate communication in the severe inter-symbol interference(ISI) environment, systems employ either some form of array processing, or equalization methods, or their combinations. Equalization methods have their limitations. Time-varying leads to the varying of channel impulse response, possibly leading to the failure of coherence and equalization. Phase conjugation has been recently introduced in array signal processing, evolving to Time Reversal Mirror(TRM)[2]-[4]. With TRM, specific communication channel environment conditions are not necessary for matching the channel and guiding the temporal compression and spatial focusing of the signal. Temporal compression recombinants multipath components to reduce ISI and improve SNR. Spatial focusing reduces effects caused by channel fading with low complexity[5]-[6].

Pro. Wang from Chinese Academy of Sciences Institute of Acoustics applied TRM in Spread Spectrum Communication, resulting in an enhancement of focus gain by 10dB. Therefore, TRM is suitable for target detection and underwater acoustic communication. YIN. J. W. applied TRM in underwater acoustic communication network[7]-[10]. Reference ([11]-[13]) studied the performance of a single carrier phase modulation with the Passive Time Reversal Mirror (PTRM). Reference([14]-[16]) applied PTRM in MIMO underwater acoustic communication. João Gomes verified that PTRM can effectively shortening the channel length[17]-[19].

Most of the reference mentioned committed to PTRM. Research on VTRM is far less. However, VTRM has a vaster development space for its possibility to combine with Channel Estimation. This paper constructed a high-rate Sweep-Spread Carrier system, combining with VTRM and Orthogonal Matching Pursuit (OMP) Channel Estimation..

II. SSC SYSTEM

A. SSC modulation

A SSC signal is a periodic up-chirp signal, which can be written as

$$c(t) = A_c \exp[j(w_l(t - \left[\frac{t}{T_{sw}}\right]T_{sw}) + m(t - \left[\frac{t}{T_{sw}}\right]T_{sw})^2)] \quad (1)$$

Where A_c is the amplitude, $m=(wh-wl)/2Tsw$ is a coefficient denoting the frequency variation rate, w_l denotes the lowest angular frequency, while w_h denotes the highest one, and T_{sw} is the sweep duration. Supposing that $T_{sw}=kT$s, a SSC signal can carry k different phase information in a frequency-sweep period. So the system requires phase modulation for k times in every period, providing a considerable communication transmission rate.

As is showed in figure.1, if k=2, system requires phase modulation for 2 times in every period T_{sw}. When $t=t_1$, the system modulation for the first time. When $t=t_2$, the system modulation for the second time. If k=4, 4 symbol information should be carried in every period T_{sw}.

B. Dechirp Compression

In the demodulation part, a Chirp signal with the same frequency modulation rate and time width as the received

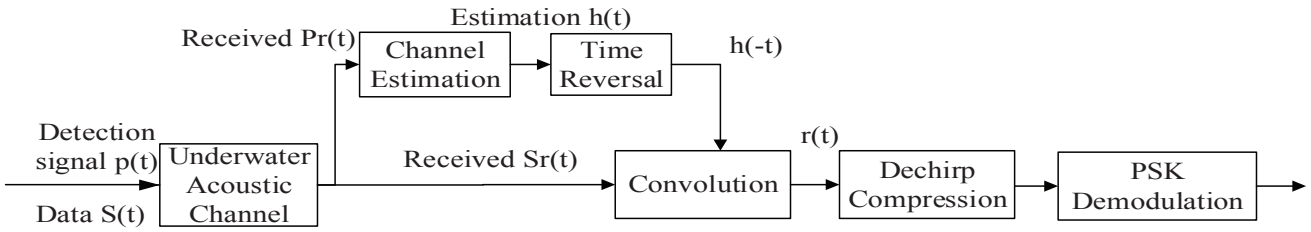

Fig. 3. System realization diagram.

signal (frequency is different, however) was generated. The received signal was dechirp-compressed with the local chirp signal generated, multiplying the two signal, then band-pass filtering. The resulting signal was a single-frequency signal which was able to be demodulated by routine PSK demodulation method. After demodulation, the data was restored.

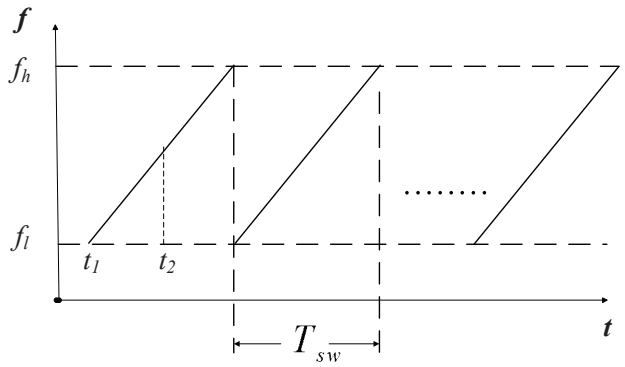

Fig. 1. Sweep-Spread Chirp signal(k=2).

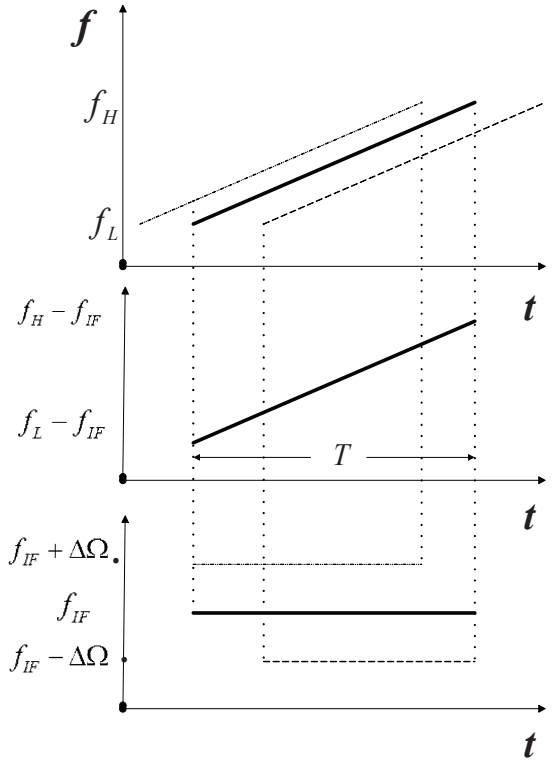

Fig. 2. Schematic drawing of Dechirp Compression.

As is showed in figure.2, there are three propagation paths ranging from f_L to f_H, while the local signal had a bandwidth from $f_L - f_{IF}$ to $f_H - f_{IF}$. After the two signal are multiplied and then band-pass filtered, the resulting signal was a single-frequency signal. The main path part has a frequency of f_{IF}. The other two paths has a time delay, resulting in frequency differences after filtering. The frequency difference $\Delta\Omega$ is a hint to find out the time delay ΔT, which is

$$\Delta\Omega = \Delta T \times m \tag{2}$$

III. Virtual Time Reversal Mirror

A. Receiver based on VTRM

At the receiver, time reversal mirror (TRM) was introduced to bring about temporal compression and spatial focusing. Multipath components can be superimposed at the same time and phase, which settles serious frequency selective fading and multipath effect. This article presented a combination of VTRM and Orthogonal Matching Pursuit Channel Estimation.

Figure. 3 is the system realization diagram. In the system, the transmitter was required to launch detection signal *p(t)*. The receiver obtained the received detection signal to estimate channel impulse function *h'(t)* by OMP channel estimation. *h'(-t)* was obtained by reversing *h'(t)* , then convolving receiving data *Sr(t)*. The to-be-demodulate data *r(t)*, which had a waveform similar to the original transmit data waveform, can be written as

$$\begin{aligned} r(t) &= S_r(t) \otimes h'(-t) \\ &= [S(t) \otimes h(t) + n_s(t)] \otimes h'(-t) \\ &= S(t) \otimes [h(t) \otimes h'(-t)] + n_s(t) \otimes h'(-t) \end{aligned} \tag{3}$$

As long as the channel impulse estimation *h'(t)* is close to the real channel impulse *h(t)*, multipath can be superimposed at the same time and phase. The ISI in the underwater channel is suppressed because the channel power has been focused. Therefore, OMP channel estimation is introduced to ensure the channel focus.

B. Orthogonal Matching Pursuit Channel Estimation

The received detection signal $P_r(t)$ is the convolution of acoustic the origin detection signal and underwater channel impulse response. So, when AWGN is considered, the received detection signal can be written as

$$P_r(t) = p(t) \otimes h(t) + n_p(t) \tag{4}$$

The main point of OMP channel estimation is as follows:

a) Rewriting the origin detection signal as a Toeplitz matrix, the received detection signal matrix can be rewritten as

$$\begin{bmatrix} P_r(0) \\ P_r(1) \\ \vdots \\ P_r(N-2) \\ P_r(N-1) \end{bmatrix} = \begin{bmatrix} p(0) \\ p(1) \\ \vdots \\ p(N-2) \\ p(N-1) \end{bmatrix} h(0) + \begin{bmatrix} 0 \\ p(0) \\ \vdots \\ p(N-3) \\ p(N-2) \end{bmatrix} h(1) + \cdots + \begin{bmatrix} 0 \\ 0 \\ \vdots \\ p(N-L-1) \\ p(N-L) \end{bmatrix} h(L-1) + \begin{bmatrix} n_p(0) \\ n_p(1) \\ \vdots \\ n_p(N-2) \\ n_p(N-1) \end{bmatrix} \tag{5}$$

The equation can be simplified as

$$P_r = \sum_{k=0}^{L-1} p_k h(k) \tag{6}$$

b) Estimulate the multipath delay. In order to obtain the Channel weighting coefficient, the matching columns bewteen P_r and P shoould be found. Supposing that the best matching columes is k_p, it is the location of the most important path.

$$K_p = \max_L \left(\frac{\left| P_L^T P_{ri} \right|^2}{\left\| P_L \right\|^2} \right) \quad L \neq k_1, k_2, \cdots k_{p-1} \tag{7}$$

c) The matching column subscripts of the two matrixs should rearranged as an array, which is

$$w = [k_1, k_2, \cdots, k_m] \tag{8}$$

Where the k_1th column is the best matching one, the k_2th is second best one, the k_mth is the least matching one. Therefore the array $\boldsymbol{w}$ is the channel weighting coefficient array.

d) Construct a diagonal sparse matrix $\boldsymbol{W}$ based on the weighting coefficient array $\boldsymbol{w}$. Define that

$$W_i = \begin{cases} 1 & , i \in w \\ 0 & , i \notin w \end{cases} \tag{9}$$

P_r can be rewritten as

$$P_r = PWh + N$$

e) Finally, the channel impulse response can be obtained by Least Square algorithm:

$$\hat{h}' = \arg\min \left\{ \left\| P_r - P \cdot diag(\hat{h}) \hat{h}' \right\|^2 \right\} \tag{10}$$

IV. Experimental Verification

A. Simulation

The simulation experiment adopted Bellhop simulation model to verify algorithm performance. Two multipath channel models were generated, which were UAMCM1 (6 paths) and UAMCM2 (10 paths), by setting offshore transceiver distance at 1km and 5km. The parameters are setting as

TABLE I. Bellhop Parameters Setting

Channel	UAMCM1	UAMCM2
Distance /km	1	5
Transmitter Depth/m	10	10
Receiver Depth/m	15	15
RMS/m	2	3
Transverse Wave Velocity /m/s	1530-1533	1540-1543
Absorption Coefficient	0.5	0.53
Seawater Depth /m	20	50

Figure.4 shows the impulse response of the two Bellhop models. In this simulation, the available bandwidth was 20 kHz-30 kHz, the symbol time of the Chirp signal was 10ms, and the sampling rate was 204.8 kHz. The frequencies of the transmission Chirp signal and the local Chirp signal had a difference of 5 kHz. Figure.5 and figure.6 show the BER of the system in UAMCM1 and UAMCM2. In the figure, 4BPSK means that the system requires BPSK modulation for 4 times in every period. As is showed in the figure, after VTRM, the performances of different systems had a significant enhancement in no matter high or low SNR. Obviously, the system enhancement was greater in UAMCM2 because the UAMCM2 channel was more complicate. Based on the TRM theory, if the channel estimation is accurate, the more complicate the channel is, the better the VTRM focus performance will be.

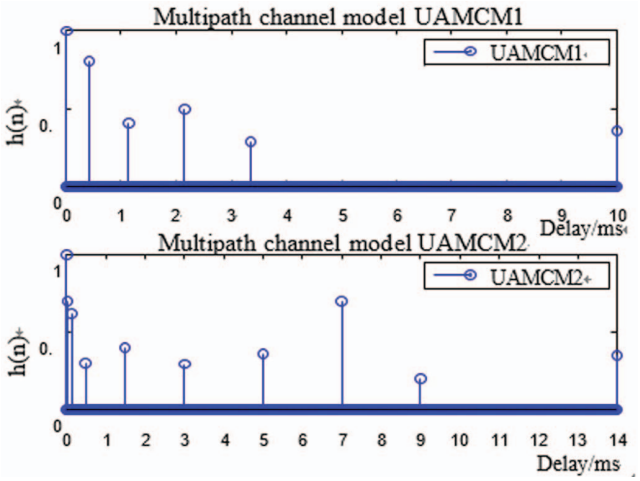

Fig. 4. Bellhop simulation model.

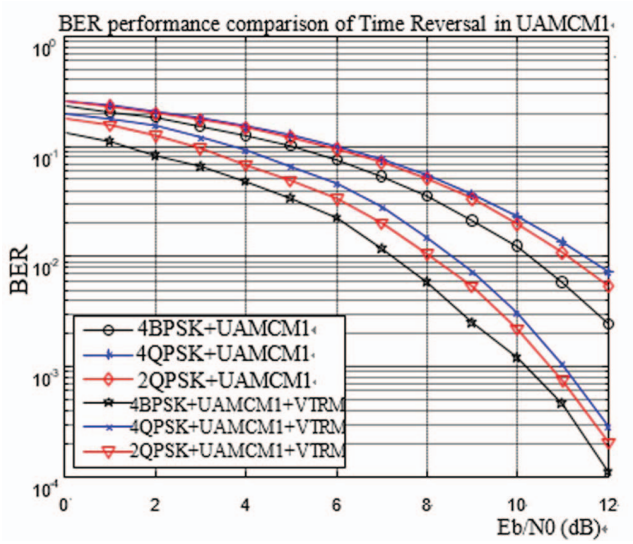

Fig. 5. Error rate plot(UAMCM1).

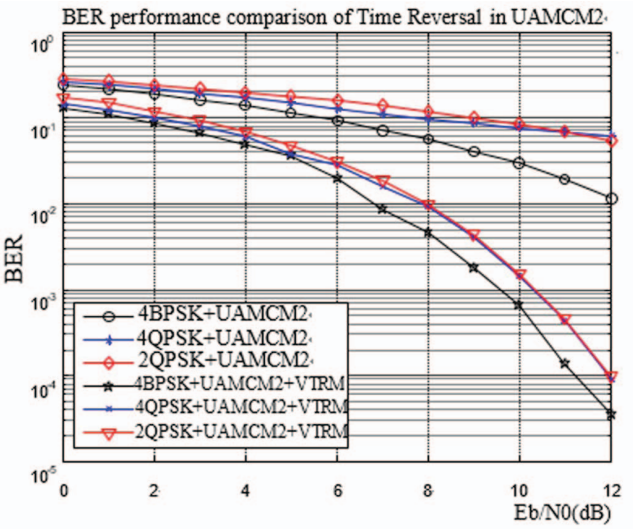

Fig. 6. Error rate plot(UAMCM2).

B. *Pool Experiment*

After the simulation experiment, a poor experiment was conducted as a further verification. Figure. 7 is the scene of the laboratory pool. The size of the experiment pool was about 22.89×5.18×1.92m. It had tile wall. The depth of the pool was about 2m. In this non-anechoic pool, sound waves were effected by their reflex on the water, the wall and the bottom. So multipath effect were more apparent here than general shallow channel.

The vertical distance of the transmitter from the water surface was 0.5m, while that of the receiver was 1m. The distance between the transmitter and the receiver was 14m. When the water surface in the pool was calm, the transducer received a signal under a SNR of 3-5dB.

The transmission signal was 4DQPSK, which meant the system required DQPSK modulation for 4 times in every period. The communication rate was 800bps. Figure.9 and figure.10 shows the time-domain and power spectrum diagram of the received signal.

The constellation diagram of received signal without VTRM was shows in figure. 11. The BER was 0.061. After VTRM, the constellation diagram of received signal was almost completely separated and legible, as was showed in figure.12. The BER reduced to less than . Therefore, The system performance was significantly enhanced after introducing VRTM.

Fig. 7. The photo of the experiment pool.

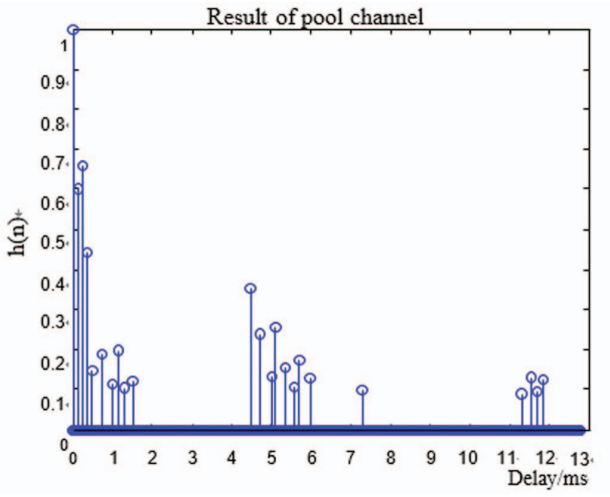

Fig. 8. Result of pool channel estimation.

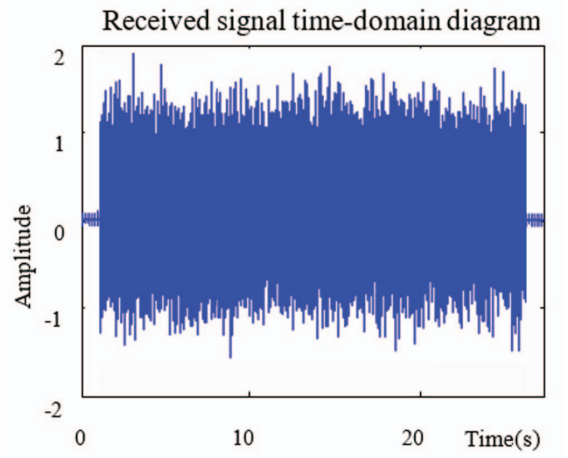

Fig. 9. Received signal time-domain diagram.

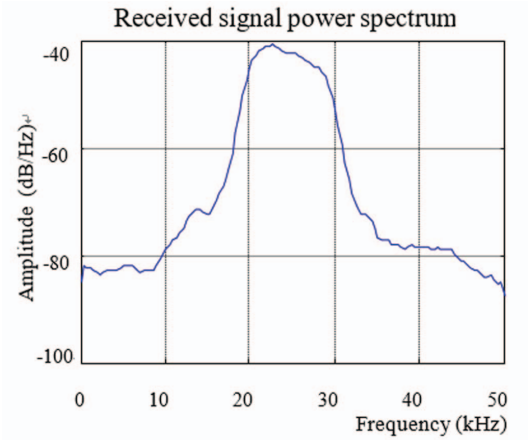

Fig. 10. Received signal power spectrum diagram.

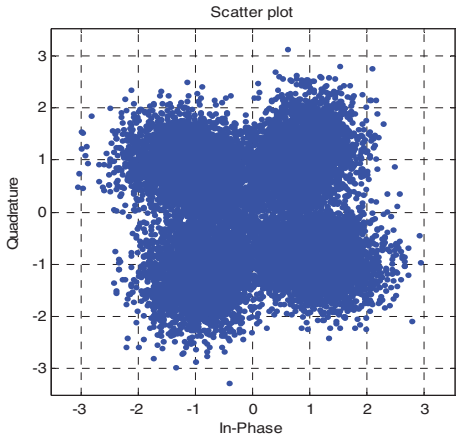

Fig. 11. Constellation diagram of received signal in pool experiment

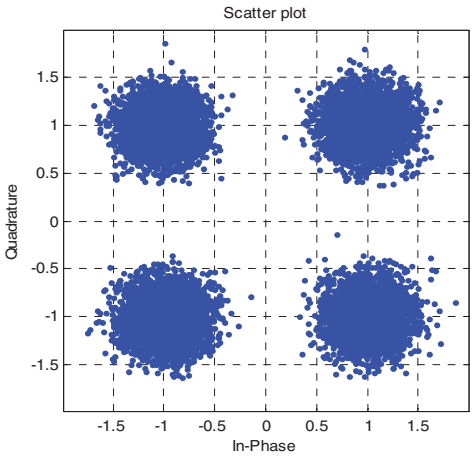

Fig. 12. Constellation diagram of received signal after VTRM

ACKNOWLEDGMENT

This work was supported by the National Natural Science Foundation of China (61571377, 61471308, 61501386)

REFERENCES

[1] Chitre M, Shahabudeen S, Stojanovic M, "Underwater acoustic communications and networking: Recent advances and future challenges," Marine technology society journal, vol. 42, no. 1, pp. 103–116, 2008.

[2] Cronin‐Golomb M, Fischer B, White J O, et al, "Passive phase conjugate mirror based on self‐induced oscillation in an optical ring cavity," Applied Physics Letters, vol. 42, no. 11 , pp.919-921, 1983.

[3] Dowling D R, "Acoustic pulse compression using passive phase‐conjugate processing," The Journal of the Acoustical Society of America, vol. 95, no. 3, pp. 1450-1458, 1994.

[4] Hursky P, Porter M B, Rice J A, et al, "Passive phase-conjugate signaling using pulse-position modulation," IEEE Conference and Exhibition, vol. 4, pp. 2244-2249, 2001

[5] Song H C, Kuperman W A, Hodgkiss W S, "A time-reversal mirror with variable range focusing," The Journal of the Acoustical Society of America, vol. 103, no. 6, pp. 3234-3240, 1998.

[6] Edelmann G F, Akal T, Hodgkiss W S, et al, "An initial demonstration of underwater acoustic communication using time reversal," Oceanic Engineering, IEEE, vol.27, no. 3, pp. 602-609, 2002.

[7] YIN Jing-wei, HUI Jun-ying, "Classified Study on Time Reverse Mirror in Underwater Acoustic Communication," Journal of System Simulation, vol. 20, no. 9, pp. 2449-2453, 2008.

[8] YIN Jingwei, ZHANG Xiao, ZHAO Anbang, SHENG Xueli, "The application of a virtual time reversal mirror to upstream communication of underwater acoustic networks," Journal of Harbin Engineering University, vol. 32, no. 1, pp. 1-5, 2011.

[9] Yin Jingwei, Wang Yilin, Sun Liqiang, "Time reversal mirror-based underwater acoustic," Journal of Huazhong University of Science and Technology(Nature Science Edition), vol. 9, pp. 16-20, 2009.

[10] YIN Jing-wei, HUI Jun-ying, CAI Ping, GUO Long-xiang, "Application of Fractional Fourier Transform in Long Range Deep-Water Acoustic Communication," Electronica Sinica, vol. 35, no.8, pp. 1499—1504,2007.

[11] SONG A J, MOHSEN B, ARTHUR E, "Passive time reversal acoustic communications through shallow-water internal waves," IEEE J Oceanic Eng, vol. 35, no. 4, pp. 756-765, 2010.

[12] NIE X Y, XU W, ZHENG J C, "Time reversal acoustic communication with concatenated reed-solomon code," OCEANS, Yeosu, 2012, pp. 1-4.

[13] ZHANG G S, PENG B, DONG H F, "Experimental assessment of sparse channel estimations for passive-phase conjugation communications'" IEEE International Conference on Acoustics, Speech and Signal Processing Bremen, pp. 2701-2704, 2012.

[14] SAKTHIVEL M S, NATARAJAN V, "Performance analysis of signal to noise ratio and bit error rate for multiuser using passive time reversal technique in underwater communication," Wireless Communication and Sensor Computing, Chennai, 2010, pp. 1-4.

[15] SONG H C, HODGKISS W S, KUPERMAN W A, "MIMO multi-access passive time reversal communications," OCEANS 2006, Boston, MA,pp. 1-6, 2006.

[16] SONG H C, HODGKISS W S, KUPERMAN W A, "Multiuser communications using passive time reversal," IEEE Journal of Oceanic Engineering, 2007, vol. 32, no. 4, pp. 915-926.

[17] JOÃO G, VICTOR B, "Time-reversed OFDM communication in underwater channels," IEEE 5th Workshop on Signal Processing Advances in Wireless Communications, Lisboa, 2004, pp. 11-14.

[18] JOÃO G, VICTOR B, "Time-reversed OFDM communication in underwater channels," IEEE 5th Workshop on Signal Processing Advances in Wireless Communications, Lisboa, 2004, pp. 11-14.

[19] JOÃO G, CHRISTIAN R B, ANTÓNIO S, "Demodulation of underwater OFDM transmissions by time reversal and basis pursuit meth-ods," Sustainable Wireless Technologies, Vienna, Austria, 2011, pp. 1-9.

Peer-Reviewed Technical Communication

An Efficient Receiver Structure for Sweep-Spread-Carrier Underwater Acoustic Links

Leonardo Marchetti and Ruggero Reggiannini

***Abstract*—In this paper, we present an improved receiver architecture for sweep-spread-carrier modulation, a spread-spectrum technique proposed to effectively contrast the effects of time dispersion over multipath propagation channels in underwater acoustic wireless links. The proposed structure is capable of taking advantage of the energy received from all propagation paths rather than only from the strongest path, as envisaged in the pioneering paper introducing this modulation technique. A hardware version of the modem was implemented in the laboratory and its behavior was assessed and compared, using standard propagation models, to that exhibited by the traditional single-path-based scheme in terms of bit error rate. Results are presented showing that gains of a few decibels can be achieved in signal-to-noise-plus-interference ratio. Issues relevant to carrier/symbol synchronization, channel estimation, and sensitivity to Doppler distortion are also addressed.**

***Index Terms*—Maximal ratio combining, multipath propagation, multiple-branch receiver, rake receiver, spread spectrum, sweep-spread carrier, underwater acoustic communications.**

I. Introduction

UNDERWATER acoustic (UWA) communication systems have attracted considerable attention in recent years due to the growing interest for issues related to exploration, surveillance, and exploitation of the submarine environment (e.g., [1]–[6]). Most of these applications require some form of wireless communication capability between submerged terminals such as autonomous underwater vehicles (AUVs), platform/mother ships, nodes of underwater networks, etc. As is well known, the UWA multipath channel is plagued by several impairments, notably: 1) severe time dispersion due to the low sound propagation speed with consequent possible distortion of the received waveform; 2) for the same reason, amplification of Doppler shifts/rates associated to relative movements of terminals, possibly leading to significant signal distortion for wide signal bandwidths; 3) large propagation delays; and 4) lowpass behavior of the propagation channel caused by sound absorption, leading to strong limitation of bandwidth usage. These factors considerably limit transmission rates and coverage of UWA links in comparison with their electromagnetic radio counterparts and call for the search of more specific and robust signaling schemes. Comprehensive accounts of the above issues along with presentation and discussion of specific transmission schemes can be found in, for example, [3]–[6] and references therein.

A few years ago, an unconventional interesting spread-spectrum transmission technique was proposed in [7] and applied to the UWA channel. The basic idea is to employ a sawtooth-frequency-modulated waveform as signal carrier [termed sweep-spread carrier (S2C)], with linear frequency ramps, such as to facilitate separation at the receiver of the signal replicas collected from the various channel paths. Actually, since these replicas undergo different propagation delays, they are mapped to different positions on the frequency axis when the received signal is downconverted to baseband using a locally generated copy of the S2C synchronized to the strongest path. A proper design of the signal parameters permits to space the spectral replicas associated with the various paths far enough from one another so as to avoid their overlap. It is therefore possible to single out the strongest path with no interference from the others, thus canceling multipath-induced distortion.

From the pioneering paper [7] to date a number of improvements and variants of the initial scheme of the S2C receiver have been proposed and analyzed. In particular, the patent document [8] presents some conceptual receiver architectures making use of the energy received through multiple propagation paths instead of that from the strongest path only. Specifically, in [8, Fig. 19], a receiver block diagram is sketched wherein two signal replicas collected from different paths are processed by parallel receiver branches, and their individual phases and relative delay are corrected before the waveforms are applied to a block identified as "combined demodulator." The document however does not specify how the cited phases and delays are estimated, nor does it provide details about the operation of the demodulator. Furthermore, it was out of the scope of [8] to analyze and compare the performance of the above architectures. Additional related qualitative and quantitative results can be found in [9]–[11] addressing the impact of imperfect separation (and consequent onset of mutual interference) of the signal replicas being processed by the receiver branches on the estimation of their indi-

Manuscript received July 14, 2014; revised October 17, 2014, January 10, 2015, and June 03, 2015; accepted June 09, 2015. This work was supported in part by Tuscany Region, Italy in the framework of the project V-FIDES within the PAR FAS 2007-2013 program.

Associate Editor: S. Zhou.

L. Marchetti was with the Department of Information Engineering, University of Pisa, Pisa 56122, Italy. He is now with Intermarine S.p.A., 19038 Sarzana SP, Italy (e-mail: l.marchetti@intermarine.it).

R. Reggiannini is with the Department of Information Engineering, University of Pisa, Pisa 56122, Italy (e-mail: ruggero.reggiannini@iet.unipi.it).

Digital Object Identifier 10.1109/JOE.2015.2445251

vidual phases and relative delays, needed for combined demodulation.

In this paper, we make some steps ahead, by proposing and discussing a further implementation of the S2C receiver which integrates the schemes presented in the above references. As in [8], we consider an advanced receiver structure capable of enhancing the power efficiency of the scheme in [7] through exploitation of the energy received from multiple nonnegligible acoustic paths rather than only from the strongest path.

This goal can be achieved by first identifying the paths of significant level, then performing extraction and parallel elaboration for each of them, and finally combining the decision metrics from each processing branch. A noteworthy difference with respect to the schemes enumerated in [8] is that here we resort to an optimal approach to combine the branch outputs. The resulting multiple-branch receiver architecture is similar to that used for the reception of direct-sequence spread-spectrum (DS–SS) signals over time-dispersive wireless links, known as "rake receiver" [12, Ch. 13.5], but the context considered here is different as we now have to face the peculiar issues related to the unconventional format of the S2C waveform, involving, for instance, a different mechanism through which the received signal replicas interfere with each other after the despreading/demodulation stage.

A further contribution of this paper is to propose and assess a synchronization technique for the joint recovery of carrier and clock references for each of the signal replicas processed by the receiver. Its accuracy is provided in terms of root-mean-square (RMS) synchronization errors.

A real-time hardware version of the modem, complete with synchronization functions, was implemented in the laboratory and its behavior was assessed over standard UWA channel emulators and compared to that exhibited by the traditional strongest-path-based scheme in terms of bit error rate (BER) versus signal-to-noise ratio (SNR). Moreover, the sensitivity of the multiple-branch receiver to residual Doppler distortion is assessed and compared to that exhibited by the single-branch scheme.

The paper is organized as follows. In Section II, we briefly review signal and channel models, while in Section III, we illustrate the modem architecture with emphasis on the multiple-branch receiver section. Section IV discusses the algorithms for channel estimation and carrier/timing synchronization. Section V defines conditions for path resolvability, provides details on how the received waveform is processed in the multiple-branch structure, and also describes the system hardware implementation. Section VI presents simulation setup and results. Conclusions are finally drawn in Section VII.

II. Signal and Channel Models

Now we briefly review the S2C signal format paralleling the presentation in [7], which the reader is referred to for further details. We assume information is transmitted in the form of data packets, each starting with a preamble of P known pilot symbols, to be employed for carrier and symbol synchronization/tracking, followed by a payload of D symbols. Letting T denote the symbol spacing, the packet length is $T_B = (P + D)T$. The number of packets and the instants for their transmission depend on both the amount of information to be transferred and the specific link protocols, and are not of interest for the paper scope.

Focusing then on a generic packet at the transmitter side, the signal at baseband, before spectral expansion and frequency upconversion, is a conventional linearly modulated waveform

$$s(t) = \sum_{i=0}^{P+D-1} a_i g(t - iT) \tag{1}$$

where

$$\mathbf{a} \triangleq [a_0, \ldots, a_{P+D-1}]^T = [p_0, \ldots, p_{P-1}, d_0, \ldots, d_{D-1}]^T$$

denotes the vector of (differentially encoded) quadrature phase-shift keying (QPSK) symbols in the packet, and $g(t)$ is a root-raised-cosine pulse with rolloff factor α. In particular, the pseudorandom sequence $\mathbf{p} \triangleq [p_0, \ldots, p_{P-1}]^T$ of pilot symbols is common to all packets, while the sequence $\mathbf{d} \triangleq [d_0, \ldots, d_{D-1}]^T$ represents a specific data segment.

After spectral spreading and frequency upconversion, the bandpass signal to be fed to the acoustic projector can be written as

$$x(t) = \Re\{s(t)c(t)\} \tag{2}$$

where $c(t)$ denotes a frequency-modulated carrier achieving both frequency conversion and bandwidth expansion, as follows:

$$c(t) = \exp\left\{j2\pi\left[f_L\tau(t) + m\tau^2(t)\right]\right\} \tag{3}$$

where $\tau(t)$ is a sawtooth-shaped periodic sweep function, with period T_{sw}

$$\tau(t) = t - \left\lfloor \frac{t}{T_{sw}} \right\rfloor T_{sw} \tag{4}$$

$\lfloor z \rfloor$ being the largest integer not exceeding z. In (3), f_L represents the lower limit of the frequency ramps, while $2m$ is the ramp slope. The instantaneous carrier frequency during a ramp is proportional to the derivative of the argument of the exponential in (3)

$$f_i(t) = f_L + 2m\left(t - \left\lfloor \frac{t}{T_{sw}} \right\rfloor T_{sw}\right). \tag{5}$$

It follows that the upper frequency limit is $f_H = f_L + 2mT_{sw}$. The limits f_L and f_H, along with the sweep interval T_{sw}, usually taken as an integer multiple of the symbol spacing, are key design parameters as they define the slope $2m = (f_H - f_L)/T_{sw}$ of the ramps and characterize the ability of the receiver to resolve the multipath channel structure (i.e., to separate the signal replicas arriving from the various paths).

After spreading and frequency upconversion, the signal bandwidth amounts to approximately $B \approx f_H - f_L$, i.e., it is expanded by a factor (spreading factor)

$$\mathcal{M} \triangleq \frac{f_H - f_L}{\frac{1+\alpha}{T}} \tag{6}$$

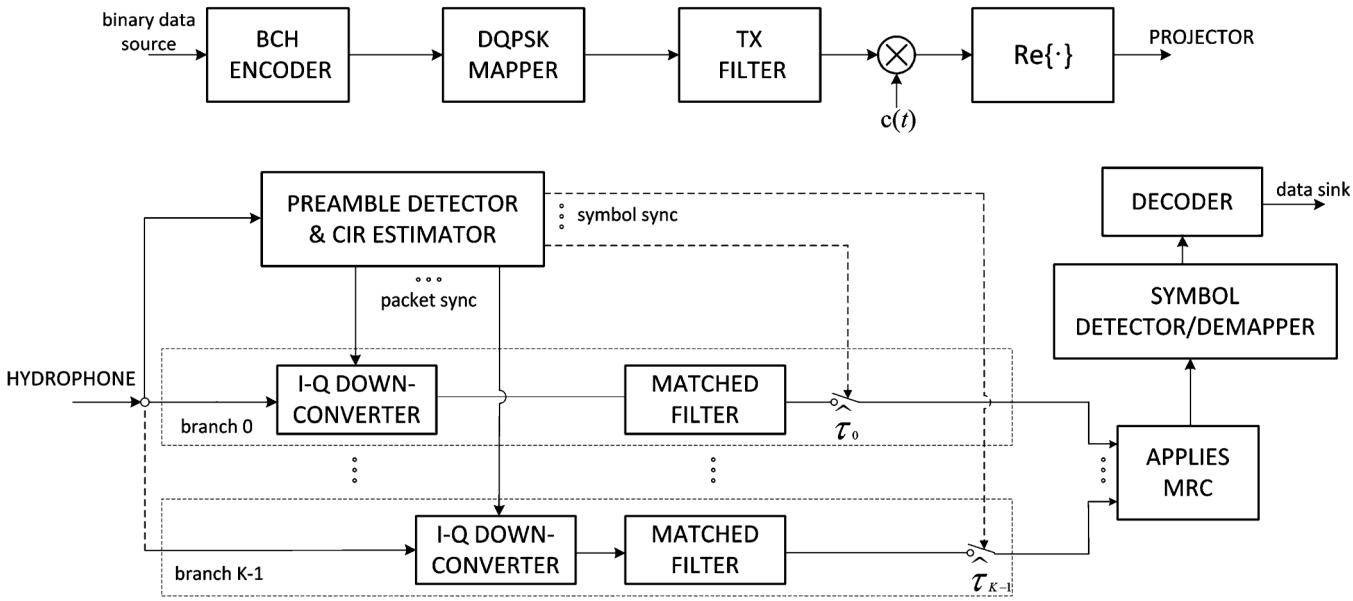

Fig. 1. Modem architecture.

with respect to a conventional narrowband signal, $\mathcal{M}$ usually being much greater than unity.

A general expression of the multipath time-varying UWA channel impulse response is as follows:

$$r_c(t, t_0) = \sum_{k=0}^{N_p(t_0)-1} h_k(t_0)\delta\left[t - t_0 - \tau_k(t_0)\right] \qquad (7)$$

where $N_p(t_0)$ is the number of (nonnegligible-level) paths and $h_k(t_0)$ and $\tau_k(t_0)$ are the (complex-valued) gain and delay of the kth path, respectively, all evaluated at the instant of application of the impulse $t = t_0$. In the following, we assume that the channel variations are negligible in a time span comparable to the packet length, so that the information about the channel parameters in (7), estimated from the packet preamble, can be considered reliable throughout the whole payload segment. This is not a severe constraint since transmission on the UWA link is normally preceded by a procedure of adjustment of the transmission parameters to the channel conditions. Accordingly, the dependence of the model in (7) on t_0 can be dropped and all channel parameters can be regarded as random variables (RVs) instead of random processes. Therefore, the received waveform can be written as

$$y(t) = \sum_{k=0}^{N_p-1} y_k(t) + w(t) \qquad (8)$$

where $w(t)$ is additive white Gaussian noise (AWGN) of double-sided spectral density $N_0/2$, accounting for both external and internal disturbance sources affecting the receiver, and $y_k(t)$ is the waveform received through the kth path, i.e., scaled by the coefficient h_k and delayed by τ_k

$$y_k(t) = \Re\left\{h_k s(t - \tau_k) c(t - \tau_k)\right\}. \qquad (9)$$

We observe that the main purpose of this paper is to propose a multiple-branch receiver architecture alternative to the schemes presented in [8] and to demonstrate that it may lead to a significant gain in power efficiency in comparison with the basic scheme in [7]. In this perspective, we felt it adequate to assume the relatively simple path model (9) and to limit the receiver functions to those strictly required to pursue the above goal. In particular, we decided not to tackle in detail the issues related to time variability and Doppler distortion, that in a practical receiver must be dealt with at an early stage of processing of the incoming packets. This approach is in line with that followed in [7]. However, in Section VI, we provide results about the sensitivity of multiple-branch and single-branch receivers to residual Doppler errors on each receiver branch.

III. Modem Architecture

A functional block diagram of the S2C modem is depicted in Fig. 1. The transmitter section consists of a standard S2C modulator similar to that discussed in [7]. The information bits are fed to a BCH encoder followed by a DQPSK symbol mapper. The resulting symbol sequence is used to build the data packet (function not detailed in the figure) that is passed through the shaping filter and finally applied to the S2C frequency upconverter.

The receiving section includes a block for preamble detection and channel impulse response (CIR) estimation, whose task is to identify, for each packet, the times of arrival of the preamble from the K strongest paths and also to estimate the (complex-valued) gains of these paths. This leads to the receiver architecture indicated in Fig. 1, wherein each of the K parallel branches is used to process the signal received from a single path. Specifically, with regard to the kth branch, the input is applied to an in-phase and quadrature converter which multiplies it by a replica of the S2C waveform synchronized with that received from the kth path. In this way, the signal spectrum relative to that path is despread and exactly converted to baseband, while subsequent matched filtering removes interference from the other paths provided that their spectra do not overlap

the "good" spectrum at baseband, i.e., their differential propagation delays with respect to the kth path are sufficiently large. The design criteria for this condition to hold true are discussed in Section V.

As the next step, the matched filter output is sampled at symbol rate at instants $iT + \hat{\tau}_k$, where $\hat{\tau}_k$ is an estimate of τ_k provided by the CIR estimator. Assuming exact intersymbol interference (ISI) cancellation, from (1), (8), and (9), the generic sample takes on the form

$$v_{k,i} = h_k a_i + w_{k,i}, \qquad i = 0, \ldots, D-1 \tag{10}$$

where the term $w_{k,i}$ denotes the noise sample generated from $w(t)$ in (8) after the above processing steps through the kth branch.

Finally, the K samples relevant to the symbol a_i are combined according to the maximal ratio combining (MRC) criterion [12, Ch. 13.4] before being fed to the symbol detector and the decoder. With regard to the MRC block, we observe that a sufficient condition for the noise terms $\{w_{k,i}\}_{k=0}^{K-1}$ to be mutually uncorrelated is that the differential delays between the various paths obey the same conditions allowing separation of the respective signal replicas, to be established in Section V. Indeed, the spectra of two incoming signal replicas can be separated by the despreader/demodulator on condition that their relative delay and the slope of the frequency ramps are sufficiently large. When this happens, the noise processes at the output of the matched filters on the respective receiver branches occur as well to be generated from the demodulation of frequentially nonoverlapping segments of the broadband input noise, and are therefore uncorrelated, this independently of the wideband noise spectral shape.

Finally, it is noted that when $K = 1$, the receiver structure reduces to that discussed in [7] where only the strongest path is processed.

IV. Timing and Channel Estimation

As mentioned earlier, the first operation to be accomplished at the receiver site is estimation of the timing of arrival of the signal replicas propagating along the channel paths. This permits to synchronize locally generated copies of the S2C waveform with those associated with the K strongest paths and then proceed to separate the signal replicas received from these paths. Another important related task is estimation of the complex-valued channel gains so as to identify the strongest paths and correctly apply the MRC technique.

Both the above operations are carried out by means of a correlator, as is now briefly outlined. Let $s_P(t)$ denote the baseband continuous-time version of the preamble separated from the payload, as follows:

$$s_P(t) = \sum_{i=0}^{P-1} p_i g(t - iT) \tag{11}$$

and also let

$$x_T(t) = s_P(t)c(t) \tag{12}$$

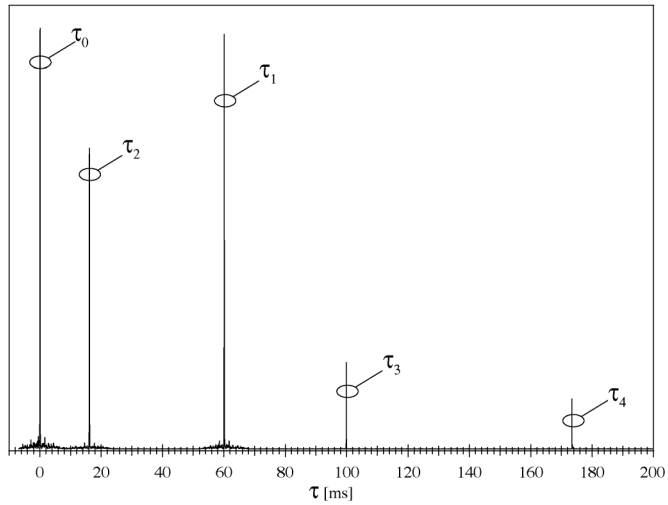

Fig. 2. Sample correlation function (square modulus). The vertical scale is arbitrary. The number of paths is $N_p = 5$, and the other system parameters are specified in Section VI.

denote the complex-valued bandpass version of the preamble incorporating both frequency upconversion and bandwidth expansion. It is noted from (2) that the real part of (12) represents the transmitted preamble.

Using for simplicity continuous-time notation, the task of the correlator is to calculate the inner product between the template function (12) and a newly received segment of the input waveform, and then take its squared modulus, as follows:

$$z(t) = |r(t)|^2, \qquad t \in \mathcal{T} \tag{13}$$

where

$$r(t) = \int_0^{T_P} y(t + \tau - T_P) x_T^*(\tau) d\tau, \tag{14}$$

$\mathcal{T}$ is a time interval in which the preamble is expected to be received and $T_P = PT$ is the preamble length. The receiver stores the functions (13) and (14) in memory along with the raw received waveform $y(t)$ for subsequent processing.

When path delays are sufficiently spaced from one another and the signal-to-noise-plus-interference ratio on the paths is high, the squared correlation $z(t)$ exhibits a definite peak in correspondence with each of the delays $\{\tau_k\}$. This can be verified observing that the width of the correlation peaks is approximately equal to the inverse of the bandwidth of the template waveform to be detected. Fig. 2 shows an example of such a function, obtained from the set of parameters specified in Section VI. Here the symbol spacing is 1.5 ms and the template signal bandwidth is approximately equal to the difference between the upper and lower limits of the frequency ramp, i.e., 16 kHz. Thus, the correlation peaks have a width in the order of 0.1 ms, which represents a measure of the delay resolution capability of the correlator. In the time scale of Fig. 2, covering several tens of symbols, and in comparison with typical values of differential delays (see Table II in Section VI), these peaks are very narrow and easily detectable at the operating SNRs.

More specifically, assuming for a moment that the receiver is driven by a single noiseless signal replica received from the kth

path [see (9)], it is found that (13) peaks at the instant $T_P + \tau_k$, and the corresponding value for the inner product (14) is

$$r(T_P + \tau_k) = \frac{E_{S_P}}{2} h_k \tag{15}$$

where $E_{S_P} = \int_0^{T_P} |s_P(\tau)|^2 d\tau$ is the energy of $s_P(t)$. From (15), it is seen that at the instant where the squared correlation peaks, the inner product yields a value proportional to the path gain h_k, while the squared peak level is proportional to $|h_k|^2$. Therefore, (14) provides all information necessary for path sorting, ramp synchronization, and implementation of the MRC detector.

Collecting the above, once correlation (13) has been calculated, a maximum search procedure must be initiated to obtain an estimate of the delay associated to each preamble replica arriving at the receiver. Of course, the procedure must be capable of detecting "good" correlation peaks against false peaks produced by noise and possibly by sidelobes associated to good peaks. This can be achieved through a simple approach consisting of the following steps. First, the noise level must be estimated by the receiver during the silent periods before transmissions or between the transmission of two consecutive messages. Knowledge of the noise level along with the correlator parameters allows to infer the noise-only statistics of the correlator output, and to fix a threshold λ yielding a desired tradeoff between false and missed detection probabilities, with reference to limit conditions characterized by the least operating SNRs, e.g., when the distance between terminals is at the limit of coverage. As the next step, the search algorithm looks for the peaks exceeding the threshold and tries to classify them according to their strength and differential delays. This operation is aimed at identifying the "best" paths, i.e., those with largest level and with sufficient delay from one another so as to be easily separable by the despreading/demodulation block. The algorithm starts by estimating the delay associated to the strongest replica (assumed relevant to the path of index zero), as follows:

$$\hat{\tau}_0 = \arg \max_{\substack{z(t)>\lambda \\ t\in\mathcal{T}}} z(t). \tag{16}$$

The delays associated to the other $N_p - 1$ paths of significant gain are identified by looking for the other local maxima of $z(t)$, using the following iterative approach:

$$\hat{\tau}_i = \arg \max_{\substack{z(t)>\lambda \\ t\in\mathcal{T} \\ t\notin\mathcal{I}_i}} z(t), \qquad i = 1, 2, \ldots, N_p - 1 \tag{17}$$

where $\mathcal{I}_i$ denotes a set of subintervals of $\mathcal{T}$ centered around the values of delay already identified through step $i-1$, that must be excluded from the search at the current step i, i.e.,

$$\mathcal{I}_i = \{(\hat{\tau}_0 - T_{\rm cor}, \hat{\tau}_0 + T_{\rm cor}) \cup \cdots \cup (\hat{\tau}_{i-1} - T_{\rm cor}, \hat{\tau}_{i-1} + T_{\rm cor})\}. \tag{18}$$

In this way, the N_p strongest paths are orderly identified along with their delays. However, problems may arise at this stage if the peaks are spaced too tightly, i.e., if the corresponding relative path delays are too close to one another. As noted earlier, the width of the correlation peaks is given approximately by the inverse of the template signal bandwidth. This provides a measure of the delay resolution capability of the correlator, inasmuch as peaks that are spaced less than this measure cannot be distinguished. A further aspect to be taken into account is the presence of sidelobes around the correlation peaks in (13), which for very strong signal level could exceed the threshold and be misdetected as additional independent peaks. To avoid the latter type of error, it is convenient that the length $2T_{\rm cor}$ of the windows centered on the correlation peaks be selected large enough to include a few sidelobes as well, at the cost of accepting a further slight degradation in the detector resolution properties. With reference to the set of parameters in the example of Section VI, the parameter $2T_{\rm cor}$ can be fixed at 1 ms (covering the main correlation lobe plus a few sidelobes on each side), which is still far smaller than the channel delay spread in a typical scenario.

When the above procedure of multiple path detection and classification is over, the receiver must select a number $K \leq N_p$ of paths to be processed in its K branches. A reasonable criterion is to select the strongest K paths, but some of these could be discarded at this stage if their differential delay is not sufficient to ensure adequate separation of their spectra after despreading/demodulation.

In addition to estimating the delay of the main usable paths of the UWA channel, the receiver must proceed to evaluate the relevant complex-valued path gains in view of their usage within the MRC block (see Fig. 1). As noted earlier, these gains are provided by (15) as a byproduct of the same correlation algorithm employed for path delay estimation.

V. Design Issues and Hardware Implementation

A. Conditions for Path Resolvability

Recalling the discussions in Sections II and III, for the K-branch receiver of Fig. 1 to work properly it is required that, for each branch, the signal spectrum converted to baseband does not collide with the spectra of the signal replicas being processed by the other branches. This allows the signal at baseband to be extracted by means of a simple (lowpass) matched filter. For these conditions to be met, it is necessary that the differential delays between all pairs of paths do not drop below a certain threshold. A further constraint is that the maximum differential delay must not exceed T_{sw} to avoid ambiguities in delay estimation.

More specifically, with no loss of generality, we can treat $\{\tau_k\}_{k=0}^{K-1}$ as differential delays with respect to τ_0, arranged in nondecreasing order, i.e., we set $\tau_0 = 0 \leq \tau_1 \leq \cdots \leq \tau_{K-1}$. Then, the constraints to be put on these differential delays are as follows (see also [7]):

$$\begin{cases} 2m\delta\tau_{\min} \geq \dfrac{1+\alpha}{T} \\ -2m\delta\tau_{\max} + f_H - f_L \geq \dfrac{1+\alpha}{T} \end{cases} \tag{19}$$

where

$$\delta\tau_{\min} = \min_{0\leq i,j\leq K-1} |\tau_i - \tau_j|, \qquad i \neq j$$

is the minimum (absolute) differential path delay and

$$\delta\tau_{\max} = \max_{0\leq i,j\leq K-1} |\tau_i - \tau_j| = \tau_{K-1}, \qquad i \neq j$$

is the maximum differential path delay, or channel time dispersion. Using (6) in (19) yields

$$\begin{cases} T_{sw} \leq \mathcal{M}\delta\tau_{\min} \\ T_{sw} \geq \dfrac{\mathcal{M}}{\mathcal{M}-1}\delta\tau_{\max}. \end{cases} \tag{20}$$

For the existence of values of T_{sw} satisfying both above conditions it is required that

$$1 \leq \frac{\delta\tau_{\max}}{\delta\tau_{\min}} \leq \mathcal{M} - 1. \tag{21}$$

The first inequality in (20) sets a lower limit to the absolute difference between the arrival times of any two signal replicas. When the difference exceeds this limit, the receiver is able to accurately resolve the channel multipath structure. Otherwise, when two received replicas are spaced too closely, after despreading they will overlap in the frequency domain, thus preventing their exact separation. On the other hand, the second inequality in (20) puts an upper limit to the differential path delays, approximately equal to T_{sw} when $\mathcal{M}$ is large. Actually, a signal replica delayed more than T_{sw} with respect to the one traveling on the shortest path would generate a timing estimate affected by an ambiguity equal to an integer multiple of T_{sw} that could not be detected and recovered, with a negative impact on the MRC algorithm.

Fig. 3 shows a realization of power spectral density of the received signal after downconversion/despreading for a five-ray scenario, assuming that downconversion is carried out for the strongest path. Transmission parameters are the same as in the example of Fig. 2. Inspection of the figure reveals that in this case all paths are resolvable (apart from a marginal overlap of two small spectral replicas located midway on the frequency axis), and in particular the useful signal (whose spectrum lies around the origin) can be recovered by means of a lowpass filter, without (or with negligible) interference from the other replicas. The latter signal components, carrying useful power as well, can in turn be extracted by multiplication of the received waveform by properly delayed replicas of $c(t)$ followed by lowpass filtering, as illustrated in Section III. More specifically, from Fig. 3, it is seen that, in addition to the signal spectrum centered on the origin, there are eight other spectral replicas generated by the paths with delays τ_1, τ_2, τ_3, and τ_4. Indeed, recalling (19) and the ensuing discussion, the kth path gives rise to two spectral components (identified with the indices k_1 and k_2 in Fig. 3), centered around the frequencies $2m\tau_k$ and $f_H - f_L - 2m\tau_k$, $k = 1, 2, 3, 4$, respectively. The actual values of these frequencies are specified in Table II.

B. Merging Branch Outputs

As mentioned earlier, the receiver is made up of K parallel branches, designed to jointly extract and elaborate up to K replicas of the signal received from the multipath UWA channel. The kth branch proceeds to despread/downconvert the received signal through its multiplication by $c(t - \hat{\tau}_k)$, as described in Section IV, where $\hat{\tau}_k$ is an estimate of the propagation delay on the kth path. Assuming error-free delay estimates and exact resolvability of the signal on all branches according to the criteria identified in Section V-A, the sampled

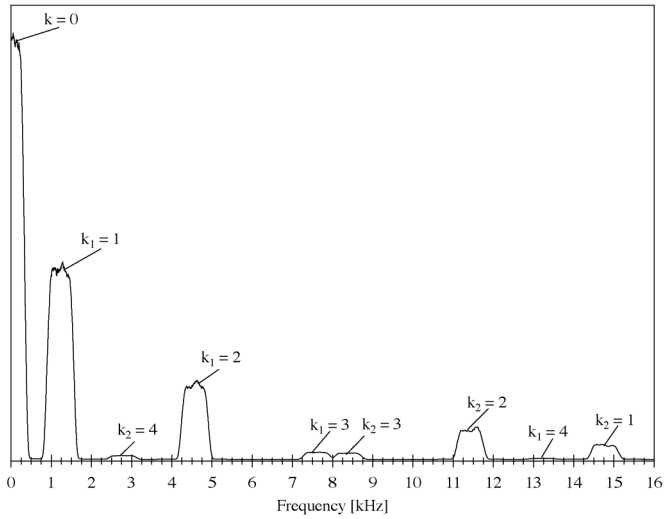

Fig. 3. Power spectral density of the received signal after downconversion/despreading of the strongest path ($k = 0$). The vertical scale is arbitrary. The system parameters are the same as in Fig. 2 and are specified in Section VI.

output of the kth branch takes on the form of (10). All branch outputs are then combined according to the MRC optimality criterion, as follows:

$$q_i = \sum_{k=0}^{K-1} \hat{h}_k^* v_{k,i} \tag{22}$$

where $\hat{h}_k$ is the estimate of the kth path gain. The sequence of samples (22) is then fed to the decoder/data detector for further processing.

As mentioned in the Introduction, the above approach is reminiscent of that employed in the so-called "rake receiver" proposed for conventional DS–SS modulations [12, Ch. 13.5], even though the context here is different from that envisaged in typical electromagnetic wireless links. Actually the mechanism generating mutual interference between two replicas of the signal arriving from different paths is not the same in DS–SS and S2C. In the case of a DS–SS system, the spreading code is normally designed so as to be self-uncorrelated, i.e., it is sufficient to shift two signal replicas by just one code chip, and the mutual interference, after the despreading and matched filtering stages, is reduced by approximately the spreading factor. This interference does not decrease further if the delay between replicas grows. In the frequency domain, the presence of the interfering signal results in a small increase in the (approximately white) spectral level of noise and interference. Conversely, in the case of an S2C system, achievement of orthogonality between the signal replicas relies on the ability of the frequency ramp to separate their spectra, and in turn this depends jointly on the relative time delay between the paths and on the slope of the ramp itself. It follows that, due to the presence of the out-of-band ripple in the baseband signal spectrum and the rolloff region (with sidelobes as well) of the matched filter responses, the amount of mutual interference depends on the frequency-domain distance between the spectra after despreading/demodulation: the larger this distance, i.e., the larger the relative delay between the two replicas and/or the ramp slope, the lower will be the interference, and *vice versa*.

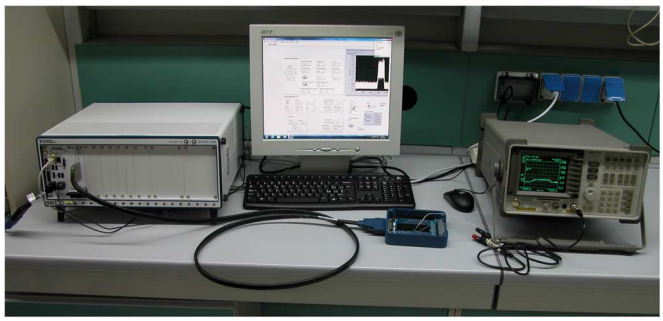

Fig. 4. Test bench: NI chassis hosting controller and data acquisition board, PC with LabView, spectrum analyzer.

Furthermore, the demodulation process in the S2C system is affected by occasional frequency jumps of the interfering replicas (see, e.g., [7, Fig. 4]), representing a specific form of disturbance that is absent in the DS–SS context.

However, assuming the K paths can be resolved, we can borrow from the rake receiver the expression of the asymptotic gain in power efficiency

$$G_R = \frac{\sum_{k=0}^{K-1} E\left\{|h_k|^2\right\}}{E\left\{|h_0|^2\right\}} \tag{23}$$

where $E\{\cdot\}$ denotes statistical expectation that can be achieved with respect to the receiver operating on the single path of gain h_0. This result has been confirmed by simulations (Section VI).

C. Hardware Implementation

Now we briefly present our real-time implementation of the modem architecture discussed in the foregoing sections. The testbed is based on National Instruments (NI) hardware [13], controlled by LabView (LV) applications. Specifically, we used the chassis NI PXIe-1085 equipped with the controller NI PXIe-8135 and the data acquisition board NI PXIe-6361. The entire system is controlled by an LV-based code that exploits the built-in functions provided in the RF Communications toolkit. The transmitter and receiver sections of the modem were both entirely implemented in hardware. Fig. 4 shows the complete test bench used for the modem implementation, composed by the controller board within the chassis, a PC running *ad hoc* LV application software and also a spectrum analyzer.

VI. Simulation Results

The transmission architecture in Fig. 1 was implemented and assessed using the hardware testbed described in Section V-C, in conjunction with the software package Bellhop [14], a popular open-source simulator of the UWA environment. In particular, this simulator permits to identify both the coherent and noncoherent channel profile, i.e., for a fixed number of paths, their complex-valued (modulus and phase) gains, or simply their RMS values, versus propagation delay, to be associated to an arbitrary UWA operating scenario.

For simplicity, in the following, we limit our consideration to a single scenario, characterized by shallow water (130 m) with sound-speed profile versus depth typical of the summer period and plotted in the left section of Fig. 5. The values assumed for the main geometric and acoustic parameters of the UWA scenario are summarized in Table I, while Fig. 6 provides a pictorial

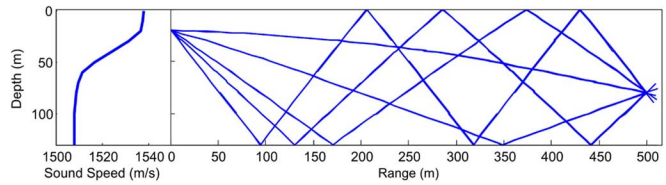

Fig. 5. Ray tracing produced by Bellhop.

TABLE I
Main Acoustic and Geometric Parameters of the UWA Scenario

TX depth	20 m
RX depth	80 m
Horizontal distance	500 m
Bottom type	gravel
Bottom depth	130 m
Surface (for reflection properties only)	sea state 0
Sound-speed profile	see Fig. 5
Center frequency	26 kHz
TX launching angles	0° : +180°

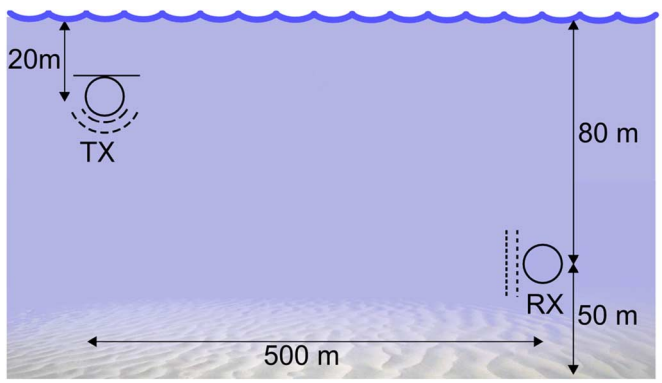

Fig. 6. Geometry of the UWA link.

representation of the link geometry. In the right section of Fig. 5, we also show the curves produced by the Bellhop ray tracing tool that can be used to calculate the channel power-delay profile.

Using the ambient parameters of Table I and the Bellhop tool it is possible to create a multipath propagation model with a fixed number of paths. Here we limit our attention to the first five strongest paths (direct plus four experiencing single or multiple reflections from the surface and/or the bottom). We note that simulations carried out with a larger number of paths (up to 15) showed negligible deviations from the results obtained with five paths.

With reference to the link geometry of Fig. 6, the resulting power-delay profile is visible in Table II. From Bellhop, it can be seen that the power associated to these five paths amounts to more than 96% of the total received power in the above scenario. For simplicity, the powers associated to the paths in Table II are normalized so that they sum up to unity. Moreover, the attenuation over the direct path is assumed deterministic, while the other path coefficients are modeled as independent identically distributed circular Gaussian variables with zero mean and normalized powers given in column 2, rows 1–4 of Table II. As to the spectral shifts specified in the last column of Table II, their meaning is defined at the end of Section V-A.

TABLE II
POWER-DELAY PROFILE FOR THE FIVE-PATH CHANNEL

Path	Normalized power	Relative delay [ms]	Spectral shifts [kHz]
0	0.388	0	0
1	0.380	16.11	1.227, 14.773
2	0.198	60.04	4.575, 11.425
3	0.025	99.84	7.607, 8.393
4	0.009	173.49	13.218, 2.782

TABLE III
PHYSICAL LAYER PARAMETERS

T_{sw}	210 ms
T_P	$2T_{sw}$
$\mathcal{M}$	20
α	0.2
Symbol spacing	1.5 ms
Payload length	1024 symbols
Modulation	DQPSK
Codec	uncoded, BCH (1431, 2047)
Data rate (payload)	1333 bit/s, 931 bit/s
f_L	18 kHz
f_H	34 kHz
T_{cor}	$8/(f_H - f_L)$

Finally, the physical layer communication parameters used throughout the trials are specified in Table III.

The five-path channel defined by Table II was implemented on the NI testbed using the previously described model. In particular, for every channel realization, the receiver input is generated by combining five versions of the transmitted waveform, each with a different delay and attenuation according to the statistics specified in Table II and remarks thereof. The SNR, defined as the ratio between the average energy per symbol received through all considered paths to the noise power spectral density, is varied by injecting AWGN with variable spectral level.

Specifically, our purpose here is to compare the performance of the conventional receiver in [7] with that achievable by the multiple-branch parallel structure in Fig. 1 where we assume $K = 3$. This seems a reasonable choice to achieve a substantial gain without exceeding in receiver complexity. To this aim, we observe that, from (23) and from the values in the first three rows of Table II, corresponding to the three strongest paths, the maximum expected gain of the three-branch receiver is $G_R \approx 3.96$ dB. This margin seems to be actually achievable in view of the fact that the parameters $\delta\tau_{\min}$ and $\delta\tau_{\max}$ do largely satisfy condition (21): $\delta\tau_{\max}/\delta\tau_{\min} \approx 10.77 \ll \mathcal{M} - 1$. Further to be noted, since the three considered signal components can be exactly separated by the receiver, the relative phase rotations associated to the path gains are immaterial, and the receiver performance is only affected by the noncoherent power-delay profile.

Fig. 7 shows plots of the BER versus SNR obtained for uncoded transmission assuming error-free channel estimation and carrier/symbol synchronization in all receiver branches. The plots were obtained from Monte Carlo simulations over a large number of channel and symbol realizations. The two curves of BER are relevant to the conventional single-branch receiver $(K = 1)$ and to the three-branch receiver $(K = 3)$. It is observed that the latter scheme asymptotically outperforms the former by around 3.3 dB, very close to the asymptotic gain G_R.

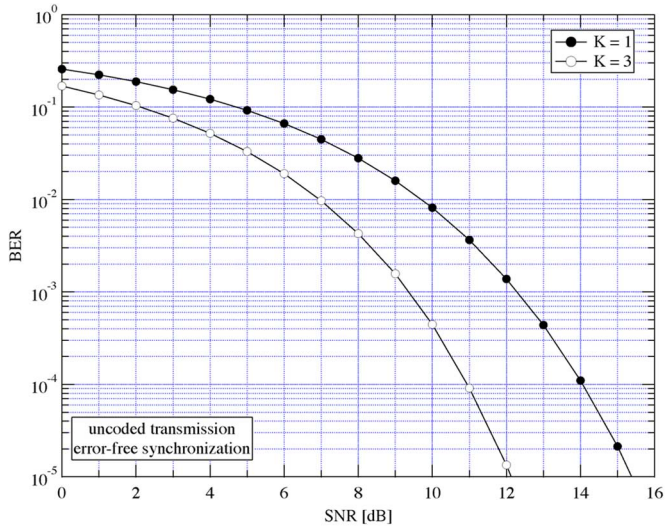

Fig. 7. BER versus SNR, uncoded transmission, five-path channel, single-branch receiver, and three-branch receiver.

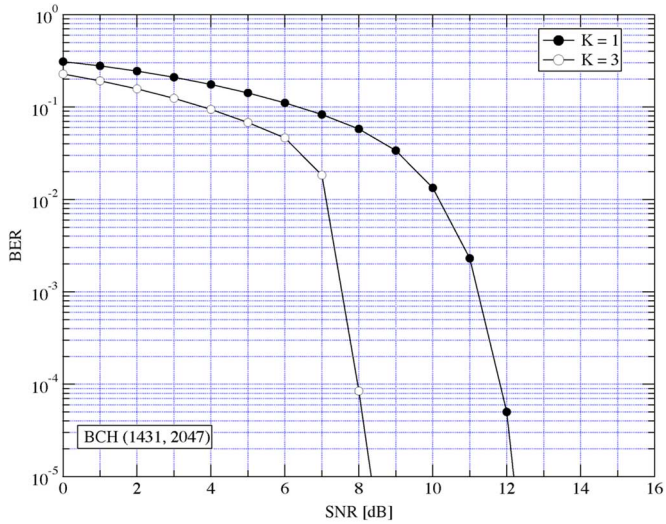

Fig. 8. BER versus SNR, coded transmission, five-path channel, single-branch receiver, and three-branch receiver.

Fig. 8 shows curves of BER versus SNR for the same single-branch and three-branch receivers, obtained in the more realistic situation in which the transmitter employs a BCH encoder, with coding rate $r = 1431/2047 \simeq 0.7$, and the receiver actually incorporates the channel estimator and the carrier/symbol synchronizer discussed in Section IV. The benefit in terms of SNR gain provided by the multiple-branch receiving structure is still apparent. For example, at BER $= 10^{-5}$, this gain is around the asymptotic value of 4 dB, while the advantage provided by the BCH encoder with respect to uncoded transmission (curves in Fig. 7) is more than 3 dB.

In passing, we also assessed the receiver behavior with the MRC replaced by the simpler scheme known as equal gain combiner (EGC) [12, Ch. 13.4] where the combination rule is as in (2) with $\hat{h}_k^*$ replaced by $\hat{h}_k^*/|\hat{h}_k|$. This led to a negligible performance degradation (results not shown) with respect to MRC in the scenario of Table II, as is to be expected when there is no definite predominant path, as in links where the transmit and receive transducers are weakly directive, and thus the strength of the surface-reflected (and possibly bottom-reflected) path is comparable to that of the direct path. Conversely, when the path levels are strongly unbalanced, the MRC approach is likely to exhibit an edge.

It is now appropriate to briefly discuss the performance of the path delay estimator which, as we have seen, plays an important role for synchronization of the despreading waveforms in the multiple-branch receiver, as well as for symbol timing recovery.

As discussed in Section IV, the delay is estimated by determining the instant at which the squared correlation (13) exhibits a peak. Of course, a necessary condition to get an accurate estimate is that the sampling rate at the receiver input be adequately high. The results presented here are obtained using a sampling rate of 100 kHz, a condition which, recalling the data of Table III, corresponds to taking 100 samples per symbol and slightly more than three samples per cycle at the highest instantaneous frequency f_H of the waveform $c(t)$. In addition, to further improve the accuracy of the above estimator, we resorted to a parabolic interpolator operating on the highest sample of the squared correlation and on the adjacent two. This scheme was considered satisfactory insofar as a further increase of the sampling rate was observed not to entail any additional gain in terms of root-mean-square estimation error (RMSEE).

Fig. 9 shows plots of RMSEE affecting the delay estimates for the three strongest paths of the five-path scenario defined by Tables I–III as a function of SNR. As expected, the lowest curve is the one relevant to the strongest (direct) path ($k = 0$) while the other two curves, relative to paths experiencing a single ($k = 1$) or a double ($k = 2$) reflection, are somewhat shifted versions of the former along the SNR axis, where the shifts are to be ascribed to the different (statistically smaller) path gains. Also to be noted, when the SNR grows, all curves do not decrease indefinitely, but rather they tend asymptotically to different constant (floor) values. This behavior can be explained observing that even though the five signal replicas are sufficiently shifted from one another as to be substantially uncorrelated, nevertheless they exert a mutual irreducible disturbance whose impact is felt even when the noise vanishes. Accordingly, the different floor levels are related to the different values of signal-to-mutual-interference ratio existing between the signal replicas.

Furthermore, we found that the delay estimates are substantially unbiased for all paths, and this holds true in general provided that the correlation peaks are well separated from one another, i.e., when conditions (21) are met.

We also assessed the sensitivity of the data detector to residual errors after estimation and compensation of the Doppler-induced distortion on each receiver branch. Indeed, in the presence of relative motion between the transmitter and the receiver, the signal replicas received from the channel paths are compressed or expanded in time by the factors $b_k \triangleq \nu_k/c_s$,

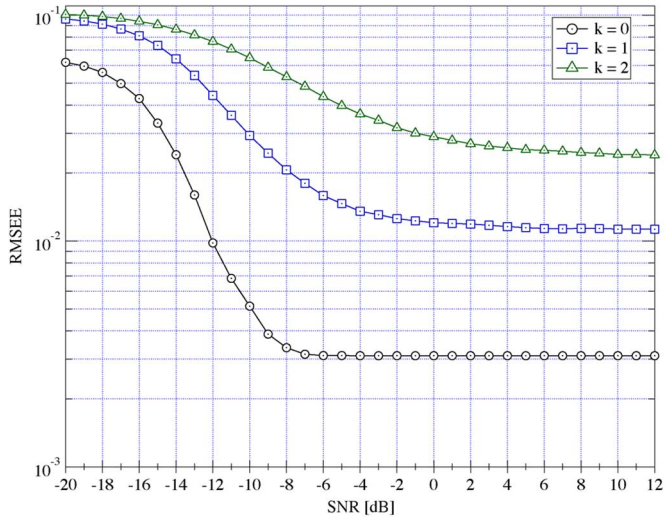

Fig. 9. RMSEE versus SNR, five-path channel, delay estimate for $k = 0, 1, 2$.

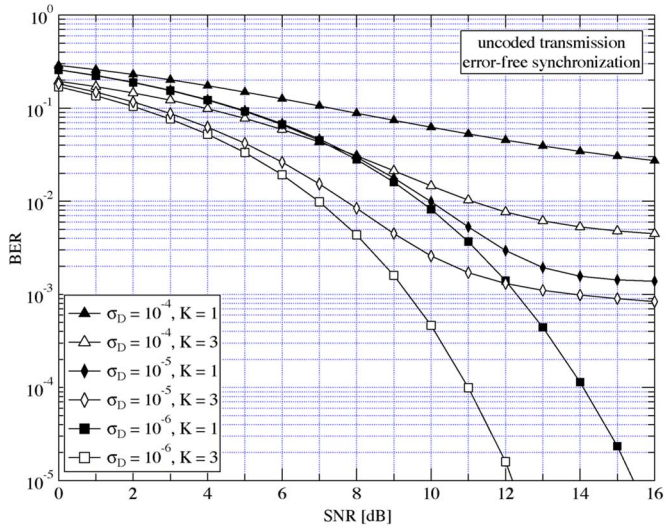

Fig. 10. BER versus SNR with residual Doppler distortion, uncoded transmission, five-path channel, single-branch receiver, and three-branch receiver.

$k = 1, \ldots, K$, where ν_k is the relative speed between the two terminals, and c_s is the sound speed. We note that 1) this distortion cannot be merely regarded as a frequency shift, in view of the large relative bandwidth occupied by the S2C waveform, entailing different Doppler shifts at the band edges; and 2) each path undergoes a specific distortion depending on its angle of arrival at the receiver. As noted at the end of Section II, when the above effects cannot be neglected, the receiver must incorporate a block for estimation of the factors b_k and cancellation of the Doppler distortion from each receiver branch. Here we do not focus on any specific algorithm for estimation/cancellation of the Doppler distortion, and limit ourselves to evaluate the sensitivity of the receiver BER to errors in the estimation of the b_k's. Our aim is to provide a measure of the errors the receiver can tolerate with negligible performance loss and also to compare the behavior of the multiple-branch receiver versus the single-branch receiver to this specific type of channel impairment. To proceed we let ϵ_k denote the error in the estimation (and subsequent compensation) of b_k for the kth receiver branch, and model the quantities ϵ_k, $k = 1, \ldots, K$, as independent zero-mean Gaussian RVs with equal variance σ_D^2.

In Fig. 10, we provide some results for the uncoded case, in the form of BER curves versus SNR obtained in the same conditions as Fig. 7, except for the presence of the residual Doppler errors ϵ_k on the receiver branches. Similar results were observed for coded transmission. Inspection of the figure reveals that these errors affect the multiple-branch and single-branch receivers approximately in the same way. Specifically, we note that: 1) the impact of residual Doppler distortion is negligible provided that σ_D is around 10^{-6} or smaller; 2) larger values of σ_D, say $\sigma_D = 10^{-5}$ or $\sigma_D = 10^{-4}$, progressively degrade the receiver performance and introduce a floor in the BER curves; and 3) in any case, the multiple-branch receiver exhibits a significant edge over the single-branch structure for a given σ_D.

VII. Conclusion

We have proposed and assessed an alternative implementation of a receiver for S2C transmissions over time-dispersive UWA channels, based on a multiple-branch parallel architecture. Each branch has the task to extract and process the signal received from one of the paths, and the outputs of the branches are finally combined together in an optimal way. We have shown that the above structure is capable of significantly improving the system power efficiency with respect to the classical single-path-based S2C receiver. In particular, we have identified conditions allowing the signal replicas from the various paths to be exactly separated. A real-time version of the system has been implemented on a hardware testbed, and its performance has been assessed in the laboratory using typical UWA channel models. For the common situation where in addition to the direct path there are also a few single- or double-bounce reflected paths of nonnegligible level, we have shown that it is possible to achieve power gains of a few decibels in comparison with the single-path receiver. We also discussed an algorithm for synchronization of the despreading signal and for symbol timing recovery, and analyzed its impact on the receiver performance. Finally, we assessed the sensitivity of the multiple-branch receiver to residual Doppler distortion, showing that it still provides a significant margin with respect to the single-branch structure.

References

[1] D. B. Kilfoyle and A. B. Baggeroer, "The state of the art in underwater acoustic telemetry," *IEEE J. Ocean. Eng.*, vol. 25, no. 1, pp. 4–27, Jan. 2000.

[2] E. M. Sozer, M. Stojanovic, and J. G. Proakis, "Underwater acoustic networks," *IEEE J. Ocean. Eng.*, vol. 25, no. 1, pp. 72–83, Jan. 2000.

[3] M. Stojanovic and J. Preisig, "Underwater acoustic communication channels: Propagation models and statistical characterization," *IEEE Commun. Mag.*, vol. 47, no. 1, pp. 84–89, Jan. 2009.

[4] P. A. van Walree, "Propagation and scattering effects in underwater acoustic communication channels," *IEEE J. Ocean. Eng.*, vol. 38, no. 4, pp. 614–631, Oct. 2013.

[5] M. Stojanovic, J. A. Catipovic, and J. G. Proakis, "Phase-coherent digital communications for underwater acoustic channels," *IEEE J. Ocean. Eng.*, vol. 19, no. 1, pp. 100–111, Jan. 1994.

[6] S. Zhou and Z. Wang, *OFDM for Underwater Acoustic Communications*. New York, NY, USA: Wiley, 2014.

[7] K. G. Kebkal and R. Bannasch, "Sweep-spread carrier for underwater communication over acoustic channels with strong multipath propagation," *J. Acoust. Soc. Amer.*, vol. 112, no. 5, pp. 2043–2052, Nov. 2002.

[8] R. Bannasch and K. G. Kebkal, "Method and devices for transmitting and receiving information," U.S. Patent 6,985,749 B2, Jan. 2006.

[9] K. G. Kebkal, A. K. Kebkal, and G. A. Ermolin, "Mathematic and experimental evaluation of phase errors when receiving hydro-acoustic PSK-signals with sweep-spread carrier in reverberant underwater environments," in *Proc. MTS/IEEE OCEANS Conf.*, Bergen, Jun. 10–13, 2013, DOI: 10.1109/OCEANS-Bergen.2013.6608155.

[10] K. G. Kebkal, V. K. Kebkal, O. G. Kebkal, and R. Petroccia, "Clock synchronization in underwater acoustic networks during payload data exchange," in *Proc. 2nd Int. Conf. Exhibit. Underwater Acoust.*, Rhodes, Greece, Jun. 22–27, 2014, pp. 1181–1190.

[11] K. G. Kebkal, A. G. Kebkal, and V. K. Kebkal, "Synchronization tools of acoustic communication devices in control of underwater sensors, distributed antennas, autonomous underwater vehicles," in *Gyroscopy and Navigation*. Austin, TX, USA: Pleiades Publishing, 2014, vol. 5, pp. 222–230.

[12] J. G. Proakis and M. Salehi, *Digital Communications*, 5th ed. New York, NY, USA: McGraw-Hill, 2007.

[13] National Instruments [Online]. Available: http://www.ni.com/

[14] Ocean Acoustics Library [Online]. Available: http://oalib.hlsresearch.com/

Leonardo Marchetti received the M.Sc. degree in telecommunications engineering and the Ph.D. degree in information engineering from the University of Pisa, Pisa, Italy, in 2010 and 2015, respectively.

From 2011 to 2014, he was with the Department of Information Engineering, University of Pisa, first as a CNIT Research Fellow and then as a Ph.D. student. Since 2015, he has been with Intermarine S.p.A., Sarzana SP, Italy, as a Combat System Manager of the Production Department. His research interests focused on the area of multicarrier multiantenna wireless communication systems, and underwater communication systems.

Ruggero Reggiannini received the Dr.Ing. degree in electronics engineering from the University of Pisa, Pisa, Italy, in 1978.

From 1978 to 1983, he was engaged in the design and development of underwater acoustic systems. Since 1984, he has been with the Department of Information Engineering, University of Pisa, where he is currently Full Professor of Radio Communications. He is the author of several scientific papers. He has participated in several projects with private and public organizations.

Dr. Reggiannini has served as editor for the IEEE Transactions on Communications.

Soft Symbol Decoding in Sweep-Spread-Carrier Underwater Acoustic Communications: A Novel Variational Bayesian Algorithm and its Analysis

Arunkumar K.P. and Chandra R. Murthy

***Abstract*—Sweep spread carrier (S2C) based underwater acoustic (UWA) communications is a practically attractive but less explored modulation scheme in the published literature. In this paper, we present a rigorous treatment of the S2C communication receiver design and propose a data detection scheme that can handle challenging UWA channels. State-of-the-art S2C receivers based on the gradient heterodyne processing are only effective when the path delay and Doppler spread are moderate. We develop a new variational soft symbol decoding (VSSD) algorithm based on the principle of variational Bayes' inference for a general linear channel model. In channels with moderate delay and Doppler spreads, we show that the VSSD algorithm is equivalent to the existing gradient heterodyne receivers for S2C communications. We apply the VSSD algorithm to the i.i.d. Gaussian multiple-input multiple-output channel and show, through numerical simulations, that it far outperforms the minimum mean squared error (MMSE) data detection. We illustrate the dramatic improvement in the performance of the VSSD based S2C receiver in two different models of simulated UWA channels and two contrasting measured UWA environments publicly available in the WATERMARK channel dataset. The proposed VSSD algorithm recovers data symbols at a signal-to-noise ratio (SNR) which is at least 10 dB (8 dB) lower than the MMSE decoder for uncoded (rate 2/3 LDPC coded) communications over UWA channels where the existing receivers either fail completely or must compromise on the data rate to maintain the bit error rate (BER) performance.**

***Index Terms*—Underwater acoustic communications, sweep spread carrier communication, variational Bayes'.**

I. INTRODUCTION

Undersea exploration and monitoring presents vast opportunities and challenges alike – but a major hurdle to such missions arises from the difficulties in communicating underwater over long distances. Severe attenuation in the marine medium limits the range of electromagnetic, optical and magnetic induction based communications to just a few meters, leaving acoustic communications as the *de facto* means for wireless data transfer across tens of kilometers [2]–[4]. All the same, underwater acoustic (UWA) channels are by far the most difficult media for communication. They present a serious bottleneck in marine data networks due to limited data rate and large power demand. In particular, the data rates are limited by large delay spreads and path-dependent Doppler shifts. Multipath propagation of sound results in a delay spread in the order of tens of milliseconds [5] and time variations cause path-dependent Doppler shifts that are non-uniform over the bandwidth of the acoustic signal. Also, the communication nodes in an underwater sensor network are usually battery operated, and are therefore highly constrained on the amount of transmission power. High performance receivers, that recover data symbols at a low signal-to-noise ratio, are highly desirable in these applications.

Sweep spread carrier (S2C) communications [6] is inspired by the chirp, whistle and song type signaling used by dolphins and whales to communicate over long distances [7]. It uses linear frequency modulated (LFM) waveforms as carriers of digital data. The S2C transmission waveform, modulated by unimodular signal constellations such as quadrature phase shift keying (QPSK), has an ideal peak-to-average power ratio (PAPR). The technique is therefore battery friendly and implemented in a wide range of full-duplex commercial acoustic modems that are used in underwater sensor networks comprising autonomous underwater vehicles (AUVs), autonomous surface vehicles (ASVs), and moored underwater sensor nodes [8]–[11]. Secure, reliable and covert communications, with a low probability of intercept, is rendered possible due to use of high bandwidth coded chirp carriers whose exact pattern is known only to the transmitter and designated receiver. The details of the S2C transmitter and receiver side processing, performance analysis, and experimental results can be found in [12]–[16]. Despite its practical merits, success with real world deployment, and commercialization, relatively few published works such as [17] have explored and developed S2C communication further. In this paper, we present a rigorous treatment of the S2C design principles, and propose an improved S2C receiver that can handle challenging UWA channels.

The S2C receiver in [6] extracts only the copy of a symbol arriving along the direct path. As a consequence, the part of the transmitted symbol energy arriving along paths other than the direct path is ignored. In [17], the authors use a maximum ratio combiner (MRC), which improves the performance of an S2C receiver by leveraging multipath diversity. The receiver in [17] performs well only when: (a) the ratio of the maximum delay spread to minimum differential delay among path arrivals is below a certain value, and (b) the Doppler spread is small. If either condition is violated, the intersymbol interference (ISI) cancellation becomes imperfect and MRC becomes suboptimal and ineffective.

The authors in [6] and [17] did not consider the effect

Arunkumar K. P. is with the Naval Physical Oceanographic Laboratory, Kochi 682 021, India (e-mail: arunkumar@npol.drdo.in). This work was carried out as part of the PhD program at Indian Institute of Science, Bangalore. Chandra R. Murthy is with the Dept. of ECE, Indian Institute of Science, Bangalore 560 012, India (e-mail: cmurthy@iisc.ac.in). A part of this work was published in [1].

of Doppler. Doppler due to relative motion between the source and receiver manifests as dilation/compression of the transmitted waveform. The effect of Doppler in underwater acoustic communications cannot be modeled as a frequency shift unless the waveform has a small time-bandwidth product. For large time-bandwidth product waveforms, typical of S2C communications, even for small relative speeds (comparable to $c/2\gamma$, where c is the speed of sound in water and γ is the time-bandwidth product of the transmitted signal), the underwater channel is best modeled as a wideband delay-scale channel [18]–[20]. In this paper, we consider an S2C communication system similar to [6] and [17] but for the more general underwater channel model that includes the time-scaling effect of Doppler on the transmitted waveform.

Previous studies on UWA communications have considered the MMSE equalizer for (hard) data symbol detection or joint channel estimation and data detection in orthogonal frequency division multiplex (OFDM) and code division multiple access (CDMA) based communications [21]–[25]. However, in coded communications, it is more important to estimate the soft symbols rather than perform hard symbol decision [26]. The variational Bayes' (VB) inference is a promising approach to obtain soft symbol estimates because, by design, it directly infers the posterior distributions of the transmitted data symbols. However, to the best of our knowledge, other than our initial work in the area [1], [27], [28], VB based soft symbol estimation has not been explored in the literature.

In this paper, we present a new mathematical framework for S2C communications. Based on this, we develop a new decoder that uses the principle of variational Bayes' inference to determine the soft symbol estimates in harsh UWA channel environments. Our specific contributions are:

1) We present a mathematical framework for S2C data detection in doubly-spread UWA channels.
2) We show that the S2C receivers in [6] and [17] closely approximate the minimum mean squared error (MMSE) decoder for the AWGN channel and moderately delay spread UWA channels with well resolved path delays.
3) Previous works considered benign channels, but in practice the channel is rarely benign. We theoretically analyze the limitations of the existing S2C receivers in highly spread UWA channels and elicit the need to consider better receivers such as the MMSE receiver designed for the system model in this paper.
4) In coded communications, it is required to obtain good soft-symbol estimates, which the previous S2C receivers do not consider. Using the VB inference approach, we derive a new iterative log-likelihood ratio (LLR) based soft symbol decoding receiver.
5) We show that the fixed point iterations for LLR based soft symbol decoding converge to a local optimum in the general case, and to a global optimum for orthogonal channel matrices whose important special cases are the AWGN and Rayleigh channels. Specifically, in AWGN and Rayleigh channels, we show that the proposed variational soft symbol decoder (VSSD) is a maximum-likelihood (ML) decoder and converges in a single iteration.
6) Through extensive numerical studies, we demonstrate the strong performance of the VSSD in harsh simulated channels where existing S2C receivers fail completely. For the WATERMARK channel dataset, we develop a suitable baseband measurement model for the S2C system and present the superior performance of the proposed decoder in two contrasting real world channels.

We develop the system model in Section II. In Section III, we derive the existing S2C receivers as specialized MMSE symbol decoders and elicit the limitations of these receivers in Section IV. In Section V, we present improved S2C receivers – the MMSE decoder and the new VSSD – that can handle harsh channel conditions. We present the results of our numerical studies in Section VI and conclude in Section VII.

II. SYSTEM MODEL

Consider an S2C system as in [6] and [17]. At the transmitter side, the carrier waveform is a succession of linear frequency modulated chirp pulses, each swept from a lower frequency limit f_L to an upper frequency limit f_H over a sweep duration T_{sw}, given by:

$$c(t) = e^{j\phi(t)},\ 0 \le t \le T_c, \tag{1}$$

where

$$\phi(t) \triangleq 2\pi \left(f_L t_r(t) + m_c t_r^2(t) \right) \tag{2}$$

is the time varying phase of the carrier waveform, with $t_r(t) = t - \left\lfloor \frac{t}{T_{\text{sw}}} \right\rfloor T_{\text{sw}}$ being the periodic ramp function having period T_{sw}, $2m_c = \frac{f_H - f_L}{T_{\text{sw}}}$ is the chirp rate, $T_c = N_c T_{\text{sw}}$ is the total carrier duration, and N_c is the number of chirp pulses comprising the carrier waveform.

The message signal containing pilot and data symbols is:

$$s(t) = \sum_{k=0}^{N-1} s_k g(t - kT), \tag{3}$$

where $s_k, k = 0, \ldots, N-1$, are a sequence of symbols drawn from a constant-modulus constellation such as quadrature phase shift keying (QPSK), T is the symbol duration, $N = \frac{T_c}{T}$ is the number of symbols in the data packet and $g(t)$ is a pulse shaping function, for example, a root-raised-cosine pulse with roll-off factor α. We denote the symbol bandwidth by B, which is given by $B \approx \frac{1+\alpha}{T}$. For a symbol interval T ($< T_{\text{sw}}$), we can mount up to $M = \lfloor T_{\text{sw}}/T \rfloor$ symbols within a chirp pulse. Note that there are $N = MN_c$ symbols in a data packet. For simplicity, we assume that T_{sw}/T is an integer.

The modulated transmit signal is given by

$$x(t) = \text{Re}\left[s(t)c(t) \right], \tag{4}$$

which is prefixed with a preamble pulse and appended with a post-amble pulse to form a transmission frame. The preamble and post-amble are used for timing and synchronization, and for estimating the channel. A guard interval of T_g is used after (before) the preamble (post-amble) pulse to facilitate channel estimation. Using $N_c > 1$ helps in amortizing the overhead due to the guard interval over the total carrier duration of T_c.

The time-varying impulse response of the UWA channel is modeled as [29]:

$$h(t,\tau) = \sum_{p=0}^{N_{\rm P}-1} h_p(t)\delta\left(\tau - \tau_p(t)\right), \tag{5}$$

where $h_p(t)$ and $\tau_p(t)$ are the time-varying amplitude and delay, respectively, of the pth path, and $N_{\rm P}$ is the number of significant paths in the channel. The delay-scale model in (5) capture the effects of multipath propagation (i.e., reflection, scattering, and refraction) and the time variation of the propagation delays due to source-receiver motion, scattering by fluctuating ocean surfaces, and internal gravity waves such as interfacial waves and solitons within the fluid medium. As in [21]–[24], we assume that the path amplitudes are constant within a data packet, that is, $h_p(t) = h_p$, and that the time variation of the path delays due to Doppler rate a_p can be approximated as

$$\tau_p(t) = \tau_p - a_p t. \tag{6}$$

After coarse Doppler scale compensation and synchronization, the received signal is given by

$$y(t) = \sum_{p=0}^{N_{\rm P}-1} y_p(t) + w(t), \tag{7}$$

where $w(t)$ is the additive white Gaussian noise (AWGN), $y_p(t) = h_p \mathrm{Re}\{s(\tilde{t} - \tau_p(\tilde{t}))c(\tilde{t} - \tau_p(\tilde{t}))\}$ is the Doppler compensated and timing adjusted version of the S2C signal reaching via the pth path, $\tilde{t} = \frac{t+\hat{\tau}}{1+\hat{a}}$ is the rescaled and shifted time-axis, $\hat{a}$ is the coarse Doppler scale estimated using the preamble and post-amble as in [29], and $\hat{\tau}$ is the starting time instance of the first (data) chirp pulse estimated from the preamble/post-amble as in [6] but after resampling. Using (6), we can write,

$$y_p(t) = h_p \sum_{k=0}^{N-1} \left(s_{k,\mathrm{Re}} \cos\phi_p(t) - s_{k,\mathrm{Im}} \sin\phi_p(t)\right) g_{p,k}(t), \tag{8}$$

where $g_{p,k}(t) \triangleq g\left(\overline{1+b_p}t - \tilde{\tau}_p - kT\right)$, with $b_p = \frac{a_p - \hat{a}}{1+\hat{a}}$ and $\tilde{\tau}_p = \tau_p - (1+b_p)\hat{\tau}$ being the residual Doppler scale and delay of the pth path after compensation, respectively, $s_{k,\mathrm{Re}}$ ($s_{k,\mathrm{Im}}$) is the real (imaginary) part of the symbol s_k, and $\phi_p(t) = \phi(\overline{1+b_p}t - \tilde{\tau}_p)$ is the time-scaled and delayed version of the carrier phase in (2).

Upon sampling at a rate F_s ($= 1/T_s$, where T_s is the sampling period), we may re-express the received signal in (7) in a vector form relevant to data detection, as:

$$\mathbf{y} = H\mathbf{s} + \mathbf{w}, \tag{9}$$

where

$$\begin{aligned} H &= [C_0\mathbf{h}, -S_0\mathbf{h}, \ldots, C_{N-1}\mathbf{h}, -S_{N-1}\mathbf{h}] \in \mathbb{R}^{NL\times 2N}, \\ \mathbf{h} &= [h_0, h_1, \ldots, h_{N_{\rm P}-1}]^T \in \mathbb{R}^{N_{\rm P}\times 1}, \\ \mathbf{s} &= [s_{0,\mathrm{Re}}, s_{0,\mathrm{Im}}, \ldots, s_{N-1,\mathrm{Re}}, s_{N-1,\mathrm{Im}}]^T \in \mathbb{R}^{2N\times 1}, \\ \mathbf{w} &\sim \mathcal{N}\left(\mathbf{0}, \sigma^2 I_{2N}\right), \end{aligned}$$

$L = \lfloor F_s T \rfloor$ is the number of samples in the symbol duration, $C_k \in \mathbb{R}^{NL\times N_{\rm P}}$ and $S_k \in \mathbb{R}^{NL\times N_{\rm P}}$ are matrices whose entries are given by $C_k(l,p) = \cos\phi_p(lT_s)\, g_{p,k}(lT_s)$ and $S_k(l,p) = \sin\phi_p(lT_s)\, g_{p,k}(lT_s)$, for $0 \le k \le N-1$, $0 \le l \le NL-1$ and $0 \le p \le N_{\rm P}-1$, and I_{2N} denotes the $2N \times 2N$ identity matrix. Since $g(t) = 0, t \notin [0,T]$, entries of $C_k(:,p) \in \mathbb{R}^{NL\times 1}$ and $S_k(:,p) \in \mathbb{R}^{NL\times 1}$ are zeros except for $l \in \left\{\left\lceil \frac{\tilde{\tau}_p + kT}{1+b_pT_s}\right\rceil, \ldots, \left\lfloor \frac{\tilde{\tau}_p + k+1T}{1+b_pT_s}\right\rfloor\right\}$.

We now address the problem of data detection for the S2C communication model. First, we examine the two existing S2C receivers in the literature – the gradient heterodyne (GradH) receiver, pioneered in [6], and the path-based gradient heterodyne (pGradH) receiver proposed in [17].

III. Existing S2C Receivers: GradH and pGradH

We show that the GradH and pGradH based S2C receivers are minimum mean square error (MMSE) symbol detectors for the AWGN channel and a delay spread channel with well resolved path delays, respectively. We then introduce the reduced data measurement model, at the output of the GradH and pGradH preprocessors, that will be used in this work.

A. Optimality of GradH Receiver

Consider the received signal for the AWGN channel ($N_{\rm P} = 1, \tilde{\tau}_0 = 0, b_0 = 0, h_0 = 1$), given by

$$y(t) = \sum_{k=0}^{N-1} (s_{k,\mathrm{Re}} \cos\phi(t) - s_{k,\mathrm{Im}} \sin\phi(t)) g\left(t - kT\right) + w(t).$$

Upon sampling, the received signal is as in (7) with the channel matrix taking the block-diagonal form $H = Q = \mathrm{diag}\{Q_0, Q_1, \ldots, Q_{N-1}\} \in \mathbb{R}^{NL\times 2N}$, where,

$$Q_k = \mathrm{diag}\left(\mathbf{g}\right) \begin{bmatrix} \cos\phi^{(k)}[0] & \sin\phi^{(k)}[0] \\ \cos\phi^{(k)}[1] & \sin\phi^{(k)}[1] \\ \vdots & \vdots \\ \cos\phi^{(k)}[L-1] & \sin\phi^{(k)}[L-1] \end{bmatrix} \in \mathbb{R}^{L\times 2},$$

$\mathbf{g} = \left[g(0), g(T_s), \ldots, g\left(\overline{L-1}T_s\right)\right]^T \in \mathbb{R}^L$, and $\phi^{(k)}[l] = \phi\left((\tilde{k}-1)T + lT_s\right)$, $\tilde{k} = k - \lfloor \frac{k}{M} \rfloor M$, $l = 0, \ldots, L-1$, $k = 0, 1, \ldots, N-1$. In this case, there is no inter-symbol interference (ISI), and the measurement corresponding to the kth symbol is given by

$$\mathbf{y}_k = Q_k \mathbf{s}_k + \mathbf{w}_k, \tag{10}$$

where, for $k = 0, \ldots, N-1$,

$$\begin{aligned} \mathbf{y}_k &= [\, y[(k-1)L], y[(k-1)L+1], \ldots, y[kL-1]\,]^T, \\ \mathbf{s}_k &= \left[s_{k,\mathrm{Re}}, s_{k,\mathrm{Im}}\right]^T \in \left\{\left[\pm 1/\sqrt{2}, \pm 1/\sqrt{2}\right]^T\right\}, \\ \mathbf{w}_k &= \left[w_k[0], \ldots, w_k[L-1]\right]^T \sim \mathcal{N}\left(\mathbf{0}, \sigma^2 I_L\right). \end{aligned}$$

For equiprobable symbols $\mathbf{s}_k$, the MAP solution to (10) is the same as the ML estimator, and is given by

$$\hat{\mathbf{s}}_k^{(\mathrm{ML})} = \underset{\mathbf{s}_k \in \left\{\left[\pm 1/\sqrt{2}, \pm 1/\sqrt{2}\right]^T\right\}}{\arg\min} \|\mathbf{y}_k - Q_k\mathbf{s}_k\|_2, \tag{11}$$

and the MMSE solution to (10) is given by

$$\hat{\mathbf{s}}_k^{(\mathrm{MMSE})} = \mathcal{S}\left[\left(Q_k^T Q_k + \sigma^2 I_2\right)^{-1} Q_k^T \mathbf{y}_k\right], \tag{12}$$

where $\mathcal{S}[\cdot]$ is the slicing operation that quantizes each entry of its argument vector to the nearest symbol in the QPSK constellation.

Suppose the symbol time T (and hence L) is sufficiently large and the pulse shaping function, $g(t)$, is smooth, so that the following holds for all $0 \le k \le N-1$:

$$\sum_{l=0}^{L-1} g^2(lT_s)\cos^2\left(\phi^{(k)}[l]\right) \approx \sum_{l=0}^{L-1} g^2(lT_s)\sin^2\left(\phi^{(k)}[l]\right) \approx \beta,$$

and

$$\frac{1}{\beta}\sum_{l=0}^{L-1} g^2(lT_s)\cos\left(\phi^{(k)}[l]\right)\sin\left(\phi^{(k)}[l]\right) \approx 0,$$

where $\beta \triangleq \frac{1}{2}\sum_{l=0}^{L-1} g^2(lT_s)$. Then, we have $Q_k^T Q_k \approx \beta I_2$. To observe the goodness of this approximation, consider the S2C system in Table I, $L = 50$ raw samples per symbol, and a root-raised cosine pulse shaping function $g(t)$ with a roll-off $\alpha = 0.25$ and truncated to the symbol span. The diagonal entries of $Q_k^T Q_k$ differ by at most 0.09 dB, since

$$\max_k \frac{1}{\beta}\left|\sum_{l=0}^{L-1} g^2(lT_s)\cos\left(2\phi^{(k)}[l]\right)\right| < 0.02,$$

and the off-diagonal entries are at least -20 dB down compared to diagonal entires, since

$$\max_k \frac{1}{\beta}\left|\sum_{l=0}^{L-1} g^2(lT_s)\cos\left(\phi^{(k)}[l]\right)\sin\left(\phi^{(k)}[l]\right)\right| < 0.01.$$

Under these conditions, the MMSE receiver in (12) simplifies to the symbol-by-symbol decoder:

$$\hat{\mathbf{s}}_k^{(\text{GradH})} = \mathcal{S}\left[\mathbf{z}_k\right], \tag{13}$$

where $\mathbf{z}_k = Q_k^T \mathbf{y}_k$. Note that Q_k can be viewed as a lowpass filter, and there is a decimation by a factor of L in going from $\mathbf{y}_k$ to $\mathbf{z}_k$. From (10), we see that $\mathbf{z}_k \approx \beta \mathbf{s}_k + \mathbf{v}_k$, where $\mathbf{v}_k = Q_k^T \mathbf{w}_k \sim \mathcal{N}(\mathbf{0}, \beta\sigma^2 I_2)$, is affected only by the kth symbol. Also, $\mathbf{z}_k$ is a sub-vector of $\mathbf{z} = Q^T\mathbf{y} \in \mathbb{R}^{2N\times 1}$, whose entries are precisely the sampled versions of the lowpass filtered in-phase and quadrature outputs of gradient heterodyne operation, as in [6], on the received signal. Therefore, the GradH receiver in [6] realizes a near MMSE decoder for S2C communication over an AWGN channel.

While the GradH receiver in (13) is an MMSE symbol detector for the AWGN channel, the receiver works reasonably well even for ISI channels with *moderate* delay spreads, as elaborated in [6]. It is shown in [17] that the GradH receiver recovers the symbol arriving along the *direct path* when

$$\frac{\mathcal{M}}{\mathcal{M}-1}\delta\tau_{\max} \le T_{sw} \le \mathcal{M}\delta\tau_{\min}, \tag{14}$$

where $\delta\tau_{\min} = \min_{0\le i<j\le N_\text{P}-1}|\tau_i - \tau_j|$ and $\delta\tau_{\max} = \max_{0\le i,j\le N_\text{P}-1}|\tau_i - \tau_j|$ are the smallest and largest separation between any two path arrival times τ_i and τ_j, and $\mathcal{M} \triangleq \frac{f_H - f_L}{B}$ is called the spreading factor.

B. Optimality of pGradH Receiver

The pGradH receiver in [17] combines the symbol arriving along paths other than the direct path to leverage multipath diversity in addition to the gradient heterodyne and lowpass filtering operation. Here, we show that pGradH is a near MMSE decoder when the path delays are well resolved and condition (14) holds.

For a given channel H, the MMSE receiver is given by

$$\hat{\mathbf{s}}^{(\text{MMSE})} = \mathcal{S}\left[\left(H^T H + \sigma^2 I_{2N}\right)^{-1} H^T \mathbf{y}\right]. \tag{15}$$

When condition (14) holds, $C_i^T C_j \approx \kappa_C I_{N_\text{P}}\delta_{i,j}$, where $\kappa_C = C_i(:,p)^T C_i(:,p)$ is nearly the same for all $0 \le i \le N-1$ and $0 \le p \le N_\text{P}-1$, and $\delta_{i,j}$ is the Kronecker delta function. Similarly, $S_i^T S_j \approx \kappa_S I_{N_\text{P}}\delta_{i,j}$, where $\kappa_S = S_i(:,p)^T S_i(:,p)$, and $C_i^T S_j \approx 0$. Under these approximations, the MMSE receiver in (15) simplifies to the pGradH receiver in [17],

$$\hat{\mathbf{s}}_k^{(\text{pGradH})} = \mathcal{S}\left[\sum_{p=0}^{N_\text{P}-1} \frac{h_p}{|h_p|^2}\mathbf{z}_k^{(p)}\right], \tag{16}$$

where

$$\mathbf{z}_k^{(p)} = Q_k^{(p)T}\mathbf{y}_k, \tag{17}$$

$$Q_k^{(p)} = \text{diag}\left(\mathbf{g}^{(p)}\right)\begin{bmatrix} \cos\phi_p^{(k)}[0] & \sin\phi_p^{(k)}[0] \\ \cos\phi_p^{(k)}[1] & \sin\phi_p^{(k)}[1] \\ \vdots & \vdots \\ \cos\phi_p^{(k)}[L-1] & \sin\phi_p^{(k)}[L-1] \end{bmatrix},$$

$\mathbf{g}^{(p)} \in \mathbb{R}^L$ has entries that are samples of the compressed/dilated and delayed pulse shaping function, $g_l^{(p)} = g\left(\overline{1+b_p}lT_s - \tilde{\tau}_p\right)$, $\phi_p^{(k)}[l] = \phi_p\left((\tilde{k}-1)T + lT_s\right)$, $\tilde{k} = k - \lfloor\frac{k}{M}\rfloor M$, $l = 0,\ldots,L-1$, $p = 0,\ldots,N_\text{P}-1$, and $k = 0,1,\ldots,N-1$. Stacking up $\mathbf{z}_k^{(p)}, k = 0,1,\ldots,N-1$, into a vector, we get

$$\mathbf{z}^{(p)} = Q^{(p)T}\mathbf{y} \in \mathbb{R}^{2N\times 1}, \tag{18}$$

where $Q^{(p)} = \text{diag}\{Q_0^{(p)}, Q_1^{(p)}, \ldots, Q_{N-1}^{(p)}\} \in \mathbb{R}^{NL\times 2N}$. The entries of $\mathbf{z}^{(p)}$ are sampled versions of the lowpass filtered in-phase and quadrature outputs of *path-matched* gradient heterodyne operation, as in [17], on the received signal.

C. Reduced Data Measurement Model

We now present the data model for measurements, at *symbol rate*, at the output of the GradH and pGradH preprocessors. Henceforth, we use this reduced data measurement model instead of the raw signal samples at receiver front-end sampling rate, F_s, in (9).

The measurements at the output of GradH preprocessing, i.e., gradient heterodyne operation and lowpass filtering, can be written in the form

$$\mathbf{z} = G\mathbf{s} + \mathbf{v}, \tag{19}$$

where $G = Q^T H \in \mathbb{R}^{2N\times 2N}$ is the channel matrix at the output of the GradH preprocessor and lowpass filter, and $\mathbf{v} = Q^T\mathbf{w} \sim \mathcal{N}(\mathbf{0}, \sigma^2 Q^T Q)$. In the special case of an AWGN channel (i.e., $H = Q$), with a large enough symbol

duration T and smoothly varying pulse shaping function $g(t)$, the channel matrix $G = Q^T Q \approx \beta I_{2N}$ is nearly diagonal and $\mathbf{v} \sim \mathcal{N}(\mathbf{0}, \beta\sigma^2 I_{2N})$, as shown in Sec. III-A.

The measurement model at the output of pGradH preprocessing assumes the same form as in (19), where $\mathbf{z} \in \mathbb{R}^{2N}$ is the output of the MRC processor given by $\mathbf{z} = \sum_{p=0}^{N_\text{P}-1} \frac{h_p}{|h_p|^2}\mathbf{z}^{(p)}$, $G = \sum_{p=0}^{N_\text{P}-1} \frac{h_p}{|h_p|^2} G^{(p)} \in \mathbb{R}^{2N\times 2N}$ is the effective channel matrix at the output of the MRC processor, $G^{(p)} = Q^{(p)T} H \in \mathbb{R}^{2N\times 2N}$ is the channel matrix at the output of the pth branch of the pGradH preprocessor, $\mathbf{v} = \sum_{p=0}^{N_\text{P}-1} \frac{h_p}{|h_p|^2}\mathbf{v}^{(p)} \in \mathbb{R}^{2N}$ and $\mathbf{v}^{(p)} = Q^{(p)T}\mathbf{w} \sim \mathcal{N}(\mathbf{0}, \sigma^2 Q^{(p)T} Q^{(p)})$. For a moderately delay spread channel with well resolved path delays and large symbol duration, $Q^{(p)T} Q^{(q)} \approx \beta\delta_{p,q} I_{2N}, 0 \le p, q \le N_\text{P}-1$ due to (14). In this case, $G^{(p)} \approx \beta h_p I_{2N}$, $\mathbf{v}^{(p)} \sim \mathcal{N}(\mathbf{0}, \beta\sigma^2 I_{2N})$, and therefore G, the channel matrix at the output of the GradH and pGradH preprocessors, is nearly diagonal.

In the next section, we bring out the need to consider alternate S2C receiver processing in large delay spread channels.

IV. Limitations of GradH and pGradH Receivers

For both GradH and pGradH receivers, the condition in (14) is needed to ensure that the ISI is negligible after gradient heterodyne operation and lowpass filtering. The condition (14) places a *lower limit* on the minimum differential path delay, $\delta\tau_{\min}$, of the multipath arrivals to avoid ISI ensuing from the mixing of adjacent symbols at the GradH and pGradH preprocessor outputs [17]. The condition (14) also places an *upper limit* on the channel delay spread, $\delta\tau_{\max}$, to avoid interference between the symbols on the corresponding frequency sweep slots of different chirp pulses. Together, these limits require the symbol rate, $R = 1/T$, of the existing S2C receivers to satisfy

$$R \le \left(\frac{f_H - f_L}{1+\alpha}\right) \frac{\min\{\delta\tau_{\min}, T_{\text{sw}} - \delta\tau_{\max}\}}{T_{\text{sw}}}. \tag{20}$$

The upper limit on the achievable rate, in (20), is maximized when $T_{\text{sw}} = \delta\tau_{\max} + \delta\tau_{\min}$, and the maximum rate achievable by the existing S2C receivers is given by

$$R_{\max} = \left(\frac{f_H - f_L}{1+\alpha}\right) \frac{\delta\tau_{\min}}{\delta\tau_{\max} + \delta\tau_{\min}}. \tag{21}$$

Note that the rate limiting condition $R \le R_{\max}$ to avoid ISI at the preprocessor output of the existing S2C receivers, is equivalent to imposing a lower bound on the spreading factor: $\mathcal{M} \ge \frac{\delta\tau_{\max}}{\delta\tau_{\min}} + 1$. When the system is operated at a symbol rate $R = R_{\max}$, the spreading factor $\mathcal{M} = \frac{\delta\tau_{\max}}{\delta\tau_{\min}} + 1$.

Existing S2C receivers entail ISI when operating at a symbol rate greater than $R_{\max}$. Consider, for example, the S2C system in Table I operating in a UWA channel simulated in Sec. VI-B1. There are 20 QPSK symbols (i.e., 40 bits) in one chirp pulse (S2C block) of duration $T_{\text{sw}} = 10$ ms. Figure 1 shows a transmitted S2C frame, where the symbols $s_{i,j}$ and $s_{i,j+1}$ can potentially interfere with the detection of $s_{i,j+2}, j = 1, 2, 3$. Figures 2 and 3 display the images of the raw channel matrix H, in (9), and the corresponding effective channel G, in (19), respectively. Yellow pixels show

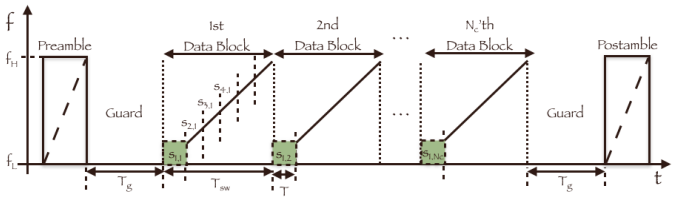

Fig. 1. An S2C frame consisting of preamble, N_c chirp pulses (data blocks), and post-amble. Although $T \ge \frac{1}{\sqrt{2m_c}}$ avoids ISI among adjacent symbols, inter-block interference (IBI) among the symbols mounted on the same frequency sweep slots (green slots) can happen if T_{sw} is smaller than the channel delay spread.

the large magnitude entries in the visual images of $|H|$ and $|G|$. Large magnitude off-diagonal entries lead to ISI. Compared to the raw channel matrix H, the effective channel G after gradient heterodyne and lowpass filtering exhibit reduced ISI. This is shown by the relatively weaker (blue) off-diagonal entries of $|G|$. The gradient heterodyne and lowpass filtering operation has reduced the strength of the off-diagonal entries in G that contribute to ISI among symbols within a chirp pulse (intra-block interference). But, strong residual inter-block interference remains at the GradH/pGradH preprocessor output as shown by the large magnitude (yellow) pixels around $G_{i,i-40}, 40 < i \le 2N$, in Figure 3. In turn, this adversely affects the performance of the existing S2C receivers in a severely delay spread UWA channel. In such channels, existing S2C receivers must compromise on the data rate in order to restore the symbol recovery performance.

In the following section, we consider alternate receivers for S2C communications that can handle channel delay spreads greater than the chirp pulse duration and work well for symbol rates higher than the upper limit on the data rate, $R_{\max}$.

V. Variational Soft Symbol Decoder (VSSD)

We now develop a symbol detector based on the variational Bayes' inference that approximates the optimum MAP decoder and offers significantly improved performance over the MMSE receiver. The development of the VSSD is the main contribution of this work.

The optimum (MAP) decoder outputs the symbol vector $\mathbf{s} \in \mathcal{P} = \{-\frac{1}{\sqrt{2}}, +\frac{1}{\sqrt{2}}\}^{2N}$ that maximizes the posterior $p(\mathbf{s}|G, \mathbf{z}) = p(\mathbf{z}|G, \mathbf{s})p(\mathbf{s})/p(\mathbf{z}|G)$. Direct maximization of the posterior requires a computationally intensive search over 2^{2N} lattice points in $\mathcal{P}$. Computing the posterior symbol probabilities, which in turn yield the soft symbols to be input to the channel decoder, is also hard since the marginalization over $\mathbf{s}$ in $p(\mathbf{z}|G) = \sum_{\mathbf{s}\in\mathcal{P}} p(\mathbf{s}, \mathbf{z}|G)$ is involved. We instead seek a good approximation to the posterior, $q_\phi(\mathbf{s}|G, \mathbf{z})$, called the variational decoder. Here, ϕ represents the model parameters whose values are estimated based on the variational inference principle, as explained below.

To make the problem tractable, we assume that the approximate posterior is fully factorizable:

$$q_\phi(\mathbf{s}|G, \mathbf{z}) = \prod_{k=0}^{N-1} q_\phi(s_{k,\text{Re}}|G, \mathbf{z}) q_\phi(s_{k,\text{Im}}|G, \mathbf{z}). \tag{22}$$

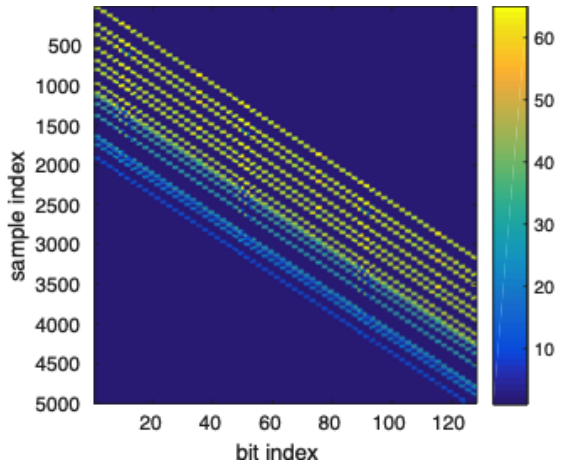

Fig. 2. Channel matrix image, $|H| \in \mathbb{R}^{NL \times 2N}$, before GradH processing. Pixel intensities are in linear units and only the portion corresponding to first 128 bits is shown. For the purpose of visualization, $|H|$ is scaled such that the median of the entires of its scaled version assumes a value of $\frac{1}{6}$ on the color bar shown.

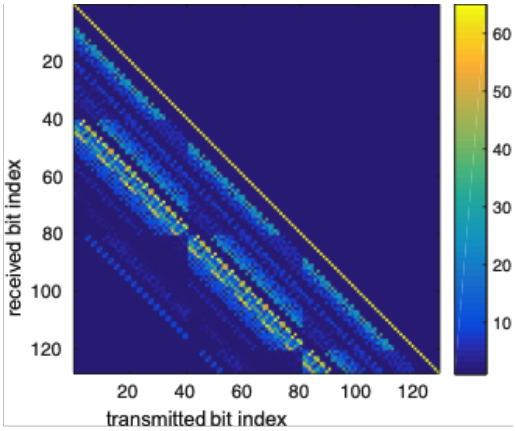

Fig. 3. Channel matrix image, $|G| \in \mathbb{R}^{2N \times 2N}$, after GradH processing. Pixel intensities are in linear units and only the portion corresponding to first 128 bits is shown. For the purpose of visualization, $|G|$ is scaled such that the median of the entires of its scaled version assumes a value of $\frac{1}{6}$ on the color bar shown.

Following Kingma et al. [30], the evidence lower bound (ELBO) on the log likelihood of the observation is given by

$$\mathcal{L}(\theta, \phi, \mathbf{z}) = \mathbb{E}_{q_{\phi(\mathbf{s}|G,\mathbf{z})}} \log p_\theta(\mathbf{z}|G, \mathbf{s}) - \mathbb{E}_{q_{\phi(\mathbf{s}|G,\mathbf{z})}} \left[\log \frac{q_\phi(\mathbf{s}|G, \mathbf{z})}{p_\theta(\mathbf{s})} \right], \quad (23)$$

where $\log p_\theta(\mathbf{z}|G, \mathbf{s})$ is the likelihood function and $p_\theta(\mathbf{s})$ is a prior on the symbol vector.

To bring $q_\phi(\mathbf{s}|G, \mathbf{z})$ close to $p(\mathbf{s}|G, \mathbf{z})$, we maximize the ELBO, $\mathcal{L}(\theta, \phi, \mathbf{z})$. The ELBO consists of the likelihood term

$$\mathbb{E}_{q_{\phi(\mathbf{s}|G,\mathbf{z})}} \log p_\theta(\mathbf{z}|G, \mathbf{s}) = -N \log(2\pi\sigma^2) - \mathbb{E}_{q_{\phi(\mathbf{s}|G,\mathbf{z})}} \left[\frac{\|\mathbf{z} - G\mathbf{s}\|^2}{2\sigma^2} \right], \quad (24)$$

and the regularizing term,

$$\mathbb{E}_{q_{\phi(\mathbf{s}|G,\mathbf{z})}} \left[\log \frac{q_\phi(\mathbf{s}|G, \mathbf{z})}{p_\theta(\mathbf{s})} \right] = KL(q_\phi || p_\theta). \quad (25)$$

We assume a simple uniform prior $p_\theta(\mathbf{s}) = \frac{1}{2^{2N}}$. Therefore, when maximizing ELBO, the regularizing term acts to penalize the departure of the variational approximation q_ϕ from the uniform prior. On maximizing the ELBO, we get the following fixed point equations (see appendix for details):

$$\mathbf{q} = \varphi(\boldsymbol{\alpha}), \quad (26)$$

where

$$\begin{aligned} \alpha_j &= \frac{\sqrt{2}}{\sigma^2} \left(\mathbf{z}^T G_{:,j} - \sum_{l=0}^{2N-1} G_{l,j} \left(\sum_i v_{l,i} - v_{l,j} \right) \right), \\ v_{l,j} &= \frac{1}{\sqrt{2}} G_{l,j} \left(2q_j - 1 \right), \quad (27) \\ \varphi(\alpha_j) &= \frac{1}{1 + e^{-\alpha_j}}, \end{aligned}$$

for $j = 1, \ldots, 2N - 1$.

Note that the fixed point iterations lead to *soft symbol* estimates in the form of the probability vector $\mathbf{q}$. We perform symbol detection by slicing the probability vector in uncoded communications. In coded communications, the soft symbols are converted to LLRs and fed to the channel decoder.

The fixed point updates do not involve any matrix inversions and their computational complexity, $\mathcal{O}(N^2)$, is an order of magnitude smaller than the computational complexity, $\mathcal{O}(N^3)$, of the MMSE receiver.

Special Channels: It is insightful to specialize the fixed point iterations for some simple channel models. Consider the case when the channel matrix is orthogonal, i.e.,

$$G_{:,i}^T G_{:,j} = \| G_{:,i} \|_2^2 \, \delta_{i,j}.$$

Note that the AWGN channel and Rayleigh fading channel are examples of orthogonal channels. In this case, the fixed point iterations in (26) reduce to the following one point update:

$$\mathbf{q} = \frac{1}{1 + e^{-\left(\frac{\sqrt{2}}{\sigma^2} G^T \mathbf{z}\right)}}. \quad (28)$$

Therefore, deciding the hard symbols from the probability vector $\mathbf{q}$ is tantamount to slicing the matched filtered observation: $\tilde{\mathbf{z}} = G^T \mathbf{z}$. Deciding $s_k = \pm \frac{1}{\sqrt{2}}$ based on $q_k \gtrless 0.5$ is equivalent to that based on $\tilde{z}_k \gtrless 0$. In other words, VSSD is an ML decoder for orthogonal channels.

Convergence: We show that every update of the fixed point iteration in (26) is along the gradient of the ELBO (ascent direction), and therefore cannot decrease the ELBO. To see this, consider the inner product of $\varphi(\boldsymbol{\alpha}) - \mathbf{q}$ and $\nabla\mathcal{L}$:

$$\left(\varphi(\boldsymbol{\alpha}) - \mathbf{q}\right)^T \nabla\mathcal{L} = \sum_{j=0}^{2N-1} \left(\varphi(\alpha_j) - q_j\right) \nabla\mathcal{L}_j. \quad (29)$$

We show in the appendix (see equation (66)) that $\nabla\mathcal{L}_j = \alpha_j - \log q_j + \log(1 - q_j)$. Each term in (29) is nonnegative since $\varphi(\alpha_j) - q_j \gtrless 0 \Leftrightarrow \alpha_j - \log q_j + \log(1 - q_j) \gtrless 0$. Thus, the inner product is nonnegative and hence the update $\mathbf{q} \to \varphi(\boldsymbol{\alpha}(\mathbf{q}))$ cannot decrease ELBO. Further, for any channel matrix, the ELBO is upper bounded by the marginal log likelihood, $\log p_\theta(\mathbf{z})$. Therefore, the fixed point iterations always converge to a stationary point of the ELBO.

Next, we characterize the stationary points of the ELBO and elicit sufficient conditions that make these points a *global maximum*, *local maximum* or a *saddle point*.

Global Maximum: The entries of the Hessian matrix of $\mathcal{L}$ with respect to $\mathbf{q}$, i.e., $\nabla^2_{\mathbf{q}}\mathcal{L} \in \mathbb{R}^{2N\times 2N}$, are given by

$$\frac{\partial^2 \mathcal{L}}{\partial q_j^2} = -\frac{1}{q_j(1-q_j)} < 0, \quad (30)$$

$$\frac{\partial^2 \mathcal{L}}{\partial q_i \partial q_j} = \frac{\partial^2 \mathcal{L}}{\partial q_j \partial q_i} = -\frac{2}{\sigma^2}\sum_l G_{l,i}G_{l,j}, i \neq j, \quad (31)$$

where $i, j \in \{0, 1, \ldots, 2N-1\}$. For orthogonal channel matrices, the matrix G satisfies $\sum_l G_{l,i}G_{l,j} = 0$, which makes the Hessian negative definite and therefore the stationary point $\mathbf{q}_\star$ a global maximizer of the ELBO.

A larger class of channel matrices for which global convergence is guaranteed can be found by requiring $-\nabla^2_{\mathbf{q}}\mathcal{L}$ to be diagonally dominant, i.e.,

$$\eta_j \triangleq \frac{2}{\sigma^2}\sum_{i\neq j}\left|\sum_l G_{l,i}G_{l,j}\right| < \frac{1}{q_j(1-q_j)}, \forall j, \quad (32)$$

which implies:

$$q_j^2 - q_j + 1/\eta_j > 0, \forall j. \quad (33)$$

Now, the condition in (33) holds for every $0 \leq q_j \leq 1$ if and only if $0 \leq \eta_j < 4$. Note that $-\nabla^2_{\mathbf{q}}\mathcal{L}$ is symmetric and all its diagonal entries are positive. Since diagonal dominance of $-\nabla^2_{\mathbf{q}}\mathcal{L}$ implies its positive definiteness (p.d.), $-\nabla^2_{\mathbf{q}}\mathcal{L}$ is p.d. for the class of channel matrices $\mathcal{G} = \{G \in \mathbb{R}^{2N\times 2N} : \sum_{i\neq j}|\sum_l G_{l,i}G_{l,j}| < 2\sigma^2, \forall j\}$ and therefore global convergence is guaranteed whenever $G \in \mathcal{G}$.

Local Maximum: If $G \in \mathcal{G}$, the limit point $\mathbf{q}_\star$ is a global maximizer. Or else, if $G \notin \mathcal{G}$ and $q_{j,\star} \notin (\kappa_j^{(1)}, \kappa_j^{(2)}) \subset [0,1], \forall j$, where $\kappa_j^{(1,2)}$ are the roots of the equation $q_j^2 - q_j + 1/\eta_j = 0$ ($\eta_j > 4$) given by

$$\kappa_j^{(1,2)} = \frac{1 \pm \sqrt{1-4/\eta_j}}{2}, \forall j, \quad (34)$$

then the limit point $\mathbf{q}_\star$ is a local maximum.

Either Local Maximum or Saddle Point: If $G \notin \mathcal{G}$ and $q_{j,\star} \in (\kappa_j^{(1)}, \kappa_j^{(2)})$, for some j, then the limit point $\mathbf{q}_\star$ is either a local maximum or a saddle point.

Consider, for example, a channel matrix with i.i.d. $\mathcal{N}(0,1)$ entries. The length of the interval $(\kappa_j^{(1)}, \kappa_j^{(2)})$ is given by

$$l_{N,j} = \kappa_j^{(2)} - \kappa_j^{(1)} = \sqrt{1-4/\eta_j}. \quad (35)$$

From the definition of η_j in (32), triangle inequality, and the i.i.d. property of the entries of G, we have:

$$\mathbb{E}[\eta_j] \leq \frac{2}{\sigma^2}\sum_{i\neq j}\sum_l \mathbb{E}\left[|G_{l,i}|\right]\mathbb{E}\left[|G_{l,j}|\right] = \frac{8N(2N-1)}{\pi\sigma^2}, \quad (36)$$

and therefore,

$$\mathbb{E}[l_{N,j}^2] = 1 - 4\mathbb{E}[1/\eta_j] \leq 1 - 4/\mathbb{E}[\eta_j] = 1 - \frac{\pi\sigma^2}{2N(2N-1)}, \quad (37)$$

where we used the fact that $\mathbb{E}[1/\eta_j] \leq 1/\mathbb{E}[\eta_j]$ which follows from Jensen's inequality and the convexity of $f(\eta) = 1/\eta, \eta > 0$. Since $\mathbb{P}\{\eta_j > 4\} \to 1$, as $N \to \infty$, for i.i.d. Gaussian channel matrices, the fixed point is in $(\kappa_j^{(1)}, \kappa_j^{(2)})$ with high probability. Furthermore, since for every $\delta > 0$, $\mathbb{P}\{l_{N,j}^2 > 1-\delta\} \to 1$ as $N \to \infty$, we have $l_{N,j} \xrightarrow{p} 1$.

Since, in this case, $\mathbf{q}_\star$ could be a saddle point, we perturb $\mathbf{q}_\star$ so as to move out of the saddle region in an attempt to further increase the ELBO. If the ELBO is found to increase for a few attempts of random perturbation, we continue the iterations from the point yielding the highest ELBO.

Acceleration: Finally, we propose to accelerate the fixed point updates to achieve faster convergence. Specifically, we choose γ_n at the nth iterate so that the update,

$$\mathbf{q}_n = \mathbf{q}_{n-1} + \gamma_n\left[\varphi(\boldsymbol{\alpha}_{n-1}) - \mathbf{q}_{n-1}\right], \quad (38)$$

results in maximal increase of ELBO. The optimum value of γ_n can be found through a 1-D search over a bounded interval in $\mathbb{R}$. Specifically, the optimum value of γ_n in (38), that best increases ELBO, lies within $[\gamma_{\min}, \gamma_{\max}] \in \mathbb{R}$, with

$$\gamma_{\min} = \max\Big\{\max_{\varphi(\alpha_j)>q_j}\frac{-q_j}{\varphi(\alpha_j)-q_j}, \max_{\varphi(\alpha_j)<q_j}\frac{1-q_j}{\varphi(\alpha_j)-q_j}\Big\},$$

$$\gamma_{\max} = \min\Big\{\min_{\varphi(\alpha_j)<q_j}\frac{-q_j}{\varphi(\alpha_j)-q_j}, \min_{\varphi(\alpha_j)>q_j}\frac{1-q_j}{\varphi(\alpha_j)-q_j}\Big\}.$$

TABLE I
S2C PARAMETERS USED IN THE SIMULATION.

Carrier frequency (f_c)	15 kHz
Bandwidth (W)	10 kHz
Chirp rate ($2m_c$)	1 MHz/s
Symbol duration (T)	0.5 ms
Sweep duration (T_{sw})	10 ms
Guard interval (T_g)	25 ms

VI. Numerical Simulations

We demonstrate the performance of VSSD in three different settings: the benchmark i.i.d. Gaussian multiple-input multiple-output (MIMO) channel, UWA channels simulated according to two different models in the literature, and real-world measured UWA channels. We define the signal to noise ratio (SNR) at the receiver as

$$\text{SNR} = \frac{E\{\|G\mathbf{s}\|_2^2\}}{E\{\|\mathbf{v}\|_2^2\}}. \quad (39)$$

A. IID Gaussian MIMO Channel

We generate the channel matrix G, with entries $G_{i,j} \overset{i.i.d.}{\sim} \mathcal{N}(0,1)$. First, we evaluate the BER of the VSSD receivers for $N = 10, 100$ symbols, for the uncoded QPSK signaling, and with perfect channel knowledge. We terminate the VSSD iterations at the nth iteration if $\|\mathbf{q}_n - \mathbf{q}_{n-1}\|_2 < 10^{-3}$. Figure 4 shows the BER plots for different SNR values. For $N = 10$ symbols, we show the BER of the ML decoder obtained by using the soft sphere decoder (SSD) in [31], [32] and whose implementation is available in [33]. The VSSD

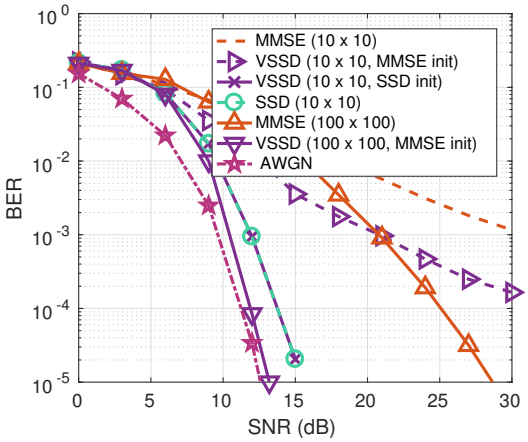

Fig. 4. BER of VSSD, SSD and MMSE receivers for i.i.d. Gaussian channel matrix ($N = 10, 100$) and AWGN channel.

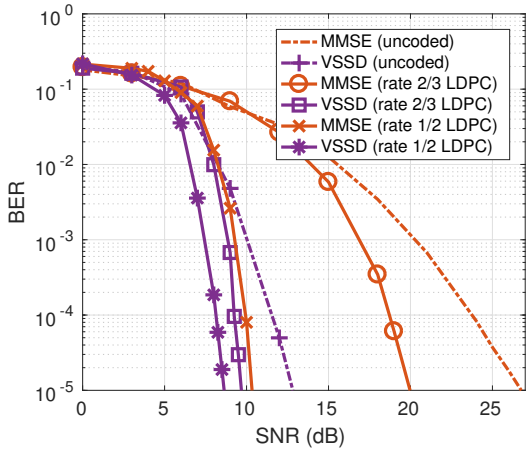

Fig. 5. BER of VSSD and MMSE receivers for i.i.d. Gaussian channel matrix.

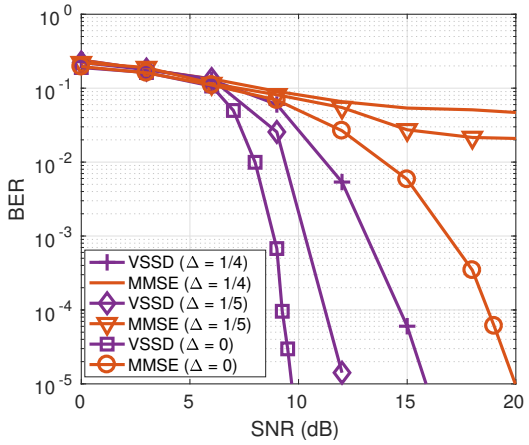

Fig. 6. BER of VSSD and MMSE receivers, under channel estimation errors, for i.i.d. Gaussian channel matrix.

receiver, initialized with the soft symbol estimate of SSD, retains the SSD's optimum (ML) performance, as expected. When initialized with the MMSE estimate of the symbol vector, VSSD outperforms the MMSE receiver by a margin of about 8-9 dB at a BER of 10^{-3} for $N = 10$. Note that, while SSD outperforms VSSD for $N = 10$, sphere decoding is not practical at large values of N due to its high computational complexity.[1] Moreover, for $N = 100$, the performance of the VSSD receiver on the i.i.d. Gaussian MIMO channel is close to that on an AWGN channel. On the AWGN channel, all receivers perform equally well, as expected.

In Figure 5, we compare the BER of the receivers for $N = 288$ symbols, for uncoded and coded QPSK communications, assuming perfect channel knowledge. For coded communication, we use a rate $1/2$ and rate $2/3$ LDPC code from [34]. In uncoded communication, the VSSD receiver achieves a BER of 10^{-3} at about 10 dB lower SNR than the MMSE receiver. In the rate $2/3$ ($1/2$) coded communication, for a BER of 10^{-3}, VSSD outperforms MMSE receiver by an SNR margin of 8 dB (2 dB). For the same BER (10^{-3}), the VSSD receiver with a rate $2/3$ code works at about 1 dB lower SNR than the MMSE receiver with a rate $1/2$ code. Therefore, VSSD receiver offers 33% higher data rate than the MMSE receiver, while achieving the same BER.

Next, we consider the effect of imperfect channel knowledge due to channel estimation error on the BER. To do so, we perturb the entries of the i.i.d. Gaussian channel matrix with i.i.d. Gaussian noise, i.e. $G_{i,j} = G_{i,j} + \epsilon_{i,j}$, where $\epsilon_{i,j} \sim \mathcal{N}(0, \Delta), 1 \leq i, j, \leq 2N$. Figure 6 shows the BER of VSSD and MMSE decoders for $\Delta = 1/4, 1/5$ and coded communications using a rate $2/3$ LDPC code. VSSD receiver retains its performance advantage over MMSE even with channel estimation errors.

[1]On a 2.4 GHz Intel Xeon(R) processor, SSD takes 4.5 s on average to decode $N = 20$ symbols at SNR = 10 dB. For $N = 30$ symbols and at the same SNR, decoding does not finish within 5 minutes.

B. Simulated UWA Channels

We now consider the performance of VSSD based receiver for the S2C communication system in Table I over a simulated UWA channel. Note that the symbol rate that is two times the upper limit, $R_* = \sqrt{2m_c} = 1$ kHz, on the existing S2C receivers.[2] A total of $N = 288$ QPSK symbols are mounted on a train of $N_c = 15$ chirp pulses. We investigate the performance for two models of UWA channels.

1) Model I: The first UWA channel model we consider is as in [21], [22] and used by numerous researchers in the field. The channel is generated with $N_{\text{P}} = 16$ discrete paths whose inter-arrival times are exponentially distributed with a mean of 1 ms. The Doppler rates are uniformly distributed in $[-b_{\max}, b_{\max}]$, where $b_{\max} = 5 \times 10^{-4}$. The path amplitudes are Rayleigh distributed with the average power decreasing exponentially with delay, where the difference between the beginning and the end of the guard time is 20 dB. Notice that neither of the narrowband approximation conditions [20] $B/f_c \ll 1$ or $b_{\max} \ll 1/BT$ are met in this case. Therefore,

[2]Adjacent symbol interference, within a chirp pulse, is avoided in existing S2C receivers only if $2m_cT \geq B \approx \frac{1+\alpha}{T} \Rightarrow R \leq \sqrt{\frac{2m_c}{1+\alpha}} \leq \sqrt{2m_c} \triangleq R_*$.

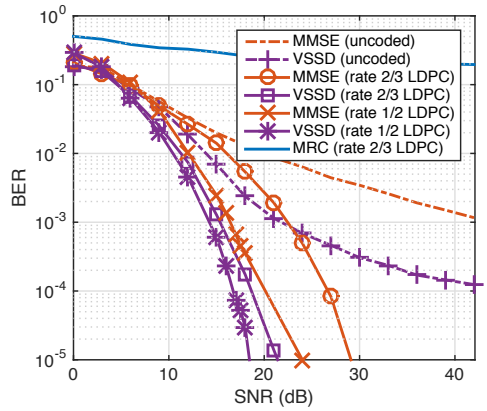

Fig. 7. BER of VSSD and MMSE receivers over a UWA channel simulated according to the model in Berger et al. [21].

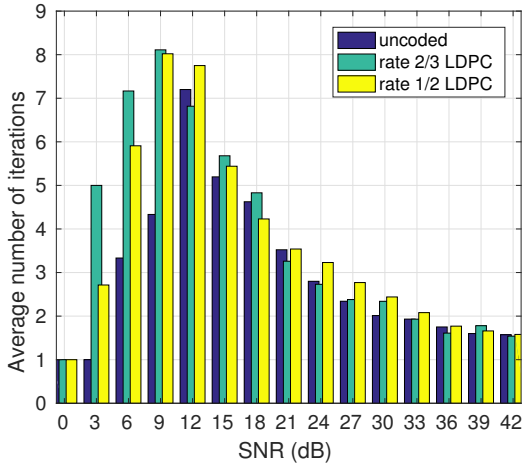

Fig. 8. Number of VSSD iterations averaged over 1000 trials for each SNR.

it is pertinent to evaluate the symbol recovery schemes based on the system model (9) for S2C communications over such a wideband delay-scale channel.

Figure 7 shows the BER of the MRC [17], VSSD and MMSE based data detection assuming perfect channel knowledge. The MRC receiver has completely failed due to severe ISI at pGradH preprocessor output (see Figure 3). Again, from these plots, we notice a strong performance of the VSSD based symbol detection in an S2C receiver. The VSSD receiver attains a BER $= 10^{-3}$ at about 18 dB lower SNR than MMSE in uncoded communication. In coded communication, the SNR margin of VSSD over the MMSE receiver is 8 dB (3 dB) for rate $2/3$ ($1/2$) LDPC code.

Figure 8 shows the number of VSSD iterations (averaged over at least 1000 trials) for different SNR. On an average, the number of iterations stay below 10 and the maximum number of iterations never crossed 15.

2) Model II: We consider the UWA channel model proposed in [35]. The acoustic channel simulator code, available at [36], is used for generating the time-varying channel. Table II lists the parameters of the channel. A sample realization of the time-varying channel impulse response is shown in

TABLE II
UNDERWATER CHANNEL SIMULATION PARAMETERS.

Ocean depth (m)	100
Transmitter depth (m)	90
Receiver depth (m)	50
Channel distance (m)	1000
Spreading factor	1.7
Sound speed in water, c_w (m/s)	1500
Sound speed in bottom, c_b (m/s)	1200
Surface variance, σ_s^2 (m^2)	1.125
Bottom variance, σ_b^2 (m^2)	0.5
3 dB width of the PSD of intra-path delays, $B_{\delta,p}$ (Hz)	0.05
Number of intra-paths, S_p	20
Mean of intra-path amplitudes, μ_p	0.3
Variance of intra-path amplitudes, ν_p	10^{-4}
Transmitter drifting speed, v_{td} (m/s)	0.3
Transmitter drifting angle, θ_{td} (rad)	$\mathcal{U}(0, 2\pi)$
Receiver drifting speed, v_{rd} (m/s)	0.1
Receiver drifting angle, θ_{rd} (rad)	$\mathcal{U}(0, 2\pi)$
Transmitter vehicular speed, v_{tv} (m/s)	$\mathcal{N}(0, 1)$
Transmitter vehicular angle, θ_{tv} (rad)	$\mathcal{U}(0, 2\pi)$
Receiver vehicular speed, v_{rv} (m/s)	-3
Receiver vehicular angle, θ_{rv} (rad)	$\mathcal{U}(0, 2\pi)$
Surface variation amplitude, A_w (m)	0.9
Surface variation frequency, f_w (mHz)	0.6

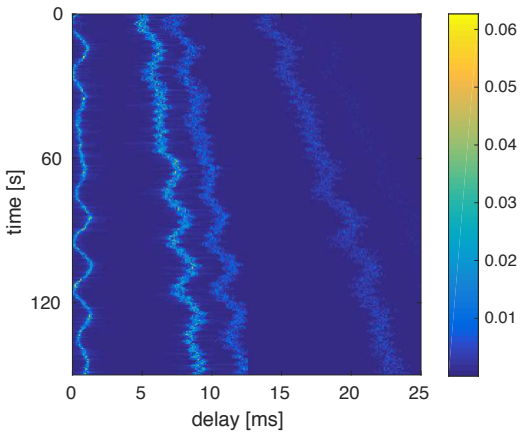

Fig. 9. Acoustic channel impulse response based on model in [35]. The first, second and third arrivals from the left correspond to the direct, bottom-reflected, and surface-reflected paths, respectively. The last arrival corresponds to a multiply reflected surface-bottom arrival.

Figure 9. Figure 10 shows an instance of the channel matrix (G) at the output of S2C preprocessing during the UWA channel simulation run. The inter symbol interference for this UWA channel is milder than the channel simulated according to the model in [21] (see Figure 3). Figure 11 shows the BER plots of the VSSD and MMSE receivers with and without channel errors. VSSD maintains a significantly better performance than MMSE decoder, as before.

C. WATERMARK *Channels*

The underWater AcousTic channEl Replay benchMARK (WATERMARK) is a publicly available realistic simulation tool that comes packaged with five measured UWA channels [37], [38]. We use two of channel datasets, NOF1 and NCS1, that present two contrasting environments in the Norwegian seas [39]. The NOF1 channel is a Fjord in a shallow stretch of

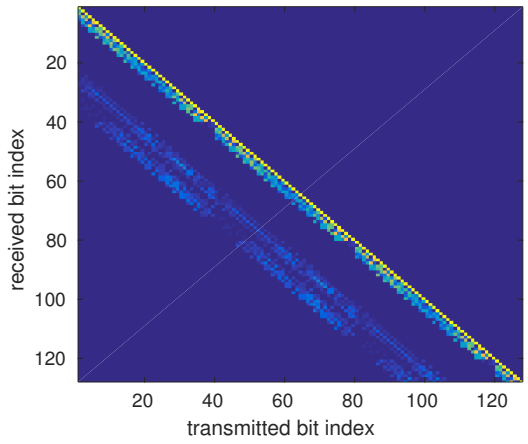

Fig. 10. Channel matrix after GradH processing at an instance during the simulation run of the UWA channel model in [35].

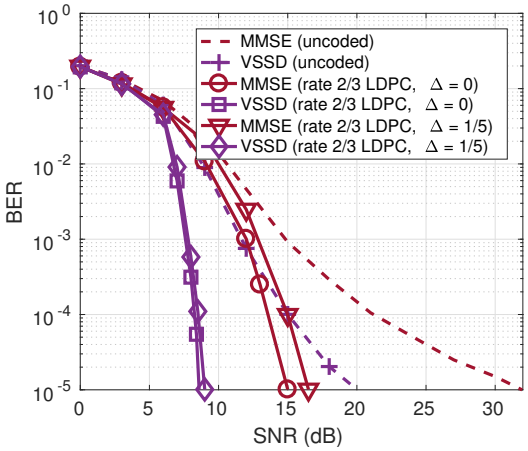

Fig. 11. BER of VSSD and MMSE receivers for S2C communications over UWA channel simulated according to [35].

Oslofjorden, and the NCS1 channel is a continental shelf in the Norwegian sea. The measured time-varying channel impulse responses include the effects of system hardware impairments such as clock frequency offset, sampling jitter etc, apart from the acoustic propagation effects.

Channel Matrix Computation: We first relate the complex baseband form of the measured channel impulse response data in WATERMARK, denoted by $h_{\rm B}(t,\tau)$, and the channel matrix, G, at the output of the gradient heterodyne and lowpass filtering operation. Towards that end, we start with the baseband transmitted signal, given by

$$x_{\rm B}(t) = s(t)c(t)e^{-j2\pi f_c t}. \tag{40}$$

The received baseband signal is given by

$$y_{\rm B}(t) = \int_{\tau_{\min}(t)}^{\tau_{\max}(t)} h_{\rm B}(t, t-\tau)x_{\rm B}(\tau)d\tau + w_B(t), \tag{41}$$

where $\tau_{\min}(t) = \max\{0, t-T_d\}$, $\tau_{\max}(t) = \min\{t, T_c\}$, T_d denotes the maximum delay spread of the propagation channel and $w_B(t)$ is the complex valued noise in the baseband. Here, we made use of the fact that $h_{\rm B}(t,\tau) = 0$ for $\tau < 0$ (due to causality) and $\tau > T_d$, and $x_B(\tau) = 0$ for $\tau > T_c$, to arrive at the upper and lower limits of the integral in (41). Using (3), (40) and (41), the in-phase and quadrature components of the received signal can be expressed in the form:

$$y_{\rm B,Re}(t) = \sum_{k=0}^{N-1} H^{\rm Re}_{k,\rm Re}(t)s_{k,\rm Re} + H^{\rm Im}_{k,\rm Re}(t)s_{k,\rm Im} + w_{B,\rm Re}(t), \tag{42}$$

$$y_{\rm B,Im}(t) = \sum_{k=0}^{N-1} H^{\rm Re}_{k,\rm Im}(t)s_{k,\rm Re} + H^{\rm Im}_{k,\rm Im}(t)s_{k,\rm Im} + w_{B,\rm Im}(t), \tag{43}$$

where,

$$H^{\rm Re}_{k,\rm Re}(t) = \int_{\tau^{(k)}_{\min}(t)}^{\tau^{(k)}_{\max}(t)} h_{\rm B,Re}(t, t-\tau)g(\tau - kT)\cos\phi_{\rm B}(\tau)d\tau - \int_{\tau^{(k)}_{\min}(t)}^{\tau^{(k)}_{\max}(t)} h_{\rm B,Im}(t, t-\tau)g(\tau - kT)\sin\phi_{\rm B}(\tau)d\tau, \tag{44}$$

$$H^{\rm Im}_{k,\rm Re}(t) = -\int_{\tau^{(k)}_{\min}(t)}^{\tau^{(k)}_{\max}(t)} h_{\rm B,Re}(t, t-\tau)g(\tau - kT)\sin\phi_{\rm B}(\tau)d\tau - \int_{\tau^{(k)}_{\min}(t)}^{\tau^{(k)}_{\max}(t)} h_{\rm B,Im}(t, t-\tau)g(\tau - kT)\cos\phi_{\rm B}(\tau)d\tau, \tag{45}$$

$$H^{\rm Re}_{k,\rm Im}(t) = \int_{\tau^{(k)}_{\min}(t)}^{\tau^{(k)}_{\max}(t)} h_{\rm B,Re}(t, t-\tau)g(\tau - kT)\sin\phi_{\rm B}(\tau)d\tau + \int_{\tau^{(k)}_{\min}(t)}^{\tau^{(k)}_{\max}(t)} h_{\rm B,Im}(t, t-\tau)g(\tau - kT)\cos\phi_{\rm B}(\tau)d\tau, \tag{46}$$

$$H^{\rm Im}_{k,\rm Im}(t) = \int_{\tau^{(k)}_{\min}(t)}^{\tau^{(k)}_{\max}(t)} h_{\rm B,Re}(t, t-\tau)g(\tau - kT)\cos\phi_{\rm B}(\tau)d\tau - \int_{\tau^{(k)}_{\min}(t)}^{\tau^{(k)}_{\max}(t)} h_{\rm B,Im}(t, t-\tau)g(\tau - kT)\sin\phi_{\rm B}(\tau)d\tau, \tag{47}$$

$\phi_{\rm B}(t) = 2\pi\left(f_L t_r(t) + m_c t_r^2(t) - f_c t\right)$, $\tau^{(k)}_{\min}(t) = \max\{0, t-T_d, kT\}$, $\tau^{(k)}_{\max}(t) = \min\{t, T_c, (k+1)T\}$, $w_{B,\rm Re}(t)$ and $w_{B,\rm Im}(t)$ are the real valued additive noises in the in-phase and quadrature channels. After sampling along t and τ axes, the received signal samples from (42)-(43) can be stacked and expressed in the form of (9). Entries of the channel matrix, $H \in \mathbb{R}^{NL\times 2N}$, are found from discretized versions of (44)-(47). At time $t = nT_s$, the in-phase and quadrature measurement samples are given by

$$\mathbf{y}_B[n] = \sum_{k=0}^{N-1} H_{n,k}\mathbf{s}_k + \mathbf{w}_B[n], \tag{48}$$

where $\mathbf{y}_B[n] = [y_{\rm B,Re}(nT_s), y_{\rm B,Im}(nT_s)]^T$, $H_{n,k} \in \mathbb{R}^{2\times 2}$ is the block matrix,

$$H_{n,k} = \begin{bmatrix} H^{\rm Re}_{k,\rm Re}(nT_s) & H^{\rm Im}_{k,\rm Re}(nT_s) \\ H^{\rm Re}_{k,\rm Im}(nT_s) & H^{\rm Re}_{k,\rm Im}(nT_s) \end{bmatrix} \in \mathbb{R}^{2\times 2}, \tag{49}$$

TABLE III
S2C PARAMETERS USED IN SEC. VI-C

Frequency band ($f_L - f_H$)	10 - 18 kHz
Chirp rate ($2m_c$)	800 kHz/s
Symbol duration (T)	0.5 ms
Sweep duration (T_{sw})	10 ms
Guard interval (T_g)	25 ms

The channel matrix, G_{B}, after gradient heterodyne and lowpass filtering is given by

$$G_{\text{B}} = Q_{\text{B}}^T H \in \mathbb{R}^{2N\times 2N}, \tag{50}$$

where $Q_{\text{B}} = \text{diag}\{Q_{\text{B},0}, Q_{\text{B},1}, \ldots, Q_{\text{B},N-1}\} \in \mathbb{R}^{2NL\times 2N}$,

$$Q_{\text{B},k} = \text{diag}\,(\tilde{\mathbf{g}}) \begin{bmatrix} R_{\phi_{\text{B}}^{(k)}[0]} + R_{\phi_{\text{B}}^{(k)}[0]-\frac{\pi}{2}} \\ R_{\phi_{\text{B}}^{(k)}[1]} + R_{\phi_{\text{B}}^{(k)}[1]-\frac{\pi}{2}} \\ \vdots \\ R_{\phi_{\text{B}}^{(k)}[L-1]} + R_{\phi_{\text{B}}^{(k)}[L-1]-\frac{\pi}{2}} \end{bmatrix} \in \mathbb{R}^{2L\times 2},$$

R_θ is the rotation matrix,

$$R_\theta = \begin{bmatrix} \cos\theta & -\sin\theta \\ \sin\theta & \cos\theta \end{bmatrix} \in \mathbb{R}^{2\times 2},$$

$\tilde{\mathbf{g}} = [g[0], g[0], g[1], g[1], \ldots, g[L-1], g[L-1]]^T \in \mathbb{R}^{2L\times 1}$ and $\phi_{\text{B}}^{(k)}[l] = \phi_{\text{B}}\left((\tilde{k}-1)T + lT_s\right)$, $\tilde{k} = k - \lfloor \frac{k}{M} \rfloor M$, $l = 0, \ldots, L-1$.

Performance Evaluation: We now consider the performance of the proposed VSSD receiver over the WATERMARK channels for the S2C system in Table III. The channel datasets NOF1 and NCS1 in WATERMARK have a delay (τ) coverage of $T_d = 128$ ms and $T_d = 32$ ms respectively. Therefore, the measured impulse response of NOF1 (NCS1) channel is available only at an interval of $\Delta t = 128$ ms ($\Delta t = 32$ ms) along the t-axis. To compute the entries of the channel matrix, H and hence G, we require the channel impulse response at finer intervals corresponding to the baseband sampling frequency $F_s = 16$ kHz used in WATERMARK. We linearly interpolate the samples of measured baseband channel impulse response to obtain the response at finer intervals.

For timing and synchronization, a chirp pulse of duration $T_p = 20$ ms in the frequency band 10-18 kHz, called preamble, is prefixed to the transmission waveform. A guard interval of $T_g = 25$ ms is inserted between the preamble and the start of modulated waveform to avoid interference. Note that, although the delay coverage of NOF1 channel is $T_d = 128$ ms, the channel power delay profile falls by more than 20 dB beyond $T_g = 25$ ms. Matched filtering with the preamble waveform is used for detecting the start of the received waveform.

Figure 12 shows the computed channel matrix, G_{B}, for the first few bits in a received packet at one of the instances in the WATERMARK channel record NOF1. Significant ISI remains even after gradient hetrodyne and lowpass filtering, as indicated by the strong off-diagonal entries in matrix G_{B}.

Figure 13 shows the performance of VSSD and MMSE receivers on the WATERMARK channel NOF1. NOF1 is a stable channel with coherence time spanning over several seconds. VSSD outperforms MMSE receiver by a margin

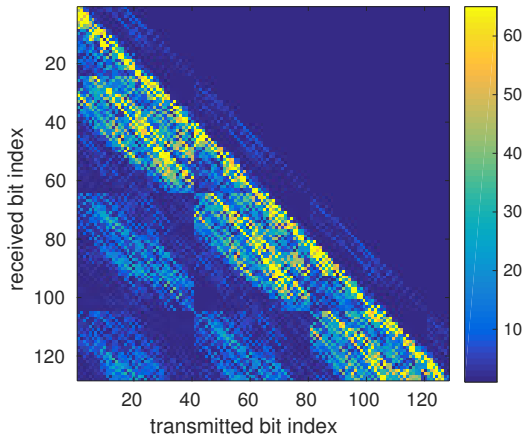

Fig. 12. Channel matrix after GradH processing at an instance in the WATERMARK channel record NOF1.

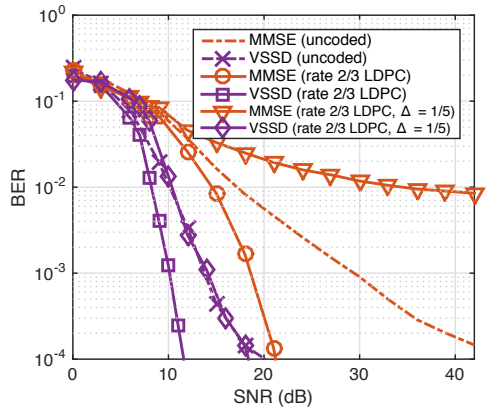

Fig. 13. BER of VSSD and MMSE receivers for S2C communications over the NOF1 channel in WATERMARK.

comparable to that in simulated UWA channels for both coded and uncoded communications in this real world channel also.

Figure 14 shows the BER of the proposed receiver on the NCS1 channel. NCS1 is characterized by a larger Doppler spread and therefore its impulse response varies significantly faster than NOF1. Both receivers require a higher SNR to achieve the same BER in NOF1 than NCS1. However, the strong relative performance of the VSSD receiver is maintained for both coded and uncoded communications even in this harsher UWA channel. While both NOF1 and NCS1 channels exhibit a comparable power delay profile, the coherence time of NCS1 is only about a tenth of a second that makes the channel prone to estimation errors. We see that, even in such challenging channel conditions as NCS1, VSSD is relatively resilient to channel estimation errors.

VII. CONCLUSIONS

In this work, we considered data symbol detection in an S2C receiver for doubly spread UWA channels. We formulated the problem of data detection for S2C communications over a wideband delay-scale channel and showed that the two existing S2C receivers are near MMSE decoders in only certain benign UWA channels. In more severe channels, where the existing

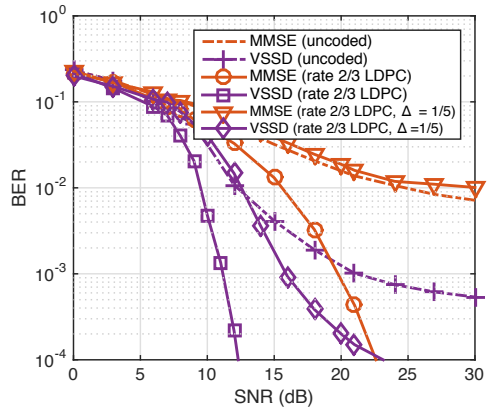

Fig. 14. BER of VSSD and MMSE receivers for S2C communications over the NCS1 channel in WATERMARK.

receivers either completely fail or must compromise on the data rate, we developed a new soft symbol decoder based on variational Bayes' inference. The input to the new decoder is the reduced data measurements at the output of the gradient heterodyne preprocessor of the existing S2C receivers.

Our proposed VSSD decoder estimates a probability vector (soft symbols) whose KL-distance to the true posterior of the symbol vector is minimized by iterating through a fixed point equation. In benign UWA channels, the VSSD decoder reduces to the existing S2C receivers. We showed that the fixed point iterations converge to a stationary point of the evidence lower bound in variational inference. We presented a few sufficient conditions that help to characterize the stationary point as a global maximum, local maximum or saddle point. Simulation results showed that VSSD significantly outperforms the MMSE decoder and maintains a robust performance, even under channel estimation errors, in challenging UWA channels. We applied the VSSD decoder on two contrasting real world UWA channels in the publicly available WATERMARK datasets. The new decoder outperforms the MMSE decoder in these channels as well, by a margin comparable to that in simulated UWA channels.

The ideal PAPR and low probability of intercept properties of S2C communications make it a promising candidate for terrestrial radio-frequency (RF) communications as well. Also, the VSSD algorithm developed in this paper is potentially applicable to other prevalent and emerging wireless communication systems.

APPENDIX

Evidence Lower Bound (ELBO): We derive the ELBO for soft symbol estimation. The first term in (23) is given by

$$\mathbb{E}_{q_{\phi(\mathbf{s}|G,\mathbf{z})}} \log p_\theta(\mathbf{z}|G,\mathbf{s}) = -N\log(2\pi\sigma^2) - \mathbb{E}_{q_{\phi(\mathbf{s}|G,\mathbf{z})}}\left[\frac{\|\mathbf{z}-G\mathbf{s}\|^2}{2\sigma^2}\right]. \quad (51)$$

Expanding the last term in (51), we get

$$\mathbb{E}_{q_{\phi(\mathbf{s}|G,\mathbf{z})}}\left[\|\mathbf{z}-G\mathbf{s}\|^2\right] = \|\mathbf{z}\|^2 - 2\mathbf{z}^T G\,\mathbb{E}_{q_{\phi(\mathbf{s}|G,\mathbf{z})}}[\mathbf{s}] + \mathbb{E}_{q_{\phi(\mathbf{s}|G,\mathbf{z})}}\left[\|G\mathbf{s}\|^2\right]. \quad (52)$$

We define:

$$q_{k,\text{Re}} \triangleq q_\phi\left(s_{k,\text{Re}} = \frac{1}{\sqrt{2}}\middle| G,\mathbf{z}\right) \in [0,1], \quad (53)$$

$$q_{k,\text{Im}} \triangleq q_\phi\left(s_{k,\text{Im}} = \frac{1}{\sqrt{2}}\middle| G,\mathbf{z}\right) \in [0,1]. \quad (54)$$

Note that the approximate posterior is completely specified by the soft symbol vector $\mathbf{q} \in \mathbb{R}^{2N}$ formed by stacking up $\mathbf{q}_k = [q_{k^*,\text{Re}}, q_{k^*,\text{Im}}]^T \in \mathbb{R}^2, k = 0,1,\ldots,N-1$. For our problem, we let the parameter $\phi \triangleq \mathbf{q}$.

The expectations in (52) can be evaluated as follows:

$$\mathbb{E}_{q_{\phi(\mathbf{s}|G,\mathbf{z})}}[s_{k,\text{Re}}] = \frac{1}{\sqrt{2}}(2q_{k,\text{Re}}-1), \quad (55)$$

$$\mathbb{E}_{q_{\phi(\mathbf{s}|G,\mathbf{z})}}[s_{k,\text{Im}}] = \frac{1}{\sqrt{2}}(2q_{k,\text{Im}}-1), \quad (56)$$

$$\mathbb{E}_{q_{\phi(\mathbf{s}|G,\mathbf{y})}}\left[\|G\mathbf{s}\|^2\right] = \sum_{l=0}^{2N-1}\mathbb{E}_{q_{\phi(\mathbf{s}|G,\mathbf{z})}}[G\mathbf{s}]_l^2, \quad (57)$$

$$\mathbb{E}_{q_{\phi(\mathbf{s}|G,\mathbf{z})}}[G\mathbf{s}]_l^2 = \sum_{k=0}^{N-1}\left(\eta_{l,k} + \nu_{l,k}\sum_{m\neq k}\nu_{l,m}\right), \quad (58)$$

where

$$\eta_{l,k} = \frac{1}{2}G_{l,k,\text{Re}}^2 + \frac{1}{2}G_{l,k,\text{Im}}^2 + G_{l,k,\text{Re}}G_{l,k,\text{Im}}(2q_{k,\text{Re}}-1)(2q_{k,\text{Im}}-1), \quad (59)$$

$$\nu_{l,m} = \frac{1}{\sqrt{2}}G_{l,m,\text{Re}}(2q_{m,\text{Re}}-1) + \frac{1}{\sqrt{2}}G_{l,m,\text{Im}}(2q_{m,\text{Im}}-1). \quad (60)$$

The ELBO regularizing term in (23) is

$$\mathbb{E}_{q_{\phi(\mathbf{s}|G,\mathbf{z})}}\left[\log\frac{q_\phi(\mathbf{s}|G,\mathbf{z})}{p_\theta(\mathbf{s})}\right] = KL(q_\phi||p_\theta). \quad (61)$$

We assume a uniform prior $p_\theta(\mathbf{s}) = \frac{1}{2^{2N}}$. We have:

$$\mathbb{E}_{q_{\phi(\mathbf{s}|G,\mathbf{z})}}\left[\log\frac{q_\phi(\mathbf{s}|G,\mathbf{z})}{p_\theta(\mathbf{s})}\right] = \log 2^{2N} - \sum_{k=0}^{N-1}\left[\mathcal{H}(q_{k,\text{Re}}) + \mathcal{H}(q_{k,\text{Im}})\right], \quad (62)$$

where $\mathcal{H}$ is the binary entropy function given by

$$\mathcal{H}(q) = -q\log q - (1-q)\log(1-q). \quad (63)$$

On combining the likelihood and regularization terms, we find the overall ELBO to be

$$\mathcal{L}(\theta,\mathbf{q},\mathbf{z}) = -N\log(2\pi\sigma^2) - \frac{\|\mathbf{z}\|^2}{2\sigma^2} + \frac{1}{\sqrt{2}\sigma^2}\mathbf{z}^T G(2\mathbf{q}-1) - \frac{1}{2\sigma^2}\sum_{l=0}^{2N-1}\sum_{k=0}^{N-1}\left(\eta_{l,k} + \nu_{l,k}\sum_{m\neq k}\nu_{l,m}\right) - \log 2^{2N} + \sum_{k=0}^{N-1} -q_{k,\text{Re}}\log q_{k,\text{Re}} - (1-q_{k,\text{Re}})\log(1-q_{k,\text{Re}}) + \sum_{k=0}^{N-1} -q_{k,\text{Im}}\log q_{k,\text{Im}} - (1-q_{k,\text{Im}})\log(1-q_{k,\text{Im}}). \quad (64)$$

Known Noise Variance: In this case, we take θ to be the empty set. The derivative of the overall cost function with respect to $q_{k^*,\text{Re}}$ is given by

$$\frac{\partial \mathcal{L}}{\partial q_{k^*,\text{Re}}} = \frac{\sqrt{2}}{\sigma^2}\mathbf{z}^T G_{:,k^*,\text{Re}} - \frac{1}{2\sigma^2}\sum_{l=0}^{2N-1}\left(\frac{\partial \eta_{l,k^*}}{\partial q_{k^*,\text{Re}}} + 2\frac{\partial \nu_{l,k^*}}{\partial q_{k^*,\text{Re}}}\sum_{m\neq k^*}\nu_{l,m}\right) - \log q_{k,\text{Re}} + \log(1-q_{k,\text{Re}}). \quad (65)$$

We have $\frac{\partial \eta_{l,k}}{\partial q_{k,\text{Re}}} = 2G_{l,k,\text{Re}}G_{l,k,\text{Im}}(2q_{k,\text{Im}}-1)$ and $\frac{\partial \nu_{l,k}}{\partial q_{k,\text{Re}}} = \sqrt{2}G_{l,k,\text{Re}}$. The above can be simplified to

$$\frac{\partial \mathcal{L}}{\partial q_{k^*,\text{Re}}} = \alpha_{k^*,\text{Re}} - \log q_{k,\text{Re}} + \log(1-q_{k,\text{Re}}), \quad (66)$$

where

$$\begin{aligned}\alpha_{k^*,\text{Re}} &= \frac{\sqrt{2}}{\sigma^2}\mathbf{z}^T G_{:,k^*,\text{Re}} \\ &- \frac{1}{\sigma^2}\sum_{l=0}^{2N-1} G_{l,k^*,\text{Re}}G_{l,k^*,\text{Im}}(2q_{k^*,\text{Im}}-1) \\ &- \frac{\sqrt{2}}{\sigma^2}\sum_{l=0}^{2N-1} G_{l,k^*,\text{Re}}\sum_{m\neq k^*}\nu_{l,m}. \quad (67)\end{aligned}$$

Setting $\frac{\partial \mathcal{L}}{\partial q_{k^*,\text{Re}}} = 0$, we get $q_{k^*,\text{Re}} = \varphi(\alpha_{k^*,\text{Re}})$, where $\varphi(x) = \frac{1}{1+e^{-x}}$. Similarly, setting $\frac{\partial \mathcal{L}}{\partial q_{k^*,\text{Im}}} = 0$, we get $q_{k^*,\text{Im}} = \varphi(\alpha_{k^*,\text{Im}})$ where

$$\begin{aligned}\alpha_{k^*,\text{Im}} &= \frac{\sqrt{2}}{\sigma^2}\mathbf{z}^T G_{:,k^*,\text{Im}} \\ &- \frac{1}{\sigma^2}\sum_{l=0}^{2N-1} G_{l,k^*,\text{Im}}G_{l,k^*,\text{Re}}(2q_{k^*,\text{Re}}-1) \\ &- \frac{\sqrt{2}}{\sigma^2}\sum_{l=0}^{2N-1} G_{l,k^*,\text{Im}}\sum_{m\neq k^*}\nu_{l,m}. \quad (68)\end{aligned}$$

Stacking up $\mathbf{q}_k = [q_{k^*,\text{Re}}, q_{k^*,\text{Im}}]^T \in \mathbb{R}^2$ into a vector, we get the following fixed point equations:

$$\mathbf{q} = \varphi(\boldsymbol{\alpha}), \quad (69)$$

where the vector $\boldsymbol{\alpha} \in \mathbb{R}^{2N}$ is formed by stacking $\boldsymbol{\alpha}_k = [\alpha_{k^*,\text{Re}}, \alpha_{k^*,\text{Im}}]^T \in \mathbb{R}^2, k = 0, 1, \ldots, N-1$.

Unknown Noise Variance: In this case, we take $\theta = \{\sigma^2\}$. Differentiating the ELBO in (64) with respect to σ^2, we get

$$\frac{\partial \mathcal{L}}{\partial \sigma^2} = -\frac{N}{\sigma^2} + \frac{\|\mathbf{z}\|^2}{2\sigma^4} - \frac{1}{\sqrt{2}\sigma^4}\mathbf{z}^T G(2\mathbf{q}-1) + \frac{1}{2\sigma^4}\sum_{l=0}^{2N-1}\sum_{k=0}^{N-1}\left(\eta_{l,k} + \nu_{l,k}\sum_{m\neq k}\nu_{l,m}\right). \quad (70)$$

Setting $\frac{\partial \mathcal{L}}{\partial \sigma^2} = 0$ and solving for σ^2, we find

$$\hat{\sigma}^2 = \frac{\|\mathbf{z}\|^2}{2N} - \frac{1}{\sqrt{2}N}\mathbf{z}^T G(2\mathbf{q}-1) + \frac{1}{2N}\sum_{l=0}^{2N-1}\sum_{k=0}^{N-1}\left(\eta_{l,k} + \nu_{l,k}\sum_{m\neq k}\nu_{l,m}\right). \quad (71)$$

Unknown Channel and Noise Variance: In this case, we take $\theta = \{\sigma^2, G\}$. To differentiate the ELBO with respect to G, we notice that the terms in (64) that depend on G come from the left hand side of (52), i.e.,

$$\mathcal{L}_G = \mathbb{E}_{q_{\phi(\mathbf{s}|G,\mathbf{z})}}\left[(\mathbf{z}-G\mathbf{s})^T(\mathbf{z}-G\mathbf{s})\right]. \quad (72)$$

On differentiating $\mathcal{L}_G$ with respect to $G_{i,j}$ and setting to zero we get the following system of equations:

$$G\bar{\mathbf{s}} = \mathbf{z}, \quad (73)$$

where $\bar{\mathbf{s}} \triangleq \mathbb{E}_{q_{\phi(\mathbf{s}|G,\mathbf{z})}}[\mathbf{s}]$. The jth entry of $\bar{\mathbf{s}}$ is given by $\bar{s}_j = \frac{1}{\sqrt{2}}(2q_j - 1)$, if a data symbol is mounted at jth symbol location. At locations where the pilot symbols are mounted (to facilitate channel estimation), we have $\bar{s}_j = p_j$, where p_j is a known pilot symbol mounted at jth location. The channel matrix estimate can be refined using (73) once an initial estimate of the soft symbol vector is obtained through the fixed point update in (69). Note that G has $4N^2$ entries that need to be estimated from $2N$ equations in (73). One way to accomplish this is to exploit channel sparsity as in [21]. To see that, we make use of the relation $G = Q^T H$ and rewrite (73) in the form:

$$A\mathbf{h} = \mathbf{z}, \quad (74)$$

where $A = \sum_{i=0}^{N-1}\left(\bar{s}_{2i}Q^T C_i - \bar{s}_{2i+1}Q^T S_i\right) \in \mathbb{R}^{2N\times N_\text{P}}$. Now, following the approach in [21], equation (74) can be readily turned into a form suitable for estimating the channel parameters $\{h_p, \tilde{\tau}_p, b_p : p = 0, 1, \ldots, N_\text{P}-1\}$. The expression for the noise variance is the same as in (71), and is evaluated during the iterations once the soft symbol vector and the channel estimates are obtained using the fixed point update and (73), respectively.

REFERENCES

[1] K. P. Arunkumar and C. R. Murthy, "Variational soft symbol decoding for sweep spread carrier based underwater acoustic communications," in *IEEE 20th International Workshop on Signal Processing Advances in Wireless Communications*, Cannes, France, Jul. 2019.

[2] F. Campagnaro, R. Francescon, P. Casari, R. Diamant, and M. Zorzi, "Multimodal underwater networks: Recent advances and a look ahead," in *WUWNet 2017, Halifax, Canada*, Nov. 2019.

[3] Y. Li, Y. Zhang, W. Li, and T. Jiang, "Marine wireless big data: Efficient transmission, related applications, and challenges," *IEEE Trans. Wireless Commun.*, vol. 25, no. 1, pp. 19–25, Feb. 2018.

[4] Y. Li, S. Wang, C. Jin, Y. Zhang, and T. Jiang, "A survey of underwater magnetic induction communications: Fundamental issues, recent advances, and challenges," *IEEE Commun. Surveys Tuts.*, vol. 21, no. 3, pp. 2466–2487, third quarter 2019.

[5] M. Stojanovic and J. Preisig, "Underwater acoustic communication channels: Propagation models and statistical characterization," *IEEE Commun. Mag.*, vol. 47, no. 1, pp. 84–89, Jan. 2009.

[6] K. G. Kebkal and R. Bannasch, "Sweep-spread carrier for underwater communication over acoustic channels with strong multipath propagation," *J. Acoust. Soc. Am.*, vol. 112, no. 5, pp. 2043–2052, Nov. 2002.

[7] Evologics GmbH. Ackerstrasse 76, 13355 Berlin, Germany. [Online]. Available: https://evologics.de/acoustic-modems

[8] "Underwater acoustic MODEMS," in *Product Information Guide*. Evologics GmbH.

[9] D. Robb, J. Willners, N. Valeyrie, F. Garcia, A. Laskov, X. Liu, P. Patron, H. Hastie, and Y. Petillot, "A natural language interface with relayed acoustic communications for improved command and control of AUVs," in *2018 IEEE/OES Autonomous Underwater Vehicle Workshop (AUV)*. IEEE, Nov. 2018.

[10] A. Signori, F. Campagnaro, F. Steinmetz, B.-C. Renner, and M. Zorzi, "Data gathering from a multimodal dense underwater acoustic sensor network deployed in shallow fresh water scenarios," *Journal of Sensor and Actuator Networks*, vol. 8, no. 55, Nov. 2019.

[11] D. Carlson, A. Ostrovskii, K. Kebkal, and H. Gildor, *Moored automatic mobile profilers and their application*. LAP LAMBERT Academic Publishing, June 2013, pp. 169–206.

[12] K. G. Kebkal and R. Bannasch, "Method and devices for transmitting and receiving information," *U.S. Patent*, vol. 6,985,749 B2, Jan. 2006.

[13] K. Kebkal, A. K. Kebkal, and G. A. Ermolin, "Mathematic and experimental evaluation of phase errors when receiving hydro-acoustic PSK-signals with sweep-spread carrier in reverberant underwater environments," in *Proc. MTS/IEEE OCEANS Conf.*, June 2013.

[14] K. G. Kebkal, O. G. Kebkal, and R. Bannasch, "Synchronisation of underwater communication receivers by means of swept pulses," in *Proc. of the 4th Int. Conf. on Underwater Acou. Measurements: Technologies and Results*, June 2011.

[15] K. G. Kebkal, V. K. Kebkal, O. G. Kebkal, and R. Petroccia, "Clock synchronization in underwater acoustic networks during payload data exchange," in *Proc. 2nd Int. Conf. Exhibit. Underwater Acoust.*, June 2014.

[16] K. Kebkal, A. Kebkal, and V. Kebkal, "Synchronization tools of acoustic communication devices in control of underwater sensors, distributed antennas, autonomous underwater vehicles," in *Gyroscopy and Navigation*, vol. 5, no. 4. Pleiades Publishing, 2014, pp. 257–265.

[17] L. Marchetti and R. Reggiannini, "An efficient receiver structure for sweep-spread-carrier underwater acoustic links," *IEEE J. of Ocean. Eng.*, vol. 41, no. 2, pp. 440–449, April 2016.

[18] Y. Jiang and P. Antonia, "Discrete time-scale characterization of wideband time-varying systems," *IEEE Trans. Signal Process.*, vol. 54, no. 4, pp. 1364–1375, April 2006.

[19] H. Franz and M. Gerald, *Wireless Communications Over Rapidly Time-Varying Channels*. Burlington, MA 01803, USA: Elsevier, 2011.

[20] X. Jiang, W.-J. Zeng, and X.-L. Li, "Time delay and Doppler estimation for wideband acoustic signals in multipath environments," *J. Acoust. Soc. Am.*, vol. 130, no. 2, pp. 850–857, Aug. 2011.

[21] C. R. Berger, S. Zhou, J. C. Preisig, and P. Willett, "Sparse channel estimation for multicarrier underwater acoustic communication: From subspace methods to compressed sensing," *IEEE Trans. Signal Process.*, vol. 57, no. 5, pp. 2941–2965, May 2011.

[22] J. Z. Huang, S. Zhou, J. Huang, C. R. Berger, and P. Willett, "Progressive inter-carrier interference equalization for OFDM transmission over time-varying underwater acoustic channels," *IEEE J. Sel. Topics Signal Process.*, vol. 5, no. 8, pp. 1524–1536, Dec. 2011.

[23] S. Zhou and Z. Wang, "OFDM for underwater acoustic communications." Wiley, 2014.

[24] M. Stojanovic and L. Freitag, "Multichannel detection for wideband underwater acoustic CDMA communications," *IEEE J. of Ocean. Eng.*, vol. 31, no. 3, pp. 685–695, Jul. 2006.

[25] Z. Wang, S. Zhou, G. B. Giannakis, C. R. Berger, and J. Huang, "Frequency-domain oversampling for zero-padded OFDM in underwater acoustic communications," *IEEE J. of Ocean. Eng.*, vol. 37, no. 1, pp. 14–24, Jan. 2012.

[26] A. Goldsmith, *Wireless Communications*. Cambridge University Press, 2005.

[27] S. S. Thoota and C. R. Murthy, "Variational Bayesian inference based soft-symbol decoding for uplink massive MIMO systems with low resolution ADCs," in *Proc. Asilomar Conference on Signals, Systems and Computers*, Nov. 2019.

[28] ——, "Quantized variational Bayesian joint channel estimation and data detection for uplink massive MIMO systems with low resolution ADCs," in *Proc. IEEE International Workshop on Machine Learning for Signal Processing, Pittsburg, PA, USA*, Oct. 2019.

[29] B. Li, S. Zhou, M. Stojanovic, L. Freitag, and P. Willett, "Multicarrier communication over underwater acoustic channels with nonuniform Doppler shifts," *IEEE J. Ocean. Eng.*, vol. 33, no. 2, pp. 1638–1649, Apr. 2008.

[30] D. P. Kingma and M. Welling, "Auto-encoding variational Bayes," in *Proceedings of the 2nd International Conference on Learning Representations*, Apr. 2014.

[31] C. Studer, M. Wenk, A. Burg, and H. Bölcskei, "Soft-output MIMO detection algorithms: Performance and implementation aspects," in *Proc. of the 40th Asilomar Conference on Signals, Systems, and Computers*, Oct. 2006.

[32] C. Studer, A. Burg, and H. Bölcskei, "Soft-output sphere decoding: Algorithms and VLSI implementation," *IEEE J. Sel. Areas Commun.*, vol. 26, no. 2, pp. 290–300, Feb. 2008.

[33] "MATLAB Communications System Toolbox, version 6.3," The Mathworks, Inc., Natick, Massachusetts.

[34] M. Helmling, S. Scholl, F. Gensheimer, T. Dietz, K. Kraft, S. Ruzika, and N. Wehn, "Database of Channel Codes and ML Simulation Results," www.uni-kl.de/channel-codes, 2019.

[35] P. Qarabaqi and M. Stojanovic, "Statistical characterization and computationally efficient modeling of a class of underwater acoustic communication channels," *IEEE J. Ocean. Eng.*, vol. 38, no. 4, pp. 701–717, Oct. 2012.

[36] M. Stojanovic. Acoustic channel simulator. [Online]. Available: http://millitsa.coe.neu.edu/?q=research/simulator

[37] P. A. van Walree, F. Socheleau, R. Otnes, and T. Jenserud, "The Watermark benchmark for underwater acoustic modulation schemes," *IEEE J. Ocean. Eng.*, vol. 42, no. 4, pp. 1007–1018, Oct. 2017.

[38] R. Otnes, P. A. van Walree, and T. Jenserud, "Validation of replay-based underwater acoustic communication channel simulation," *IEEE J. Ocean. Eng.*, vol. 38, no. 4, pp. 689–700, Oct. 2013.

[39] P. A. van Walree, R. Otnes, and T. Jenserud, "The Watermark manual and users guide version 1.0," in *Norwegian Defense Research Establishment (FFI)*, Nov. 2016.

Arunkumar K. P. received the B. Tech. (Hons) degree in Electrical and Electronics Engineering, in 1998, from the Calicut University, India. Since 2000, he has been working as a Scientist at Naval Physical & Oceanographic Laboratory, Defence Research & Development Organization (DRDO), Kochi, India. He received the M. E. degree, in 2007, in Signal Processing, from the Indian Institute of Science (IISc), Bangalore, India, as a sponsored candidate from DRDO. He was awarded the Prof. I. S. N. Murthy medal for the best M. E. student in Signal Processing discipline at IISc, Bangalore, for the year 2005-2007. He is currently pursuing Ph. D. as an external registrant from DRDO at the Signal Processing for Communications Lab in the Department of Electrical Communication Engineering, IISc, Bangalore. His research interests include sparse signal recovery algorithms, sensor array signal processing and underwater acoustic communications.

Chandra R. Murthy (S'03–M'06–SM'11) received the B. Tech. degree in Electrical Engineering from the Indian Institute of Technology, Madras in 1998, the M. S. and Ph. D. degrees in Electrical and Computer Engineering from Purdue University and the University of California, San Diego, in 2000 and 2006, respectively. From 2000 to 2002, he worked as an engineer for Qualcomm Inc., where he worked on WCDMA baseband transceiver design and 802.11b baseband receivers. From Aug. 2006 to Aug. 2007, he worked as a staff engineer at Beceem Communications Inc. on advanced receiver architectures for the 802.16e Mobile WiMAX standard. In Sept. 2007, he joined the Department of Electrical Communication Engineering at the Indian Institute of Science, Bangalore, India, where he is currently working as a Professor.

His research interests are in the areas of energy harvesting communications, multiuser MIMO systems, and sparse signal recovery techniques applied to wireless communications. He has 50+ journal and 80+ conference papers to his credit. He is a recipient of the MeitY Young Faculty Fellowship from the Govt. of India and the Prof. Satish Dhawan state award for engineering from the Karnataka State Government. His paper won the best paper award in the Communications Track in the National Conference on Communications 2014. He was an associate editor for the IEEE Signal Processing Letters during 2012-16. He is a past Chair of the IEEE Signal Processing Society, Bangalore Chapter. He was an elected member of the IEEE SPCOM Technical Committee for the years 2014-16, and has been re-elected for the years 2017-19. He is serving as an associate editor for the IEEE Transactions on Signal Processing, the IEEE Transactions on Communications, and Sadhana Academy Proceedings in Engineering Sciences.